OPTIMAL THERMAL COMPRESSORS FOR MINIATURIZED AMMONIA-WATER ABSORPTION SYSTEMS

A Dissertation
Presented to
The Academic Faculty

by

Marcel Staedter

In Partial Fulfillment
of the Requirements for the Degree
Doctor of Philosophy in Mechanical Engineering

Georgia Institute of Technology
May 2018

OPTIMAL THERMAL COMPRESSORS FOR MINIATURIZED AMMONIA-WATER ABSORPTION SYSTEMS

Approved by:

Dr. Srinivas Garimella, Advisor
George W. Woodruff School of
Mechanical Engineering
Georgia Institute of Technology

Dr. Thomas Fuller
School of Chemical and Biomolecular
Engineering
Georgia Institute of Technology

Dr. Sheldon Jeter
George W. Woodruff School of
Mechanical Engineering
Georgia Institute of Technology

Dr. S. Mostafa Ghiaasiaan
George W. Woodruff School of
Mechanical Engineering
Georgia Institute of Technology

Dr. Yogendra Joshi
George W. Woodruff School of
Mechanical Engineering
Georgia Institute of Technology

Date Approved: February 22, 2018

For Mahsa

ACKNOWLEDGEMENTS

I would like to express my deepest gratitude to Dr. Srinivas Garimella, my advisor and mentor, for his guidance, support, and encouragement throughout this work. It is with great appreciation that I look back at the opportunity to be part of the Sustainable Thermal Systems Laboratory to conduct my research work. The last few years may not have been the easiest but they have formed a strong foundation for many years of collaboration and interaction to come.

I would like to thank my Ph.D. committee members Drs. Sheldon Jeter, Thomas Fuller, S. Mostafa Ghiaasiaan and Yogendra Joshi for their time and suggestions during the process of this work.

It has been a privilege to work with the members, past and present, of the Sustainable Thermal Systems Laboratory. In particular, I need to thank Drs. Anand Nagavarapu and Christopher Keinath for their help during the early stages of this work; Drs. Alexander Rattner and Adrienne Little for their camaraderie and inspiring commitment to excellence; Khoudor Keniar, Dr. Dhruv Hoysall and Anurag Goyal for their collaboration and interesting discussions.

While I deeply appreciate all the lessons I learned during this Ph.D., I am immeasurably grateful for what my daughter, Ellen Soraya Staedter, was able to teach me over the past 15 months - lessons that no academic institution can provide in a lifetime. Most importantly, I need to thank my wonderful wife, Mahsa, for her wisdom, kindness and strength.

TABLE OF CONTENTS

LIST OF TABLES

LIST OF FIGURES

NOMENCLATURE

A	Area, m^2
AAD	Absolute average deviation
AD	Absolute deviation
AHRI	Air Conditioning, Heating and Refrigeration Institute
ANN	Artificial Neural Network
C_T	Total molar concentration, kmol m^{-3}
c_P	Specific heat capacity, kJ kg^{-1} K^{-1}
CAT	Closest approach temperature, K
CCFL	Countercurrent flow limitations
COP	Coefficient of performance
CR	Circulation ratio
CV	Control volume
D	Diameter, m
D_{aw}	Ammonia-water mass diffusivity, m^2 s^{-1}
EX	Exergy rate, kW
f	Fraction
GAX	Generator-Absorber-Exchange
h	Specific enthalpy, kJ kg^{-1}
i	Segment, state point or frame number
K	Binary mixture correction factor
k	Thermal conductivity, W m^{-1} K^{-1}
LMTD	Logarithmic mean temperature difference, K
M	Molar mass, kg mol^{-1}
$\dot{m}$	Mass flow rate, kg s^{-1}

N	Total number of stages
NPS	Nominal Pipe Size
Nu	Nusselt number
$\dot{n}$	Molar flux, kmol m^{-2} s^{-1}
P	Pressure, kPa
PAC	Process Automation Controller
PID	Proportional-Integral-Derivative
Pr	Prandtl number
PWM	Pulse with modulation
q	Vapor quality, Specific heat input, kJ kg^{-1}
$\dot{Q}$	Heat duty, kW
R	Thermal transfer resistance, K W^{-1}
R^2	Coefficient of determination
Re	Reynolds number
s	Specific entropy, kJ kg^{-1} K^{-1}
SBG	Silver-Bell-Ghaly
Sc	Schmidt number
SCC	Simple cooling cycle
Sh	Sherwood number
T	Temperature,°C
TC	Thermal compressor
TR	Temperature ratio
th	Thickness, m
U	Overall heat transfer coefficient, W K^{-1} m^{-2}
UA	Overall heat transfer conductance, W K^{-1}
VGU	Vapor Generation Unit
x	Ammonia concentration (mass basis)

$\tilde{x}$	Ammonia concentration (molar basis)
Z	Ratio of sensible to total heat transfer
$\overline{a}$	average value of generic variable, a
Z	Ratio of sensible to total heat duty
z	Concentration of condensing flux (mass basis)
$\tilde{z}$	Concentration of condensing flux (molar basis)

Greek Symbols

α	Heat transfer coefficient, W m^{-2} K^{-1}
β	Mass transfer coefficient, m s^{-1}
Φ	Optimization parameter
Δ	Difference
ρ	Density, kg m^{-3}
Λ	Binary mixture boiling correction term
ε	Heat exchanger effectiveness, emissivity
σ	Stefan-Boltzman constant (5.670367×10^{-8} W m^{-2} K^{-4}) or surface tension, N m^{-1}
ψ	Specific flow exergy, kJ kg^{-1}
η	Efficiency

Subscripts/Superscripts

A	Ammonia
abs	Absorber
amb	Ambient
bulk	Bulk
CF	Coupling fluid
comb	Combustion
con	Condenser
cond	Condensation
conv	Convection heat transfer

cs	Concentrated solution (high ammonia concentration)
cycle	Thermodynamic absorption cycle
des	Desorber
ds	Dilute solution (low ammonia concentration)
evap	Evaporator
feed	Desorber concentrated solution inlet state point
gas	Natural gas or heat source gas stream
glide	Temperature change in evaporator
h	Hydraulic
high	High pressure side of absorption system
hot	Desorber dilute solution outlet state point
i	Segment, state point or frame number
ideal	Ideal
in	Inlet
ineq	In-equilibrium condition
ins	Insulation
int	Interface
L	Liquid state
latent	Phase change specific
loss	Thermal loss
low	Evaporator inlet state point, low pressure side of system
NH_3	Ammonia
H_2O	Water
opt	Optimal
out	Outlet
pur	Purification
rad	Radiation heat transfer

rect	Rectifier
ref	Refrigerant
reflux	Rectifier condensate reflux
RPC	Refrigerant Precooler
sat	Saturated liquid or vapor state
sens	sensible
SHX	Solution heat exchanger
sol	Solution
sub	Subcooling
sur	Surface
T	Total
TC	Thermal compressor
total	Total
V	Vapor state
wall	Wall
0	Reference/dead state
I	First-law based
II	Second-law based
*	Thermodynamic equilibrium

SUMMARY

The design and optimization of the thermal compressor for small-capacity ammonia-water absorption chillers was conducted. In an initial investigation, a complete absorption chiller, driven by natural gas and based on microscale heat exchanger technology, was designed, fabricated and tested. Experiments validated the scalability of microscale heat exchangers and their application to small-capacity absorption chillers. Optimization of the thermal compressor was identified as a key research objective for further development of this technology, which is the core work of the present study. Ammonia-water desorption and rectification components are the main elements of the thermal compressor, dictating performance and size. A quantitative thermodynamic framework for thermal compressor performance was developed and guided design concepts for desorption and rectification. These are based on diabatic distillation principles and include a microchannel based desorber and rectifier as well as a gas-coupled desorber to address a range of applications. The framework was used to develop a data-driven thermodynamic model for the development of a thermal compressor module. Two optimal desorption temperatures were identified to maximize energetic and exergetic performance, respectively.

A hydrodynamic study was conducted to validate the feasibility of the proposed design concepts. Liquid-vapor countercurrent flow limitations were addressed through a hydrodynamic design methodology devised in this study. This allowed for the specification of geometric features of the proposed designs. High-speed video analysis was conducted to quantify hydrodynamic parameters relevant for the development of a

coupled heat and mass transfer model. These parameters included characteristic size of vapor structures, vapor structure velocity, liquid-vapor interfacial area and heat transfer area.

Heat and mass transfer models were developed, incorporating hydrodynamic data. A modular modeling approach was used, whereby physical consistency of various heat and mass transfer processes is achieved while reducing model complexity. Various pool boiling and binary mixture correction correlations available in the literature were compared. Model results show that highly compact, lightweight desorption and rectification components can be realized.

A test facility was constructed to simulate operation of the thermal compressor within an absorption heat pump and conduct an experimental investigation to validate the performance of the proposed design concepts. Prototype desorption and rectification components were fabricated for a nominal system cooling capacity of 3.5 kW. Two types of heat source coupling were tested. A thermal oil coupling fluid was used for the microchannel based desorber and an exhaust gas simulator was used for the gas-coupled desorber concept. A range of desorption pressures from 1300 kPa to 2600 kPa was investigated. Each desorption pressure was tested for a range of concentrated solution ammonia mass fraction ranging from 37% to 52% as well as a range of desorption temperatures that included model predictions for optimal desorption temperatures. Optimal exergetic and energetic thermal compressor performance could be demonstrated, validating the thermal compressor concept.

Data were analyzed to determine heat and mass transfer coefficients. Desorption heat transfer coefficients were found to range from 1500 to 3500 W m^{-2} K^{-1}. A mass

transfer correction correlation was developed for use with pool boiling correlations from the literature. Good agreement was achieved with average and absolute average deviation of 2.7% and 13.6%, respectively. Component level results for overall heat transfer coefficient and vapor purification efficiency were determined. For the microchannel design concept, the former ranged between 600 W m^{-2} K^{-1} and 1100 W m^{-2} K^{-1} while the latter was shown to be relatively constant at approximately 93%. Gas-side pressure drop limitations governed the overall heat transfer coefficient for the gas-coupled design concepts. Gas-side heat transfer coefficients of 100 W m^{-2} K^{-1} were measured at a maximum pressure drop of 1200 Pa. Very high purification efficiency of greater than 95% could be demonstrated in the direct-coupled desorber design concept. Vapor heat transfer coefficients in the partial condensation process of the rectifier were found to range between 70 and 170 W m^{-2} K^{-1}. A sensible vapor heat transfer correlation was developed for use with an equilibrium heat and mass transfer correction scheme and was shown to have excellent agreement with experimental results. A comparative assessment between direct gas-coupled and microchannel desorber designs was made. It was shown that the choice of desorber configuration strongly depends on the specific application.

Finally, a data-driven control strategy for the thermal compressor was developed and experimentally validated. The thermodynamic model is applied in combination with system specific operating data to enable the *variable thermal compressor* control scheme. Solution pump speed modulation and active desorption temperature control allow for highly flexible system operation while maintaining optimal performance over a wide range of operating conditions. Effective response to changes in capacity, ambient temperature, and evaporator temperature was demonstrated.

CHAPTER 1. INTRODUCTION

The widespread and successful application of refrigeration and space conditioning technologies can be attributed, in part, to the fact that the commonly employed vapor compression cycle is simple and allows for compact, small capacity machines that can be economically produced at high volume. Also, the development of an electric grid facilitated the widespread use of these machines (Cooper, 2002). While vapor compression technology benefits from the use of well optimized compact systems, their reliance on high-grade electrical energy has led to interest in alternative technologies for some applications. In general, thermally driven systems replace electricity as the main energy input with low grade thermal energy, which can be in the form of waste heat. Benefits include a more efficient overall energy system, flexible use of energy sources and avoidance of environmentally deleterious synthetic refrigerants. Specifically, the vapor absorption cycle has been in use for over a century. But due to typical component size requirements for absorption systems, the proliferation of vapor compression machines relegated absorption systems to large capacity industrial applications (Briley, 2004). However, recent developments in microscale heat and mass exchangers enables research and development efforts on small capacity machines for residential, mobile and light commercial applications (Garimella, 2003).

1.1 The Thermal Compressor

Figure 1.1 (left) shows a single-effect ammonia-water absorption cycle. The left side of the cycle, i.e., condenser, evaporator and recuperative heat exchanger (optional), closely resembles the corresponding portion of a vapor compression cycle. In the vapor

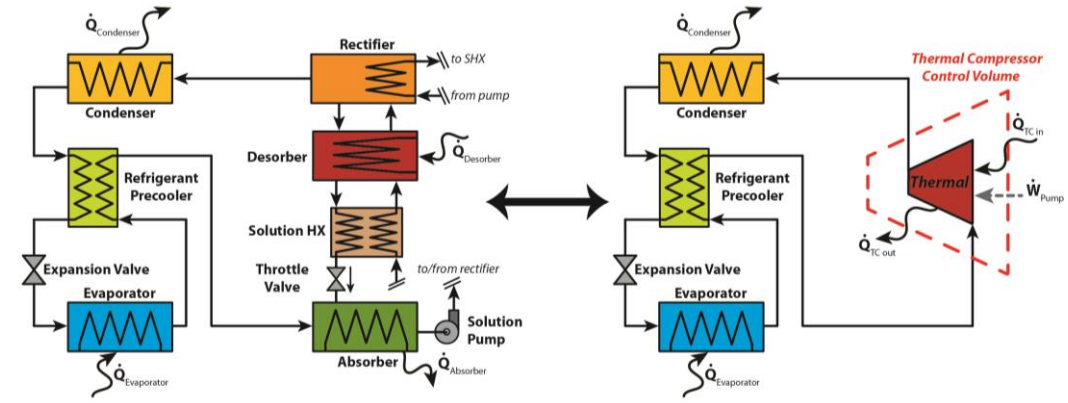

Figure 1.1: Simple absorption cycle (left), conceptual representation of thermal compression cycle (right)

absorption cycle, however, the mechanical compressor is replaced with a set of heat exchangers and a pump. The objective of this part of the vapor absorption cycle is to produce high pressure refrigerant vapor while receiving low pressure refrigerant. Thus, the concept of the *thermal compressor* as shown in Figure 1.1 (right) can be applied to provide a qualitative analogy to the vapor compression cycle. Its main energy input is low-grade thermal energy in contrast to high-grade mechanical or electric energy required by a mechanical compressor.

Compact thermal compressors can be integrated with a wide range of applications throughout the thermal energy chain. Heat recovered from engine exhaust in the transportation sector can be used for cabin air-conditioning. Energy required for cargo cooling in the refrigerated trucking industry can be provided in the form of exhaust heat, reducing overall fuel consumption in the transportation sector. Small-capacity stationary power generation is another potential application. For example, military applications can particularly benefit from this technology. Waste heat recovery from diesel generators deployed in field operations results in better utilization of fuel delivered to conflict zones.

Finally, heat pump water heating is an example of the use of the existing natural gas infrastructure to increase energy utilization. Specifically, replacing conventional natural gas driven water heaters with small-capacity absorption heat pumps can contribute to a meaningful reduction of residential energy use Keinath *et al.* (2017).

Heat input to the thermal compressor is used in a thermal separation process of a mixture consisting of an absorbent and a refrigerant. The latter is the more volatile constituent, allowing for separation from the absorbent during phase change. This process occurs in the desorber component shown in Figure 1.1. The refrigerant-depleted absorbent (dilute solution) is expanded to a low pressure at the absorber inlet. Refrigerant from the evaporator and, if used, the refrigerant precooler, is absorbed into that stream in the absorber component. This process is exothermic and requires heat rejection. The incompressible solution of refrigerant and absorbent (concentrated solution) requires very little pump work compared to the energy input required in the desorber. While pump work is typically provided in the form of electricity, only approximately 1% of the total energy input is required by the solution pump (Herold *et al.*, 1996).

Many working fluid combinations have been considered in the literature for use in vapor absorption systems (Boman *et al.*, 2017), but only the working pairs of ammonia-water and lithium bromide-water are currently considered to be commercially viable. Lithium bromide-water is not suitable for operation below freezing temperatures as water is the refrigerant. Further, crystallization concerns limit the range of operating conditions. Moreover, low working pressures and a high specific volume of the refrigerant limit the use of microchannel heat exchangers for this working fluid pair due to pressure drop constraints. Ammonia as a refrigerant has favorable transport and thermodynamic

properties and is suitable for refrigeration and low-temperature applications. In addition, the specific volume of ammonia vapor at typical operating pressures is sufficiently small to enable the use of microchannel heat exchangers without excessive pressure drop requirements. Therefore, ammonia-water is selected as the working pair for the thermal compressor.

The ammonia-water working fluid pair poses several challenges (Bogart, 1982). The vapor pressure of water during the thermal separation process in not negligible and reduces refrigerant purity of the vapor leaving the desorber. The presence of water in the refrigerant causes system performance degradation due to an excessive temperature increase during evaporation. This reduces the amount of latent heat available to meet evaporator cooling load below a certain temperature. The decrease in the amount of refrigerant that can be effectively used for cooling necessitates increased vapor generation rates and heat input requirements to meet a specific cooling load. This directly results in *COP* reduction. Figure 1.1 shows the use of a solution cooled rectifier to purify the vapor stream through partial condensation. Vapor purification requires heat and mass transfer area to achieve a target ammonia mass fraction. This contributes significantly to overall system size and weight (Fernandez-Seara *et al.*, 2003). Therefore, optimization of the vapor desorption and purification stages are key objectives for the development of thermal compressors for small capacity applications. Component size reduction also addresses the concern of exposure to ammonia. Specifically, working fluid inventories are reduced with the use of highly compact components. This, in turn, reduces risk of exposure to ammonia in the event of a system leak.

The ability to utilize low-grade thermal energy is accompanied by constraints such as capital cost and component size. Thermal compressor components consist primarily of heat and mass exchangers. While conventional heat exchangers can be used in large-scale, centralized applications with sufficient economic justification, size, weight and economic constraints have prevented small-capacity thermal compressor developments. Many low-grade heat sources such as waste heat including engine exhaust are, however, dispersed. The current state of commercially available, thermally activated chillers and heat pumps does not provide a feasible solution for the widespread utilization of these resources.

Thermal compressor optimization enables the development of compact and efficient absorption systems. The results can be applied in techno-economic analyses to accurately identify applications with highest economic feasibility. It should be noted that the replacement of vapor compression systems is not the primary objective of the development of small-capacity absorption systems. Rather, the optimal utilization of thermal energy is the overarching goal. In some situations, this may result in the replacement of conventional vapor compression systems, while in other cases, it may lead to a combined use of vapor absorption and vapor compression systems to meet cooling and heating demands and maximizing thermal energy utilization. Detailed techno-economic analyses for specific applications are beyond the scope of this study. However, the results of this study could lead to favorable techno-economic metrics by enabling the development of high performance compact vapor absorption systems. The analysis tools

developed in this study for thermal compressor characterization simplify vapor absorption cycle analysis and, therefore, facilitate techno-economic analyses.

1.2 Research Scope and Objectives of the Present Study

The first objective of this study is to demonstrate the feasibility of small-capacity ammonia-water absorption systems. This is accomplished with a system level investigation of the development of a 7 kW cooling capacity chiller. Scale-up of microchannel heat exchanger design concepts and monolithic component integration is demonstrated. It is shown that further progress at the system level requires research efforts that focus on thermal compressor optimization.

An optimal thermal compressor for small-capacity applications has the following characteristics:

- Minimization of temperature required for heat input
- Minimization of thermal energy required
- Minimization of component size and weight
- Production of high purity vapor
- Wide range of application and use of various heat sources
- Ability to respond to demand variation and operating conditions while maintaining optimal performance

The approach taken in this study is shown in Figure 1.2. Findings from the system level investigation are applied to individual areas of investigation. First, a thermodynamic framework for the thermal compressor is developed. This extends the concept of the thermal compressor from a qualitative descriptor to a quantifiable entity with

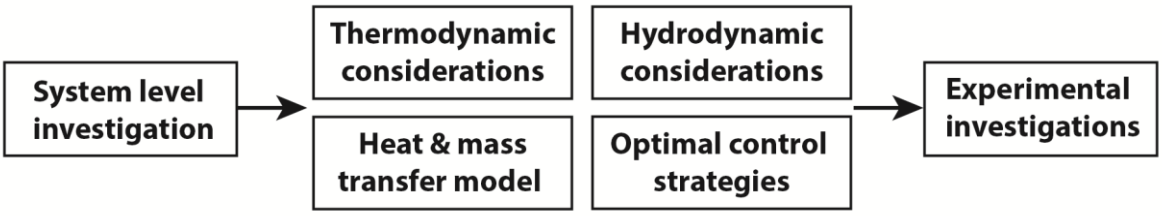

Figure 1.2: Outline of research approach in present study

performance metrics. It is shown that desorption and rectification components are critical to achieving optimal thermal compressor objectives. The thermodynamic framework is used to guide component designs for a wide range of applications as well as optimal control strategies.

Thermodynamically optimized desorption and rectification design concepts are developed and their feasibility is established in a hydrodynamic investigation that addresses liquid-vapor countercurrent flow limitations. The hydrodynamic investigation also includes high-speed flow visualization to evaluate parameters that are relevant for the development of heat and mass transfer models.

A principal objective of this study is to further the understanding of binary mixture heat and mass transfer during phase change. This allows for the design of highly compact and effective desorption and rectification components. Detailed heat and mass transfer models are developed for the proposed desorption and rectification components. These models are used to optimize component designs and provide further insight into optimal system control.

Results from the system level investigation as well as from other aspects of this study are applied to develop an effective control strategy that enables flexible and efficient thermal compressor control.

Finally, an experimental investigation is conducted for the evaluation of the thermal compressor as well as performance of desorption and rectification components. Heat and mass transfer models are refined based on experimental results. The proposed control strategy is validated through testing of thermal compressor response to variation in capacity demand and operating conditions.

1.3 Dissertation Organization

The organization of subsequent chapters is as follows:

- Chapter 2 presents the results of a system-level investigation. Recent advances in absorption technology are applied to model, design, fabricate and test a 7-kW cooling capacity ammonia-water absorption chiller.
- Chapter 3 presents thermodynamic considerations for thermal compressor optimization.
- Chapter 4 presents two novel desorption designs and one rectification design based on the findings in Chapter 3. Results of a hydrodynamic investigation are presented.
- Chapter 5 describes the development of a heat and mass transfer model for desorption and rectification components.
- Chapter 6 describes the development of a test facility and presents experimental results for the thermal compressor. An assessment of a quantitative thermal compressor framework is made.

- Chapter 7 presents experimental results for microchannel desorption and rectification components. These results are compared to predictions of the heat and mass transfer model developed in Chapter 5.
- Chapter 8 presents the development and experimental validation of a direct-coupled desorption concept where the heat source is a gas stream.
- Chapter 9 presents a control strategy for the thermal compressor. Experimental validation of the control strategy is shown.
- Chapter 10 summarizes important conclusions and major findings of this study. Recommendations for further research work are made.

CHAPTER 2. SMALL-CAPACITY ABSORPTION CHILLER DEVELOPMENT

2.1 Introduction

Thermally activated space conditioning and refrigeration has several advantages over conventional vapor compression machines. The ability to use versatile low-grade thermal energy instead of high-grade electricity has been increasingly recognized as a critical feature. Widespread adoption of the technology reduces grid electricity demand and leads to operating cost reduction in many climatic regions. In the developing world, it can provide improvements to the living standard without excessive increase in electricity demand. Additionally, these systems use environmentally benign refrigerants in contrast to synthetic refrigerants, which may have high global warming potentials. The use of absorption systems has been limited to large capacity machines in industrial and district energy applications. However, advances in miniaturization of heat exchangers allow for the development of small capacity absorption systems for residential applications (Garimella, 2003). The development and testing of a 7 kW cooling capacity absorption chiller delivering chilled water at 7.2ºC is presented here. Recent developments in microchannel heat exchanger technology, component design and controls are reviewed. The most promising advances are applied to develop a fully integrated, standalone system.

2.2 Technology Review

While the literature offers a large number of thermodynamic and cycle modeling studies, very few small-capacity ammonia-water absorption systems are available. The realization of small capacity systems requires the development of compact components with simple geometries. A general overview of the development of microscale heat exchangers and their potential for a wide range of application in thermal and process engineering is provided by Schubert *et al.* (2001). They present various heat and mass exchanger types and report heat transfer coefficients of up to 54,000 W m^{-2} K^{-1} and heat transfer rates of up to 200 kW. Specifically for ammonia-water absorption systems, Garimella (1999) developed a microchannel falling-film absorber designed for residential applications. Meacham and Garimella (2002) validated that design experimentally and showed high heat and mass transfer rates. The same design was shown by Determan and Garimella (2011) to effectively operate as a desorber. A forced-convective plate-plate type microchannel absorber was developed by Nagavarapu and Garimella (2011). The plate-plate microchannel design was extended to a monolith concept by Determan and Garimella (2012). This monolith encapsulates all core components of the absorption system. It further reduces system size by eliminating external fluid routing and facilitates cost effective fabrication. The proof-of-concept prototype was shown to deliver 300 W of cooling. Delahanty *et al.* (2015) extended the plate-plate microchannel concept to the development of a compact desorber-analyzer-rectifier unit. Keinath *et al.* (2015) validated the performance of this Vapor Generation Unit (VGU) for systems with cooling capacities of up to 3.5 kW. Few complete small-capacity system studies are available. Priedeman *et al.* (2001) presented the results of a natural gas fired machine with 17.6 kW

cooling capacity at Air Conditioning, Heating and Refrigeration Institute (AHRI) test conditions for residential and light commercial applications. A Generator-Absorber-Heat Exchange (GAX) cycle was employed and a *COP* of 0.68 was achieved at full capacity. The system was reported to be limited by high pressure drops between evaporator and pump inlet, lower-than-design combustion efficiency, and limited internal heat exchanger effectiveness. Zetsche *et al.* (2010) present the results of the development of a 10 kW solar thermal system. The complete system includes ice thermal storage to decouple the system from time-varying availability of solar thermal energy. The core system is integrated into a packaged system that is coupled to a separate ambient air heat sink. A complete system design with integrated ambient heat rejection was presented but not constructed and tested. The non-integrated core system was tested for wide range of evaporator temperatures, i.e. -11ºC to 14.5ºC. Heat sink temperatures for absorber and condenser were reported to range between 27ºC and 29ºC. Heat source temperatures varied between 85ºC and 120ºC. Cooling capacity ranged from 2.29 kW to 10.33 kW while a *COP* range of 0.31 to 0.72 was reported. The reported heat sink temperature range is comparatively low and limits the applicability of the system to climatic regions with moderate temperatures. The same researchers report results for high heat sink temperatures of up to 45ºC. However, cooling capacity declined to 3.6 kW and evaporator temperatures were set to 14.5ºC to maintain a *COP* of 0.52. Moser and Rieberer (2006) report the development of a 15 kW heating capacity prototype heat pump for use with biomass as the heat source. Conventional plate-plate heat exchangers were used for all components except for the column type desorber and rectifier. No overall size or dimensions were reported and an external secondary fluid coupling was used,

including for desorber coupling. The reported *COP* in heating mode ranged from 1.4 to 1.5 for condenser/absorber temperatures between 32ºC and 40ºC and evaporator temperatures between -3ºC and 7ºC. The cooling mode *COP* ranges between 0.45 and 0.55 for condenser, absorber and evaporator conditions identical to the heating mode. The ability to use absorption systems for refrigeration, space heating and cooling as well as domestic hot water heating has led to the concept of the modular thermal hub as presented by Determan and Garimella (2012), where all utilities are envisioned to be provided by a centralized absorption heat pump system.. An intermediate scale, 3.5 kW cooling capacity packaged system for standalone operation was also developed and reported by Garimella *et al.* (2016). In addition, a small capacity, standalone absorption heat pump hot water heater has been demonstrated by Keinath *et al.* (2017).

Zotter and Rieberer (2015) and Imroz Sohel and Dawoud (2006) present developments of thermally driven, and gravity assisted solution pumps, respectively. These are examples of research efforts to eliminate auxiliary electricity consumption. However, given that these efforts are still in the developmental stage, the fact that electricity consumption of the solution pump is marginal (Herold *et al.*, 1996), and that additional auxiliary power consumption is required by the ambient air fan, only motorized pump options are considered for the present study.

Thermally driven chillers and heat pumps provide the potential to integrate distributed electricity generation. This further increases the need for the development of compact and economical small capacity systems. For example, Rossa and Bazzo (2009) describe the thermodynamic modeling of a 5 kW ammonia-water absorption chiller integrated with a 28 kW_e microtubrine. Modeling results predict an overall thermal

efficiency of 41% which is reported to be a 67% improvement over the individual turbine efficiency.

This technology review reveals that significant progress has been made in miniaturization of individual heat pump components. This enables the development of small capacity systems for various applications. The wide range of potential applications creates the opportunity for highly efficient integrated and cascaded thermal systems. However, limited complete system developments are available, which necessitates further research that addresses associated challenges.

2.3 Cycle Design

The ammonia-water working pair was selected for this development. While a large number of working pairs have been identified as potentially suitable for absorption systems, the only two working pairs that can be currently considered as viable for a residential or commercial system are lithium bromide-water and ammonia-water (Ziegler, 2002). Due to its relatively low specific volume, the ammonia-water working pair allows for more compact heat and mass exchanger design. There are no crystallization and freezing concerns, which enable the ammonia-water absorption system to be operated as a heat pump at very low ambient temperature or for refrigeration applications. The ability to use solar thermal as a heat source in combination with ice thermal storage to buffer variations in heat source availability is an example of these advantages. However, ammonia absorption has its unique challenges (Bogart, 1982), some of which complicate reduction of system capacity and size. Particularly, refrigerant purity due to the volatile absorbent has significant implications for system performance (Fernandez-Seara and

Sieres, 2006), and requires additional components and, therefore, additional space and weight.

Many cycle designs with varying degrees of complexity exist (Kang *et al.*, 2000). While some configurations can provide meaningful performance improvements (Engler *et al.*, 1997), their implementation also adds complexity, size and weight, and additional controls challenges. Small-capacity heat pumps must be fabricated economically, have low weight and a small footprint, and their operation must be robust and reliable. Given the current state of the technology, a single-stage, single-effect cycle is considered most appropriate for the present application. However, future developments could consider advanced cycle designs.

Internal heat recovery leading to better performance can be achieved with two recuperative heat exchangers, the solution heat exchanger and a refrigerant pre-cooler. While both heat exchangers yield performance improvements, the benefit from incorporation of the solution heat exchanger is most significant (Herold *et al.*, 1996).

The final configuration consideration pertains to the desorber, rectifier, and refrigerant vapor purity. (Fernandez-Seara *et al.* (2003)) conducted a comparative study of several common approaches to purification. In general, the use of a partial condensation rectification method was identified as thermodynamically favorable compared to full condenser reflux. The authors recommend rectifier cooling with concentrated solution leaving the absorber. They also conclude that the use of an adiabatic stripping section, termed analyzer, improves system performance significantly. Therefore, a concentrated solution-cooled rectifier is used here in addition to an analyzer.

Based on the preceding considerations, a schematic of the cycle used in the present study is shown in Figure 2.1.

The coupling of all heat flows to and from the cycle is also specified in Figure 2.1. Chilled water is used to couple cooling from the evaporator to conditioned spaces as it minimizes the possibility of refrigerant leaks into the conditioned space. It also provides versatility with respect to the distribution of chilled water without affecting system performance. In general, the use of microchannel heat exchangers in combination with hydronic coupling fluids allow for the design of highly compact core components with very low working fluid volume, which reduces the total charge of refrigerant in the system (Garimella, 2003). Therefore, a single air-coupled heat exchanger is used as the combined heat sink for the condenser and absorber in combination with a hydronic coupling fluid loop. This also allows for operation as a heat pump through simple switching of hydronic fluid valves.

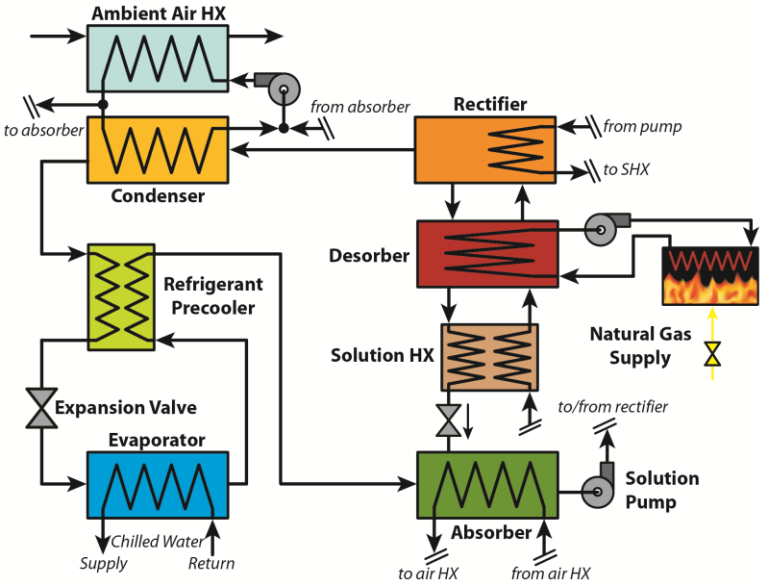

Figure 2.1: Cycle schematic

A coupling fluid loop using heat transfer oil (ParathermTM NF) in combination with a natural gas combustion module was selected as the system heat source. This allows for construction of a complete self-contained working fluid part of the system. It also maintains versatility of application as the combustion module can be replaced with a waste heat recovery heat exchanger.

2.4 Thermodynamic Model

A thermodynamic model was developed to completely define each state point, determine flow rates and obtain *UA*-value requirements for each heat exchanger. The cycle model results also provide performance predictions and information about the sensitivity to changes in operating conditions and individual heat exchanger *UA*-values. Table 2.1 lists global inputs to the model. The model also requires initial assumptions about heat exchanger performance and certain thermodynamic states, which are listed in Table 2.2.

The model is implemented in *Engineering Equation Solver* (EES) (Klein, 2015). Ammonia-water property routines are based on the work of (Ibrahim and Klein (1993)).

Table 2.1: Model inputs

Input	Value
Ambient Temperature, (T_{amb})	35°C
Evaporator Chilled Water Inlet Temperature, ($T_{evap,CF,in}$)	12.8°C
Evaporator Chilled Water Outlet Temperature, ($T_{evap,CF,out}$)	7.2°C
Heat Source Temperature, ($T_{des,CF,in}$)	180°C
Evaporator Temperature Glide ($\Delta T_{evap,glide}$)	3 K
Refrigerant Concentration (x_{ref})	0.9985

Table 2.2: Thermodynamic model assumptions

Assumption	Value
Solution Heat Exchanger Effectiveness (ε_{SHX})	0.8
Refrigerant Pre-cooler Effectiveness (ε_{RPC})	0.8
Absorber Closest Approach Temperature (CAT_{abs})	3 K
Concentrated Solution Subcooling in Absorber ($T_{sub,abs}$)	2 K
Condenser Closest Approach Temperature (CAT_{con})	3 K
Refrigerant Subcooling in Condenser ($T_{sub,con}$)	2 K
Evaporator Closest Approach Temperature (CAT_{evap})	3 K
Analyzer Vapor In-equilibrium Temperature ($T_{ineq,vap}$)	7.5 K
Rectifier Reflux In-equilibrium Temperature ($T_{ineq,rec}$)	3 K
Condenser Closest Approach Temperature (CAT_{des})	25 K
Dilute Solution State at Desorber Outlet	Saturated Liquid
Refrigerant State at Rectifier Outlet	Saturated Vapor

Conservation equations for mass, species and energy are applied to each component and solved iteratively. The refrigerant mass flow rate required to achieve an evaporator cooling capacity of 7 kW with an evaporator temperature glide, $\Delta T_{evap,glide}$ is determined to establish design values for concentrated and dilute solution flow rates. Specifically, the evaporator refrigerant inlet temperature is determined using CAT_{evap} and $T_{evap,CF\text{-}out}$ as specified in Table 2.1 and Table 2.2. Thus, $\dot{m}_{ref}$ can be determined. Circulation ratio, $CR = \dot{m}_{ref} / \dot{m}_{cs}$ can be determined through Eq. 2.1 which then fixes values for $\dot{m}_{cs}$ and $\dot{m}_{ds}$.

$$CR = \frac{x_{ref} - x_{ds}}{x_{cs} - x_{ds}} \qquad 2.1$$

Key state points, flow rates and component heat duties are listed in Table 2.3. The combination of mass flow rates, *CAT* assumptions and component level energy balances allows for the determination of all state points in the system as well as heat duty values for every component. *UA*-values for each component are determined based on the component duty and its *LMTD*.

For design purposes, it is important to evaluate off-design conditions. The effect of varying ambient temperature on the system is shown in Figure 2.2A. System performance monotonically degrades with rising ambient temperature, which is expected.

Table 2.3: Thermodynamic model results

Component or State Point	Value
Evaporator Duty	7.03 kW
Evaporator *UA*-value	1.70 kW K^{-1}
Desorber Duty	11.14 kW
Desorber *UA*-value	0.29 kW K^{-1}
Rectifier Duty	1.83 kW
Rectifier *UA*-value	0.06 kW K^{-1}
Absorber Duty	11.47 kW
Absorber *UA*-value	1.07 kW K^{-1}
Condenser Duty	6.76 kW
Condenser *UA*-value	1.10 kW K^{-1}
SHX Duty	4.91 kW
SHX *UA*-value	0.21 kW K^{-1}
RPC Duty	0.69 kW
RPC *UA*-value	0.07 kW K^{-1}
Refrigerant Flow Rate	6.17×10^{-3} kg s^{-1}
Concentrated Solution Flow Rate	19.09×10^{-3} kg s^{-1}
Dilute Solution Flow Rate	12.92×10^{-3} kg s^{-1}
Cycle COP	0.63

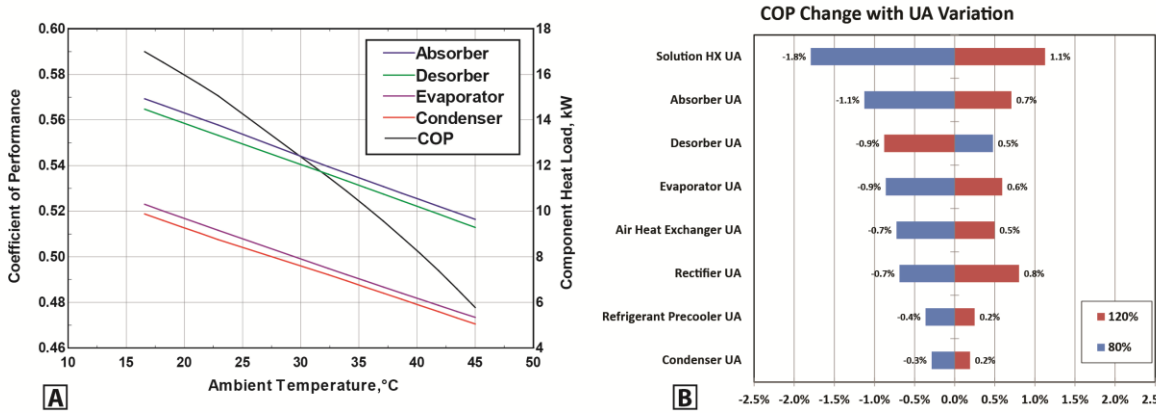

Figure 2.2: (A) *COP* and component duty for varying ambient temperature, (B) sensitivity of *COP* to variation of component *UA*-values

System high-side pressure increases substantially for the same ambient temperature range. This determines maximum expected operating pressures and sets component design pressure requirements. Additionally, several sensitivity studies were performed with this cycle model. Each heat exchanger *UA*-value was varied by ± 20% and the resulting effects on cycle *COP* were studied. *COP* sensitivity to final component *UA*-value is shown in Figure 2B. *COP* is most strongly affected by variations in solution heat exchanger size. However, overall *COP* variation is minimal in response to size variation of any heat exchanger.

2.5 Heat exchanger design

Individual segmented models were developed for each heat exchanger to determine physical size based on thermodynamic modeling results. A typical cross-section of the microchannel heat exchanger geometry is shown in Figure 2.3. Conservation equations for mass, species and energy are applied in combination with a resistance network for each segment. Nagavarapu and Garimella (2011) present a

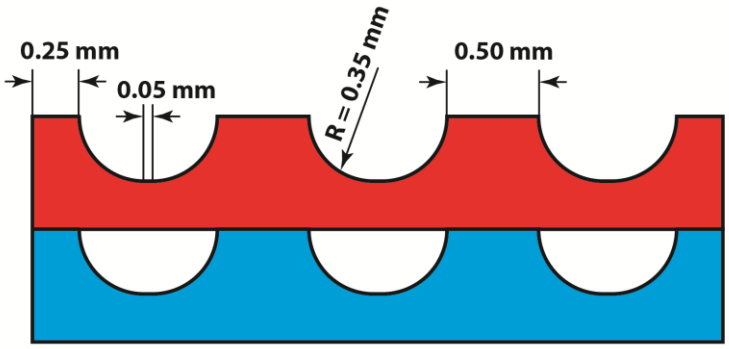

Figure 2.3: Microchannel cross-section geometry

methodology for the idealization of the microchannel geometry as a thermal resistance network of the metal sheets with the walls of the microchannels represented as fin arrays. Binary mixture effects during phase change must be considered to accurately quantify the total thermal resistance. For example, the Colburn and Drew (1937) approach as implemented by Price and Bell (1974) was applied for desorber and absorber design while the method presented by Silver (1947) and (Bell and Ghaly (1973)) was applied for condenser and rectifier designs. The *UA*-LMTD method as shown in Eq. 2.2 then determines the heat duty for each segment from which the physical size of the heat exchanger is obtained through consideration of the total heat duty as shown in Eq. 2.3.

$$\dot{Q}_i = \left(U \times A\right)_i \times LMTD_i \qquad 2.2$$

$$\dot{Q}_{total} = \sum_i \dot{Q}_i \qquad 2.3$$

The overall cross-sectional area for fluid flow in the heat exchanger is defined by specification of the number of parallel channels, including channels per sheet, and the total number of sheets. Design criteria for this choice include total pressure drop of the component, heat and mass transfer rates, and fabrication considerations. The pressure

drop of each component was limited to 25 kPa to avoid adverse effects on system performance. Component pressure drop is obtained from segmental frictional pressure drop modelling. For example, two-phase flow frictional pressure drops are calculated using the Lockhart (1949) correlation with the coefficients based on the work of Chisholm (1967). The flow regime in two-phase flow is affected by the number of parallel channels, and it is desired to maintain relatively high velocities to facilitate heat and mass transfer for two-phase flows. Additionally, homogenous flow distribution in all channels is desired. As the width of the component increases, the potential for maldistribution increases. Therefore, long and narrow components are preferred, which is in conflict with low pressure drop requirements. Finally, fabrication considerations favor fewer numbers of plates. Therefore, the individual component design goal is to minimize the number of plates and component width, and extend the channel length as much as tolerable given the pressure drop limit.

Desorber, analyzer and rectifier components are based on the VGU design presented by Delahanty *et al.* (2015). Here, a liquid-vapor countercurrent flow configuration is used to realize thermodynamic advantages. Hydrodynamic considerations such as countercurrent flow limitations (CCFL) prevent the use of microscale geometries on the working fluid side. However, the coupling fluid side employs microscale geometries leading to a compact component design. The present work seeks to achieve capacity scale-up from the 300 W cooling capacity heat pump monolith concept presented by Determan and Garimella (2012) and further scale-up from the development of a 3.5 kW cooling capacity system presented by Garimella *et al.* (2016). For this scale up, and considering the different criteria that govern the vapor

generation unit and the other components in the system, it is subdivided into two monolithic blocks.

In addition to the design considerations for individual components, integration of the components into these monolithic blocks presents additional constraints. These include the overall dimension of the monolithic block and the sheet stacking pattern. The latter constraint arises because the stacking pattern of individual components may not necessarily be the same for all components. Pressure drop constraints may lead to components that require multiple coupling fluid sheets for every working fluid sheet or vice versa. This may not be required for all components but has to be accommodated in the monolith design. The designs were optimized to accommodate individual heat exchanger as well as component integration requirements. The evaporator coupling fluid required two sheets for every refrigerant sheet due to pressure drop limitations. This resulted in a final monolith design with four different sheet designs to accommodate the component stacking order. The core monolith consisted of 66 total sheets. A sample sheet

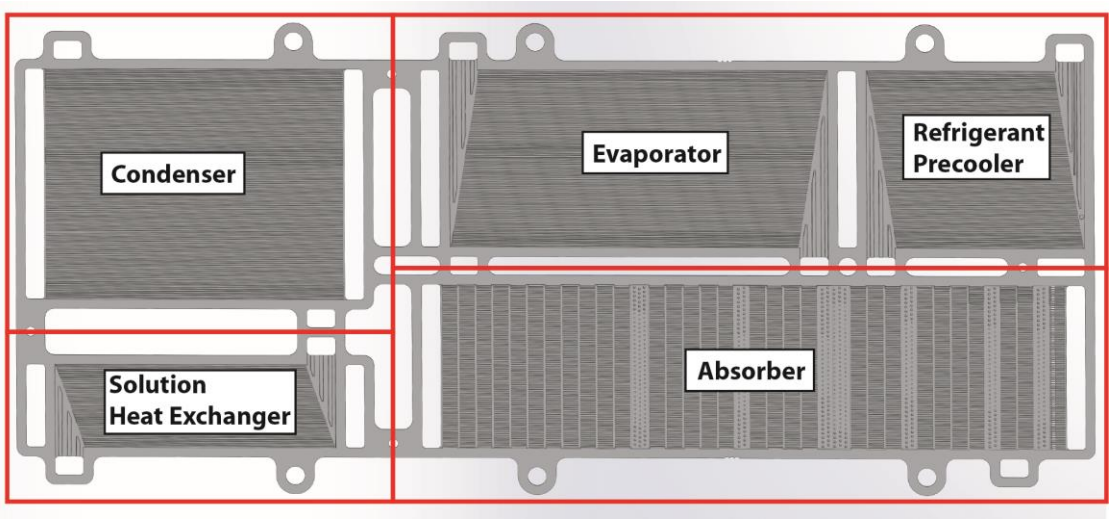

Figure 2.4: Monolith sheet layout

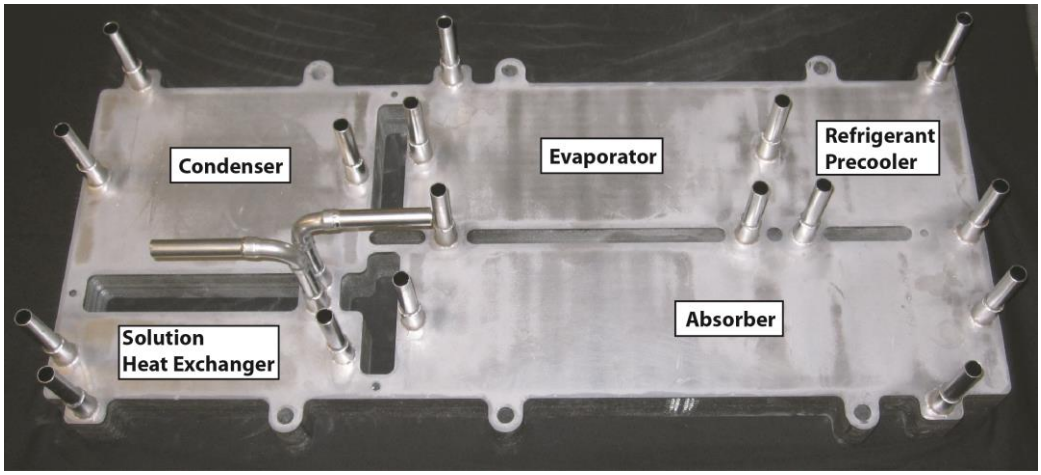

Figure 2.5: Bonded core monolith assembly

with labeled components is shown in Figure 2.4. The sheets were fabricated from 304 stainless steel with a photochemical etching process as described by Determan and Garimella (2012). A recurring subassembly of sets of five sheets is used to achieve the required stacking order.

Sheets for the absorber solution, evaporator refrigerant, and solution heat exchanger dilute solution have periodic gaps in the microchannel geometry perpendicular to the direction of flow. These features were used to mitigate maldistribution and promote inter-channel mixing. Larger mixing sections are located closer to the inlet to address potential maldistribution in the header region. An understanding of flow distribution in such geometries has been developed by the work of Hoysall *et al.* (2017). A hybrid brazing and diffusion bonding process yielded the final assembly with dimensions of 710 mm × 315 mm × 50 mm as shown in Figure 2.5. The hybrid bonding process is a transient liquid phase diffusion bonding process where a brazing alloy is applied in a high pressure, high temperature atmosphere.

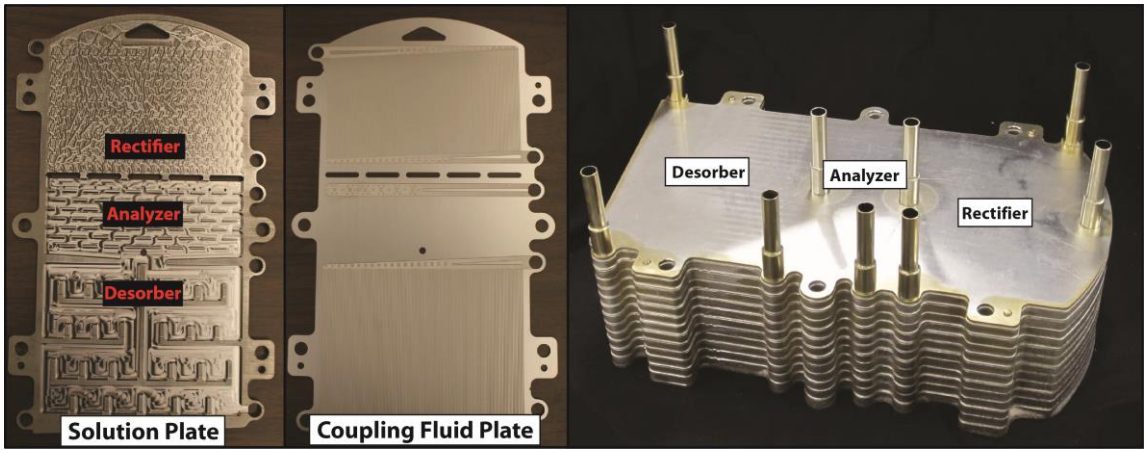

Figure 2.6: Vapor Generation Unit (VGU), individual plates (left) and bonded assembly (right).

The VGU geometry presented by Delahanty *et al.* (2015) was modified for required vapor generation rates. The complete assembly consists of 12 solution side sheets, 24 heat source coupling fluid sheets, and 12 rectifier coupling fluid sheets. The solution side sheets were milled while the coupling fluid sheets were fabricated using photochemical etching. Both sheets are shown in Figure 2.6 (left). Vacuum brazing produced the final assembly with dimensions of 400 mm × 250 mm × 130 mm as shown in Figure 2.6 (right).

2.6 Auxiliary Components

Several additional components were required for integration into a complete system. The combustion module consists of a standard fin-tube coil in combination with a flat-plate burner, and provides continuous turndown control. A positive displacement gear pump provides circulation of a coupling fluid to the VGU. A conventional, custom fabricated copper/aluminum, finned-tube heat exchanger was designed to accommodate the unique geometry required for optimal packaging. Thermal communication between

Table 2.4: System instrumentation

Instrument	Manufacturer/Model	Value	Accuracy
Thermocouple	Omega® T-type Omega® J-type	-250 – 300°C 0 – 750°C	±0.5°C ±1.1°C
Pressure Transducer	Omega® 4-20 mA Output	0 – 1000 kPa 0 – 3500 kPa	±0.03% Range
Mass Flow Sensor	Endress+Hauser® Promass 80F Coriolis	0 – 0.556 kg s^{-1}	±0.15%
Coolant Mass Flow Sensor	MicroMotion® Coriolis Sensor	0 – 0.6056 kg s^{-1}	±0.1%
Electronic Expansion Valves	Carel® E2V Series	480 motor steps	–
Data Acquisition and Control	National Instruments® c-RIO 9024	–	–
Gas dial meter	American Meter Company	–	–

the monolith block and the ambient heat sink is provided through and hydronic coupling loop with a compact centrifugal pump. A low-profile, light-weight automotive radiator fan was selected to deliver heat sink air flow. A compact piston pump was developed to deliver low concentrated solution flow rates at high differential pressure, which is characteristic for ammonia-water absorption systems. Finally, two control valves were installed for refrigerant expansion into the evaporator and dilute solution throttling. Proportional electronic positioning valves compatible with ammonia-water were chosen. Unlike thermostatic expansion valves, this allows direct control of valve position, allowing implementation of various control algorithms. A list of all relevant instrumentation is provided in Table 2.4.

2.7 Control System

A standalone packaged heat pump requires an intelligent control system. The main objective is to identify all relevant control loops and provide instrumentation to operate these loops. It is further desired to establish a control frame work for stable,

reliable and independent operation. Figure 2.7 shows the control loops that were identified as necessary to accomplish these tasks. Three internal control loops are shown, namely evaporator temperature glide control, dilute solution valve control and concentrated solution pump speed. Temperature glide control in the evaporator is one strategy for ammonia-water absorption systems whereby the temperature difference between evaporator refrigerant inlet and outlet is measured and used as the process variable. A feedback loop then uses this value to regulate valve position. The temperature glide set point is fixed at a nominal value of 3ºC. However, this value can be modified and could be used as a dynamic variable for further system optimization. The temperature glide also depends on refrigerant purity and increases as water mass fraction increases. Excessive temperature glides lead to refrigerant temperatures above target chilled water temperatures. This causes an increasing fraction of latent heat in the refrigerant vapor to be unusable for cooling. Maintaining a lower temperature glide at poor refrigerant vapor

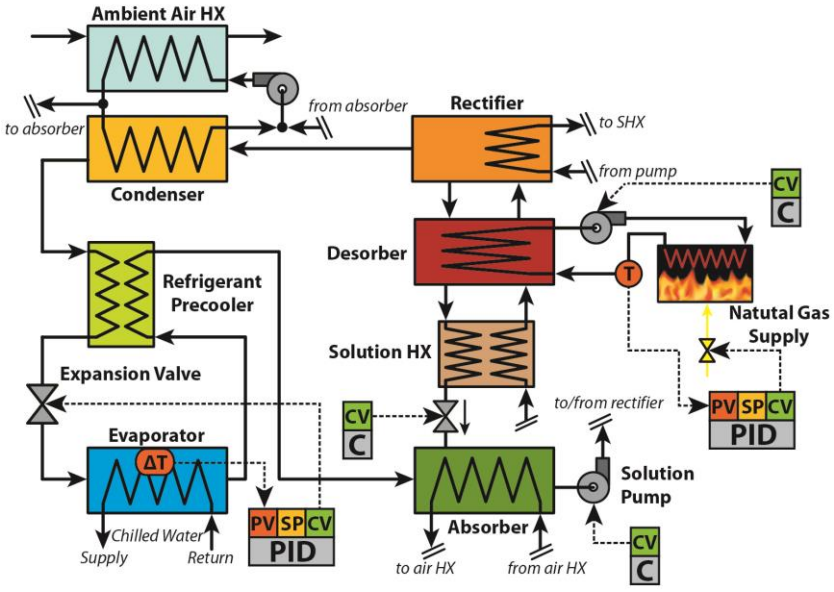

Figure 2.7: Control system loops

purity requires excessive refrigerant mass flow rates which, in turn, degrades performance due to the additional heat input necessary to generate the refrigerant. Direct control of valve position allows the controller to disable feedback loop control to provide a fixed valve positon during severe transients and start-up/shut-down situations. Concentrated solution is directly controlled through the speed of the constant displacement pump in an open loop. Solution flow rate can be set as a function of several variables including cooling load, operating conditions and start-up/shut-down routines. The dilute solution valve is also operated in an open loop and is controlled based on solution pump speed and operating conditions to maintain a liquid level in the desorber without causing flooding of solution into the condenser. Two external control loops are identified. Continuous modulation of gas input to the combustion module controls the desorber inlet temperature set-point through a feedback loop. An open loop for heat source coupling fluid flow rate is implemented with variable speed control of a positive displacement gear pump. The desired heat input to the desorber and a target temperature profile is achieved by combining both controls. Both, heat source coupling fluid flow rate and combustion module heat input were modulated during testing to achieve a target desorption temperature at the dilute solution outlet of the desorber.

Safety related control features were implemented in the controller. Specifically, several permissive checks are continuously verified without which combustion is disallowed. The permissive checks include flow verification for chilled water and desorber coupling fluid, system high side pressure, evaporator minimum temperature and desorber coupling fluid maximum temperature. All auxiliary components, i.e., ambient air fan and heat sink coupling fluid pump are simple on/off controllers. The control

system was implemented with a process automation controller (PAC). Additionally, multiple pressure transducers and thermocouples for relevant system state points were installed for experimental evaluation. The level of implemented instrumentation is much greater than that needed for a stand-alone, commercial product due to experimental nature of this work, which will provide the potential for further space and weight reduction in an eventual packaged commercial system.

2.8 System Assembly and Experimental Results

The VGU and the monolith containing the other ammonia-water components form the core of the absorption chiller. Auxiliary equipment was arranged to minimize total system volume. Consideration was given to the fact that an experimental prototype development requires additional space for instrumentation and access for potential in-situ modifications. The prototype chiller was constructed based on complete system CAD modelling that optimizes packaging of components and minimizes unit footprint. The final assembly is shown in Figure 2.8. Overall, dimensions of the packaged unit are 0.66 m × 0.66 m × 0.66 m. It should be noted that during construction of the packaged unit, a small internal leak in the absorber section of the core monolith developed. It was therefore necessary to add a set of falling-film type absorbers to the packaged system. These were two custom fabricated shell-and-tube heat exchangers, with a shell outside diameter of 0.0762 m and a height of 0.51 m, installed in a series flow configuration while the microchannel absorber was isolated. Experimental results reported in this study were consequently obtained with the falling-film type absorbers. Additional space requirements were minimal.

Figure 2.8: Complete packaged systems

A chilled water cooling load simulation loop was fabricated to provide design temperature and flowrates for the evaporator. Relevant instrumentation is listed in Table 2.4. The load simulation loop included a set of electric heaters, capable of deliver maximum heating capacity of 9 kW, a centrifugal pump and a Coriolis type mass flow meter. A 10 *wt*% propylene-glycol solution was used for the chilled water loop. Inlet and outlet chilled water temperatures at the evaporator were monitored and recorded to determine system cooling capacity. Natural gas flow rate was measured periodically with a dial meter to determine total heat input. Data were recorded with the controller every second for periods of 15 minutes and averaged to represent a data point.

Autonomous control of the system was accomplished to a high degree at steady state operation. Desorber coupling fluid temperature control operated in a completely automatic mode including system start-up. Solution pump speed modulation was identified as an effective control variable for capacity control by varying concentrated solution mass flow rate. Relatively fast capacity changes can be accomplished with this

strategy and it should be included in further development of absorption system control strategies. The CCFL in the VGU (Delahanty *et al.*, 2015) dictated the allowable concentrated solution flow rate increases and solution pump speed control. While the open loop controller operated in manual mode, automation of this loop as a function of capacity and operating conditions is considered feasible. A simultaneous increase in desorber coupling flow rate through pump control was required to provide the commensurate increase in heat input with capacity. This controller is based on the temperature difference between concentrated solution inlet and desorber coupling fluid outlet. The automatic feedback controller for natural gas supply to the combustion module maintained a target heat source temperature set point at the coupling fluid inlet of the desorber. This set point was varied as the control variable in a cascaded feedback loop that achieves a set point temperature of dilute solution temperature leaving the desorber. This last feature of the control algorithm added significant consistency and stability to system operation. In this study, dilute solution temperature was maintained at a constant value to match thermodynamic model inputs but this study shows that it is a variable that can be actively controlled to not only maintain system stability but also respond to changes in operating conditions, e.g., ambient temperature variation. Therefore, effective capacity control can be achieved with concentrated solution flow rate control, desorber heat input control and refrigerant valve control. Minimal dilute solution valve control was needed, which was done in manual mode. An open loop model based control of this valve could be implemented based on desorber-absorber pressure differential, system load and system operating conditions, e.g., evaporator temperature and ambient temperature. The refrigerant valve was set at a fixed position during start-up, but was switched to

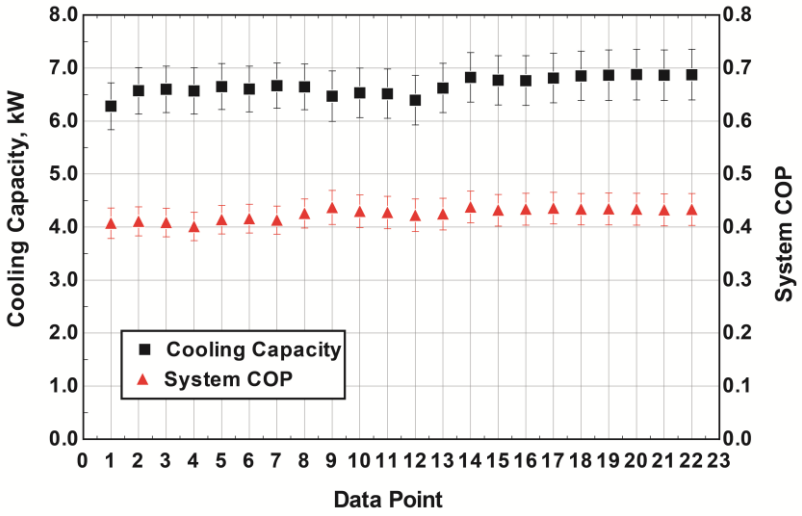

Figure 2.9: Cooling capacity and system *COP*

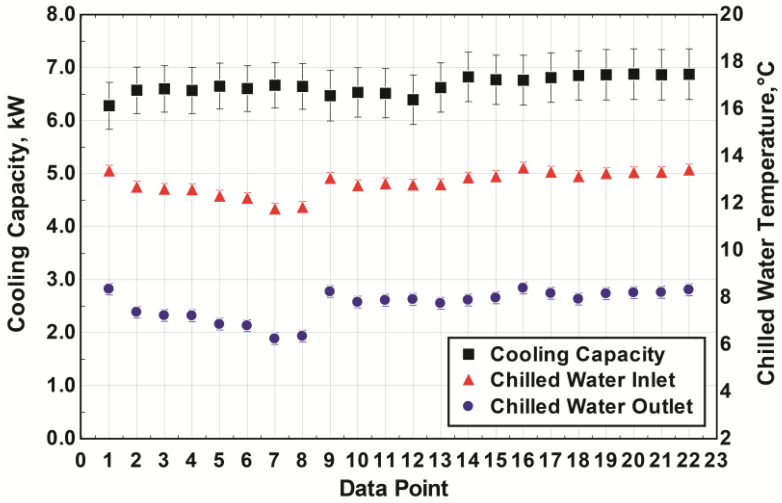

Figure 2.10: Cooling capacity and chilled water temperature

automatic control during steady state with a nominal set-point of 3ºC. Stable refrigerant flow and evaporator performance was achieved at steady state. The developed framework for system control and the identified control loops were validated and provided significant guidance for continued control algorithm developments. Further refinement and algorithm development is required to achieve robust automation that accommodates start-up/shut-down and system transients due to changing operating conditions.

Successive operational optimization was conducted to maximize capacity and test system limitations. Figure 2.9 shows a plot of data collected during system optimization. It shows increases in cooling capacity up to a maximum of 6.9 kW. Operating conditions

Table 2.5: Comparison of thermodynamic model and experimental results

State Point	Model	Experiment
Chilled Water Inlet Temperature, °C	12.8	13.1
Chilled Water Outlet Temperature, °C	7.2	7.9
Chilled Water Flow, kg s^{-1}	0.32	0.32
Cooling Duty, kW	7.0	6.9
Natural Gas Heat Input, kW	13.4	15.8
Combustion Efficiency, %	83.4%	84.6%
System *COP*, [-]	0.53	0.44
Cycle *COP*, [-]	0.63	0.51
Condenser Pressure, kPa	2087	2003
Evaporator Pressure, kPa	501	447
Evaporator Refrigerant Inlet Temperature, °C	4.2	4.8
Evaporator Refrigerant Outlet Temperature, °C	7.2	7.14
Desorber Coupling Fluid Inlet Temperature, °C	180	183
Desorber Dilute Solution Outlet Temperature, °C	155	156
Condenser Refrigerant Inlet Temperature, °C	62.1	59.4
Condenser Refrigerant Outlet Temperature, °C	49.0	40.0
Condenser Coupling Fluid Outlet Temperature, °C	48.0	51.3
Absorber Solution Outlet Temperature, °C	41.0	42.5
Absorber Coupling Fluid Outlet Temperature, °C	52.0	51.03
Coupling Fluid Inlet Temperature, °C	40.0	39.4
SHX Concentrated Sol. Inlet, °C	62.7	70.5
SHX Concentrated Sol. Outlet, °C	104.2	118.2
SHX Dilute Sol. Outlet, °C	70.5	71.8

were approximately constant during these tests as shown in Figure 2.10. The details of a representative data point are shown in Table 2.5. While the majority of state-point temperatures are in very close agreement with thermodynamic modeling results, the system *COP* is somewhat lower than design values. The *COP* is defined as shown in Eq. 2.4. Cycle *COP* accounts for combustion efficiency and provides a value independent of heat source losses for general comparison as shown in Eq. 2.5.

$$COP_{system} = \frac{\dot{Q}_{evap}}{\dot{Q}_{gas}} \tag{2.4}$$

$$COP_{cycle} = \frac{\dot{Q}_{evap}}{\eta_{comb} \times \dot{Q}_{gas}} \tag{2.5}$$

It was found that temperature glide in the evaporator required a lower set-point than the nominal value of 3ºC to maximize capacity. It can be deduced that limitations in the evaporator require a greater LMTD. Also, the inlet temperature to the evaporator was consistently 0.5-1ºC higher than its design value, suggesting that refrigerant purity was slightly lower than design values. This adversely affects evaporator *LMTD* and requires additional refrigerant mass flow. This required increased heat input to the desorber, thereby adversely affecting *COP*. The solution temperature increase across the rectifier was greater than the design value, indicating greater-than-design rectifier loads. Any rectifier load will lead to lower thermal compressor efficiency and increased heat input requirement. In addition to these observations, heat loss from the desorber, combustion module and coupling fluid loop explain the greater-than-design heat input and lower-than-design system *COP*. The solution pump capacity limit was reached at maximum cooling loads, which ultimately limited further capacity increases. An increase in dilute

solution temperature at the desorber outlet suggests insufficient solution flow. However, given the indication of greater-than-design refrigerant flow rates, improved VGU and evaporator performance at constant circulation ratio will require lower solution flow rates. This suggests that pump capacity is sufficient for the cooling capacity of this prototype.

2.9 Conclusions

The development of a compact standalone 7 kW cooling capacity, residential scale ammonia-water absorption chiller was presented. Microscale heat and mass exchangers integrated into two monolithic blocks formed the core of the chiller. Space and weight requirements for these core chiller components are only a small portion of the entire system volume, owing to highly compact heat and mass exchangers. A controls frame work that identified effective control loops was developed and implemented. The system was tested at AHRI conditions and achieved cooling near design capacities. A system cooling *COP* of 0.44 was achieved, which corresponded to a cycle *COP* of 0.51.The scale-up of the monolithic microchannel heat pump concept (Determan and Garimella, 2012) from proof-of-concept and an intermediate 3.5 kW cooling capacity scale (Garimella *et al.*, 2016) to residential scales demonstrates the feasibility of small capacity ammonia-water absorption systems. This chiller can also readily function in heating mode, increasing the functional utility of the system as a complete space-conditioning unit. Several areas of continued research needs can be identified to advance this technology. The discrepancy between predicted and measured *COP* can, in part, be explained by less than optimal operation of the VGU and the evaporator. The challenge

of combining the most compact heat exchanger designs with high purification requirements and best possible component efficiencies has to be addressed. Further development of the refrigerant generation and purification components, i.e., for the desorber, analyzer and rectifier is needed to reduce weight and size and to improve *COP*. Improved designs for highly compact evaporators should be investigated. Heat and mass transfer performance of the microchannel absorber component at design microscale geometries should be validated. Further development of the control loops within the identified framework is required to reliably provide transient, start-up/shutdown and turn-down response. Finally, high volume manufacturing methods of microchannel heat exchangers should be investigated for viable economical fabrication of small capacity absorption machines.

CHAPTER 3. THERMODYNAMIC CONSIDERATIONS

3.1 Introduction

In contrast to vapor compression cycles, thermally activated chiller and heat pump cycles require more detailed thermodynamic modeling. The concept of the *thermal compressor* (TC) is commonly used in the literature as a qualitative descriptor to provide an analogy to the vapor-compression cycle. However, these efforts have typically not been developed further to yield a quantitative TC characterization for absorption cycles. If the complexity of the analytical modeling of the TC can be reduced to approach that of vapor compression cycles, it can facilitate design and analysis of absorption heat pump technology. This approach can readily provide accurate design level data and performance predictions for stand-alone systems as well as for integration in complex and cascaded thermal systems. Additionally, the concept can be applied to provide an effective link between the physical machine and its control system allowing for optimal control, fast response and diagnostic capability.

Several modeling approaches for absorption systems have been reported in the literature. On one side of the spectrum of these studies is the rigorous thermodynamic model which requires a large amount of detailed information and provides a large number of detailed results. On the other end of the spectrum is the black-box model, which requires very few inputs and provides only few results. Ultimately, the purpose of the model dictates the required type. The level of detail in a complete thermodynamic model is required at the design stage of an actual machine, which allows for optimal development of heat and mass exchangers. However, this level of detail may not be

needed for predicting the behavior of an existing system or for high-level thermal system screening and design. In fact, if the purpose is integration into a control system, unnecessary detail may require excessive computational power and may limit the efficacy of the model to provide optimal system control. Thermodynamic modeling as the initial design stage of an absorption heat pump has been demonstrated by Herold *et al.* (1996). To facilitate thermodynamic simulations, Grossman (1994) developed the modular ABSIM software with several enhancements and application to an advanced absorption cycle presented by Garimella *et al.* (1996). A second-law model is an extension of the first law thermodynamic model to address some of its limitations. A general overview and illustration of the application of the exergy method to thermal systems is given by Kotas (2013). Ataer and Göğüs (1991) and Aprhornratana and Eames (1995) provide representative exergy studies for absorption systems. Conventional second law analysis has its own limitations (Tsatsaronis, 1999). This led to the development of advanced exergetic analyses, which overcome some of these limitations by splitting exergy destruction into four components (Morosuk and Tsatsaronis, 2013). Endogenous and exogenous parts of a specific component distinguish between irreversibility due solely to that component and the remainder of the system. Further splitting into avoidable and unavoidable exergy destruction allows for incorporation of realistic technological limitations, which aids the identification of opportunities for improvement. Specific application of the method to an ammonia-water absorption refrigeration machine was presented by Morosuk and Tsatsaronis (2008). Efforts to develop a generalized approach to modeling absorption machines that only requires a minimal number of inputs, e.g., mainly operating conditions have been reported in the literature. Gordon and Ng (1995)

apply cycle energy and entropy balances, accounting for entropy generation due to losses in each component. Hellmann and Ziegler (1999) apply the characteristic equations method and offer two simple algebraic equations that capture the thermodynamic state of the system. However, they found that actual relations between this characteristic temperature and *COP* and cooling load are not linear as predicted in the two-equation model. A modified approach presented by Kühn and Ziegler (2005) uses an arbitrarily defined characteristic temperature function for use with the two-equation model proposed by Hellmann and Ziegler (1999). A multiple linear regression analysis for experimental or manufacturer data is then required to complete the model. Puig-Arnavat *et al.* (2010) compare the latter approach to the original two-equation model and confirm that predictive ability of the regression based model is significantly better. Chen *et al.* (2006) present a four-temperature model with the assumption of a linear heat transfer law while Qin *et al.* (2007) remove that assumption and extend the model to a general non-linear heat transfer law. Successive removal of assumptions leads to increasingly complex models. While this may lead to incremental improvements in accuracy, the merit of the model must be determined by its application, which would dictate the required balance between accuracy and simplicity.

The development of the TC framework seeks to combine advantages of all modeling approaches discussed above. Detailed first-law modeling provides accuracy, while exergetic considerations address first-law limitations for thermodynamic optimization. The purpose of this framework is to provide a high-level TC module for design and control. A detailed thermodynamic model approach is used in combination with statistical analyses to maintain accuracy of the former while providing the simplicity

and ease-of-use of a black-box model. The need for explicit specification of desorption temperature is eliminated, thereby reducing the number of model inputs.

A single effect ammonia water absorption cycle is compared with the TC–simple cooling cycle (SCC) representation in Figure 3.1. By separating the TC from the SCC, endogenous effects on performance due to variations in operating parameters and cycle implementation can be quantified without reliance on specific SCC information. In this investigation, a modeling framework for the TC of a single-effect, ammonia-water absorption system is developed. Two appropriate figures of merit are defined. With the application of justified assumptions, a quantitative TC characterization requiring only two inputs, ambient temperature (T_{amb}) and evaporator temperature (T_{low}) is established. Common cycle configurations are considered and compared using this framework, arriving at an optimal configuration. The framework is applied to generate and analyze a large data set for a wide range of operating conditions. Statistical methods, i.e., regression and artificial neural networks (ANN) are used to predict performance accurately and also identify optimal heat source temperatures. The suitability of both methods is compared.

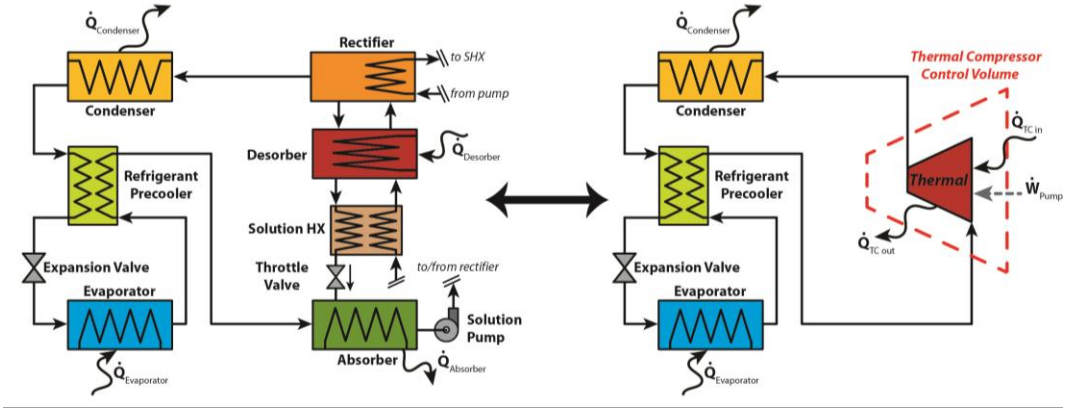

Figure 3.1: Simple absorption cycle (left), conceptual representation of thermal compression cycle (right)

3.2 Thermal Compressor Configurations

While many advanced cycle configurations are available, the target applications of this model are small-capacity systems for which the single-effect cycle is most suitable. The components that are included in the thermal compressor are the absorber, solution heat exchanger (SHX), desorber, and a refrigerant purification stage. The desorber and purification stage have several configuration options. Traditionally, a distillation column is employed in combination with a generator and complete condensation reflux from the condenser. The column consists of a stripping section below the concentrated solution feed point, also termed analyzer, as well as a rectification column above the concentrated solution feed point. The column requires a specific amount of reflux of condensate which depends on the vapor purity requirement and column efficiency. Various column configurations, including the conventional distillation column approach, were studied by Fernandez-Seara *et al.* (2003). They include a partial condenser where vapor is purified by preferentially condensing sorbent rich solution. It was shown that partial condensation leads to *COP* improvements if concentrated solution is used as the heat sink. Fernandez-Seara and Sieres (2006) quantified the effect of vapor purification on system performance. They recommend a high efficiency stripping column for all conditions while the importance of the rectification column becomes less significant at high evaporator, low lift operating conditions. An additional configuration considered here is the diabatic distillation column. In the diabatic desorption column, heat transfer is integrated into the stripping column while the diabatic rectification column integrates partial condensation stages with the rectification column. The advantages of diabatic distillation have been discussed in the literature. An instructive description of its

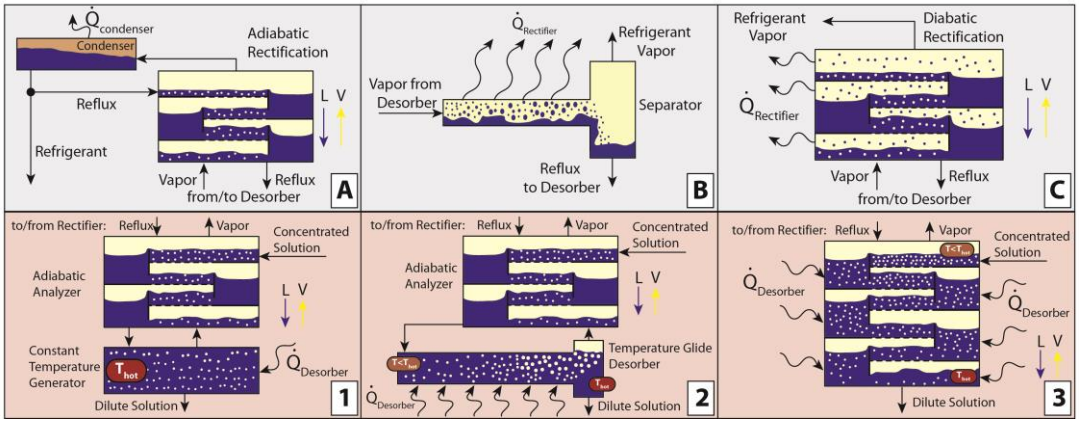

Figure 3.2: Rectification configurations (top), desorption configurations (bottom)

merits is provided by Kotas (2013) . Further quantification and experimental validation of the reduction of exergy destruction is provided by de Koeijer and Rivero (2003).

Based on the review of the literature, three rectification types are selected as shown in Figure 3.2. Type A is the conventional adiabatic column with complete condensation reflux. Type B employs solution cooled partial condensation with vapor-liquid co-flow, while type C is a solution-cooled diabatic column with liquid-vapor counter flow purification and the integration of heat rejection. Three configurations for the desorber-analyzer section as shown in Figure 3.2 are selected. Desorption Type 1 is a kettle type generator in combination with an adiabatic analyzer. Type 2 also employs an adiabatic column, but uses a counter-current heat source with liquid-vapor co-flow. Type 3 is a diabatic column where liquid-vapor counter flow purification is combined with counter-current heat transfer to the desorber. This leads to a combination of nine configurations that are compared.

3.3 Thermodynamic model and figures of merit

A thermodynamic model for the thermal compressor is developed, including two figures of merit for performance characterization. First, the delineation of the thermal compressor from the remainder of the cycle is established. Low-side and high-side pressure values are determined through a combination of inputs and assumptions. Concentrated solution ammonia mass fraction is determined through evaporator and absorber temperatures. Dilute solution temperature leaving the desorber, Thot, is identified as a suitable independent variable to identify optimal desorption temperatures. The behavior of thermal compressor figures of merit is investigated for a range of Thot values. The thermodynamic model includes detail to investigate the difference between various desorption and rectification configurations discussed above. Inputs and assumptions are listed and explained below.

The following model inputs are used:

- T_{amb} = 35°C
- T_{low} = 0°C
- $T_{hot,min} < T_{hot} < T_{hot,max}$
- $\dot{m}_{ref}$ = 1 kg s^{-1}
- x_{ref} = 0.9985

The following model assumptions are used:

- ΔT_{abs} = 5°C
- ΔT_{con} = 8°C
- ε_{SHX} = 0.85

- η_{pump} = 70%
- ε_{ad} = 0.5

Complete state point definition of TC inlet and outlet is required and can be obtained from SCC analysis. This requires a set of assumptions and definitions to arrive at a two temperature TC model. A constant refrigerant ammonia mass fraction of 99.85% is specified. This value combines achievable purity for small capacity systems (Keinath *et al.*, 2015) and high SCC performance, i.e., low evaporator refrigerant glide. The evaporator inlet temperature is defined as T_{low}. Pressure at this state point is calculated from saturated liquid assumptions. It is shown below that this assumption is justified at high ammonia concentrations. Absorber saturation pressure is obtained by assuming negligible pressure drop from the evaporator. Assuming a 5ºC temperature difference between T_{amb} and the saturated liquid temperature in the absorber, ammonia mass fraction is obtained. High-side pressure is obtained by assuming a 8ºC CAT between the saturated liquid state and heat sink inlet temperature. High side pressure TC connection is made by assuming negligible pressure drop in the desorber. A constant SHX effectiveness, ε_{SHX}, of 0.85 is assumed. Pump work requires electrical input, i.e., pure exergy, and cannot be neglected. A pump efficiency of 70% is assumed for this analysis. It should be emphasized that *CAT* and subcooling assumptions are implemented for the specific TC example presented here. In a generalized form of a TC model, known deviations from these assumptions can be accommodated through adjustments of the T_{amb} input to the model. The development of a characteristic relationship between an optimal generator operating temperature, T_{low} and T_{amb} removes the requirement of an explicit input for

generator temperature. Exergy supply to the generator depends on its temperature, which is not necessarily constant. A weighted average temperature, T_{des}, as shown in Eq. 3.1 is used to account for temperature variation between diabatic stages. It is assumed that each heat transfer stage control volume is well mixed, leading to a constant pool temperature.

$$T_{des} = \frac{\dot{Q}_{des}}{\sum_{i}^{N} \frac{\dot{Q}_i}{T_i}} \tag{3.1}$$

Two figures of merit are identified and compared. First, a second law efficiency is considered for the TC control volume shown in Figure 3.1. An energy based efficiency value requires knowledge of heat rejection from the absorber. However, heat rejection in the absorber is considered lost exergy and contributes to exergy destruction in Eq. 3.2. It can therefore be eliminated from the definition of exergetic TC efficiency, η_{TC}, as defined in Eq. 3.3.

$$\dot{Q}_{des}\left(1-\frac{T_{amb}}{T_{des}}\right)+\dot{W}_{pump} = \dot{E}x_{out} - \dot{E}x_{in} + \dot{I} \tag{3.2}$$

$$\eta_{TC} = \frac{\dot{E}x_{out} - \dot{E}x_{in}}{\dot{Q}_{des}\left(1-\frac{T_{amb}}{T_{des}}\right)+\dot{W}_{pump}} \tag{3.3}$$

An alternative figure of merit is defined as the specific heat input, q_{des}, i.e., the heat input required per unit mass of refrigerant as shown in Eq. 3.4. This value is primarily determined by TC configuration, component specification, and operating conditions. The SCC has very little effect on q_{des} and affects primarily the refrigerant

flow rate and extensive generator heat input. Therefore, this figure of merit provides a better quantification of endogenous TC performance.

$$q_{des} = \frac{\dot{Q}_{des}}{\dot{m}_{ref}} \tag{3.4}$$

Global desorption and rectification control volumes are divided into diabatic and adiabatic control volumes. For example, desorption Type 3 and rectification Type C, i.e., the diabatic distillation column configurations have a control volume arrangement as shown in Figure 3.3. Reflux is produced and vapor flow is reduced in every diabatic section of the rectifier through partial condensation. It combines with reflux leaving the adiabatic section above to enter the adiabatic section below. Some minimal net vapor

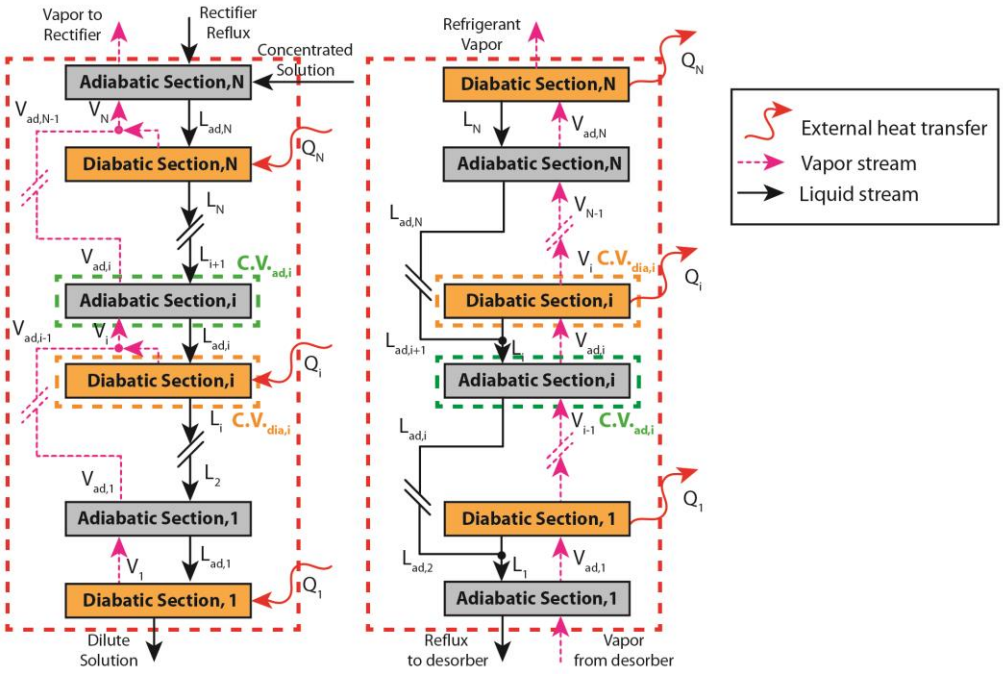

Figure 3.3: Thermodynamic model segmentation, desorption type 3 (left) and rectification type C (right)

generation occurs in each adiabatic section as reflux is heated by vapor from below. The combined reflux on the bottom of the rectification column enters the top adiabatic section of the desorber where it combines with concentrated solution. Vapor purification in each adiabatic section causes a minimal amount of vapor generation as solution is heated with hotter vapor from lower trays. Vapor generation occurs in each diabatic section in the desorber with no reflux generation as vapor from lower sections bypasses the current diabatic section. A well-mixed pool is assumed in each diabatic section with vapor generated at this mixed temperature. Configuration A-1 consists of a single diabatic and adiabatic control volume for desorption and rectification, respectively. Conservation equations for mass, species and energy are applied to each control volume as well as to the global control volume of the component. The model is based on equilibrium thermodynamics in combination with a Murphree efficiency, ε_{ad}, in the adiabatic control volume to account for liquid-vapor non-equilibrium (Fernandez-Seara *et al.*, 2003). Eq. 3.5 and Eq. 3.6 provide the definition of the Murphree efficiency for the desorber and rectifier adiabatic sections, respectively. The limiting flow rate in the desorber is that of the vapor, while liquid flow rate governs the rectifier.

$$\varepsilon_{ad,des} = \frac{x_{V,ad,i} - x_{V,i}}{x_{V,ad,i(T_{V,ad,i}=T_{L,ad,i})} - x_{V,i}} \tag{3.5}$$

$$\varepsilon_{ad,rect} = \frac{x_{L,ad,i} - x_{L,i}}{x_{L,ad,i(T_{L,ad,i}=T_{V,ad,i})} - x_{L,i}} \tag{3.6}$$

Conservative values for $\varepsilon_{ad} = 0.5$ are used for all configurations (Zavaleta-Aguilar and Simões-Moreira, 2012). For configuration C-3, uniform heat input (desorber) and uniform heat rejection (rectifier) is assumed. Thus, the global component energy

balance is used to divide heat input and rejection at each diabatic stage, $\dot{Q}_i$ into equal values. This circumvents the need for the specification of *CAT* between working fluid and heat source/sink at each diabatic stage. While the heat source temperature can be chosen based on a *CAT* assumption, heat sink temperature in the rectification stages is dictated by the concentrated solution temperature at any given operating condition. A minimum *CAT* of 3°C is used to ensure that no temperature *pinch-point* occurs. For design C-3, this *pinch-point* is avoided at all operating conditions and the corresponding rectification load requirements and solution temperatures. However, for rectifier design B, a maximum value for T_{hot} is encountered when rectification loads exceed available heat sink capacity, and a *pinch-point* occurs. Values for T_{hot} are therefore limited to rectification loads lower than maximum solution heat sink capacity. While alternative heat sinks such as ambient air could be used, this situation demonstrates that rectification type C is the preferred design as discussed below.

The resulting system of equations is solved iteratively on the *Engineering Equation Solver* (Klein, 2015) platform. The number of stages in the diabatic distillation configuration has to be specified to provide closure. A single stage represents the combination of a diabatic section and adiabatic section in Figure 3.3. Rectification Type A and Desorption Type 1 represent a single adiabatic and diabatic stage, respectively. The number of stages can be specified for configuration C-3. A single stage represents Desorption Type 1 and Rectification Type A. Significant performance improvements are achieved as the number of stages is increased at low stage numbers, while at large numbers, the improvement is marginal. (Model results for thermal compressor performance of configuration C-3 or a stage count between one and ten at T_{amb} = 35ºC

and T_{low} = 0ºC are shown in Figure 3.4.) This is to be expected for two reasons: first, a high stage number approaches a continuous temperature gradient, which reduces the grade of required heat input. Secondly, the fixed value for ε_{ad} increases overall purification efficiency with higher stage number. This reduces heat rejection in diabatic rectification sections and thereby improves TC performance. Both effects are marginalized as the number of stages is increased. In particular, if design considerations include highly compact component size as well as economical fabrication, an upper limit of stage numbers is expected. Marginal increases in operational performance do not justify increased component size and fabrication cost at higher stage counts. While a detailed exergoeconomic analysis can provide more detailed justification for optimal number of stages, a stage count of ten for desorption type 3 is chosen here for the remainder of the analysis.

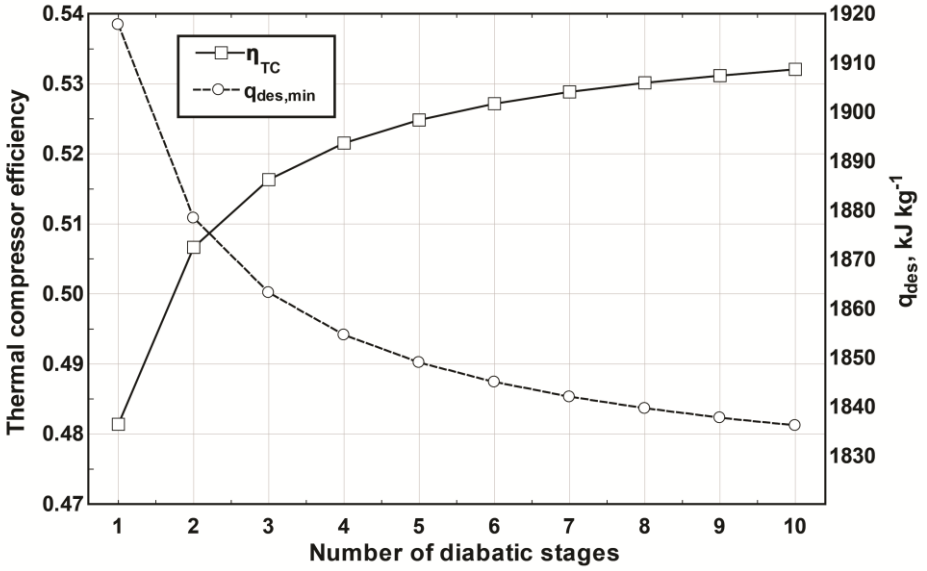

Figure 3.4: Thermal compressor performance versus diabatic stage count

3.4 Configuration Study Results

Results for all nine configurations are compared for nominal operating conditions of T_{amb} = 35ºC and T_{low} = 0ºC and a range of dilute solution temperatures leaving the desorber, T_{hot}. This temperature was chosen as a characteristic parameter as it can be easily measured and is a suitable control variable. It also provides information about heat source temperature requirements. Figure 3.5 shows TC efficiency as well as specific heat input for Desorption Type 1 in combination with all three rectification types. A distinct maximum of TC efficiency is shown for all configurations, with Rectification Type C providing the greatest value. This optimum temperature increases slightly from Rectification Type A to C. Minimum heat input is observed for all configurations at a specific temperature, which is consistent with maximum *COP* values observed in previous studies (Engler *et al.*, 1997). Minimum specific heat input decreases from Rectification Types A to C. The optimal temperature for minimum heat input is much

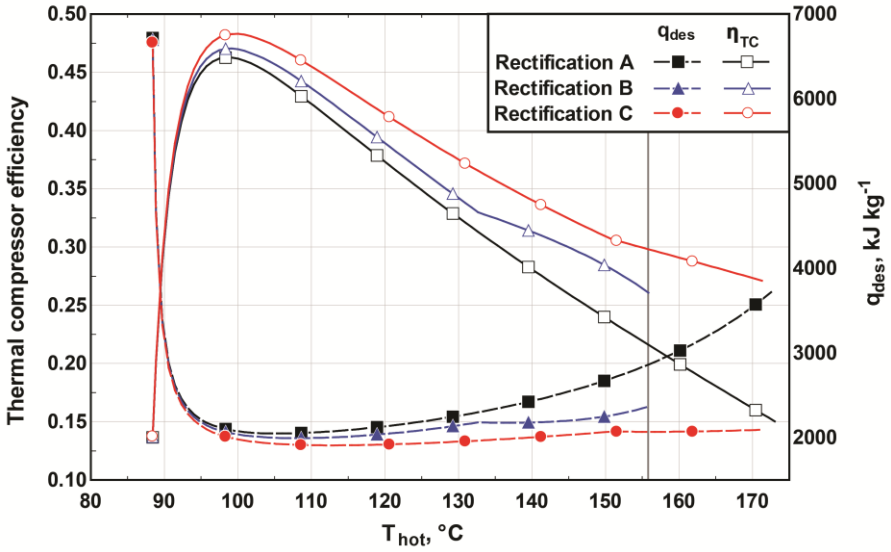

Figure 3.5: Rectification comparison for desorption Type 1

less pronounced for Rectification Type C than it is for type A. This is due to excessive purification requirements of vapor leaving the kettle-type desorber at high temperatures. Rectification Type B has a maximum temperature beyond which solution cooled partial condensation cannot provide sufficient purification to achieve the required refrigerant concentration. This poses a limitation on T_{hot} for this configuration. The sudden change in slope for both, η_{TC} as well as q_{des}, indicates that the saturated liquid state is reached in the solution cooled rectifier, underlining significant heat rejection requirements. Rectification Type C is considered optimal and used in combination with various desorption types. Liquid-vapor countercurrent flow prevents heat sink limitations and avoids excessive heat rejection requirements at high T_{des} values. Figure 3.6 shows a distinct maximum TC efficiency with Desorption Type 3 having the greatest value. Exergy destruction in Type 1 is greatest due to lack of temperature glide matching. Exergy destruction for Type 2 is somewhat greater than that for Type 3 despite temperature glide matching in both types. This is due to greater heat input requirements for Type 2. Specific heat input is also lowest for Desorption Type 3. It should be noted that these trends in heat input are due to the better purification achieved by Desorption Type 3. While the exergetic advantage of Types 2 and 3 cannot be obtained with Type 1, a large analyzer section, i.e., greater values of ε_{ad}, for Type 2, can achieve energetic and exergetic performance similar to that of Type 3. However, this will lead to greater size, weight and vapor generation requirements. The results show that the optimum temperatures are generally somewhat higher for configuration C-3. Nevertheless, the performance of configuration C-3 at slightly lower values of T_{hot} that optimize other configurations is still greatest. In other

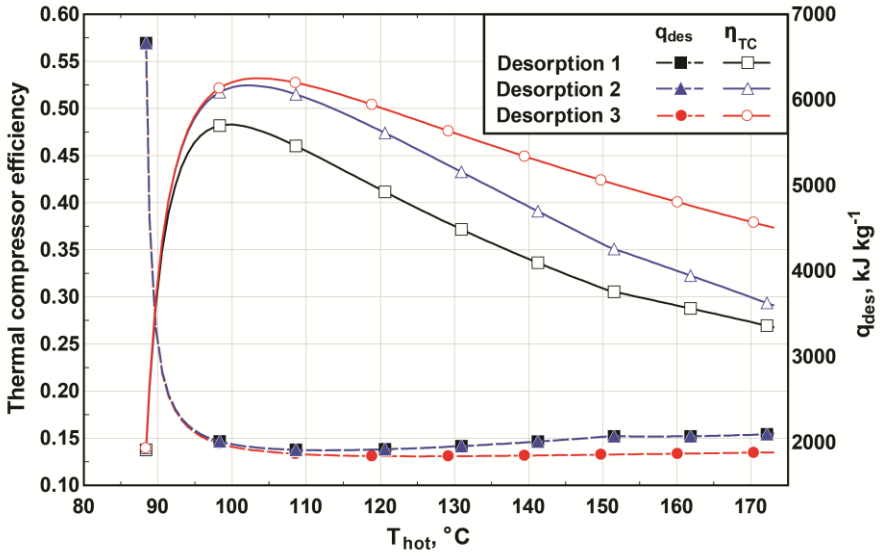

Figure 3.6: Desorption comparison for rectification Type C

words, the performance of C-3 is greater than that of any other configurations at their respective optimum temperatures.

While more detailed heat and mass transfer modeling is required to provide an exact size comparison, the amount of vapor generation required per unit mass of refrigerant delivered to the SCC is considered. The total amount of required vapor generation in the diabatic segment for configuration A-1 is compared to that of all diabatic segments in C-3 at their respective minimum heat inputs. The ratio of total diabatic vapor generation requirements for both configurations is shown in Figure 3.7 for a range of T_{amb} and T_{low}. At high temperature lift conditions, the discrepancy is greatest. Here, configuration A-1 requires almost 1.5 times the vapor generation rate as configuration 3-C. This leads to the requirement of larger diabatic sections for vapor generation and larger adiabatic sections to provide vapor-liquid interaction to achieve comparable purification. Therefore, it can

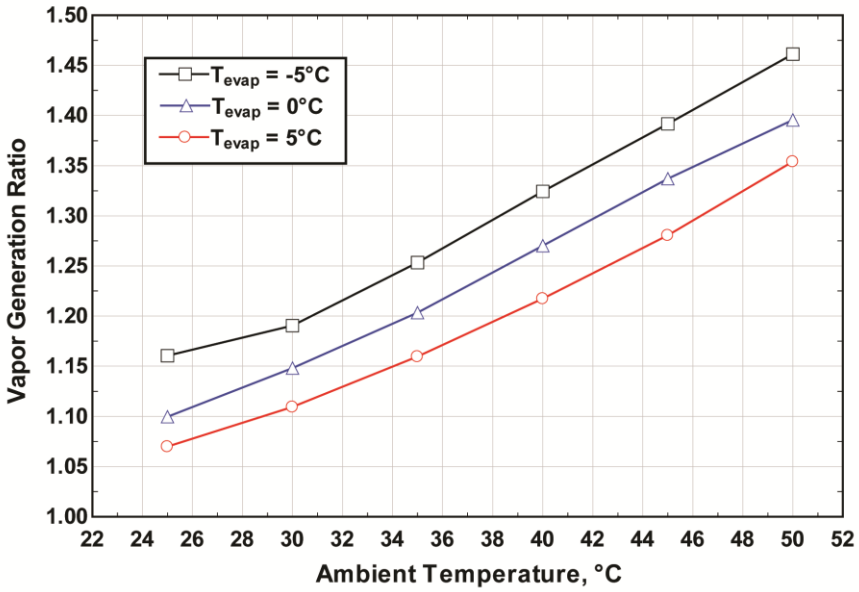

Figure 3.7: Vapor generation rates in diabatic sections

be concluded that TC configuration C-3 is optimal, particularly for small capacity machines where component size and weight reduction is important.

These results showed that η_{TC} is maximized for values of T_{hot} less than those for which q_{des} is minimized. This result can be generalized by invoking Eq. 3.2 and taking the derivative with respect to T_{hot}. Given that minimizing exergy destruction maximizes TC efficiency, Eq. 3.7 reveals that a value for T_{hot} that allows an extremum for both figures of merit would result in a trivial solution for q_{des}. This shows that these events must occur at distinctly different temperatures, leading to the definition of $T_{opt,I}$ (minimization of q_{des}) and $T_{opt,II}$ (maximization of η_{TC}). Eq. 3.8 is based on Eq. 3.7 and shows the slope of the curve for q_{des} at the point where an extremum for exergy destruction occurs. This value is shown to be negative in Eq. 3.8 . In both equations, it is assumed that $\frac{\partial T_{des}}{\partial T_{hot}} > 1$, which is justified based on the definition of T_{des} in Eq. 3.1. If it is

known that only unique and distinct values of q_{des} and η_{TC} exist, Eq. Eq. 3.8 implies that the minimum value for q_{des} occurs at a value for T_{hot} that is greater than $T_{opt,II}$, i.e., $T_{opt,I} > T_{opt,II}$. This result is expected from the definition of η_{TC}. For $T_{des} > T_{opt,I}$, both q_{des} and its associated exergy increase cause a decrease in η_{TC}. For $T_{des} < T_{opt,I}$, a small increase in q_{des} can be compensated for with a reduced exergy input due to lower T_{des} values, which further increases η_{TC} for temperatures between $T_{opt,II}$ and $T_{opt,I}$. At values of $T_{des} < T_{opt,II}$, this effect is no longer sufficient to compensate for increases in $q_{des,}$ which causes η_{TC} to increase as well.

$$\left(\frac{\partial \dot{I}}{\partial T_{hot}}\right)_{T_{amb},T_{low}} = \left(1-\frac{T_{amb}}{T_{des}}\right)\frac{\partial \dot{Q}_{des}}{\partial T_{hot}} + \dot{Q}_{des}\frac{T_{amb}}{T_{des}^2}\frac{\partial T_{des}}{\partial T_{hot}} \qquad 3.7$$

$$\left(\frac{\partial \dot{Q}_{des}}{\partial T_{hot}}\right)_{T_{amb},T_{low}} = -\dot{Q}_{des}\frac{T_{amb}}{T_{hot}^2}\left(\frac{T_{des}}{T_{des}-T_{amb}}\right)\frac{\partial T_{des}}{\partial T_{hot}} \qquad 3.8$$

In the preceding analysis, heat source coupling to the desorber was omitted to develop a general TC model. Exergy destruction in the desorber due to heat source coupling depends strongly on the specific application, with corresponding variation in η_{TC}. As a representative case, a heat transfer coupling fluid was integrated with the thermodynamic model. A *pinch-point* temperature of 5ºC was used. The addition of heat source coupling did not cause meaningful changes in values of q_{gen}, $T_{opt,I}$ and $T_{opt,II}$, only causing a reduction of $\eta_{II,TC}$ and thereby ensuring the generality of this framework for various heat source applications. *Pinch-point* location varies for operating conditions as shown in Figure 3.8, where temperature profiles of solution and coupling fluid at respective $T_{opt,I}$ are shown. Introducing a distribution, f_i, which is the fraction of total

desorber heat input at stage *i*, Eq. 3.1 is recast as Eq. 3.9. Profiles shown in Figure 3.8 are obtained for $f_i = 1/N$, i.e., uniform distribution. The variation in temperature profiles suggests that temperature profile adjustment through non-uniform heat input distribution unctions could maximize benefits of temperature glide matching. Investigations of heat distribution for diabatic tray columns were reported by de Koeijer *et al.* (2002) and de Koeijer *et al.* (2004), who compare various approaches to finding optimal distribution functions. In this study, several non-uniform distribution functions were applied to investigate the potential for optimization. However, only marginal performance improvements were achieved. Moreover, these improvements are not consistent for various operating conditions, causing slight performance decrease for some. Based on the results of the present investigation, heat distribution function optimization is not likely to result in meaningful and consistent component performance improvements. Therefore, a uniform distribution function may be applied at the design stage.

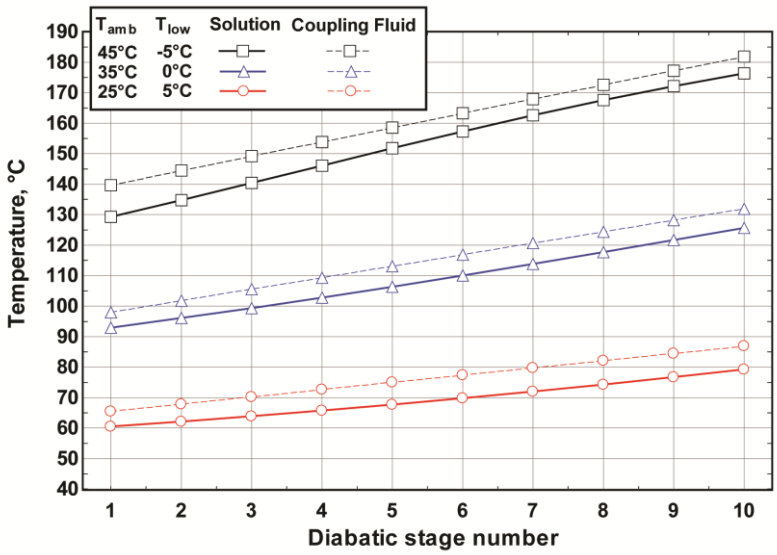

Figure 3.8: Desorber temperature profiles at various operating conditions

$$1/T_{des} = \sum_{i}^{N} f_i / T_i \qquad 3.9$$

The sensitivity of TC performance to variations in the SCC was investigated by comparing TC performance over a range of refrigerant pre-cooler (RPC) effectiveness values. This provides variation of TC inlet conditions that could be caused not only by RPC effectiveness, but also by variations of temperature glide in the evaporator. It was found that the values of q_{des}, $T_{opt,I}$ and $T_{opt,II}$ are virtually unaffected, while slight variations in η_{TC} occur as shown in Figure 3.9.

The following conclusion about the applicability of TC figures of merit can be made: The value of either $T_{opt,I}$ or $T_{opt,II}$ is relevant, depending on the specific design purpose. The qualitative behavior shown in these figures suggests that values of $T_{hot} < T_{opt,II}$ lead to rapid performance degradation due to excessive circulation ratios, $CR = \dot{m}_{cs} / \dot{m}_{ref}$. Hence, $T_{opt,II}$ can be employed as a practical minimum T_{hot} design

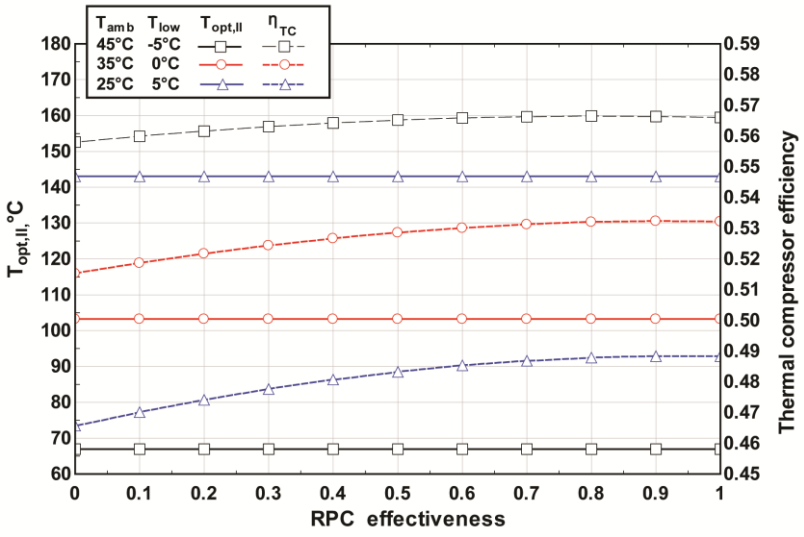

Figure 3.9: Thermal compressor exergetic performance versus RPC effectiveness

temperature. The range between $T_{opt,II}$ and $T_{opt,I}$ could be regarded as the design range for T_{hot}. Absolute values of η_{TC} depend on heat source coupling and somewhat on SCC configuration. Therefore, this figure of merit provides utility in determining the value of $T_{opt,II}$. Its absolute value may be interesting by itself, particularly for true thermodynamic comparisons to other cycles, but it has to be determined for the specific application and SCC configuration under consideration.

The optimal design as informed by thermodynamics has been established and an exergetic comparison between the conventional TC configuration, A-1, and the optimal configuration, C-3, is shown in Figure 3.10. For this comparison, heat transfer fluid coupling with a *CAT* value of 5˚C is integrated into both configurations. Values are determined for nominal operating conditions of $T_{amb} = 30^{o}C$ and $T_{low} = 0^{o}C$ at maximum thermal compressor efficiency, which corresponds to 98˚C for configuration A-1 and 104˚C for C-3. Exergy destruction values are reported per unit mass of refrigerant generated, $\dot{m}_{ref}$. Total exergy destruction is significantly reduced from 245 kJ kg^{-1} to 192 kJ kg^{-1}, which can be attributed to the optimization of the desorber and the rectifier. Exergy destruction in the absorber increased for configuration C-3. This is caused by a shift of heat rejection from the condenser to the absorber due to solution cooled rectification. The solution cooled rectifier increases the concentrated solution temperature at SHX inlet temperature, which causes an increase in dilute solution temperature at the absorber. This shows that the presence of the solution heat exchanger allows for some recuperation of rectification heat rejection while a meaningful fraction of it still has to be rejected to the ambient. However, the total heat rejection from the absorber is still less for

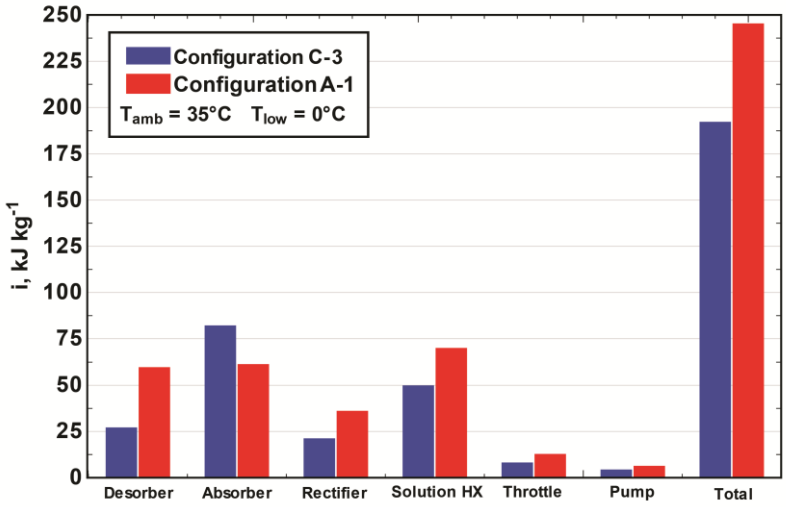

Figure 3.10: Component exergy destruction comparison for configurations A-1 and C-3

configuration C-3 than that for C-1. Absorber heat rejection is 1901 kJ kg^{-1} for configuration A-1compared to 1841 kJ kg^{-1} for configuration C-3.

3.5 Thermal Compressor Module Development

The above analysis presents the framework for developing a thermal compressor model. $T_{opt,I}$ is identified as the target operating condition of the desorber, i.e., $T_{hot} = T_{opt,I}$. $T_{hot} = T_{opt,II}$ can be considered a practical minimum temperature for operation of the absorption system. Values of $T_{hot} < T_{opt,II}$ cause excessive circulation ratio values and lead to rapid performance degradation. The range $T_{opt,II} < T_{hot} < T_{opt,I}$ can be treated as a practical operating range for the desorber. The analysis was illustrated for fixed values of T_{amb} and T_{low} and assumptions for condenser and absorber approach temperatures. A generalized thermal compressor module was developed to estimate the variation in performance over a wide range of operating conditions. Configuration C-3 was determined to be the most optimal desorption-rectification combination and is selected for the TC module development. In addition to $T_{opt,I}$ and $T_{opt,II}$, the following variables are identified as

relevant parameters: Desorber heat input at $T_{opt,I}$ *and* $T_{opt,II}$, i.e., $q_{opt,I}$ and $q_{opt,II}$. The lowest temperature in the desorber, the temperature of solution entering the desorber, T_{feed}, is also of interest. Its value can be used in combination with a nominal approach temperature to determine the lowest possible temperature of the heat source leaving the desorber. In combination with T_{hot} and a nominal approach temperature assumption, these values are particularly useful for exact heat source specification and the design of cascaded thermal systems.

A statistical approach is applied in combination with the detailed thermodynamic model developed for the thermal compressor in this study. A large data set is generated for a range of ambient temperature between 25°C and 55°C (46 values) and a range of T_{low} of -10°C to 10° (21 values). For these 966 combinations of T_{amb} and T_{low}, model results for 50 values of T_{hot} are obtained. T_{hot} ranges from 5°C above the theoretical minimum to 5°C below the theoretical maximum. Theoretical maximum and minimum values for T_{hot} are determined for each combination of T_{amb} and T_{low} based on the resulting concentrated solution ammonia mass fraction, $x_{cs,}$ and high side pressure, $P_{high.}$ The minimum value is the saturated liquid temperature of concentrated solution, i.e., infinite values for *CR*. As T_{hot} is reduced and approaches the concentrated solution saturation temperature, refrigerant vapor generation decreases and *CR* escalates. The maximum value for T_{hot} is taken as saturated liquid temperature of dilute solution leaving the desorber with zero ammonia mass fraction, i.e., complete desorption, $x_{ds} = 0$. This produced a data set of 48,300 values. Data for each combination of T_{amb} and T_{low} were scanned to find the maximum values for q_{des} and η_{TC} to determine $T_{opt,I}$ and $T_{opt,II}$ resulting in 966 values for optimal first and second law desorber heat input temperatures. The data

set also provides values for all other relevant variables identified above. Statistical characterization of these data maintains the benefits of a detailed thermodynamic model without the number of assumptions required to produce a feasible analytic model. This approach also has the benefit of black-box type models in that simple, algebraic correlations for the identified variables are developed. Two statistical methods are applied to the data set. Results for regression analyses are compared with Artificial Neural Networks (ANN) results. The latter is obtained with the Neural Network Toolbox™ by MATLAB® (2017) where 10 hidden layers are used with 70% of the data set used for training and 15% for validations and 15% for testing.

T_{amb}, T_{low} are the independent variables that determine $T_{opt,I}$ and $T_{opt,II}$ in the illustrative example discussed in this study. However, the utility of the thermal compressor module is increased if absorber and condenser approach temperature assumptions are isolated. Therefore, x_{cs} and P_{high} are used as independent variables. x_{cs} depends on the combination of T_{amb} and T_{low} while P_{high} depends on the condenser heat sink temperature, e.g., T_{amb}. Results from the regression analysis are shown in Eq. 3.10 through 3.15 for relevant variables with their associated R^2 values. A comparison between regression and ANN results for $T_{opt,I}$, $T_{opt,II}$, $q_{opt,I}$, $q_{opt,II}$ is shown in Figure 3.11. ANN results provide slightly better accuracy of data prediction. However, regression results are also very accurate and only marginal improvement is achieved with ANN for these parameters.

$$T_{opt,I} = -9.96\times10^{1} + 2.8\times10^{-2}P_{high} + 8.5\times10^{-6}P_{high}^{2} - 2.54\times10^{-9}P_{high}^{3} + 1.9\times10^{3}x_{cs} - 5\times10^{3}x_{cs}^{2} + 3.67\times10^{3}x_{cs}^{3} \quad (\mathbf{R^2 = 99.88\%}) \qquad 3.10$$

$$q_{des,I} = 5.98\times10^{3} - 2.87\times10^{-1}P_{high} + 1.22\times10^{-4}P_{high}^{2} - 1.44\times10^{-8}P_{high}^{3} - 1.65\times10^{4}x_{cs} + 2.32\times10^{4}x_{cs}^{2} - 1.26\times10^{4}x_{cs}^{3} \left(\mathbf{R^2=99.98\%}\right) \quad 3.11$$

$$T_{feed,I} = 1.8\times10^{2} + 4.3\times10^{-2}P_{high} - 4.42\times10^{-6}P_{high}^{2} - 4.27\times10^{2}x_{cs} + 2.41\times10^{2}x_{cs}^{2} \left(\mathbf{R^2=99.98\%}\right) \quad 3.12$$

$$T_{opt,II} = 2.19\times10^{2} + 4.41\times10^{-2}P_{high} - 3.68\times10^{-6}P_{high}^{2} - 5.04\times10^{2}x_{cs} + 2.77\times10^{2}x_{cs}^{2} \left(\mathbf{R^2=99.90\%}\right) \quad 3.13$$

$$q_{des,II} = 5.74\times10^{3} - 2.68\times10^{-1}P_{high} + 9.84\times10^{-5}P_{high}^{2} - 1.21\times10^{-8}P_{high}^{3} - 1.39\times10^{4}x_{cs} + 1.70\times10^{4}x_{cs}^{2} - 8.25\times10^{3}x_{cs}^{3} \left(\mathbf{R^2=99.92\%}\right) \quad 3.14$$

$$T_{feed,II} = 1.67\times10^{2} + 4.35\times10^{-2}P_{high} - 4.42\times10^{-6}P_{high}^{2} - 3.97\times10^{2}x_{cs} + 2.25\times10^{2}x_{cs}^{2} \left(\mathbf{R^2=99.99\%}\right) \quad 3.15$$

Finally, it is of interest to determine values for q_{gen} and T_{feed} at non-optimal operating conditions. The independent variables x_{cs}, P_{high} and T_{hot} are selected. The regression analysis for $T_{feed} = f\left(T_{hot}, x_{cs}, P_{high}\right)$ produced a relatively complex expression with a coefficient of determination of 99.90%. No satisfactorily accurate expression ($R^2 > 90\%$) for $q_{des} = g\left(T_{hot}, x_{cs}, P_{high}\right)$ could be found. However, the ANN analysis could provide acceptable results with R^2 values of 99.74% and 99.99% for q_{des} and T_{feed} respectively as shown in Figure 3.11 E and F.

The independent variables chosen in the analysis above only implicitly account for T_{amb} and T_{low}. These variables, however, are the main input parameters for system level modeling and must be related to x_{cs} and P_{high} used in the statistical analyses to provide useful thermal compressor characterization. x_{cs} depends on evaporator pressure, P_{low}, and saturated liquid solution temperature in the absorber. In a single constituent fluid, P_{low} can be directly correlated to T_{low}. Figure 3.12 shows how temperature varies

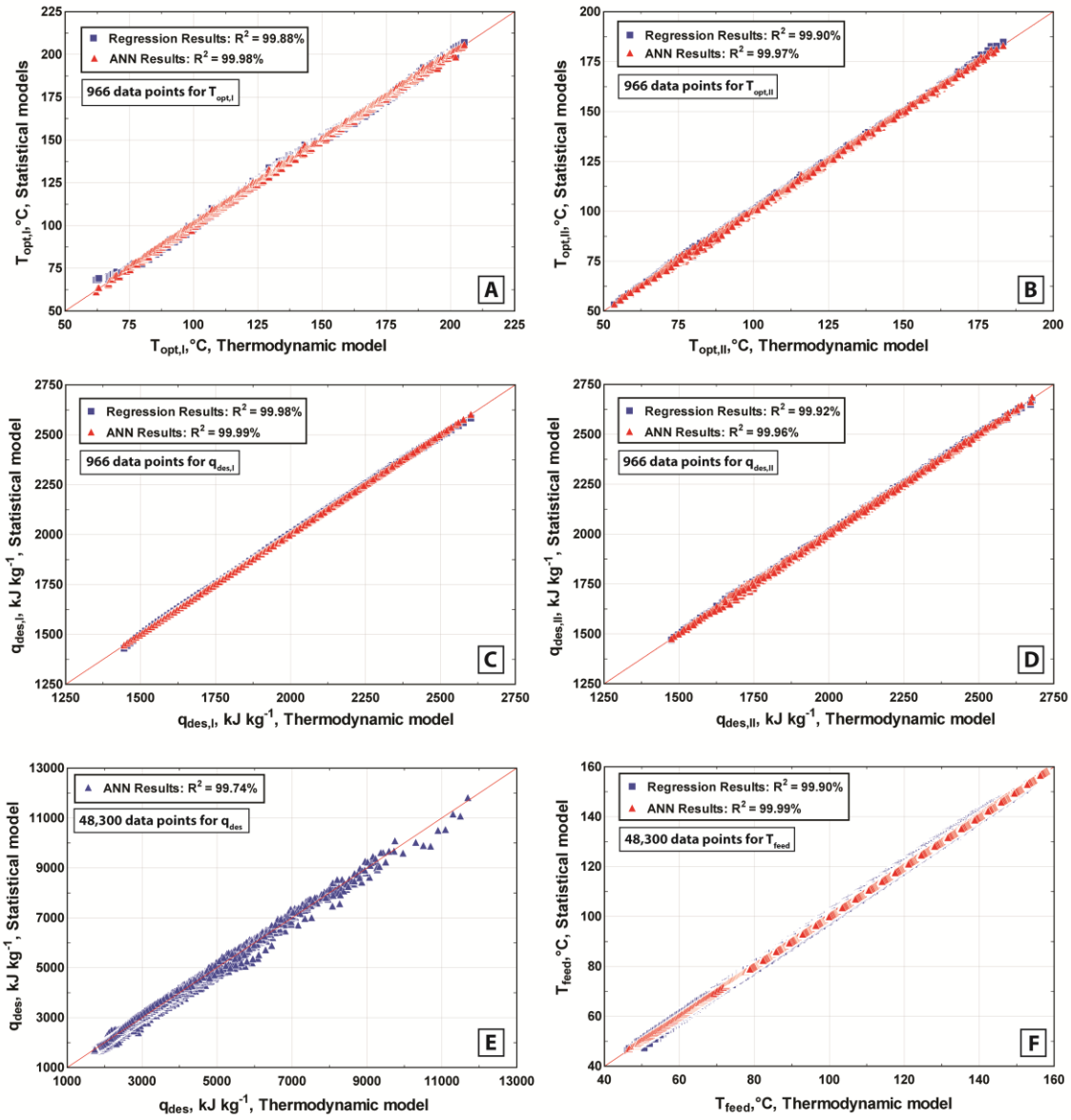

Figure 3.11: Statistical model versus thermodynamic model for various variables. A: $T_{opt,I}$, B: $T_{opt,II}$, C: $q_{des,I}$, D: $q_{des,II}$, E: q_{des}, F: T_{feed}

throughout the evaporation process, with a temperature rise at high qualities. At low qualities, the effects of refrigerant concentration, for realistic values of x_{ref} and quality changes are minimal. Moreover, typical quality values at the evaporator inlet are ~0.1-0.15, not exceeding 0.2. This suggests that binary mixture effects during the evaporation process can be ignored in the evaporator inlet region in order to directly correlate

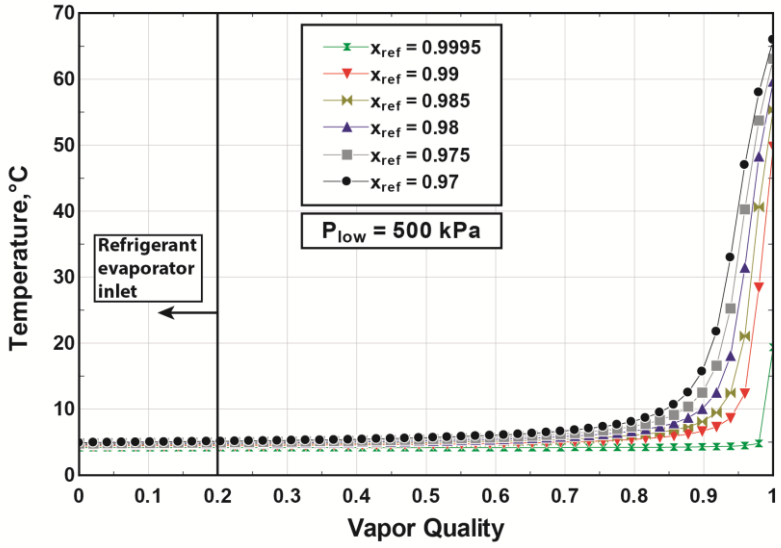

Figure 3.12: Temperature for various refrigerant concentrations and vapor qualities

evaporator inlet temperature, T_{low} to pressure, P_{low}. Using nominal and fixed values for quality and concentration of 0.1 and 0.99, respectively, T_{low} can then be used as a proxy variable for P_{low} when determining $x_{cs.}$ In combination with the saturated liquid temperature in the absorber, $T_{abs,sat}$, a data set was generated to develop an expression for $x_{cs} = f\left(T_{low}, T_{abs,sat}\right)$ with $R^2 = 99.99\%$ as shown in Eq. 3.16 for a range of $20^{o}\mathrm{C} \le \mathrm{T}_{\mathrm{abs,sat}} \le 55^{o}\mathrm{C}$ and $-20^{o}\mathrm{C} \le \mathrm{T}_{\mathrm{low}} \le 20^{o}\mathrm{C}$. $T_{abs,sat}$ is related to T_{amb} by Eq. 3.17 where the value of ΔT_{abs} depends on specific system characteristics. A nominal value, e.g., 5-7°C can be taken as an estimate for system-level modeling efforts.

$$x_{cs} = 7.72\times10^{-1} + 9.80\times10^{-3}T_{low} + 2.67\times10^{-5}T_{low}^{2} - 9.03\times10^{-3}T_{abs,sat} + 3.44\times10^{-5}T_{abs,sat}^{2} - 6.26\times10^{-5}T_{low}T_{abs,sat} \quad (3.16)$$

$$T_{abs,sat} = T_{amb} + \Delta T_{abs} \quad (3.17)$$

Similarly, Eq. 3.18 provides an expression for P_{high} as a function of saturated liquid temperature in the condenser for range of $25^{o}\mathrm{C} \le \mathrm{T}_{\mathrm{con}} \le 60^{o}\mathrm{C}$ ($R^2 = 99.99\%$). T_{con} is correlated to T_{amb} by Eq. 3.19.

$$P_{high} = 5.64\times10^{2} + 5.64T_{con,sat} + 4.68\times10^{-1}T_{con,sat}^{2} \quad 3.18$$

$$T_{con,sat} = T_{amb} + \Delta T_{con} \quad 3.19$$

Finally, an approach temperature between T_{low} and the chilled medium in the evaporator is used as shown in Eq. 3.20.

$$T_{evap,CF,out} = T_{low} + \Delta T_{evap} \quad 3.20$$

Eqs. 3.17, 3.19 and 3.20 provide coupling between external variables and system internal independent variables for the thermal compressor module. Moreover, T_{amb} does not need to be the same for both equations. That is, a series heat sink configuration can be readily modeled by prescribing separate heat sink temperatures with Eqs. 3.17 and 3.19. This corresponds to a four-temperature model for the thermal compressor. However, with the definition of $T_{opt,I}$ as the target operating condition, the value for T_{hot} is implicitly determined with T_{amb} and T_{low}. This suggests that T_{hot} can be effectively eliminated as an input parameter, reducing a three- or four- temperature model to a two- or three-temperature model, respectively. This provides a meaningful advantage over previous modeling approaches.

Both regression and ANN techniques provide accurate characterization of optimal thermal compressor performance. ANN are slightly more accurate but regression results have the advantage of providing simple and explicit algebraic equations. This facilitates

implementation of the thermal compressor module without the need to incorporate ANN and is particularly useful for the development of a model-based control algorithm in a microcontroller.

While the model in the present study can be readily applied at the design stage, a model-based controller is likely to require additional inputs and system-specific characterization data. Specifically, heat exchanger performance varies during operation of an actual heat pump. This can be addressed by replacing fixed approach temperatures in the condenser, absorber and evaporator, i.e., Eqs. 3.17, 3.19 and 3.20, with a system characterization. If high-side pressure is measured directly in an actual system, Eqs. 3.18 and 3.19 can be eliminated from the model-based controller. Calculation of q_{des} may require an additional model input and retraining of the ANN model to account for the variation of ε_{SHX} , for example.

The comparison between both methods further shows that both have the same level of physical insight, i.e., both use input variables that are informed by physical reasoning, thereby limiting the number of inputs and model complexity. However, this study also shows that the non-ideal, three input model requires ANN for acceptable model results. This suggests that advanced statistical methods such as ANN are required for general predictability of non-ideal behavior with more than two input variables. Other advantages of ANN include the ability to “re-train” the model for accuracy improvements with additional or modified data and the need to specify terms for an explicit expression is eliminated.

The set of equations presented above provides a method to model a thermal compressor for the simulation of absorption heat pump systems. Accurate specification of

heat source requirements allows for integration into cascaded thermal systems and waste heat recovery applications. With this technique, the analysis of the absorption cycle can be conducted in a simple manner similar to that used for vapor compression cycles. A particularly useful application of this thermal compressor model is system control. Results from this study can be implemented in a model-based control algorithm for optimal absorption system control. Combining a statistical black-box approach with a detailed thermodynamic model maintains the level of detail of the internal system complexity while minimizing and isolating assumptions. Internal configurations and assumptions can be modified if required and the underlying data set can be readily updated to produce a revised model in an automated fashion. This accommodates variations of system internals while maintaining a methodology to provide accurate model predictions.

3.6 Conclusions

Various TC configurations for a single-effect cycle were compared through thermodynamic modeling. Two figures of merit were established and used for comparison of different configurations for the vapor generation in a TC. Diabatic distillation was identified as the optimal design approach for both, desorption and rectification. It was found that energy based performance occurs at greater value of T_{hot} than exergy based optimization, leading to two distinct optimal TC temperatures, $T_{opt,I}$ and $T_{opt,II}$. T_{hot} was found to be a critical variable for TC modeling and design as well as for an optimized control algorithm. It was shown that these values as well as specific TC heat input are independent of SCC. The definition of these optimum temperatures

eliminates the need for explicit specification of T_{hot}, which can be obtained through specified values of T_{amb} and T_{low}. Additional important TC parameters, e.g., heat input, were identified and statistical analyses, i.e. regression and ANN, yield accurate thermal compressor models for a wide range of operating conditions. It was shown that regression is able to provide concise algebraic equations for optimal thermal compressor performance, while ANN are required to provide general, non-ideal performance prediction. This modeling approach combines benefits of exergetic and exergetic analyses with benefits of detailed thermodynamic modeling and black-box type modeling. Results of this study can be applied to system level modeling, including cascaded thermal systems. These results can also form the foundation of model-based control algorithms for optimal thermal compressor control. Future work includes experimental validation of optimal performance and the development of a model-based controller with experimental validation. Eventually, the TC concept could be extended to include more complex cycle configurations and working pairs other than ammonia-water.

CHAPTER 4. HYDRODYNAMIC CONSIDERATIONS

4.1 Introduction

In thermally activated vapor absorption cooling and refrigeration cycles, the mechanical compressor of the vapor compression cycle is replaced with a set of heat and mass exchangers and a liquid pump. This is commonly referred to as the thermal compressor. Its key components are the absorber, the desorber and a recuperative heat exchanger, the solution heat exchanger. In the case of ammonia-water absorption systems (AAS), an additional vapor purification stage, i.e., a rectification stage, is added to the desorber. Research focus on improved absorber designs has resulted in increased heat and mass transfer fluxes and more compact components (Nagavarapu and Garimella, 2011) that address the limitations of the absorber to the overall system, i.e., the system "bottleneck" (Beutler *et al.,* 1996). However, additional research focus on the desorber and rectifier components is required to ensure optimal design and operation of the thermal compressor based on the following design criteria:

1. Optimal exergy utilization of heat input
2. High purity vapor generation
3. Compact component size
4. Flexible and reliable operation and control

The first criterion ensures optimal utilization of the driving heat source, allowing applications with low heat source temperatures and optimal primary energy utilization. Refrigerant vapor purity is of critical importance for many applications of AAS (Bogart, 1982). Fernandez-Seara and Sieres (2006) quantify the detrimental effect of reduced

purification performance of the desorber and rectifier on overall system performance. Hence, optimal thermal compressor design must allow for highest possible overall AAS performance, which requires delivery of high purity refrigerant to the remainder of the cycle, the simple cooling cycle (SCC). Highly compact components with simple geometries designed for manufacturing feasibility are of particular importance for small capacity applications. This enables economically feasible system designs with low weight and small envelopes (Garimella, 2003). Optimal thermal compressor design must also accommodate a range of operating conditions and reliable operation with flexible control schemes at part load operation.

Typical AAS designs use a conventional fractioning columns approach for desorption and rectification. Bogart (1982) provides an overview of this approach as applied to AAS and identifies typical hydrodynamic challenges such as liquid entrainment and carry-over into the SCC. Anand and Erickson (1999) present a design methodology for adiabatic sieve-tray columns applied to small capacity AAS to determine hydrodynamic limits and mass transfer efficiencies. Fernández-Seara *et al.* (2002) developed a coupled heat and mass transfer model for a packed column and Sieres and Fernández-Seara (2007) present an experimental investigation of mass transfer characteristics of a structured packing in an AAS adiabatic column. Few deviations from the conventional column design have been reported. Various rectification column configurations in combination with the conventional reboiler and stripping sections are compared by Fernandez-Seara *et al.* (2003). Partial condensation with internal heat recovery through the concentrated solution was shown to be thermodynamically most favorable. More recently, designs that deviate from conventional kettle type reboiler

designs have been developed for small capacity applications. Determan and Garimella (2011) present a small capacity falling film type desorber and a coupled heat and mass transfer model with experimental validation. Delahanty *et al.* (2015) present a design that employs heat source coupling through microchannels for application in 3.5 kW cooling capacity AAS.

Further development of the desorber is presented here with the introduction of two novel, highly compact design options that remove the need for a separate stripping section and address all of the design criteria discussed above. A wide range of applications is addressed by developing two designs for various types of heat source integration, e. g., direct gas coupled, and coupling through the use of a heat source coupling fluid flowing through microchannel geometries. A microchannel based design concept for the rectifier component is also presented. It is suitable for close-coupled integration with both desorber concepts discussed here.

Successful implementation of these designs depends on the feasibility of specific hydrodynamic flow conditions, i.e., liquid-vapor countercurrent flow, which have inherent limitations such as flooding and weeping. In contrast to conventional hydrodynamic evaluations of adiabatic columns, the distribution of vapor generation along the height of the diabatic column results in significant variation of vapor flow rates. Therefore, relevant geometric variables are identified for each design and a hydrodynamic design methodology is developed to specify optimal geometries. An experimental evaluation is conducted and hydrodynamic feasibility of the proposed designs is demonstrated. In addition, parameters relevant for the development of a detailed heat and mass transfer model are identified and quantified through a high-speed

video analysis of flow visualization experiments. The results of this investigation can be applied to the development of components based on the proposed design concepts.

4.2 Design Concepts

In the concepts considered here, diabatic distillation is employed, where the heat source and vapor generation are integrated with vapor purification stages. The thermodynamic advantage of this approach is discussed in general terms by Kotas (2013). The benefits of this design approach to AAS was shown in Chapter 3. Exergy destruction caused by temperature differences between the heat source and the working fluid can be minimized through targeted distribution of heat transfer area that achieves matching of the heat source temperature profile to that of the zeotropic mixture undergoing a boiling process. This also reduces heat source temperature requirements. Integration of vapor purification within each heat transfer stage allows for the lowest possible vapor temperatures leaving each stage, which is determined by the tray efficiency. Proper

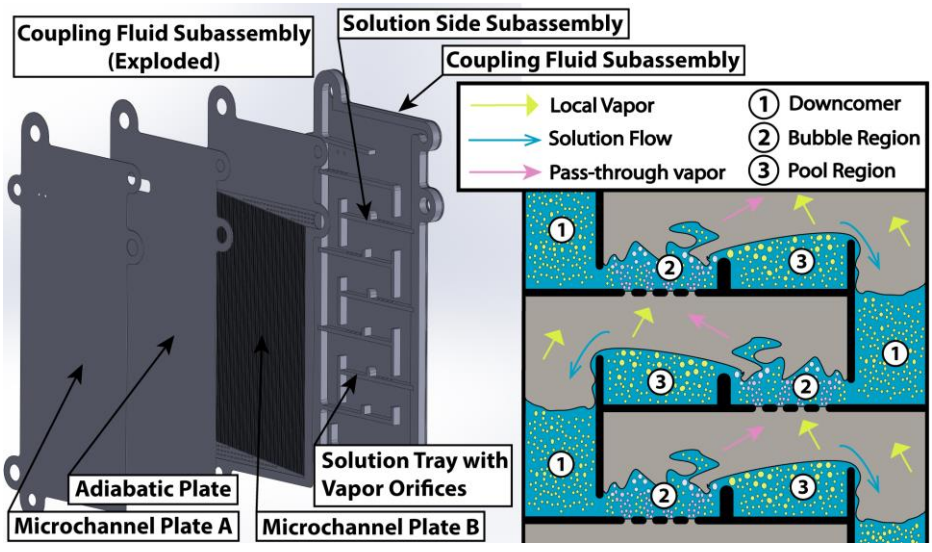

Figure 4.1: Design Concept A, component assembly (left), target flow pattern (right)

design allows for a close approach of vapor temperature leaving the desorber to that of the concentrated solution feed in the top tray. This eliminates the need for an analyzer section, i.e., no dedicated stripping column is required. This approach is therefore conducive to highly compact component designs.

The first design, Concept A, is a microchannel based desorber as shown in Figure 4.1. A coupling fluid delivers heat from a generic heat source to the component through a microchannel assembly. The solution-side assembly consists of liquid-vapor countercurrent flow paths formed by trays. Each tray has three distinct regions:

1. A downcomer where liquid from the tray above is accumulated.
2. Liquid then enters the bubble region. Here, hotter vapor from below is injected through orifices to facilitate liquid-vapor interaction and vapor purification.
3. Liquid then enters the pool region of the tray without vapor injection before it enters the downcomer of the tray below.

This pattern is repeated in each tray. Relevant geometric features are the number of orifices in each tray, their size, and the spacing of each tray.

Concept B is developed for direct-coupled heat source applications, e.g., exhaust gas heat recovery or integration with combustion systems. This application is not conducive to the use of microchannel geometries due to gas-side pressure drop limitations; therefore, conventional gas tubes are used in this concept. In the proposed flow pattern, shown in Figure 4.2, a downcomer feeds liquid from above onto the pool side of the tray. Hot gas tubes are sealed to the tray to provide an extended heat transfer surface area and to ensure liquid build-up against a weir plate. Liquid enters the bubble

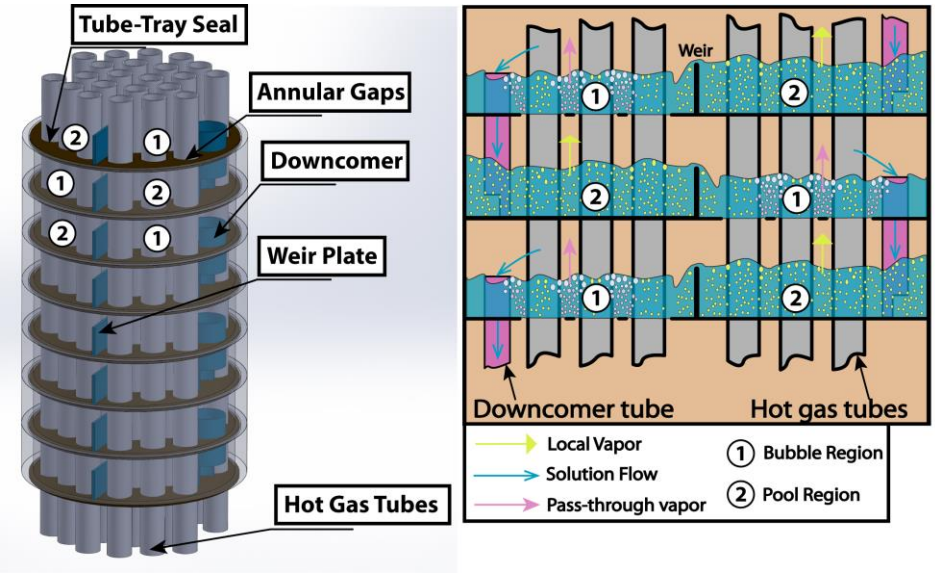

Figure 4.2: Design Concept B, component assembly (left), target flow pattern (right)

side of the tray over the weir where it develops liquid-vapor interaction with hot vapor from below. This is the result of annular gaps that are formed between the tray and hot gas tubes through which vapor injection occurs. Liquid then enters the downcomer to feed the pool side of the tray below. The dimensions of the annular gap as well spacing between trays are relevant geometric features.

A rectifier design concept is shown in Figure 4.3 where microchannel geometries are applied for the heat sink. It is particularly suited for integration with desorption design Concept A into a single vapor generation unit. It can also be readily employed with design Concept B as a compact standalone component in a close-coupled arrangement. The vapor cavity can contain a random or structured packing. Vapor leaving the desorption stage enters at the bottom and partial vapor condensation continuously produces reflux. Reflux flows in a gravity driven, countercurrent flow path. This arrangement promotes liquid-vapor interaction as continuous vapor purification occurs. High effectiveness of liquid-vapor interaction results in more efficient thermal

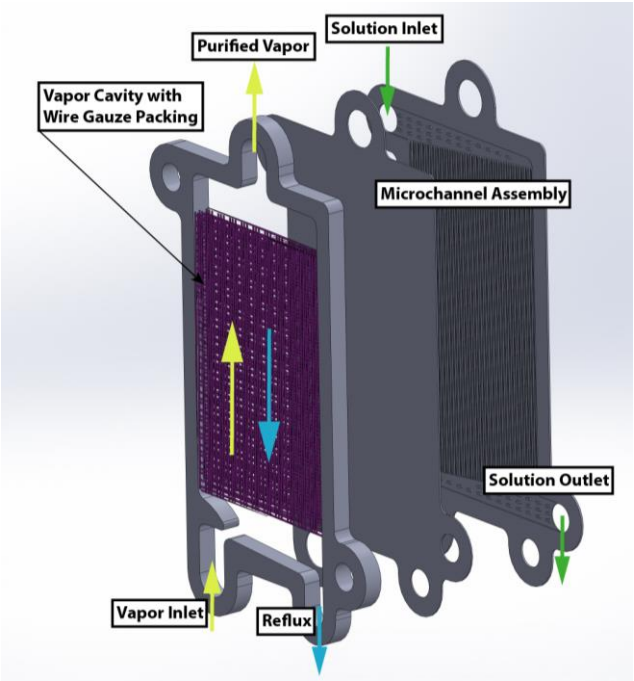

Figure 4.3: Rectifier design concept

compressor operation. In such a geometry, reflux leaves the rectifier at a temperature close to that of the inlet vapor.

4.3 Hydrodynamic Design Methodology

The design concepts considered here rely on hydrodynamic behavior that satisfies all the design criteria enumerated above. Liquid-vapor countercurrent flow is inherent to these designs and is governed by two hydrodynamic limitations. At high vapor flow rates, countercurrent flow limitations (CCFL) cause liquid entrainment and component flooding. At low vapor flow rates, liquid weeping through vapor orifices prevents tray activation in the desorber, i.e., formation of a liquid level in the bubble region of the tray, reducing purification efficiency. CCFL have long been the subject of research efforts due to their significance to many applications, e.g., nuclear reactors, distillation columns, and

gas-liquid fossil fuel pipelines. The approach presented byWallis (1969) is most widely used for CCFL predictions, particularly for small fluid passages (Ghiaasiaan, 2007). The general correlation shown in Eq. 4.1 was developed where the parameters m and C are empirically determined values that depend on the specific geometry and fluid properties. Modified superficial velocities are defined in Eq. 4.2 where *k* corresponds to the gas or liquid phase. Here, $j_k = \dot{V}_k / A_c$ is the superficial velocity where $\dot{V}_k$ and A_c correspond to volumetric flow rate and characteristic cross-section, respectively.

$$\sqrt{j_G^*} + m \cdot \sqrt{j_L^*} = C \tag{4.1}$$

$$j_k^* = \sqrt{\frac{\rho_k}{(\rho_L - \rho_G) g D_c}}\, j_k \tag{4.2}$$

Significant further development of CCFL models occurred over the last decades (Deendarlianto *et al.*, 2012). However, given that more advanced CCFL models are increasingly specific to particular geometries and fluid properties, the basic Wallis approach is applied for CCFL characterization of the novel geometries considered here. Moreover, a Wallis-type model is also commonly applied for weeping limitations in countercurrent liquid-vapor contactors (Thorat *et al.*, 2001) and is therefore employed here to characterize tray activation. The characteristic length scale, D_c, in Eq. 4.2 is the hydraulic diameter of the vapor passage in the bubble region of both designs. This is the orifice diameter in Concept A and the hydraulic diameter of the annulus, $D_h = D_o - D_i$, for Concept B. A hydrodynamic Wallis characterization of a tray for a specific geometry is shown schematically in Figure 4.4 (left). A flood line delineates the ideal operating region from CCFL where liquid entrainment compromises proper operation of the

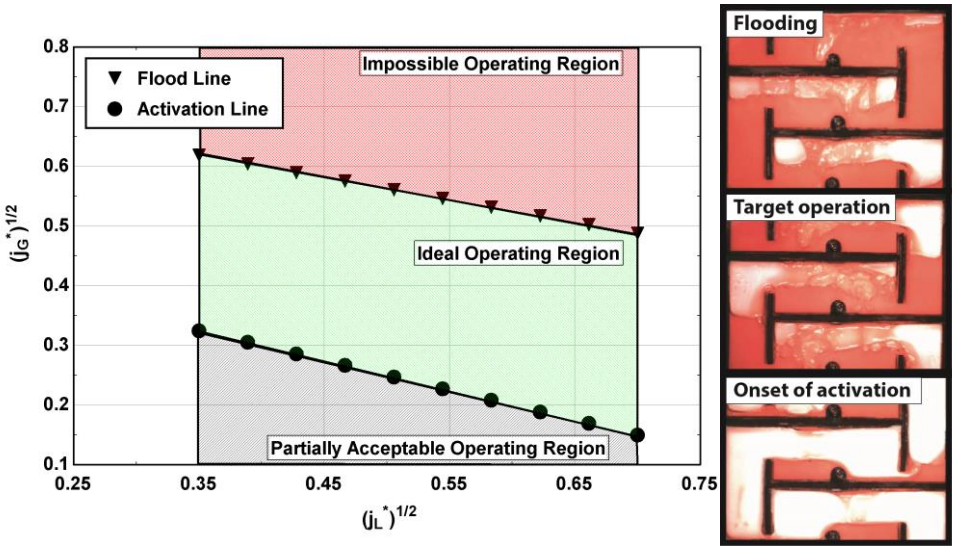

Figure 4.4: Conceptual Wallis-type graph of flooding and activation (left), corresponding flow pattern for each operating region (right)

component and the entire AAS. An activation line describes flow rates at which liquid build-up in the bubble region is achieved. A visualization of the flow pattern associated with flooding, onset of activation and the target operating flow pattern is also shown in Figure 4.4 (right). Figure 4.5 depicts the actual operating field of a specific tray geometry for a range of flow rates that correspond to a load from 33% to 100%. Each line corresponds to a position within the component. Liquid and vapor flow rates vary from the top tray to the bottom tray, and also for various loads. This is captured by various lines in the operating field. It can then be compared to the CCFL and activation lines for that specific geometry, i.e., Figure 4.5 can be superimposed onto Figure 4.4. The actual operating field shown in Figure 4.5 varies with changes to its geometry, e.g., hole diameter or number of holes. Preferably, the operating field falls within the ideal operating region shown in Figure 4.4. At low liquid and vapor flow rates, below activation, tray efficiency is reduced and heat transfer mechanisms differ. However, sufficient heat transfer may still occur in inactive trays due to falling film wetting of the

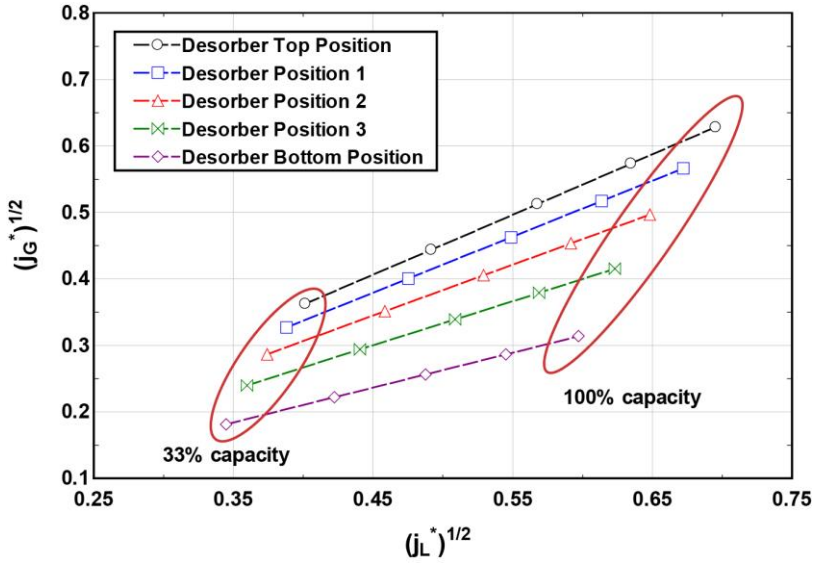

Figure 4.5: Hydrodynamic operating field for specific component geometry

heated wall. At part load operation and tray positions toward the bottom of the desorber, inactive trays may be accommodated if tray activation at higher desorber positions provides sufficient purification. Therefore, some interference between the operating field and activation line may be tolerated, which qualifies the region below the activation line in Figure 4.4 as partially acceptable. The operating field can be established with knowledge of tray geometry, fluid properties and flow rates. Flood and activation lines must be determined experimentally. Results for each considered geometry are used to properly design trays throughout the component. This accommodates high variation of vapor flow rates within the component while optimizing hydrodynamic behavior.

Beyond CCFL and activation, hydrodynamic behavior in the bubble region affects tray purification efficiency. Knowledge of this efficiency allows the use of an equilibrium method, e.g., the Ponchon-Savarit method (Zavaleta-Aguilar and Simões-Moreira, 2012), which greatly simplifies design and analysis. Factors that influence tray efficiency are interfacial area, bubble size and mass transfer rates (Akita and Yoshida, 1974). While

much research has been dedicated to the evaluation of these parameters for working fluids and column dimension commonly encountered in industrial processes (Gandhi *et al.*, 2009), very little work relevant to small capacity AAS is available. However, implementation of a heat and mass transfer analogy as demonstrated by Lee *et al.* (2008) eliminates the need for explicit mass transfer data. Therefore, a detailed heat and mass transfer model can be developed with knowledge of a characteristic length scale for vapor structures, a characteristic velocity and liquid-vapor interfacial area. This diabatic design requires quantification of heat transfer area, which can be further categorized into the type of flow to apply an appropriate heat transfer coefficient, e.g., single-phase flow, liquid pool, or two-phase flow. These parameters are determined in this investigation through flow visualization as discussed below.

4.4 Experiments

4.4.1 Experimental Facility

A test facility for air-liquid experiments was designed and constructed to simulate the hydrodynamic behavior expected in a small-capacity AAS. Figure 4.6 shows the experimental facility, which utilizes either pure distilled water (E0) or a mixture with 60% ethanol (E60). This ethanol concentration provides surface tension and density values similar to those encountered in AAS (Vazquez *et al.*, 1995). E60/E0 ratios for dynamic viscosity, density and surface tension are 2, 0.85 and 0.36, respectively. Both the Morton number, $Mo = \left(g\mu_L^4 \Delta\rho\right) / \left(\rho_L^2 \sigma^3\right)$, and Ohnesorge number, $Oh = \mu_L / \sqrt{\rho_L \sigma L_C}$, capture these properties. Assuming negligible variation in length scale, the E60/E0 ratios for Mo and Oh are 385 and 4.4, respectively. Dye is added to the liquid to facilitate

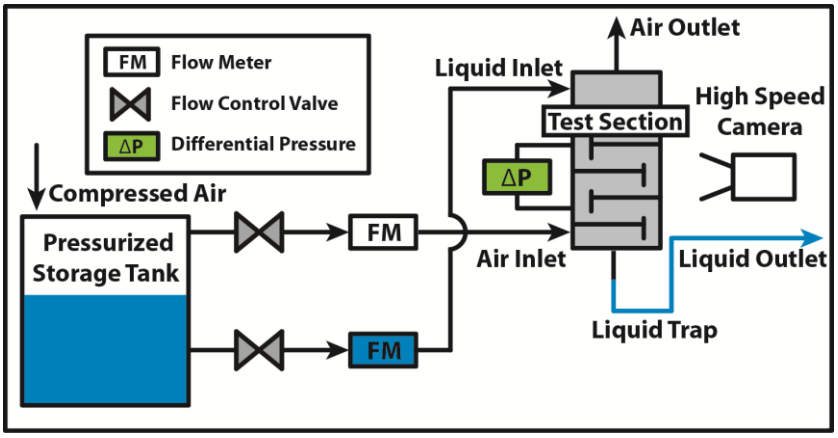

Figure 4.6: Experimental facility

visualization of hydrodynamic behavior. Compressed air is used to pressurize a tank that provides liquid flow to the test section. Air is drawn from the top of the tank to simulate vapor flow in the test section. Vapor and liquid flow rates are controlled to target values with metering valves. Turbine flow meters are used for Test Section A with flow ranges of $0.33 - 3.33 \times 10^{-5}$ m^3 s^{-1} and $0.17 - 1.75 \times 10^{-6}$ m^3 s^{-1} for gas and liquid flow, respectively. The uncertainty associated with these flow meters is ±1% and ±3% of full scale for liquid and gas flow, respectively. A set of rotameters with an uncertainty of ±4% of full scale is used for Test Section B. Two liquid flow meters with ranges of $0.53 - 5.25 \times 10^{-6}$ m^3 s^{-1} and $2.10 - 26.3 \times 10^{-6}$ m^3 s^{-1} are used for low and high liquid flow rates, while two vapor flow meters with ranges of $1.57 - 17.3 \times 10\text{-}5$ m^3 s^{-1} and $3.1 - 47.2 \times 10\text{-}5$ m^3 s^{-1} are used for low and high gas flow rates. Flow meter calibration was conducted for both liquids. A differential pressure transmitter with a range of 25 kPa (uncertainty of ±0.01 kPa) is used to measure pressure drop across each test section.

4.4.2 Test Sections

Two desorber test sections were designed and fabricated for evaluation of both design concepts as shown in Figure 4.7 and Figure 4.8. Test section A was fabricated from ABS plastic as a single part with additive manufacturing. This test section includes all proposed geometric features. The depth of the working fluid cavity is 6.3 mm. Each tray has four orifices with a diameter of 2.5 mm. Geometric modification of the tray is limited to variation of the number of orifices by successively sealing individual holes. A clear plastic cover with a gasket seal is used to provide visual access to the internal flow patterns. The assembly is compressed with a set of bolts to ensure proper internal and external sealing. Test Section B is an assembly of machined stainless steel plates. A total of three trays is used in combination with transparent sections of clear plastic tube (D_o = 114 mm) that form the shell of the assembly and provide visual access to internal flow patterns. Stainless steel tubes (D_o = 12.7 mm) are used to simulate heat source passages.

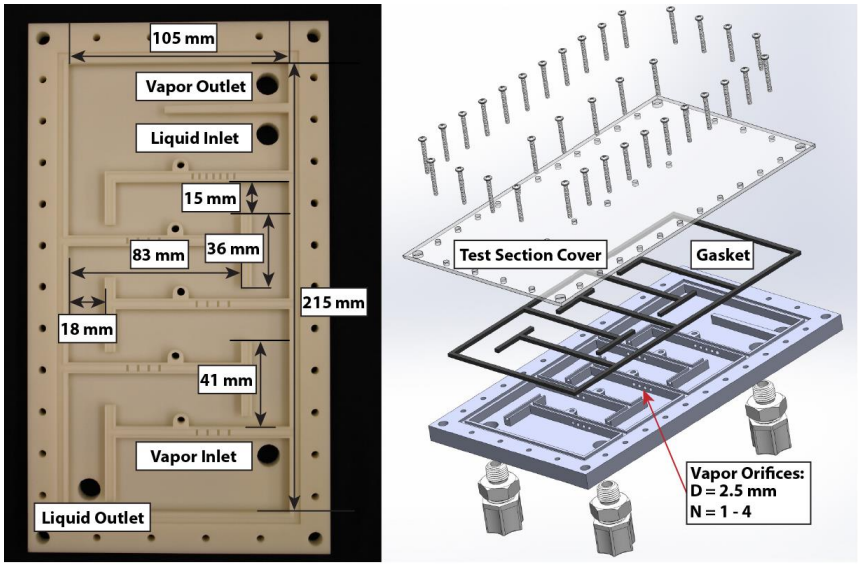

Figure 4.7: Test section for design concept A

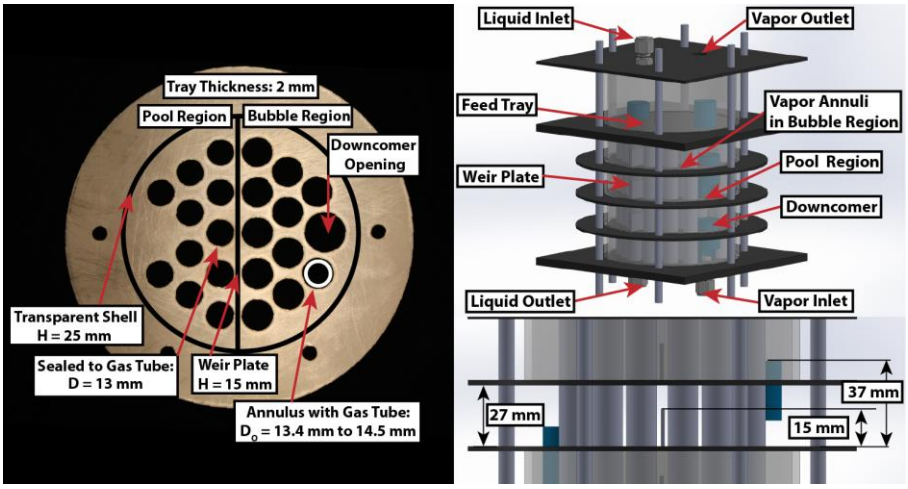

Figure 4.8: Test section for design concept B

They are sealed to the tray in the pool region and form annuli with the tray in the bubble region. Both regions are separated through a weir plate that is sealed to the tray. A stainless steel tube (D_o = 19 mm) is used as a circular downcomer in each tray and is sealed to the tray in the bubble region. Geometric modification of the trays is limited to variation of the annulus size.

Hydrodynamic behavior of the rectifier packing was investigated using a random packing. Stainless steel wire gauze (type 304) was used in the test section as shown in Figure 4.9. The geometric feature of interest is the specific surface area, i.e., the surface area of packing divided by the empty volume the packing occupies. This parameter can be modified through variation of the number of layers of gauze that are packed in the casing. Given material specification and gauze geometry, the specific surface area can be established for various packing layers. In this investigation, two, four and six layers of wire gauze are used, the last being the highest density of gauze that can readily be inserted into the test section cavity. This corresponds to packing specific surface area values of 350, 700 and 1050 m^2/m^3 respectively. Porosity values for two, four and six

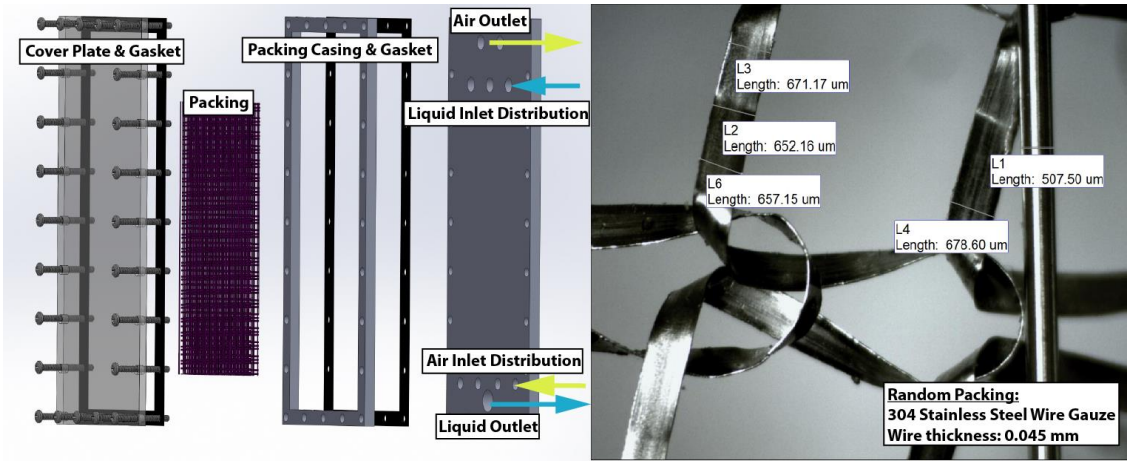

Figure 4.9: Rectifier test section (left) and wire gauze packing (right)

layers are 99, 98 and 97% respectively. High porosity values in combination with high specific surface area values are typical, indeed desirable, for a random packing and tend to result in a low pressure drop penalty for a significant increase in transfer area Kolev *et al.* (2006).

4.4.3 Experimental Procedure and Flow Visualization

Four versions of Test Section A, with one to four holes per tray are investigated. Three annulus sizes are investigated for Test Section B, i.e., values for D_o of the tray bubble side holes are 13.7 mm, 14.0 mm and 14.2 mm, while maintaining a constant value of D_o for the gas tubes, i.e., annulus D_i of 12.7 mm. Flood and activation lines are established for each geometry with E0 as well as E60 fluid. This results in eight flood lines and eight activation lines for Test Section A and six flood lines and six activation lines for Test Section B. Both, activation lines and flood lines, are established for a range of liquid flow rates that correspond to the operating field. For each liquid flow rate, the vapor flow rate is slowly increased until tray activation is observed. At this point, all gas flow passes through the bubble tray allowing build-up of a liquid-vapor region on the

bubble side of the tray. Gas flow rates are further increased until component flooding is observed. Flooding may be caused through excessive liquid build-up in the downcomer due to increased backpressure of vapor flow through tray orifices. Liquid can thereby escape through the vapor outlet port of the component, a condition called downcomer flooding. Also, entrainment of droplets into the vapor stream at high vapor flow rates may occur, a condition called entrainment flooding.

Further flow visualization is conducted for Test Section A. The shallow depth of 6.3 mm justifies the assumption of a two-dimensional flow pattern. High-speed videography is used to quantify parameters that are relevant for the development of a heat and mass transfer model:

- Working fluid heat transfer area: Liquid, vapor and two-phase regions
- Characteristic length scale for vapor structures
- Characteristic vapor structure velocity
- Liquid-vapor interfacial area

All four geometric variants of Test section A are investigated for the complete operating field. Videos are recorded for three positions within the component, i.e., top (100% vapor generated), center (60% vapor generated), and bottom (25% vapor generated), as well as for three load points: 100%, 67% and 33% of full capacity. This provides a test matrix of nine points for each liquid (E0 and E60), i.e., 18 points for each desorber geometry. Only test points that resulted in fully activated tray operation without component flooding were analyzed.

A high-speed camera (Photron FASTCAM Ultima 1024 with a Nikon Micro-NIKKOR 105 mm lens) was used and recordings were taken at 250 frames per second

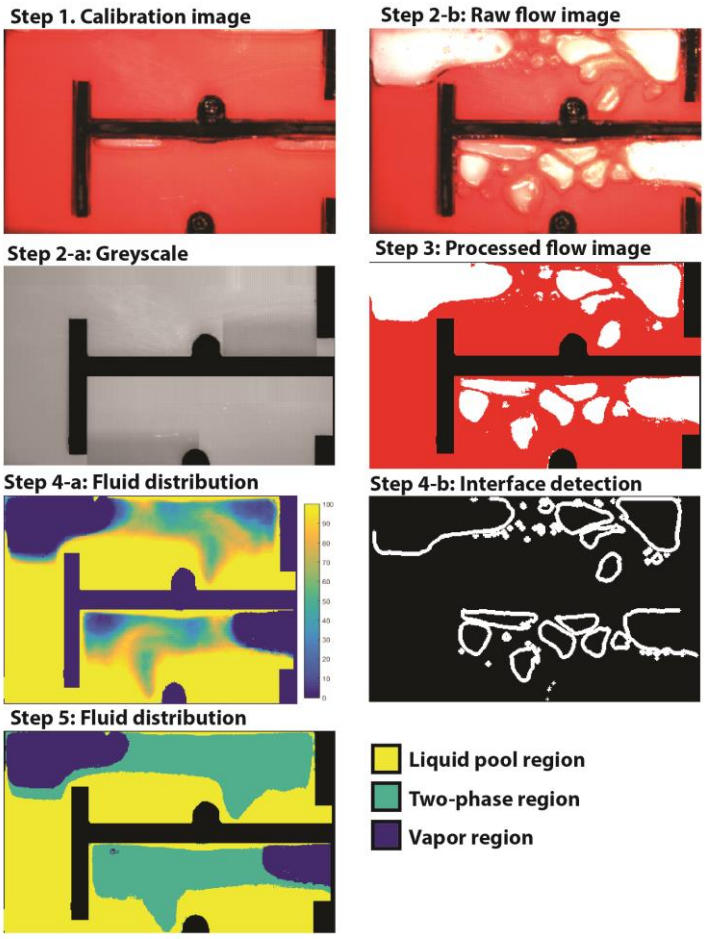

Figure 4.10: Sequence of video analysis

with a resolution of 512 × 512 pixels. A recording duration of 10 seconds was used to appropriately capture all hydrodynamic features. Videos are processed using the algorithm shown in Figure 4.10. A calibration reference image of the test section filled with dyed liquid is taken prior to flow testing. Air bubbles trapped in the calibration image are removed through an automated algorithm. The flow video is analyzed on a frame-by-frame basis to obtain raw flow images as shown in Step 2-b. Both, the calibration image, as well as the raw flow image, are converted to grayscale as shown in Step 2-a and compared. User defined threshold settings are then applied to differentiate liquid and gas regions. This produces the processed flow image shown in Step 3 that

differentiates vapor (white) from liquid (red). Subsequently, a time averaged fluid distribution image is produced from all individual binary processed flow images in a recording as shown in Step 4-a. Here, every pixel in the domain is monitored for its binary state, i.e., liquid or vapor throughout the duration of the recording. The average phase state is depicted and ranges from 0% to 100% liquid. This can then be used to define phase regions as shown in Step 5. The liquid region is defined as an average phase state of > 95% liquid, while the vapor region is defined as an average phase state of < 5% liquid. Regions within these thresholds are classified as the two-phase region. Furthermore, the Canny edge detection algorithm is applied to the processed flow image to identify the vapor-liquid interface for each frame as shown in Step 4-b. The results produced by processing of the flow images are then converted to length and area dimensions through a reference geometry and can be used to quantify parameters relevant to heat and mass transfer modeling. User defined greyscale thresholds were carefully determined for liquid-vapor differentiation by comparing raw flow images with processed flow images. Nevertheless, a degree of subjectivity is introduced through manual selection of these thresholds. The associated error is determined by Eq. 4.3. Here, Θ is a generic variable obtained from video processing, e.g., liquid area. The threshold is modified by ±10%. This range was used because at these threshold variations, noticeable deviation of the processed flow image from the raw flow image can be observed.

$$E_{\Theta} = \sqrt{\left(\Delta_{\Theta,110\%}\right)^2 + \left(\Delta_{\Theta,90\%}\right)^2} \tag{4.3}$$

It should be noted that hydrodynamic parameters determined in this this study are estimates and are based on several idealizations. This includes the assumption that three-

dimensional effects can be neglected. It is likely that some bubbles are not detected due to three-dimensional effects. In particular, the vapor injection region in the bubble region may include undetected vapor given that orifice diameters are smaller than tray depth. Moreover, the experiments conducted in this study were not conducted with ammonia-water at typical operating conditions with integrated vapor generation. It is expected that variation in fluid properties and local vapor generation may affect the hydrodynamic parameters studied somewhat. The threshold sensitivity investigation discussed above addresses these effects. The threshold variation caused visual distortion of the processed image compared to the actual flow image shown in Figure 4.10. Visual comparison at the maximum threshold variation determined that the processed flow imaged could not be considered to be an acceptable representation of observed flow patterns. However, the calculated values of hydrodynamic parameters did not result in excessive variation. For example, interfacial area only varied by ±5.3% as a result of this threshold variation. Given the low sensitivity of calculated values, the results obtained here can be considered reasonable estimates for hydrodynamic parameters within the proposed geometries and at actual operating conditions.

Detailed quantitative flow visualization analysis for Design Concept B was not performed. Flow patterns are inherently three-dimensional and complete visualization is obstructed by internal tubes of the trays, thereby preventing full visual access required for image analysis. However, qualitative assessments and parameters estimates are reported.

4.5 Results

4.5.1 CCFL and Activation

Representative results for flooding and activation for Test Section A are shown in Figure 4.11. Results for a single-orifice tray are compared with those for a four-orifice tray for E60 liquid. A shift in the operating field can be seen clearly. While volumetric flow rates are maintained constant for both cases, the reduced vapor passage area in the single-orifice tray results in higher superficial velocity values, causing the shift in operating field. The operating field of the single-orifice tray shows significant interference at high capacity and at desorber positions toward the top of the component. Activation is achieved for most of the operating field. In contrast, component flooding for the four-hole tray does not interfere with the operating field for this geometry at all. However, tray activation is limited at lower component positions and low capacities. These plots illustrate the design methodology developed in this investigation. For example, a single-orifice tray is an appropriate choice for the bottom section of the

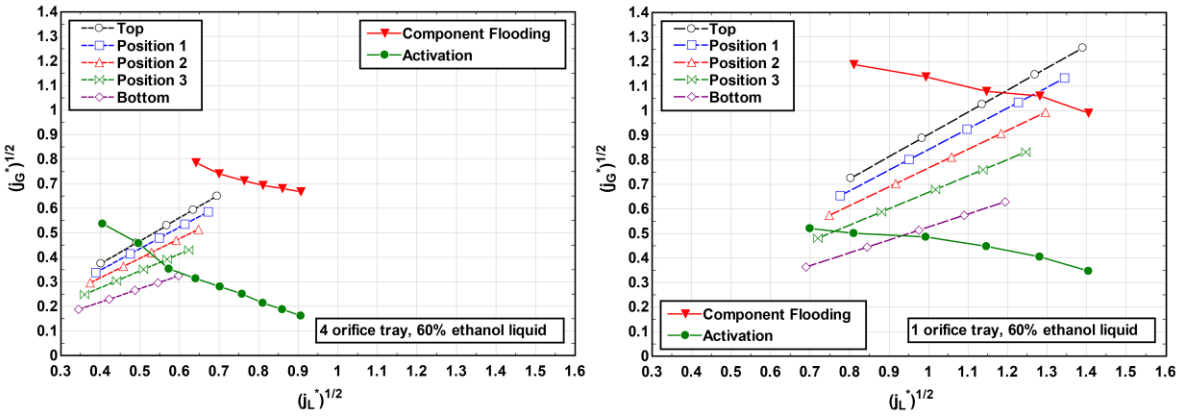

Figure 4.11: CCFL and activation results examples for design concept A with 60% ethanol liquid. Four orifice tray (left) and single orifice tray (right)

desorber, but not for the top section, as flooding is likely to occur. The four-orifice tray is an appropriate top section choice as flooding is avoided and activation is ensured for a wide capacity range. The lack of activation at low capacities is acceptable, because somewhat reduced heat and mass transfer areas can be accommodated at reduced component duties. Results for two-orifice and three-orifice trays fall between the results shown in Figure 4.11 and are used to guide geometry selection throughout the component. These results provide hydrodynamic validation of desorber Design Concept A.

Analogous results for flood and activation lines were obtained for Design Concept B and the effect of annulus dimensions in the bubble tray could be established. Results were compared with the operating field for Design Concept B and appropriate annulus dimensions for the bubble region of each tray in the component were determined. Thus, these results also validated the hydrodynamic feasibility of Design Concept B.

Results for E0 liquid did not provide significantly different results. For both design concepts, the operating field is shifted lower on the Wallis-plot as non-dimensional superficial gas velocities are reduced due to a greater liquid density. Tray activation was achieved at somewhat lower gas flow rates for both test sections. This caused a slightly lower activation line, i.e., slightly less interference with the operating field. Likewise, flooding occurred at somewhat lower gas flow rates for both designs. However, the differences in the results with E0 compared to those with E60 do not require different design solutions. Flooding prevention can be ensured for both liquids with the proposed designs through judicious tray geometry distribution across the component. The qualitative difference of hydrodynamic behavior due to variation in

surface tension and density was shown through these experiments. Thus, greater resilience to CCFL and greater activation gas flow rates were observed for E60 liquid. Separate Wallis parameters, *m* and *C*, in Eq. 4.1 can be found for each flood and activation line, but depend on geometry and fluid properties. Limited research is available on surface tension effects on CCFL (Ousaka *et al.*, 2006) and quantification of fluid property effects is challenging. This is further complicated by the unique geometries investigated. Zapke and Kröger (2000) propose Froude number $\left(Fr_k = \rho_k U_k^2 / \left(gL_C \Delta\rho_k\right)\right)$ and Ohnesorge number dependencies for simple geometries and show greater resilience to CCFL at low values for Oh_L. However, the opposite trend is observed in this investigation given that Oh_{E60}/Oh_{E0} = 4.4. This could be attributed to the unique geometries where different CCFL mechanisms take place compared to simple tube geometries typically investigated in the literature.

CCFL results for wire gauze packing are shown in Figure 4.12. Similar to desorber CCFL results, the test section experiences flooding at slightly lower gas flow rates with E0 liquid than with E60. A reduction in permissible gas flow rate with increased packing density is shown, which is expected. As local vapor and liquid flow rates increase due to higher specific surface area, flooding is initiated. Here, the characteristic length scale used in Eq. 4.2 is the width of the test section according to Osakabe and Kawasaki (1989) who investigated CCFL in rectangular geometries with dimensions similar to those of this test section. The same authors proposed a Wallis-type model with factors of m = 0.8 and C = 0.58 for their data. The model, as applied to this test section, is shown in Figure 4.12. The present results provide a more conservative prediction of CCFL. Different injection and distribution of liquid and vapor could explain

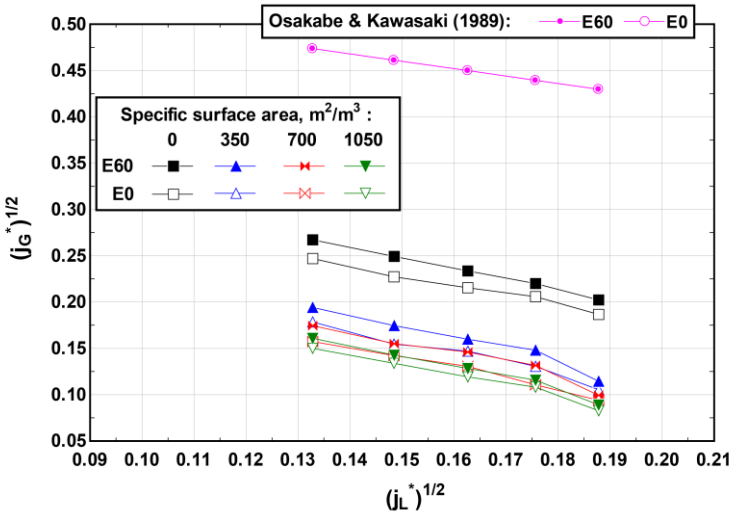

Figure 4.12: Flood lines for packed rectifier

the discrepancy in flood line despite similar geometries. While the investigated vapor flow rates are representative of small capacity AAS, liquid flow rates that cause flooding are significantly greater than typical reflux rates in a corresponding partial condenser. Therefore, it can be concluded that the proposed rectifier design is not CCFL limited.

4.5.2 Pressure Drop

Pressure drop data were collected for both test sections at flow rates representative of their operating fields. The maximum pressure drop observed for Test Section A is 350 Pa per tray at the highest liquid and gas flow rates that avoid component flooding. Implementation of Design Concept A for small capacity systems is expected to require less than 10 trays, limiting total expected pressure drop to 3.5 kPa. The maximum pressure drop for design concept B at flow conditions close to component flooding is 270 Pa per tray. Less than 12 trays are expected to be required in an actual component, limiting pressure drop to less than 3.2 kPa. Projected pressure drops for either design solution are well within acceptable limits for desorption components in AAS. This is due

to relatively large flow areas required for liquid-vapor countercurrent flow. These low expected pressure drops eliminate the need for further modeling and minimization of pressure drop in the proposed geometries.

4.5.3 Flow Visualization

Hydrodynamic parameters relevant for heat and mass transfer were listed above. The most coherent and consistent trends for these parameters were observed with bubble tray superficial gas velocity, j_G. The choice of j_G as the primary independent variable for hydrodynamic characterization is consistent with the literature on bubble columns as shown by Chaumat *et al.* (2005) and Kantarci *et al.* (2005). Akita and Yoshida (1973) showed that the isolated effect of liquid flow rate on hydrodynamic behavior is negligible in typical bubble columns. The results of this study are used to develop relationships for the relevant parameters that can be readily incorporated in a heat and mass transfer model for Design Concept A. The power law form, shown for a generic hydrodynamic parameter, Θ, in Eq. 4.4, is commonly used in the literature. Shah *et al.* (1982) present it as a general formulation for gas holdup correlations.

$$\Theta = \lambda j_G^{\gamma} \tag{4.4}$$

A power law can be applied to correlate interfacial area to superficial velocity (Schumpe and Deckwer, 1982). The liquid property dependent bubble size correlation presented by Pohorecki *et al.* (2005) is also of this form. Table 4.1 summarizes the results for all hydrodynamic parameters considered in this study, which are discussed below.

Table 4.1: Hydrodynamic parameter estimation for design concept A

Component or State Point	E0	E60	E0 & E60
Gas Holdup, ε_G	$0.18 \cdot j_G^{0.25}$	$0.3 \cdot j_G^{0.4}$	$0.24 \cdot j_G^{0.33}$
Specific Interfacial Area, A_{int} m^2 m^{-3}	$500 \cdot j_G^{0.3}$	$840 \cdot j_G^{0.5}$	$600 \cdot j_G^{0.4}$
Length Scale, L_C, mm	No discernable liquid property dependence		$4.2 \cdot j_G^{-0.1}$
Velocity, $\bar{U}_G$, m s^{-1}	$6.5 \cdot j_G^{0.8}$	$5.2 \cdot j_G^{0.8}$	$5.8 \cdot j_G^{0.8}$
Liquid tray area fraction	~ 0.42	~ 0.38	~ 0.4
2-phase tray area fraction	No discernable liquid property dependence		$0.85 \cdot j_G^{0.25}$
Downcomer liquid fraction	$j_G^{0.15}$	$0.8 \cdot j_G^{0.1}$	$0.9 \cdot j_G^{0.125}$

Separate results are presented for E0 and E60 if a discernable effect of liquid properties could be observed. A single power law correlation is provided if liquid properties did not affect results for a hydrodynamic parameter. The results presented in Table 4.1 omit the effect of injection geometry, i.e., number of vapor orifices in the tray. Variation of this parameter depends primarily on CCFL as discussed above. A slight effect of injection geometry could be observed for some parameters. However, its effects were sufficiently small to justify the choice of j_G as the only dependent variable in combination with appropriate adjustment of the power law for liquid properties. This provides a general quantification of important hydrodynamic parameters for the specific design proposed with Concept A. The error defined in Eq. 4.3 was quantified by repeating the analysis with the upper and lower threshold values. The average error for heat transfer area and interfacial area are ±1.7% and ±5.3%, respectively. For $\bar{U}_G$ and L_C, the average errors were ±6.0% and ±2.9%, respectively.

Interfacial Area and Gas Holdup: This parameter can be determined with results for interfacial length and vapor face area as shown in Steps 3 and 4-b of Figure 4.10. Only the two-phase region of the tray area is considered to determine interfacial area and gas hold-up values. It is assumed that a thin liquid film exists between the wall and the vapor in that region. This is a justifiable assumption given the stochastic behavior of vapor flow within the liquid pool. If the thickness of the liquid film is known, the depth of the vapor structure can be determined. Film thickness in the two-phase region is not measured directly but the liquid mass flux independent length scale proposed by (Hu and Jacobi (1996)), $\delta = \left(\nu_L^2 / g\right)^{1/3}$, is used to estimate its value. Vapor depth can then be multiplied by interfacial length and added to vapor face area results to complete the interfacial area calculation. A more common figure of merit for liquid-vapor contactors, however, is specific interfacial area, $a_{int} = A_{int} / V_{tray}$, which is used for further analysis. Results for interfacial area are shown in Figure 4.13 and the positive trend with j_G is

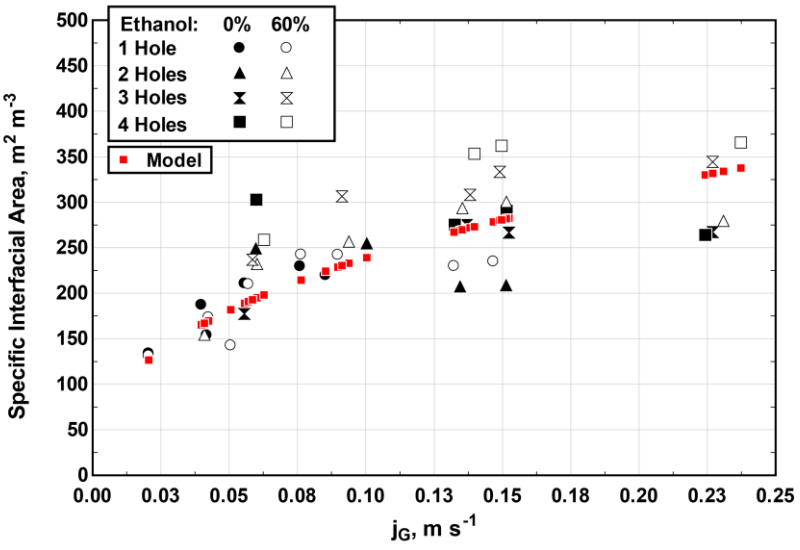

Figure 4.13: Specific interfacial area as a function of superficial vapor velocity

consistent with the literature (Kantarci *et al.*, 2005). Results for specific interfacial area are also in general agreement with experimental values available in the recent literature (Gómez-Díaz *et al.*, 2008). A slight dependence of a_{int} on geometry can be observed. Geometries with a larger number of orifices tend to produce slightly greater interfacial area. This is expected as the injection region in the tray is widened as the number of orifices is increased. This results in an increased number of vapor streams entering the bubble region, causing an increase in interfacial area. No discernable effect of tray geometry on gas holdup was observed. Liquid properties appear to have a slight effect, because E60 produces somewhat greater a_{int} values. This is suggestive of an inverse relationship of a_{int} to Ohnesorge and Morton numbers. Figure 4.13 also shows the combined E0-E60 model results as listed in Table 4.1.

Gas holdup, ε_G, is defined as the ratio of vapor volume to total volume in a region of interest and is used to determine vapor velocity as discussed below. If spherical vapor bubbles can be assumed, ε_G can be related to a_{int} by $a_{int} = 6\varepsilon_G / D_B$, where D_B is the diameter of a spherical bubble (Winterson, 1994). In the present study, vapor structure dimension is a calculated variable and the spherical shape assumption is not justified. Therefore, a_{int} and ε_G, are both determined independently with available image data. Lau *et al.* (2010) investigated shallow columns with low height-to-diameter ratios. The trend and values for gas holdup in the present study are in good agreement with their results for similar ranges of j_G.

Characteristic Length Scale: Various methods can be used to quantify characteristic length scales of vapor structures. The Sauter diameter, D_S, is a common length scale used in liquid-vapor contactors (Schäfer *et al.*, 2002) and is selected as the

characteristic length scale, i.e., $L_C = D_s$. For the data obtained in this investigation, it is defined as shown in Eq. 4.5. Here, the vapor volume in the two-phase region is used with interfacial area results for each video frame analyzed. Table 4.2 lists four bubble size correlations found in the literature. Results from these correlations are used as alternative values for L_C for the analyzed data.

$$D_S = 6\left(\frac{\sum_i^N V_i}{\sum_i^N A_i}\right) \tag{4.5}$$

Figure 4.14 shows characteristic length scale results vs. $j_{G,}$ including results for the proposed model correlation listed in Table 4.1. A relatively constant value of $L_C = 5mm$ can be established for the range of superficial velocities considered here. Only a slight increase in L_C with decreasing j_G is observed The effect of liquid properties is not clearly discernable. Also, geometric variation does not cause noticeable effects. A comparison with the literature reveals that bubble size estimates provided by Blass (1990) and Pohorecki *et al.* (2005) show reasonable agreement with the results of the present study, while the dependence on superficial velocity in the classic Davidson and Schüler

Table 4.2: Vapor structure length scale comparison with literature

Study	Expression for L_C
Davidson and Schüler (1960)	$\left(2.63Q_G^{1.2}g^{-0.6}\right)^{1/3}$
Akita and Yoshida (1974)	$1.88U_{G,in}^{1/3}g^{-1/6}d_{orifice}^{5/6}$
Blass (1990)	$\frac{1}{2}\sqrt{\frac{9\sigma}{g\left(\rho_L-\rho_G\right)}}$
Pohorecki *et al.* (2005)	$0.289\rho_L^{-0.552}\mu_L^{-0.048}\sigma^{0.442}j_G^{-0.124}$

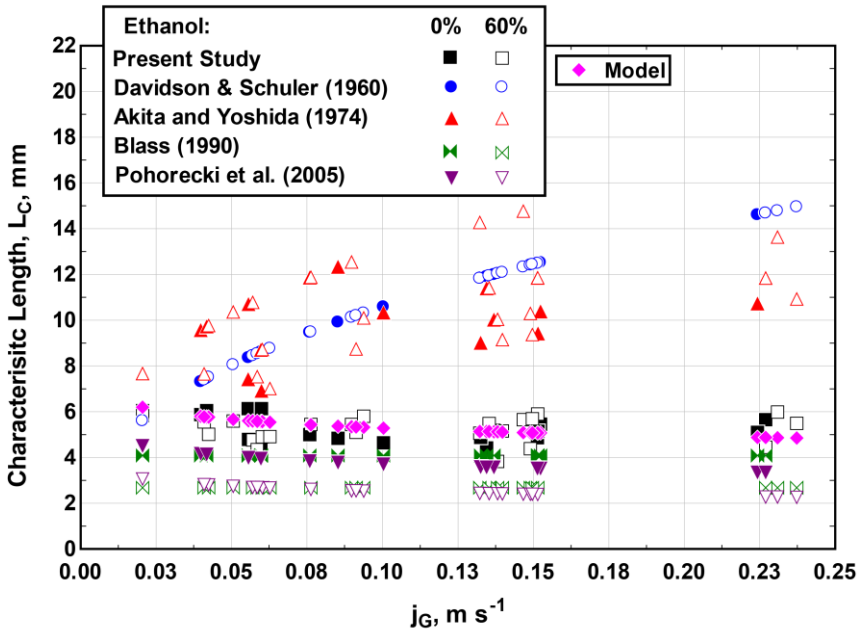

Figure 4.14: Characteristic length scale comparison

(1960) and Akita and Yoshida (1974) models causes significant deviation at higher velocities. The effect of liquid properties is more pronounced in the literature. The lower effect in the present designs may be because the particular geometry and flow pattern of the proposed design mitigate the effect of liquid properties.

Vapor Structure Velocity: Vapor structures are non-liquid regions in the two-phase region of each tray. These include bubbles and other irregular shaped vapor areas. Direct determination of vapor structure velocities is very challenging for the given flow patterns. Constant vapor bubble break-up and coalescences make tracking of individual vapor structures infeasible. Without direct tracking of vapor structures, their velocity cannot be calculated directly. Therefore, approximations are made for average vapor velocity. Given the unique geometries and flow patterns in Design Concept A, two definitions for average vapor structure velocity, $\bar{U}_G$, are proposed and compared.

Definition 1 is the average vapor velocity estimated as the average of inlet and outlet vapor velocities of the bubble region of the tray as shown in Eq. 4.6. $U_{G,in}$ is the vapor injection velocity to the tray. The average cross sectional vapor area at the outlet of the bubble region of the tray is determined from image data to determine $U_{G,out}$.

$$\bar{U}_{G,I} = \frac{1}{2} \cdot \left(U_{G,in} + U_{G,out} \right) \tag{4.6}$$

$$\bar{U}_{G,II} = \frac{\dot{V}_G}{A_x \varepsilon_G} \tag{4.7}$$

Definition 2 as shown in Eq. 4.7 is based on volumetric gas flow, $\dot{V}_G$, and applies a cross-sectional area (A_x) reduction in the bubble region of the tray by using gas holdup results. This definition is the interstitial gas velocity within the bubble region of the tray and is equivalent to the mean rise velocity of bubbles in a swarm (Shah *et al.*, 1982). Results for both definitions are shown and compared in Figure 4.15 (left). The results for both definitions are in general agreement and are proportional to j_G. However, $\bar{U}_{G,II}$ results show a more coherent dependence on j_G with a slightly discernable dependence on liquid properties. The average velocities for E60 are slightly lower than those for E0. This is a direct result of the definition of $\bar{U}_{G,II}$ and the liquid property dependence of gas holdup in the tray, as discussed above. Neither velocity definition reveals a consistent effect of tray injection geometry. No discernable liquid property dependence is observed for the results of $\bar{U}_{G,I}$, and its variation for a given value of j_G is much greater than that of $\bar{U}_{G,II}$. Therefore, $\bar{U}_{G,II}$ is considered the preferred definition for $\bar{U}_G$ for the Design Concept A.

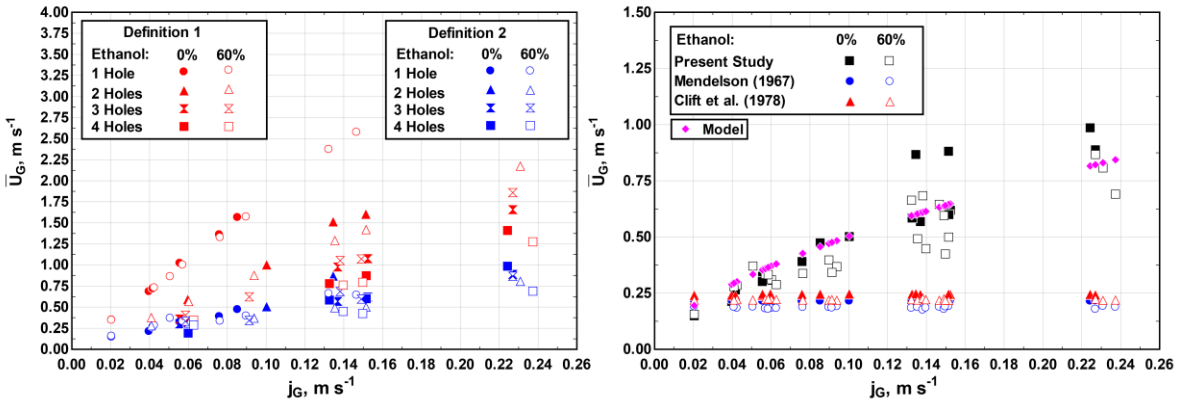

Figure 4.15: Vapor velocities. Left: comparison of two definitions. Right: comparison between literature and proposed model

Many correlations for bubble rise velocity can be found in the literature (Kulkarni and Joshi, 2005). However, a direct comparison of the results in the literature with the proposed velocity definitions is not applicable. Bubble rise velocities are typically based on terminal velocities of the vapor structure in a vertical path through a liquid column. The proposed geometries are significantly different from typical bubble columns, which results in significantly different flow patterns than those encountered in bubble columns. Bubble rise velocities in columns are only indirectly related to j_G and a dependence on bubble diameter is typical. $\bar{U}_{G,II}$ is compared with two bubble column rise velocity methods as shown in Figure 4.15 (right). Here, a wave analogy presented by Mendelson (1967) and the method of Clift *et al.* (1978) are compared. Correlations in the literature provide consistent results with each other but values for $\bar{U}_{G,II}$ deviate significantly due to the stronger effect of j_G on $\bar{U}_{G,II}$. Higher average vapor velocities produced in this design are favorable as they promote increased heat and mass transfer coefficients. Figure 4.15

also shows the velocity estimates based on the correlation developed in this study and shown in Table 4.1.

Heat Transfer Area: Design Concept A utilizes the entire wall area of the tray as heat transfer area. However, its effectiveness depends on hydrodynamics. Specifically, as shown in Figure 4.10 (step 5), the distribution of fluid over the wall area of the tray can be differentiated as vapor, liquid and two-phase. An optimal design aims to minimize the vapor region due to low heat transfer coefficients expected in that region. The liquid regions in the dowcomer and the tray can be treated as the pool region and appropriate heat transfer correlations for ammonia-water solutions are available in the literature (Táboas *et al.*, 2007). The area of the two phase region in the tray is delineated from the liquid region because the heat transfer mechanisms may be different and appropriate flow boiling correlations may be required (Ghiaasiaan, 2007). If a modification to a pool boiling correlation is required, Táboas *et al.* (2010) offer an overview of suitable expressions for ammonia-water solutions.

Figure 4.16 (left) shows heat transfer area distribution as a function of superficial vapor velocity for all three regions. Here, the fraction of total tray area covered by the respective phases is shown. Liquid coverage is relatively constant throughout the range of j_G. A slight increase at low velocities can be explained with increased tray activation and liquid holdup in the tray until a steady liquid holdup is reached. The two-phase region fraction increases with velocity, which is to be expected. Given the relatively constant value of liquid fraction, the vapor fraction behaves inversely to the two-phase fraction. The effect of liquid properties is only slightly discernable where E60 produces slightly greater vapor and lower two-phase fractions. This is expected with a decrease in surface

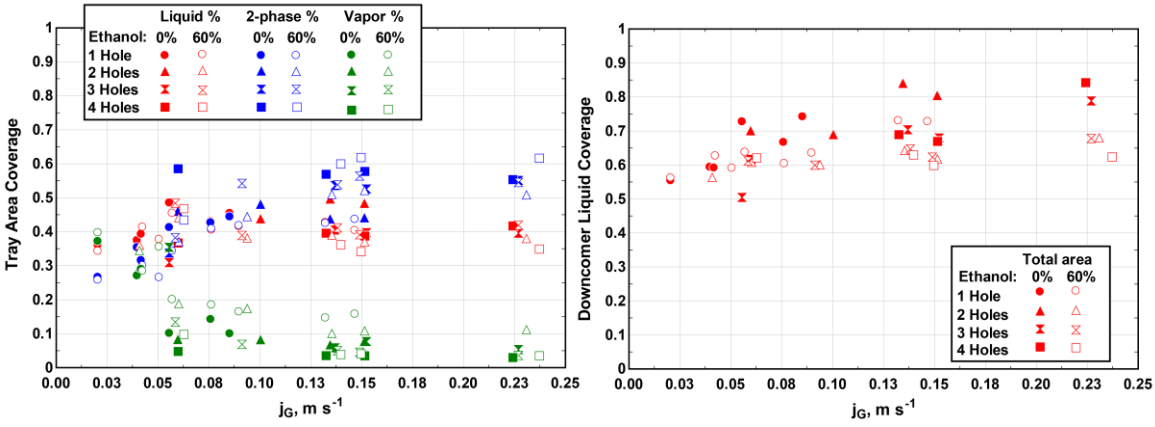

Figure 4.16: Heat transfer area as fraction of total area. Left: tray area distribution. Right: downcomer distribution.

tension and density. An increasing number of orifices cause an increased two-phase fraction and slight reduction of vapor and liquid fraction. This is also expected as a greater number of tray orifices results in a wider gas injection region.

Figure 4.16 (right) shows results for the downcomer liquid fraction. A positive correlation to j_G can be observed, which is expected as downcomer liquid fraction represents the hydrostatic head developed in the gas chamber upstream of the tray. The effect of liquid properties is pronounced, and a noticeable reduction in liquid area is shown for E60. This is consistent with the results for gas holdup in the tray. E60 produces greater gas holdup values, which results in a reduction of the effective density of the two-phase region. This in turn lowers the backpressure of the tray, and the liquid area in the downcomer region provides hydrostatic pressure approximately equal to tray back pressure. No definite conclusion about the effect of the number of holes in the bubble tray can be made.

Design Concept B: High-speed video analysis was also conducted for design concept B. However, the realistic reproduction of the proposed design concept B for

CCFL studies led to an inherently three-dimensional test section. Tubes that simulate the heat transfer area form the vapor annulus of the bubble tray and cause visual obstructions that eliminate the possibility of a computational image analysis process. Instead, the hydrodynamic behavior of the observed flow patterns is first assessed qualitatively before some estimates for bubble velocity, bubble size and gas holdup are made based on available measurements. A variation of flow rates according to the test matrix for Design Concept A was applied and E0 as well as E60 were used as the liquid. Observation of the flow patterns shows that primarily isolated vapor structures emerge from the annulus rather than consistent coalescence of bubbles, which is only observed sporadically. A bubble forms at a segment of the annulus and results in a spherical or an ellipsoidal shape. Figure 4.17 shows a sequence of bubble movement from its formation at the annulus to its exit at the pool surface. A semispherical cap is formed prior to necking and detachment. Bubble growth can be observed until vapor leaves the surface. The formation of this particular bubble occurred toward the outside edge of the tray, which allowed for unobstructed visibility.

Bubbles with unobstructed visual access were measured as approximately 5 mm in diameter. Bubble velocity could be determined through the time required for a bubble to rise through the liquid pool in combination with the height of the pool as shown in Figure 4.17. Pool height varied slightly with flow rate and ranged from ~12 mm to ~15 mm. Bubble velocities were determined to range from 0.14 m s^{-1} to 0.18 m s^{-1}. No clear effect of bubble size on velocity could be established. Liquid properties did not cause obvious effects on any parameters. Geometry variation, i.e., change in annulus size had slight effects similar to vapor flow rate variation in that it caused variation of pool height.

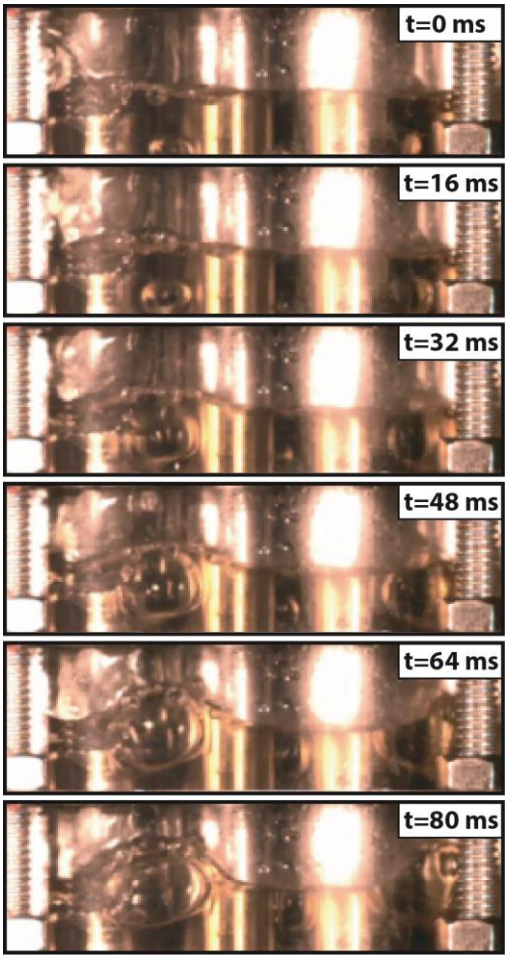

Figure 4.17: Design concept B flow visualization

However, once full activation was established, no clear effects of annulus size could be discerned.

Typically, bubbles in bubble columns accelerate to their terminal velocity as they rise and exhibit bubble growth (Shah *et al.*, 1982). To better understand the combined effects of bubble entrance and exit from a liquid pool, Lau *et al.* (2010) investigated shallow bubble columns, i.e., low height-to-diameter ratios as encountered in Design Concept B. At very low ratios, they observed a reduction in average bubble size. The average bubble size estimate in the present study is also slightly lower than comparable results in the literature (Polli *et al.*, 2002). Lau *et al.* (2010) suggest that the presence of a

liquid surface enhances bubble breakup. Disturbances in the continuous liquid by a leaving bubble cause break-up of other vapor structures within the liquid, which leads to lower bubble size. Also, the lack of liquid height prevents bubble coalescence, further contributing to lower average bubble size. These authors also report a significant increase in gas holdup and found that rise velocity decreased with height-to-diameter ratio reduction. They found velocity values around 30 – 40 cm s^{-1}, while velocity results in the present study are considerably lower, which could be attributed to confinement effects of this particular tray design. Given an estimate for bubble velocity, gas holdup can be estimated with the interstitial velocity definition in Eq. 4.7. These values range from 0.31 to 0.41. Finally, specific interfacial area can be estimated using the common bubble column relation $a_{int} = 6\varepsilon_G / D_b$. These values range between 365 – 470 m^2 m^{-3}.

4.6 Conclusions

Novel design concepts for the desorber and rectifier components of AAS were presented. Design criteria for optimal thermal compressors were identified and it was shown how the proposed designs optimize heat source utilization, allow for highly compact component design and accommodate flexible operation and reliable system operation. The proposed designs also span a wide range of applications by providing a solution for direct gas coupled desorption as well as microchannel based heat source fluid coupling. A hydrodynamic design methodology was developed to address countercurrent flow limitations. Air-liquid experiments that simulated flow conditions of actual AAS were conducted to validate feasibility of these designs and provide geometric specification for full component development. High-speed video analysis provided

additional experimental results to quantify hydrodynamic parameters that are needed for the development of a component level heat and mass transfer model. The results of this study can be used to develop compact and effective desorber and rectifier components for optimal thermal compressors in AAS.

CHAPTER 5. HEAT AND MASS TRANSFER MODEL

5.1 Introduction

Thermally driven cooling and refrigeration provides an alternative to conventional vapor compression systems. The requirement for high-grade mechanical or electrical energy can thereby be replaced with low-grade thermal energy such as waste heat, allowing for the development of energy systems with increased overall efficiency. Ammonia-water absorption systems are an example of thermally driven cooling systems with the potential for widespread adoption. Conceptually, the mechanical compressor of a vapor compression system is replaced with a thermal compressor that primarily consists of a set of heat exchangers. Among the key thermal compressor components of an ammonia-water absorption system are the desorber and rectifier. The desorber utilizes heat input to separate ammonia vapor from an ammonia-water solution, while the rectifier is required to ensure high ammonia purity (Fernandez-Seara and Sieres, 2006). Typically, conventional distillation columns are implemented in combination with various rectification options (Fernandez-Seara *et al.*, 2003). As these components contribute significantly to overall system size and weight, further development of efficient and highly compact desorption and rectification components is required, particularly for small capacity systems. Several previous studies have reported alternative desorber designs, such as those by Delahanty *et al.* (2015), Keinath *et al.* (2014) and Determan and Garimella (2011). The concept of diabatic distillation, the integration of external heat transfer with vapor purification, has been shown to be thermodynamically advantageous compared to other thermal separation processes (Kotas, 2013) but has not

been developed for ammonia-water absorption systems. This approach optimizes thermal compressor performance, reduces exergy destruction and facilitates further component size reduction (Chapter 3). In this study, design concepts for a microscale desorption and rectification component based on the diabatic distillation principle are reviewed and underlying hydrodynamics are discussed. A coupled heat and mass transfer model is developed for the processes encountered in the proposed geometries. Overall component sizes, refrigerant generation rates, and heat input requirements are determined. A parametric study is conducted to validate performance over a wide range of operating conditions. Finally, reduced order design values for vapor purification efficiency and overall heat transfer coefficient are determined to facilitate design and sizing of these components.

5.2 Design Concept and Hydrodynamics

The desorber design concept is shown in Figure 5.1 (left). Heat is continuously applied to the ammonia-water solution through a microchannel plate. This facilitates the use of a generic heat source through a coupling fluid. The working fluid side is gravity driven, entering from the top of the component. Trays are placed in an alternating pattern for continuous solution flow over each tray with simultaneous vapor generation. Vapor is forced through orifices in each tray to create the flow pattern depicted in Figure 5.1 (right). Vapor from the lower trays experiences liquid-vapor interaction with colder solution in the bubble region of each tray. This leads to vapor purification in combination with simultaneous vapor generation in a given tray. Achieving this flow pattern is governed by two hydrodynamic limitations. At low liquid and vapor flow rates, excessive weeping of solution through orifices prevents liquid build-up in the downcomer as well

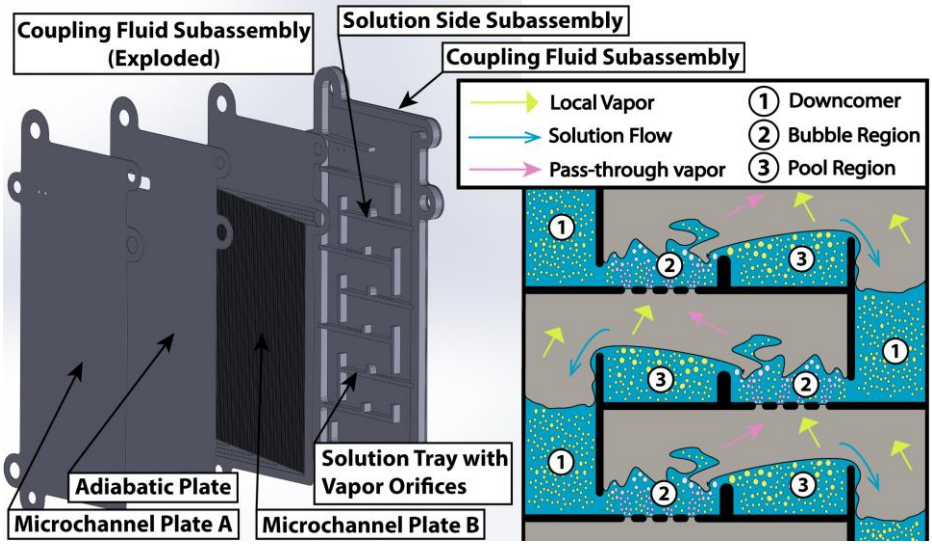

Figure 5.1: Design Concept A, component assembly (left), target flow pattern (right)

as the formation of a bubble region. Conversely, at high liquid and vapor flow rates, excessive liquid build-up in the downcomer and bubble region of the tray causes liquid entrainment into the refrigerant vapor stream, which results in an unacceptable reduction of ammonia purity, leading to poor system performance. A detailed discussion of this design concept and investigation of hydrodynamic behavior was presented in Chapter 4. A design methodology was developed and applied to the specific geometries of this design to accommodate both hydrodynamic limitations. Additionally, high-speed videography was employed in a flow visualization study to quantify hydrodynamic parameters relevant to heat and mass transfer. These parameters are single-phase and two-phase heat transfer areas, liquid-vapor interfacial area, vapor structure size and velocity as well as total liquid and vapor hold-up in a tray. Estimates of these parameters were quantified with correlations as a function of superficial vapor velocity. These expressions can be readily implemented in a heat and mass transfer model.

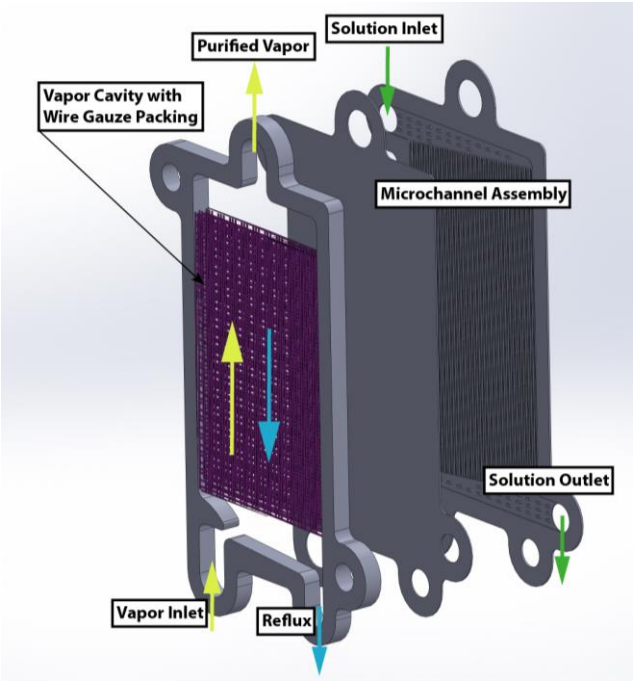

Figure 5.2: Rectifier design concept

The design of a microchannel based rectifier that uses the diabatic distillation concept as shown in Figure 5.2 was also presented in Chapter 4. The refrigerant vapor side consists of a cavity with wire gauze packing where partial condensation occurs. Generated reflux is gravity driven and countercurrent to the vapor, and the reflux flows to the top of the desorber. The presence of the wire gauze enhances vapor-side heat transfer and provides surface area for liquid-vapor interaction to facilitate the diabatic distillation process. Liquid flooding is the only hydrodynamic limitation and the design concept was included in the hydrodynamic design study to ensure proper component operation at the expected flow rates. Concentrated solution leaving the absorber is the preferred recuperative heat sink on the microchannel side.

5.3 Coupled Heat and Mass Transfer

The processes in the proposed designs rely on simultaneous heat and mass transfer of ammonia-water solution and vapor. Detailed modeling of these phenomena is required to ensure proper component design with optimal performance. Given the novel geometry and the limited body of work in the literature on coupled liquid-vapor heat and mass transfer of ammonia-water, a *non-equilibrium* model that addresses such countercurrent geometries is developed. The results of this study can be used to provide *equilibrium* estimates for reduced order modeling. This facilitates future implementation of this design concept at various scales and can guide assumptions in overall system models and dynamic models where accurate model order reduction is required for computational feasibility.

A generic diabatic distillation control volume is shown in Figure 5.3. Here, two main processes are identified. Local vapor generation is the coupled heat and mass transfer process of binary mixture boiling, while the process termed *pass-through vapor* is the heat and mass transfer process experienced by vapor that is not locally generated in a given segment but is introduced from the bottom of the segment. The resulting coupled heat and mass transfer process leads to the purification of pass-through vapor. In the proposed design, these two processes may occur simultaneously in some regions of a given tray, while the binary mixture boiling process may occur individually in other regions. Additionally, single-phase vapor heat transfer may occur in unwetted wall regions of a tray. Single-phase liquid heat transfer is not considered in this design, as realistic system operating conditions lead to saturated liquid or two-phase flow of

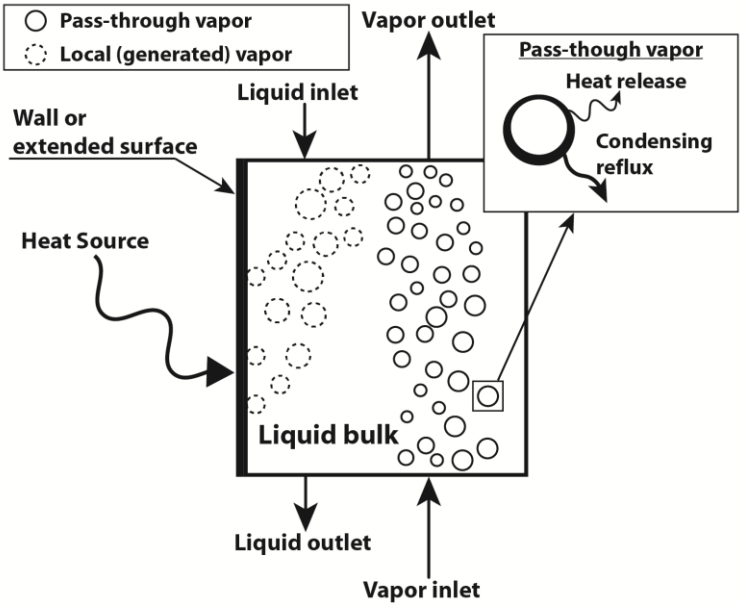

Figure 5.3: General diabatic distillation control volume

concentrated solution entering the desorber. Both these primary processes are modeled individually so that they can be combined and implemented in a modular approach.

5.3.1 Binary Mixture Boiling

In the absence of mass transfer, an ideal heat transfer coefficient can be determined based on the molar weighted average of pure component nucleate boiling coefficients as shown in Eq. 5.1. However, given that the ammonia mass fraction in the vapor phase is significantly greater than that in the liquid phase, a net mass transfer of ammonia from the bulk liquid to the vapor occurs. The non-equilibrium process results in the local depletion of ammonia at the liquid-vapor interface, which causes an increase in the local saturation temperature. As this effectively reduces the wall superheat temperature, the actual heat transfer coefficient of this process is lower than the ideal one. Typically, a correction factor, shown in generic form in Eq. 5.2, is applied to Eq. 5.1 to account for the effect of mass transfer on heat transfer.

$$\alpha_{ideal} = \left[\frac{\tilde{x}}{\alpha_{NH_3}} + \frac{1-\tilde{x}}{\alpha_{H_2O}} \right]^{-1} \quad 5.1$$

$$\frac{\alpha_{NB}}{\alpha_{NB,ideal}} = \frac{1}{(1+K)^{E}} \quad 5.2$$

Nucleate boiling correlations for both, ammonia and water, as well as a suitable mixture correction correlation, must be identified. The pool boiling correlations developed by Mostinski (1963), Stephan and Abdelsalam (1980) and Gorenflo (1993) are considered as they are suitable for both ammonia and water (Táboas *et al.*, 2007). The following binary mixture correction correlations are considered: Stephan and Körner (1969), Schlünder (1982), Thome and Shakir (1987), Táboas *et al.* (2007). While the first correlation was suggested by Inoue *et al.* (2002), the second and third were compared by Táboas *et al.* (2007). The same authors developed the last correlation specifically for ammonia-water mixtures. Application of different boiling and binary mixture correction correlations can significantly affect model results. Therefore, different correlations are compared in this study and an assessment of their effect on model predictions is made.

5.3.2 Pass-through Vapor Model

Vapor generated in lower sections of the component may enter a given control volume and experience liquid-vapor contact with colder solution in the control volume. The resulting temperature and concentration profiles of this interaction are shown in Figure 5.4. The coupled heat and mass transfer process leads to a temperature reduction and purification of vapor, i.e., an increase of ammonia mass fraction in the vapor. The modeling technique presented by Price and Bell (1974) implemented the film theory

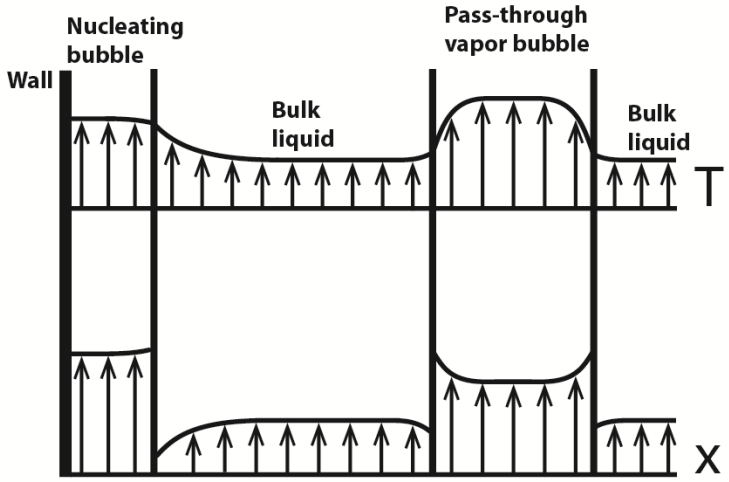

Figure 5.4: Profiles for temperature and ammonia concentration

framework of Colburn and Drew (1937) and has been applied to ammonia-water absorption and desorption modeling by several investigators, e.g., Determan and Garimella (2011) and Nagavarapu and Garimella (2011). This approach is adapted to the geometries and processes presented in this study.

The molar flux across the liquid-vapor interface can be derived analytically by assuming local equilibrium at the interface and integration over the concentration boundary layer in both, the vapor phase and the liquid phase (Hewitt *et al.*, 1994). This is shown in Eqs. 5.3 and 5.4. Here, $\tilde{x}_{i,int}$ is the equilibrium molar concentration at the liquid-vapor interface and $\tilde{x}_{i,bulk}$ is the bulk molar concentration of liquid and vapor. The quantity $\tilde{z}$ is the molar concentration of the condensing flux in binary mixture condensation and is defined as $\tilde{z} = \dot{n}_{NH_3} / \dot{n}_T$.

$$\dot{n}_T = -\beta_V C_T \ln\left(\frac{\tilde{z} - \tilde{x}_{V,\text{int}}}{\tilde{z} - \tilde{x}_{V,bulk}}\right) \qquad 5.3$$

$$\dot{n}_T = \beta_L \frac{\rho_L}{M_L} \ln\left(\frac{\tilde{z} - \tilde{x}_{L,\text{int}}}{\tilde{z} - \tilde{x}_{L,bulk}}\right) \tag{5.4}$$

Heat transfer at the liquid-vapor interface from the vapor phase is governed by Eq. 5.5. Here, the Ackermann correction factor (the term in parentheses in Eq.5.5), is defined with the parameter ϕ_V as shown in Eq. 5.6. The correction factor couples vapor phase heat transfer to mass transfer, providing a correction for the effect of latter on the former. Similarly, heat transfer between the liquid-vapor interface and bulk liquid is governed by Eq. 5.7 with the correction factor defined as in Eq. 5.8.

$$\dot{Q}_V = \alpha_V \left(\frac{\phi_V}{1 - e^{-\phi_V}}\right) A_{\text{int}} \cdot LMTD_V \tag{5.5}$$

$$\phi_V = \frac{\left(\dot{n}''_{NH_3} \tilde{C}_{p,V,NH_3}\right) + \left(\dot{n}''_{H_2O} \tilde{C}_{p,V,H_2O}\right)}{\alpha_V} \tag{5.6}$$

$$\dot{Q}_L = \alpha_L \left(\frac{\phi_L}{1 - e^{-\phi_L}}\right) A_{int} \cdot LMTD_L \tag{5.7}$$

$$\phi_L = \frac{\left(\dot{n}''_{NH_3} \tilde{C}_{p,L,NH_3}\right) + \left(\dot{n}''_{H_2O} \tilde{C}_{p,L,H_2O}\right)}{\alpha_L} \tag{5.8}$$

Implementation of the preceding coupled heat and mass transfer model requires knowledge of interfacial area values as well as transport coefficients, i.e., heat and mass transfer coefficients $\alpha_V, \alpha_L, \beta_V, \beta_L$. If one of the transport coefficients is known, its heat or mass transfer counterpart can be determined through a heat and mass transfer analogy (Mills, 1995) as shown in Eq. 5.9. Vapor Nusselt number, $Nu = \alpha L_C / k$, is related to its

mass transfer counterpart, the Sherwood number, $Sh = \beta L_C / D_{aw}$ where D_{aw} is the binary diffusion coefficient of ammonia and water in solution or vapor mixture, and L_C is the characteristic length scale of the vapor structure. Values for characteristic length scale as well as interfacial area of a typical vapor structure for this design were determined in the hydrodynamic investigation mentioned above (Chapter 4). Heat and mass transfer inside bubbles was investigated by Colombet et al. (2013) who suggested a Sherwood number value of 18 for vapor flow rates and bubble dimensions expected in the present study. This provides direct quantification of the mass transfer coefficient, β_V; the heat and mass transfer analogy is then invoked to determine the value of α_V. The sensible liquid heat transfer coefficient, α_L, of a vapor structure is estimated using the idealization of forced convective flow over a single sphere by Whitaker (1972). The liquid phase mass transfer coefficient, β_L, is the then determined through the analogy.

$$\left(\frac{Sh}{Nu}\right) = \left(\frac{Sc}{\mathrm{Pr}}\right)^{1/3} \tag{5.9}$$

5.3.3 Rectifier Model

Liquid flow rates of reflux condensate in the rectifier are expected to be very low. This causes high uncertainty of liquid-vapor interfacial area which makes a non-equilibrium framework unsuitable. As an alternative, the equilibrium method presented by Silver (1947) and Bell and Ghaly (1973), known as the Silver-Bell-Ghaly (SBG) model, is applied. Here, equilibrium is assumed throughout the vapor and liquid phases. The effect of mass transfer is accounted for by comparing sensible heat transfer of

saturated vapor to overall heat transfer of the condensing vapor. Given that a pure substance does not experience sensible temperature variation during the condensation process, this approach has been widely accepted as a suitable alternative to non-equilibrium models and has been shown to be conservative for vapor Lewis numbers of less than unity (Webb *et al.*, 1996). An effective heat transfer, α_{SBG} is defined as shown in Eq. 5.10 where the term Z_{SBG} is defined as $Z_{SBG} = \dot{Q}_{sensible} / \dot{Q}_T$, which is the ratio of vapor sensible heat transfer to overall rectifier duty. Both quantities can be readily determined if vapor inlet and outlet states of the rectifier are specified. The ideal condensation coefficient, α_{ideal}, is determined using mixture properties at the operating conditions, and the effective heat transfer coefficient can then be determined for overall component design.

$$\frac{1}{\alpha_{SBG}} = \frac{1}{\alpha_{ideal}} + \frac{Z_{SBG}}{\alpha_V} \qquad 5.10$$

5.4 Model Development and Implementation

The binary mixture boiling and pass-through vapor models are building blocks that are integrated into an overall heat and mass transfer model. First, the model topology is defined based on actual flow patterns expected in the component. Then, a suitable segmentation of each tray into regions is presented, and finally, conservation equations are applied to each region to obtain all states in the component.

5.4.1 Model Topology

Figure 5.5 shows a flow visualization image of a single tray that is fully activated and not flooded, i.e., without experiencing hydrodynamic limitations. The flow visualization study presented in Chapter 4 provided quantification of various heat transfer areas as a function of vapor and liquid flow rates. Furthermore, downcomer liquid level height and liquid-vapor interfacial area values were determined. Delineation between liquid-only, two-phase and unwetted area in the core tray allowed for the quantification of their respective areas. Based on those results, each tray is segmented into several regions to accurately model the heat and mass transfer processes specific to that region. Region sizes are variable and dependent on vapor velocity at the inlet of a given tray as well as the number of vapor orifices in that tray.

5.4.2 Bubble Tray Region

In the bubble region of the core tray, region 1 in Figure 5.1, both main heat and mass transfer processes, nucleate boiling and the pass-through vapor process, occur simultaneously. Liquid-to-wall area, as well as interfacial area, are known from the

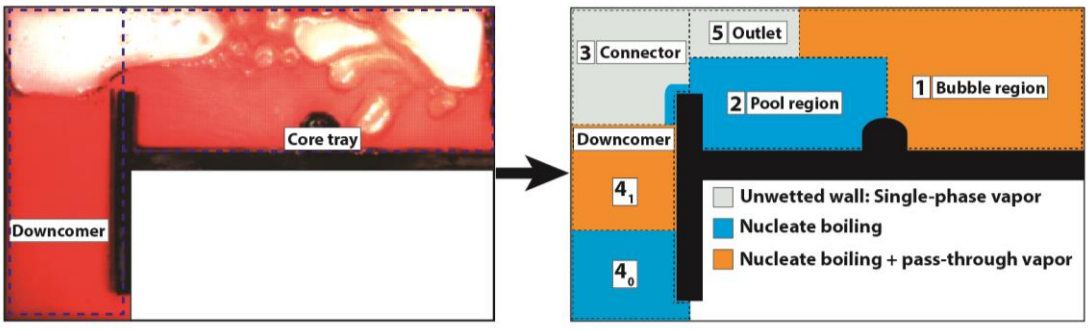

Figure 5.5: Idealization of hydrodynamic phenomena in model topology

results of the hydrodynamic study. The states for vapor and liquid inlet are determined from a complete tray analysis of the tray below and above, respectively. The nucleate boiling process as modeled with Eqs.5.1 and 5.2, as well as the pass-through vapor process modeled with Eqs. 5.3 - 5.8, are added to a set of equations used for modeling of the bubble region. Conservation equations for mass, species and energy are then added to the equation set as shown in Eqs. 5.11 - 5.13.

$$\dot{m}_{L,in} + \dot{m}_{V,in} = \dot{m}_{L,out} + \dot{m}_{V,out} \tag{5.11}$$

$$\dot{m}_{L,in} x_{L,in} + \dot{m}_{V,in} x_{V,in} = \dot{m}_{L,out} x_{L,out} + \dot{m}_{V,out} x_{V,out} \tag{5.12}$$

$$\dot{m}_{L,in} h_{L,in} + \dot{m}_{V,in} h_{V,in} + \dot{Q}_{ext} = \dot{m}_{L,out} h_{L,out} + \dot{m}_{V,out} h_{V,out} \tag{5.13}$$

External heat input to the region is determined through Eq. 5.14. Here, the total resistance includes wall and coupling fluid resistances. Its value, as well as the logarithmic mean temperature difference, can be determined as discussed below.

$$\dot{Q}_{ext} = \frac{1}{R_T} LMTD_{CF,WF} \tag{5.14}$$

System pressure is typically determined through saturation conditions in the condenser and can be treated as an input variable for this model. The final assumption required for closure is a saturated liquid state for the liquid leaving a region. This assumption is justified through the externally diabatic design and the fact that concentrated solution entering the desorber can be approximated as saturated liquid in a system at realistic operating conditions. This set of equations then fully defines the state of the working fluid in the bubble region of each tray.

5.4.3 Pool Region

The pool region is assumed to be well mixed and the only process considered is ammonia-water nucleate boiling. The area of the region is known from the hydrodynamic study, and the inlet state of the liquid is known from the solution of the bubble region. Therefore, vapor inlet terms in mass, species and energy equations can be eliminated and the system can be solved without considerations of vapor heat transfer.

5.4.4 Downcomer Regions

Overall downcomer height is known from the hydrodynamic study, which allows for division of the downcomer into two equally sized regions. A bottom region is defined to be identical to the pool boiling region described above. This assumes that no vapor inlet flow occurs at the bottom of the downcomer. This assumption is justified for fully activated tray operation. A second region at the top of the downcomer is defined to model the effect of purification of vapor generated in the bottom downcomer as it rises. The bottom downcomer region can be modeled in identical manner to the pool region discussed above. The liquid outlet stream at the bottom of the downcomer provides the fully defined solution inlet stream for the tray below. The top downcomer region is modeled similarly to the bubble region in the core tray. However, liquid-vapor interfacial area is not known directly from hydrodynamics. In order to determine this value, the bubbles size model by Idogawa *et al.* (1987) in its modified form presented by Oyevaar and Westerterp (1989) is applied. Using the average mass flow rate of vapor and its properties in this region, the number of bubbles and, consequently, the total liquid-vapor

interfacial area can be determined. The system can then be solved in a manner similar to that used for the bubble region of the core tray.

5.4.5 Connector and Outlet Region

The connector region feeds vapor generated in the downcomer to the core tray region and liquid from the core region to the downcomer. Liquid flow over the tray into the downcomer is modeled using the Francis weir equation, which is commonly used to model hydrodynamics in adiabatic column trays (Wijn, 1999). Given the liquid height of the downcomer and overall geometry of the tray, the unwetted wall area can then be determined in this region. There is sensible heat transfer between the dry wall area and the vapor. Vapor flow in this region is expected to be laminar, and the Nusselt number for a rectangular cross-section with aspect ratio of 3, i.e., $Nu_V = 4.69$, is selected (Incropera and DeWitt, 1996) to determine the vapor-side heat transfer resistance. Nucleate boiling heat transfer is applied to the liquid portion in this region. While in other regions, the major fraction of external heat transfer to solution is from the heated wall, in this region, the tray itself forms the major portion of the external heat transfer area. In all regions, the heat transfer area contribution from the actual tray is determined by applying an extended surface methodology for a rectangular fin (Mills, 1995). A representative fin efficiency value for an extended tray surface in this study is 75%. The coupled heat and mass transfer process described in Eqs. 5.3 - 5.8 is applied to the liquid-vapor interface. However, given the small liquid region, it is assumed that the liquid phase in the connector is well mixed, which eliminates the need to use Eqs. 5.7 and 5.8.

In the outlet region, vapor streams from the downcomer, the bubble region and pool region are combined and are exposed to a single-phase vapor heat transfer process with the unwetted wall as described in the discussion of the connector region. The unwetted wall area is known from the hydrodynamic investigation. The combined outlet vapor stream serves as the inlet vapor stream for the tray above.

It is desirable to minimize unwetted wall regions to maximize nucleate boiling heat transfer area, mitigate vapor superheat, and reduce overall component size. Hydrodynamic constraints dictate the amount of unwetted wall in this design. However, the contribution of superheat is small, and unwetted wall area primarily causes underutilization of heat wall area for overall component duty optimization.

5.4.6 Coupling Fluid Integration

The desorption heat duty is supplied using a coupling fluid stream flowing through microchannels. A detailed modeling approach for microscale heat and mass exchangers in absorption systems is given by Nagavarapu and Garimella (2011). They determine the total heat transfer resistance of the coupling fluid side by modeling the

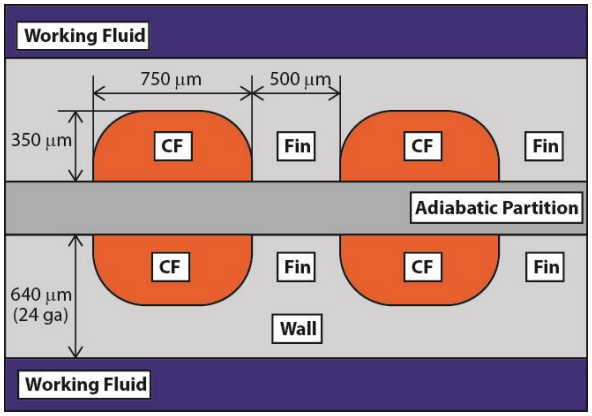

Figure 5.6: Cross-section of coupling fluid passages

channel geometry as a fin-array in combination with a laminar convection correlation for semi-circular duct geometries (Sparrow and Haji-Sheikh, 1965). This approach is slightly modified for the presented design. Here, an adiabatic partition plate is used to separate a set of two coupling fluid plates as shown in Figure 5.6. The correlation for laminar flow in a circular sector duct with an adiabatic straight side (Hong and Bergles, 1976) is applied. Additionally, a heat transfer oil is used as the coupling fluid, which results in comparatively high Prandtl number values ($Pr = \nu / \alpha$). This leads to a non-negligible thermal entrance length and the Nusselt number ($Nu = hD_h / k$) value is determined by integration over the thermal entrance length (Hong and Bergles, 1976). Eq. 5.14 can then be determined completely, providing model closure.

5.4.7 Model Implementation

The model is implemented on a modular basis. Separate stand-alone modules for pool boiling, pass-through vapor, connector and outlet region were developed to characterize the distinctly different heat and mass transfer processes. Consequently, each tray is modeled with two pool boiling modules, two pass through vapor modules, and one connector and outlet module. Each module includes hydrodynamic characterization data to accurately determine heat transfer area and volume. The solution-side heat transfer coefficient is used in combination with the coupling fluid model discussed above to determine the total heat transfer resistance in Eq. 5.14, $R_T = R_{sol} + R_{wall} + R_{CF}$. Fully defined thermodynamic states and mass flow rates of all inlet streams including coupling fluid are required for each module and determined in an iterative manner that provides the *LMTD* value for each module.

Table 5.1: Specification for desorber and rectifier operating conditions

Operating Conditions	
Operating pressure, kPa	1878
Concentrated solution flow rate, g s^{-1}	11.5
Concentrated solution ammonia mass fraction	0.47
Target vapor mass flow rate leaving rectifier, g s^{-1}	3
Target dilute solution temperature leaving desorber, °C	137
Heat source coupling fluid mass flow rate, kg s^{-1}	0.14
Rectifier heat sink inlet temperature, °C	42
Rectifier vapor outlet ammonia mass fraction	0.9985

Operating conditions and geometric data are specified for both components. Table 5.1 lists operating conditions for the desorber and rectifier. The rectifier vapor outlet flow rate of 3 g s^{-1} is typical for a system with a cooling capacity of about 3.5 kW. Given the operating pressure and concentrated solution ammonia mass fraction, a dilute solution temperature is specified. The value of 137°C is based on thermodynamic optimization. A unique optimum dilute solution temperature exists for every combination of concentrated solution mass fraction and operating pressure as shown in Chapter 3. The resulting value of system circulation ratio, $CR = \dot{m}_{cs} / \dot{m}_{ref}$, is 3.8. Table 5.2 lists geometric parameters for both components. Heat source coupling fluid inlet temperature is determined based on the required dilute solution outlet temperature.

In addition to the five regular desorber trays, a bottom section consisting of pool boiling modules is included, with a downcomer region at the inlet of the component that feeds the first tray. The complete model consists of five trays with six modules each as well as four bottom section modules and two inlet section modules. The 36 module assembly can be solved iteratively with overall boundary conditions specified as shown

Table 5.2: Specification for desorber and rectifier designs

Operating Conditions	Desorber	Rectifier
Material	304 stainless steel	304 stainless steel
Number of working fluid plates	8	8
Number of coupling fluid plates	16	8
Number of regular trays	5	N/A
Number of coupling fluid channels	1344	400
Overall component dimensions (H×W×D), mm	220×124×74	170×76×58
Overall component weight, kg	9.3	3.1

in Table 5.1. The model can accommodate two-phase inlet conditions of concentrated solution as expected in realistic operating conditions. Adiabatic liquid-vapor separation of two-phase flow at the inlet will result in liquid-vapor separation, whereby inlet vapor is combined with vapor generated in the desorber. However, in the present study, the solution inlet is assumed to be saturated liquid.

Rectifier reflux mass flow rate, ammonia mass fraction and temperature are obtained iteratively with results from the rectifier model. Reflux is combined with liquid concentrated solution at the inlet of the top tray. The complete model is implemented in Engineering Equation Solver (Klein, 2015) using ammonia-water property routines of Ibrahim and Klein (1993).

5.4.8 Rectifier Model

Ammonia mass faction of the vapor leaving the rectifier is specified as 0.9985 to ensure high refrigerant utilization in the evaporator with low temperature glide. In combination with a specified pressure and saturated vapor assumption, the vapor outlet state is fully defined. Vapor inlet to the rectifier is specified through desorber model

results. The state and flow rate of condensate reflux leaving the rectifier is determined in this model and used as an input to the desorber model. The partial condensation process requires a heat sink. In this study, concentrated solution from the absorber serves this purpose. In contrast to heat rejection to the ambient, the solution cooled rectifier provides partial heat recovery of the rectifier heat load. Total solution flow rate, inlet temperature and ammonia mass fraction are specified. Given all global rectifier inputs, a segmented equilibrium heat and mass transfer model is developed based on the SBG approach discussed above. Figure 5.7 shows a conceptual depiction of the rectifier cross-section. Vapor enters each segment from the bottom, while reflux enters from above for all segments except the top segment. Diabatic distillation is realized by the multiple layers of

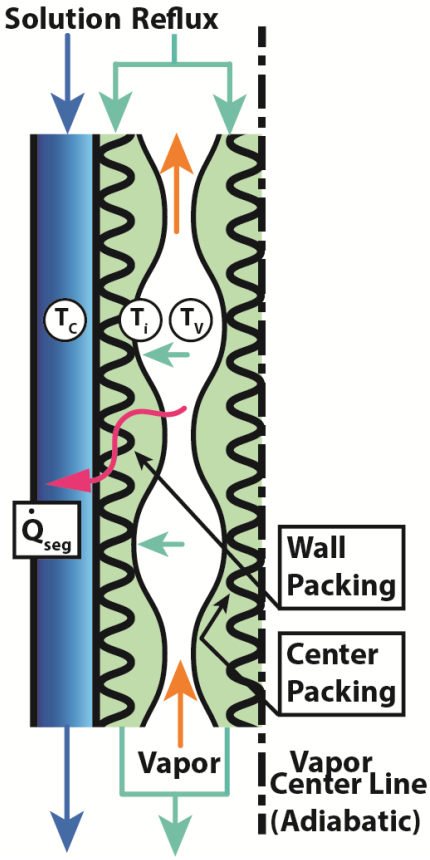

Figure 5.7: Rectifier cross-sectional view

packing. In this design, four layers of wire gauze are placed between parallel plate channels carrying working fluid liquid-vapor countercurrent flow. Both center layers act as an adiabatic liquid-vapor contactor in parallel to the partial condensation process on the wall and the packing layer adjacent to the wall. It is assumed that reflux from a higher segment is distributed at the inlet of the current segment. The partial condensation process causes additional reflux to be formed in each segment that is combined with reflux generated at higher segments. In addition, the concentration of reflux generated in the current segment can be accurately estimated as the saturated liquid concentration of the average vapor temperature. A mass and concentration balance for vapor and generated reflux provides mass flow rates of vapor leaving the segment and locally produced reflux. Finally, the system can be solved completely with a temperature assumption of reflux leaving each segment. Due to liquid-wall contact, liquid is expected to be somewhat subcooled. However, center packing layers allow for adiabatic liquid-vapor contact with high interfacial area and low liquid flow rates, which results in a portion of the reflux being in the saturated liquid state. Thus, a reflux temperature value between the saturated liquid temperature (vapor temperature) and the wall temperature is expected. An average of wall temperature and saturated liquid temperature, i.e., vapor temperature is used. Given very small reflux mass flow rates, deviation from this assumption should not lead to appreciable error in the segment energy balance and model results. The total heat transfer rate for each segment can then readily be determined while sensible vapor heat transfer can be calculated with local vapor properties as shown in Eq. 5.15. A vapor sensible heat transfer coefficient as well as an ideal condensation

coefficient needs to be determined to determine the effective heat transfer coefficient in Eq. 5.10.

$$\dot{Q}_{sensible} = \dot{m}_V c_p \left(T_{V,in} - T_{V,out} \right) \tag{5.15}$$

The wire gauze packing does not only facilitate liquid-vapor interfacial contact but it also provides vapor heat transfer enhancement. Sensible heat transfer is modeled with the packed bed correlation provided by Mills (1995) and shown in Eq. 5.16 where the hydraulic diameter of the unpacked vapor passage is applied. The ideal condensation coefficient is estimated with the correlation by Rose *et al.* (1999) as shown in Eq. 5.17. With the effective working fluid side heat transfer determined through the SBG method shown in Eq. 5.10, a resistance network is calculated and used to determine the total area of each segment and provides the total required rectifier length.

$$Nu_{D_h} = \left(0.5\sqrt{\mathrm{Re}_{D_h}} + 0.2\,\mathrm{Re}_{D_h}^{2/3} \right) \mathrm{Pr}^{1/3} \tag{5.16}$$

$$\alpha_{ideal} = T_V^{0.8} \left[5 + 0.63 \left(T_V - T_{wall} \right) \right] \tag{5.17}$$

Concentrated solution flowing through the plates with microscale passages serves as the coolant for the rectifier as shown in Figure 5.2. Coupling fluid and wall resistance are determined using the methodology presented by Nagavarapu and Garimella (2011).

5.5 Results

The dimensions of the desorber and rectifier to achieve the specified refrigerant vapor production rates and purity are shown in Table 5.2. These dimensions and the number of working fluid and coupling fluid plates can be specified such that the desorber

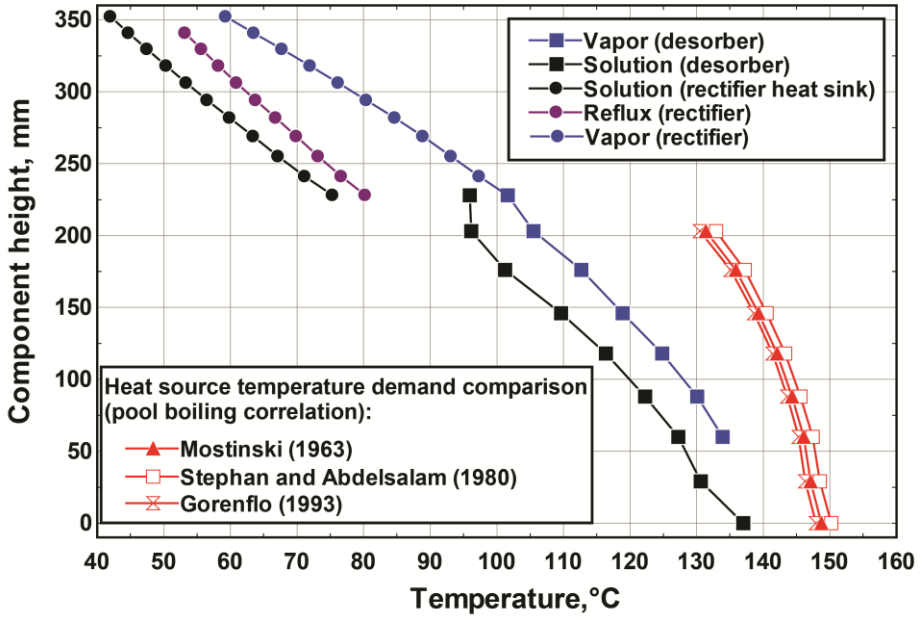

Figure 5.8: Temperature profiles and comparison of heat source temperature requirements for different pool boiling correlations

and rectifier can be integrated into a single unitary structure, which leads to a compact geometry and lower fabrication costs.

Results for baseline operating conditions are investigated by comparing the effect of the choice of pool boiling and binary mixture correlations as well as the effect of desorber mass transfer effectiveness. This is followed by a parametric study to investigate the effect of the variation of several operating parameters on system performance and to provide representative reduced order results.

5.5.1 Temperature Profiles and Correlation Comparison

Component internal temperature profiles for the desorber-rectifier assembly are shown in Figure 5.8 and Figure 5.9. The former compares the effect of the choice of pure substance pool boiling correlation, while the latter compares the effect of the choice of

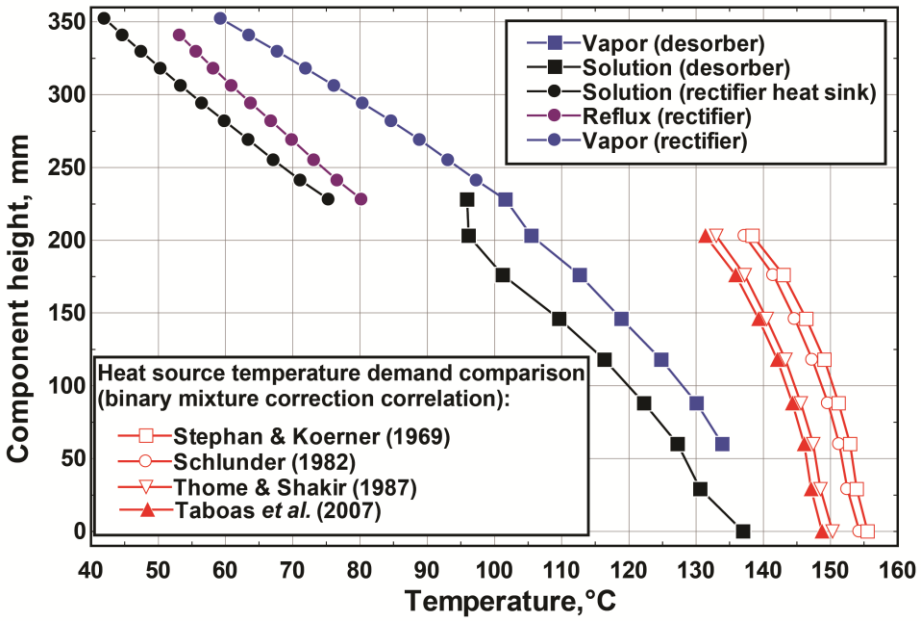

Figure 5.9: Temperature profiles and comparison of heat source temperature requirements for different binary mixture correction correlations

binary mixture correction correlation. Working fluid conditions are held constant and heat source coupling fluid flow rate is fixed. Consequently, the pool boiling heat transfer coefficient and the effect of a mass transfer correction are translated to variation in heat source temperature required to achieve identical working fluid temperatures and flow rates specified in Table 5.1. Figure 5.8 reveals that the selected pool boiling correlations provide very similar results with little effect on heat source requirements and, therefore, overall component performance. The pool boiling correlation by Mostinski (1963) is selected for the final model based on the comparative study by Táboas et al. (2007). Figure 5.9 shows that the effect of the choice of binary mixture correction correlation is more pronounced. The correlation by Stephan and Körner (1969) is the most conservative and the correlation by Táboas *et al.* (2007) results in the lowest heat source temperature demand. The former requires a heat source temperature that is 8°C greater than the latter. However, given that it is a more recent correlation and its development is based on a

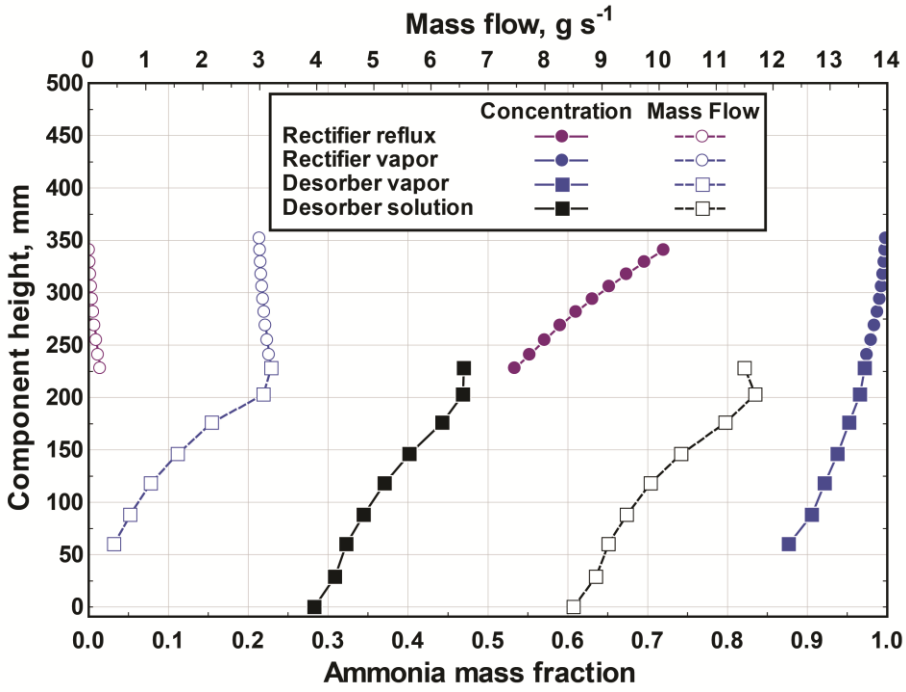

Figure 5.10: Component profiles for mass flow rates and ammonia mass fraction

comparative assessment of experimental data, the latter correlation is selected for the final model.

Mass flow rate and concentration profiles for solution, vapor and reflux at the design operating conditions are shown in Figure 5.10. The target vapor flow rate of 3 g s^{-1} as well as the target vapor ammonia mass fraction of 0.9985 is achieved at the outlet of the rectifier. The rectifier is required to provide vapor purification from an inlet ammonia mass fraction of 0.9718 and partial condensation generates reflux throughout the rectifier. However, the cumulative reflux flow rate is very small, i.e., ~ 0.2 g s^{-1}, and the vapor mass flow rate decreases accordingly. Clearly, vapor inlet concentration to the rectifier must be maximized to minimize rectifier heat duty and additional vapor generation requirements in the desorber as shown below. A continuous decrease in solution mass flow rate and solution mass fraction is shown in the desorber as vapor is generated

throughout the component. Vapor ammonia mass fraction increases toward the top of the component as vapor is generated at lower temperatures and purified through liquid-vapor contact as it flows upward.

Figure 5.11shows desorber solution and heat source temperature profiles as well as resulting local and cumulative rates for heat input and exergy destruction. An exergy balance, including the heat source stream, is used to determine the exergy destruction rate as shown in Eq. 5.18. The physical flow exergy for each stream is defined as shown in Eq. 5.19 where the reference state is chosen to be $T_o = 293K$ and $P_o = 101.325kPa$.

$$\dot{I} = \sum_i \dot{m}_{in}\psi_{in} - \sum_i \dot{m}_{out}\psi_{out} \qquad 5.18$$

$$\psi = h - h_o - T_o(s - s_o) \qquad 5.19$$

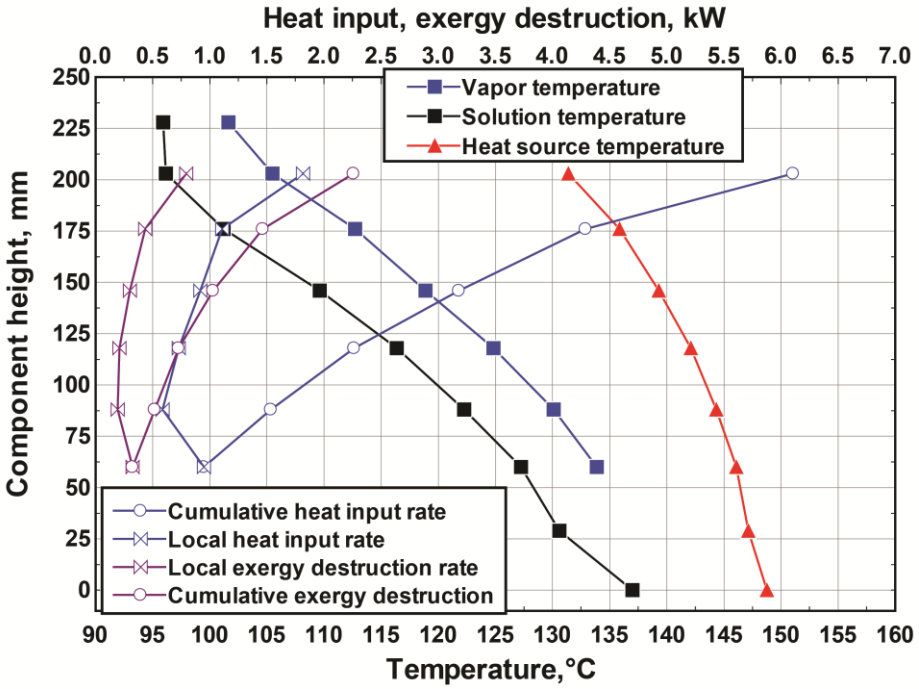

Figure 5.11: Desorber heat input and exergy destruction

Working fluid properties are determined from the ammonia-water property correlations by Ibrahim and Klein (1993). Heat source coupling fluid is specified as Paratherm^{TM} NF heat transfer fluid. The change of physical flow exergy can be determined using Eq. 5.20 and manufacturer supplied data for specific heat capacity, $c_{p.}$ The average value, $\overline{c}_p$ is calculated at the average heat source temperature, $\overline{T}_{CF}$.

$$\Delta\psi_{CF} = \overline{c}_p\left(\left(T_{CF,out} - T_{CF,in}\right) - T_o \ln\left(\frac{T_{CF,out}}{T_{CF,in}}\right)\right) \qquad 5.20$$

For the given temperature profile, local heat input rates decrease toward the bottom of the component due to the progressively lower solution ammonia mass fraction and decreased heat source temperature differences. The local increase in heat input at the bottom is due to a greater heat transfer area in the bottom segment compared to regular trays. Local and cumulative exergy destruction scales with heat input for the given temperature profile. However, exergy destruction in a diabatic distillation column depends on the temperature profiles of heat source and working fluid as (de Koeijer *et al.*, 2002; de Koeijer *et al.*, 2004). Variation of heat source coupling fluid flow rate and inlet temperature and its effect on system performance are investigated below.

5.5.2 Vapor Purification

A high degree of internal vapor purification is required in the desorber to optimize system performance. Staged vapor generation along a solution temperature profile in liquid-vapor countercurrent configuration ensures relatively high baseline vapor ammonia concentration values compared to a kettle-type desorber. Further purification is achieved through liquid-vapor contact in each tray. A qualitative assessment of the purification

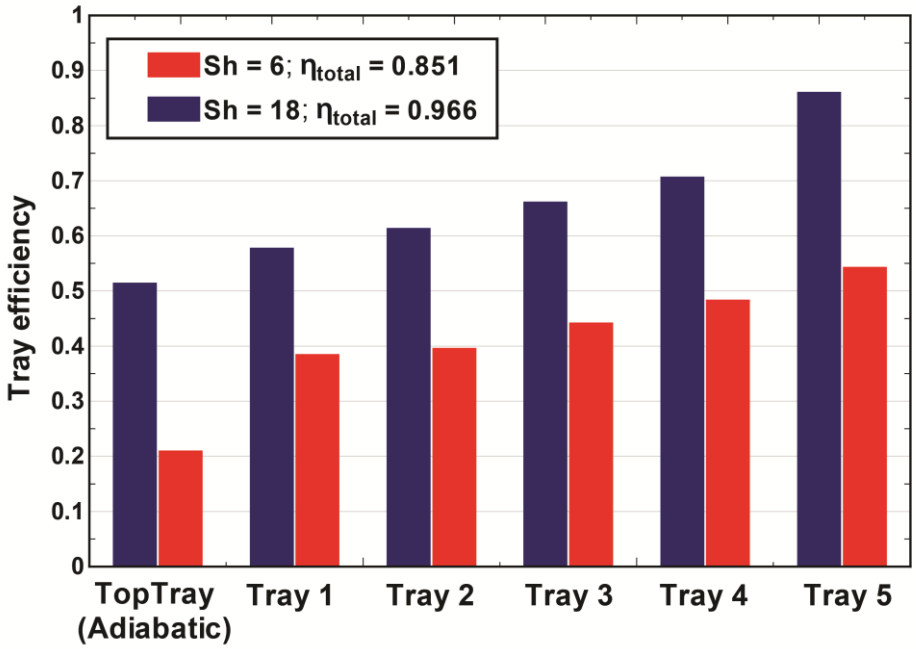

Figure 5.12: Vapor purification tray efficiencies comparison between *Sh* = 18 and *Sh* = 6

performance in an adiabatic distillation tray can be made using the Murphree tray efficiency (Zavaleta-Aguilar and Simões-Moreira, 2012). In contrast to conventional and larger dimensioned adiabatic trays, the proposed tray design does not result in a well-mixed pool. Local vapor generation and the pass-through vapor process do not occur within solution of the same temperature as shown in Figure 5.1. Therefore, an appropriate reference temperature and concentration has to be determined and a modified purification efficiency is proposed as shown in Eq. 5.21.

$$\eta_{pur} = \frac{x_{v,out} - x_{v,in}}{x^{*}_{v,out} - x_{v,in}} \qquad 5.21$$

Here, the reference concentration, $x^{*}_{v,out}$, is assumed to be the saturated vapor concentration at the temperature of liquid solution entering the tray. This approach is

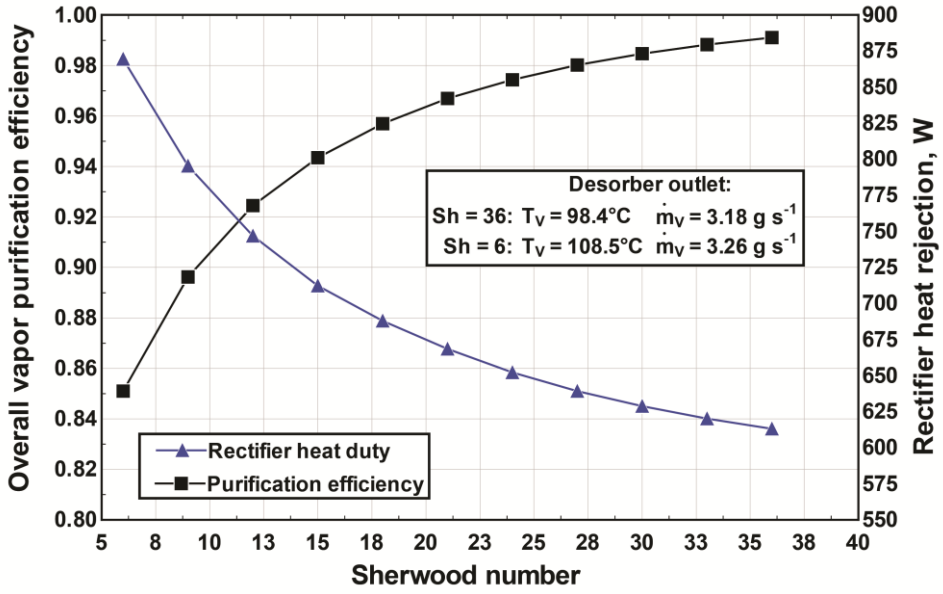

Figure 5.13: Desorber vapor purification efficiency and rectifier heat rejection vs. bubble internal Sherwood number

justified given that solution inlet to the tray feeds the bubble region where the majority of liquid-vapor contact occurs. In a well-mixed liquid tray, this modified definition provides slightly lower tray efficiency values, and the application of results from this study must be used with the definition provided here. Tray efficiency values are convenient reduced order results for vapor purification performance that facilitate system level modeling or dynamic modeling of this design.

Similarly, an overall desorber purification performance value can be determined where the reference concentration is based on concentrated solution entering the desorber and the value of $x_{v,in}$ is taken to be the saturated vapor concentration at the temperature of dilute solution leaving the desorber. Figure 5.12 shows individual tray efficiencies and overall component efficiency at design operating conditions with a Sherwood number of 18. The figure provides a comparison of tray purification and overall purification efficiency for a Sherwood number value of 6. For both cases, purification efficiency

decreases toward the top of the component as vapor mass flow rates increase. A bubble internal Sherwood number of 18 was assumed based on the study by Colombet *et al.* (2013) at design conditions. Tray efficiencies are significantly lower for $Sh = 6$. While a Sherwood number variation is used to illustrate the effect of mass transfer resistance, similar results are obtained if interfacial liquid-vapor area is varied. Figure 5.13 shows the overall desorber purification efficiency as a function of mass transfer effectiveness. The figure also depicts the link to rectifier heat duty requirements and thus lower system performance for lower mass transfer effectiveness. Thus, hotter vapor leaving the desorber results in a greater demand for vapor mass flow rate leaving the desorber for the same refrigeration load, causing greater rectifier heat duty due to purification by partial condensation.

5.5.3 Heat Source Flow Rate and Temperature

Heat source coupling fluid flow rate was fixed in the previous analysis and its inlet temperature was determined to meet design conditions in Table 5.1. However, heat source flow rate variation provides another degree of freedom and its effect on component performance is investigated in a parametric study where heat source coupling flow rate is varied from 0.03 kg s^{-1} to 1 kg s^{-1}. Figure 5.14 shows temperature profiles for both extremes of the flow rates. As expected, the pinch point changes from the bottom of the component for a high flow rate to the top of the component for a low flow rate. This variation in temperature profile causes a variation in the distribution of internal temperature profiles due to the shift in heat input from the top of the component to the bottom. Specifically, vapor leaving the desorber is hotter for high heat source coupling flow rates due to most of heat transfer occurring toward the top of the component, which

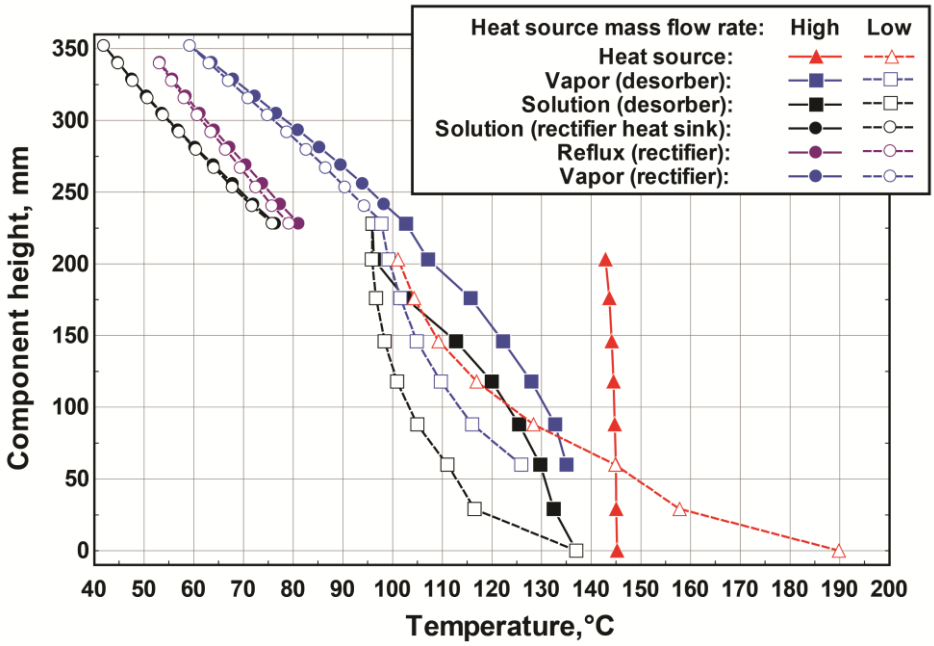

Figure 5.14: Temperature profile comparison for high and low heat source coupling fluid flow rate

reduces internal vapor purification. Conversely, a low coupling fluid flow rate produces vapor predominantly toward the bottom of the component, which facilitates component internal vapor purification. This results in a reduction of rectifier heat duty as is shown in Figure 5.15. While this suggests that a low flow rate is more favorable, Figure 5.15 also shows that much greater inlet temperatures are required to achieve a noticeable reduction in rectifier heat duty. Therefore, the active control of heat source coupling fluid flow allows for system optimization given available heat source temperatures or downstream temperature requirements of the coupling fluid. Indeed, the heat source inlet temperature curve in Figure 5.15 can be understood as a heat source demand curve that captures the trade-off between temperature and flow rate. A heat source demand curve can be determined for every target operating condition and can be contrasted to a heat source supply curve such as a waste heat temperature vs. flow rate profile of an engine.

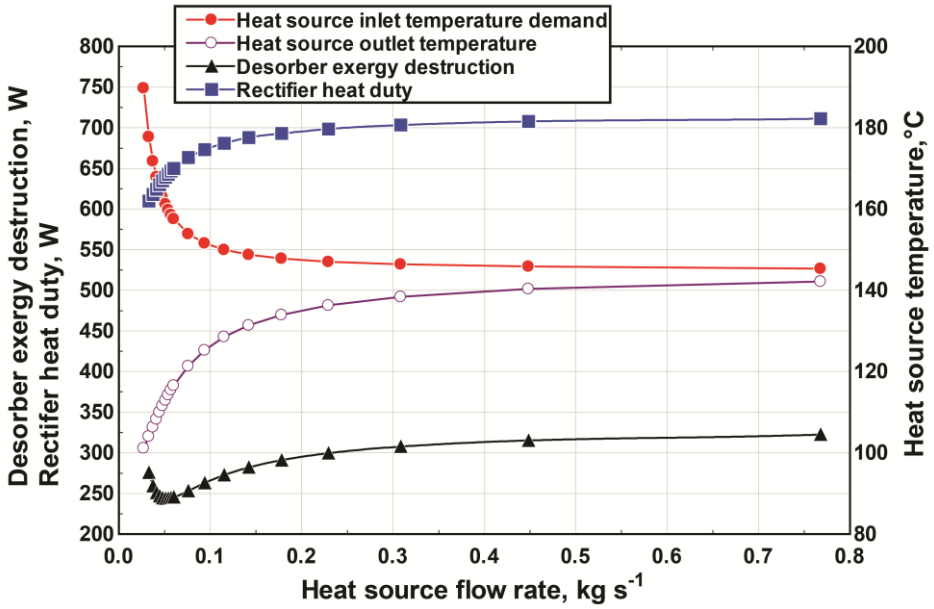

Figure 5.15: Heat source temperature variation and exergy destruction versus heat source mass flow rate

Figure 5.15 also shows how desorber exergy destruction is affected through the manipulation of component temperature profiles by coupling fluid flow rate variation. A distinct minimum can be observed, which is achieved at a flow rate that results in a relatively even temperature profile, i.e., the temperature difference between heat source and working fluid is approximately the same at the top and the bottom of the component. If minimization of exergy destruction is part of the objective of an optimal control scheme, this analysis shows that active coupling fluid flow rate control can be applied to accomplish that.

5.5.4 Variation of Ammonia Mass Fraction

The concentrated ammonia mass fraction in an actual system depends on operating conditions and is subject to variation. The sensitivity of component performance is investigated with a constant value of circulation ratio of 3.8 to maintain

consistent vapor mass flow rates leaving the desorber for the baseline concentrated solution flow rate of 11.5 g s^{-1}. Dilute solution temperature and heat source demand are varied. Maintaining a circulation ratio of 3.8 results in dilute solution temperatures near optimal thermodynamic operation (Chapter 3). Heat source coupling fluid flow rate and heat source inlet temperature requirements are determined by meeting a process variable set point defined in Eq. 5.22.

$$\Delta TR_{CF} = \frac{T_{CF,out} - T_{cs}}{T_{CF,in} - T_{ds}} \tag{5.22}$$

It is the ratio of the temperature difference between coupling fluid and working fluid at the solution inlet to the temperature difference at the solution outlet. In this study, a fixed value of $\Delta TR_{CF} = 3$ is applied. This value is consistent with baseline operating conditions shown in Table 5.1. As demonstrated in the previous section, heat source temperature

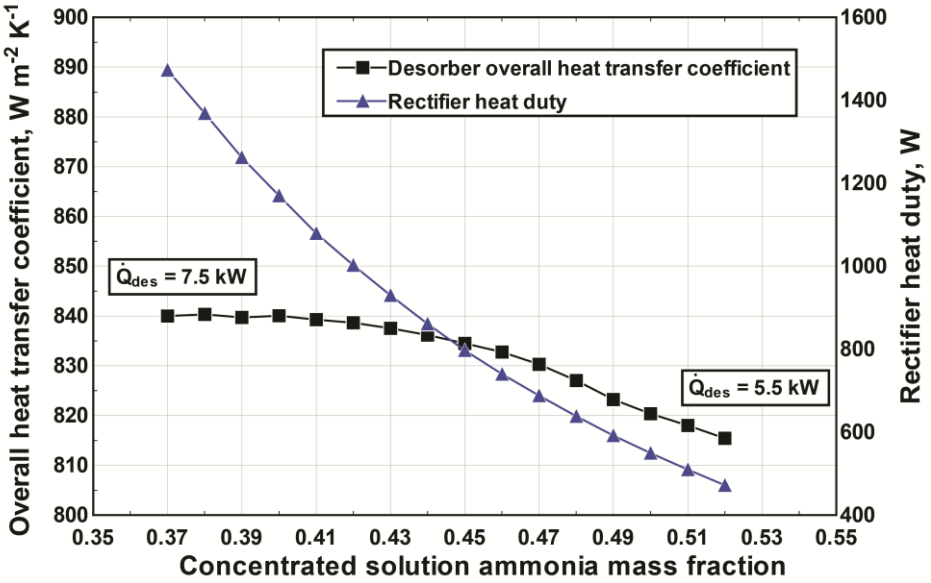

Figure 5.16: Desorber overall heat transfer coefficient and rectifier heat duty vs. solution concentration

profile variation can result in meaningful changes in component performance. Thus, maintaining constant ΔTR_{CF} values allows for the assessment of the effect of individual parameters investigated in this study without other confounding influences. Figure 5.16 shows the effect of ammonia mass fraction, x_{cs}, on desorber overall heat transfer coefficient, U_{des}, and on rectifier heat duty, $\dot{Q}_{rect}$. Desorber heat duty requirements increase as x_{cs} is decreased due to the increase in heat input required to maintain constant refrigerant vapor mass flow rates. The overall heat transfer coefficient is relatively constant. A slight increase from 815 W m^2 K^{-1} to 840 W m^2 K^{-1} is shown as x_{cs} is reduced from 0.52 to 0.37. This can be attributed to an increase in heat flux, a positively correlated variable in pool boiling correlations. Heat flux increases as desorber heat input increases to maintain a constant refrigerant generation rate. Rectifier heat duty increases

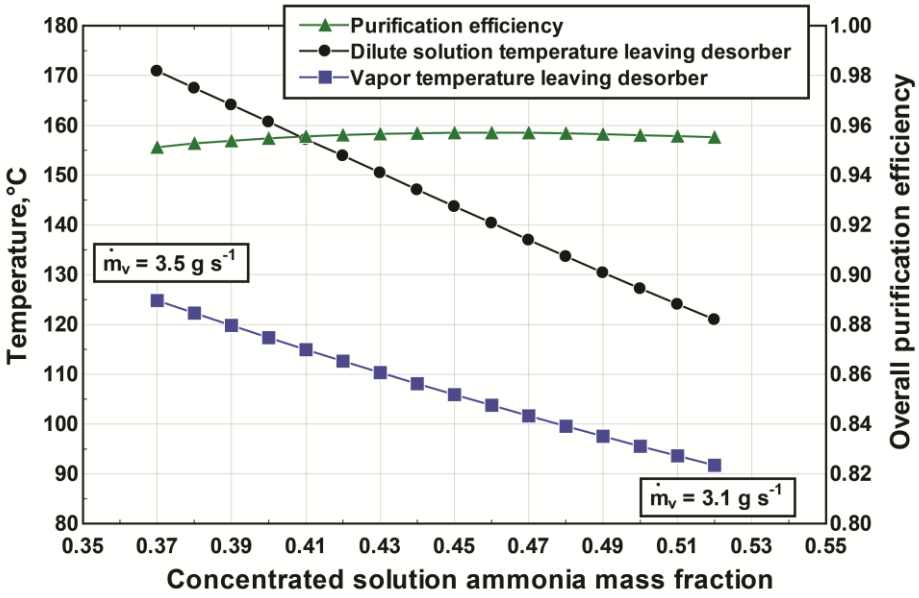

Figure 5.17: Desorber temperatures and purification efficiency vs. solution concentration

significantly as x_{cs} is decreased. This is primarily due to higher vapor temperatures and mass flow rates leaving the desorber while maintaining constant rectifier vapor outlet flow rates and purity as shown in Figure 5.17. Decreased vapor purity entering the rectifier results in an increased vapor generation requirement in the desorber due to the partial condensation process in the rectifier. Overall desorber purification efficiency is very constant at a value of 0.95. Relatively constant values for desorber purification efficiency and the overall heat transfer coefficient are useful reduced order results that can be applied as assumptions in overall system models and dynamic models.

5.5.5 Capacity Variation

The effect of capacity variation is investigated through variation of solution inlet flow rate while maintaining a constant dilute solution outlet temperature. The use of

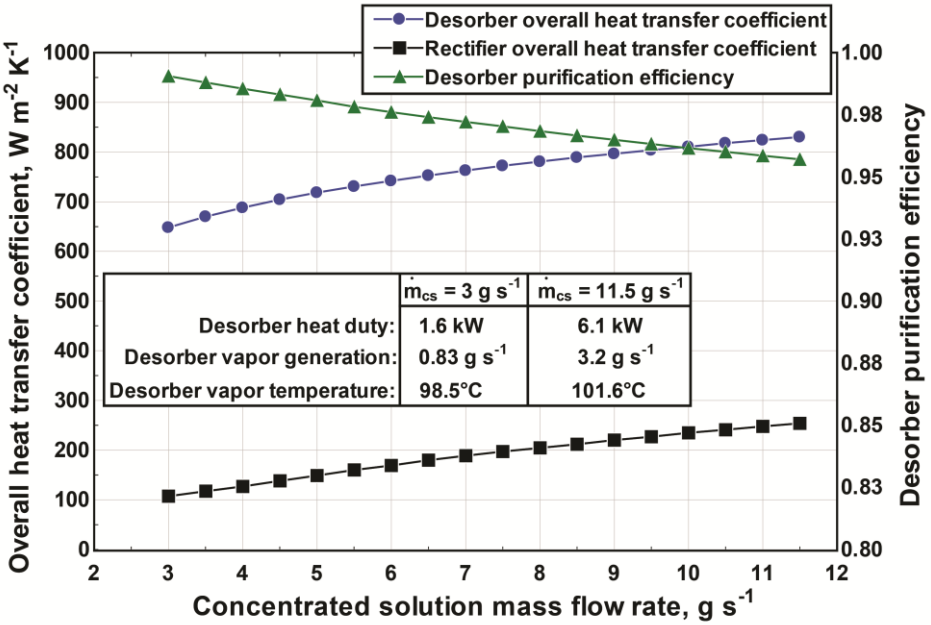

Figure 5.18: Desorber overall heat transfer coefficient and purification efficiency vs. solution mass flow rate

concentrated solution flow rate as an effective control variable for system capacity was reported by Dincer and Dost (1996). Constant circulation ratio and thermodynamic performance is achieved by maintaining a constant dilute solution temperature leaving the desorber. Therefore, if rectifier duty is controlled to maintain constant vapor outlet conditions, rectifier vapor outlet flow rates scale directly proportionally with concentrated solution flow rate. Figure 5.18 shows desorber overall heat transfer coefficient and purification efficiency. Overall heat transfer coefficient increases from 648 W m^{-2} K^{-1} to 830 W m^{-2} K^{-1} as heat duty is increased from 1.6 kW to 6.1 kW. This is due to reduced heat flux at part load operation and the inverse relationship of the pool boiling heat transfer coefficient to heat flux. Overall vapor purification efficiency increases from 0.957 to 0.991 as refrigerant vapor generation rate is reduced to 26% of design capacity, and a commensurate decrease in vapor temperature leaving the desorber is observed. This trend is expected. While interfacial liquid-vapor area in each tray increases somewhat with increased vapor flow rates (Chapter 4), it cannot adequately compensate for the increased mass transfer requirements at higher vapor flow rates.

Figure 5.18 also shows rectifier overall heat transfer coefficient as capacity is varied. Its value decreases from 254 W m^{-2} K^{-1} to 107 W m^{-2} K^{-1} as rectifier vapor inlet mass flow rate decreases from 3.2 g s^{-1} to 0.8 g s^{-1}. The vapor Nusselt number dependence on Reynolds number shown in Eq. 5.16 explains this trend. However, the vapor-side heat transfer degradation at part load can be easily accommodated given the available heat transfer area required for full capacity performance. The directly proportional increase of rectifier heat duty with concentrated solution mass flow is shown in Figure 5.19. This figure also depicts the diversion ratio of the rectifier heat sink. In this

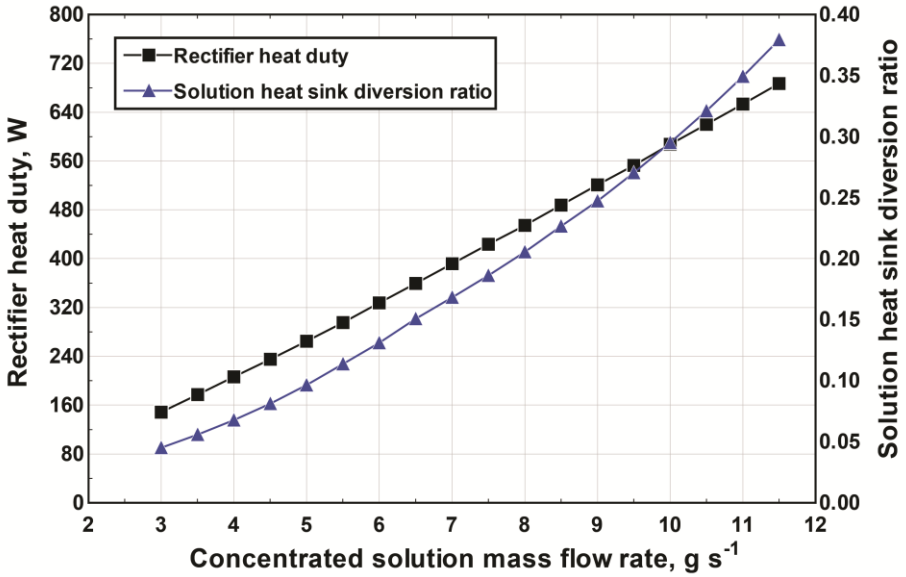

Figure 5.19: Rectifier heat duty and heat sink control vs. desorber solution mass flow rate

solution cooled rectifier, a portion of $\dot{m}_{cs}$ is diverted to the rectifier as heat sink flow. The balance of $\dot{m}_{cs}$ bypasses the rectifier and is recombined with the rectifier heat sink flow downstream of the rectifier. The ratio of concentrated solution mass flow rate required as rectifier heat sink flow to the total flow rate is the diversion ratio. It can range from very small values (very low rectification loads) to 100% at very high rectification loads. Thus, it can be used as an effective control variable to manipulate rectifier vapor outlet temperature and thereby rectifier outlet vapor ammonia mass fraction, x_{ref}. This approach can be used to maintain optimal x_{ref} values to maximize system performance while avoiding over- or under-rectification. The same control mechanism can accommodate variation in heat sink temperature and desorber operating conditions.

5.6 Conclusions

Novel configurations for desorption and rectification, incorporating the principle of diabatic distillation for small-capacity ammonia-water absorptions system, were presented. Based on previous assessment of hydrodynamic limitations and evaluation of key variables encountered in liquid-vapor countercurrent flow, a detailed non-equilibrium model was developed to predict heat and mass transfer performance. Desorption due to various mechanisms such as nucleate and film boiling, vapor-liquid mass transfer, and other relevant mechanisms were modeled as building blocks for the design and analysis of the desorber and rectifier. Results show that highly compact components can be realized for small-capacity ammonia-water absorption systems. The selection of pool boiling correlation for the ammonia-water mixture was shown to have little effect on overall component performance, while binary mixture correction correlations were shown to produce appreciable variation. Results of a parametric study emphasized the importance of mass transfer effectiveness for overall system performance. The variation of heat source temperature and mass flow rate was investigated. Heat source temperature profile manipulation to minimize desorber exergy destruction, reduce rectifier heat duty, and improve overall system performance was demonstrated. The concept of a heat source demand curve was introduced and the heat source temperature and mass flow rate were identified as effective control variables. Finally, the parametric study investigated the effect of operating conditions on component performance through variation of solution concentration and refrigerant vapor production rates. The results from this study also provide quantification of reduced order component design parameters such as vapor purification efficiency and overall heat transfer coefficient. While the novel desorption

and rectification component designs presented in this study are modeled in the context of ammonia-water absorption systems, diabatic desorption and rectification are relevant for a large range of applications. These designs and modeling framework can be readily applied to develop thermodynamically optimized components for many thermal separation processes. Examples include, but are not limited to, applications in the chemical processing industry as well as thermally driven desalination.

CHAPTER 6. THERMAL COMPRESSOR EXPERIMENTS

6.1 Introduction

Thermally activated cooling and refrigeration systems provide the opportunity to increase the overall efficiency of energy systems by utilizing low-grade heat sources instead of high-grade electricity. However, low-grade heat sources such as waste heat are typically available in dispersed form, which requires the use of small-capacity systems. Ammonia-water absorption systems have been in use for many decades, but their widespread application is limited by heat exchanger size requirements, relegating their application to large-scale and centralized high-capacity industrial applications. Recent advances in microscale heat and mass exchangers, however, enable the development of small-capacity ammonia-water absorption systems for light commercial, residential and mobile applications (Nagavarapu and Garimella, 2011). This enables the distributed use of thermally activated systems and better utilization of low-grade energy sources.

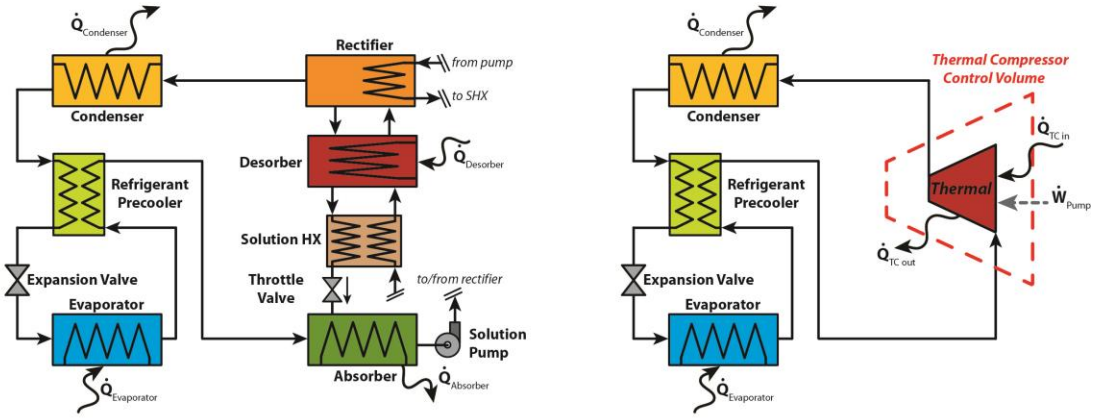

Figure 6.1: Thermal compressor analogy

A quantitative framework for the performance assessment of the thermal compressor in a single-effect ammonia-water absorption system as shown in Figure 6.1 was presented in Chapter 3. It was shown that optimal desorber operating temperatures exist for energetic and exergetic performance, i.e., $T_{opt,I}$ and $T_{opt,II}$, respectively. It was also established that $T_{opt,I} > T_{opt,II}$. Furthermore, it was shown that diabatic distillation designs for desorption and rectification maximize both performance metrics and yield highly compact components.

The desorber and rectifier produce and purify refrigerant vapor, and could contribute significantly to overall system performance, size and weight. A detailed review of the literature on ammonia-water desorption and rectification components was provided in Chapter 4. The same study presents the design of two diabatic distillation concepts for small-capacity ammonia-water absorption: a direct-coupled, gas-fired design, and a microchannel-based design that requires a heat source coupling fluid. An investigation of the hydrodynamics of these designs was conducted to validate their feasibility under hydrodynamic constraints imposed by liquid-vapor countercurrent flow. Chapter 5 presented the development of a heat and mass transfer model for the microchannel-based design concept that was applied to determine component sizes and performance predictions for a target refrigerant vapor generation rate of 3 g s^{-1} with ammonia concentration, x_{ref}, of 0.9985 at an operating pressure, P_{high}, of 1878 kPa. The design concentrated solution ammonia mass fraction, x_{cs}, was 0.47. This corresponds to a small-scale absorption chiller with a cooling capacity of 3.5 kW.

In the present study, these highly compact desorber and rectifier components are successfully fabricated. In addition, the desorber and rectifier are tested in integrated

fashion over a range of expected operating conditions in a test facility that simulates the thermal compressor of an absorption system. The thermal compressor framework is assessed and its performance metrics defined in Chapter 3 are investigated. Specifically, values for measured optimal desorption temperatures, $T_{opt,I}$ and $T_{opt,II}$ are compared with model predictions for a range of operating conditions. Energetic and exergetic thermal compressor performance is compared with model predictions for a range of desorption temperatures at each operating condition.

6.2 Component Design and Fabrication

The desorber and rectifier designs investigated in this study are shown in Figure 6.2 and Figure 6.3, respectively. Both designs incorporate microscale geometries for heat source and heat sink coupling fluid. Concentrated solution in the desorber enters the component at the top and flows over a series of alternating trays. Vapor is generated continuously through heated walls, rising toward the top of the component where it is

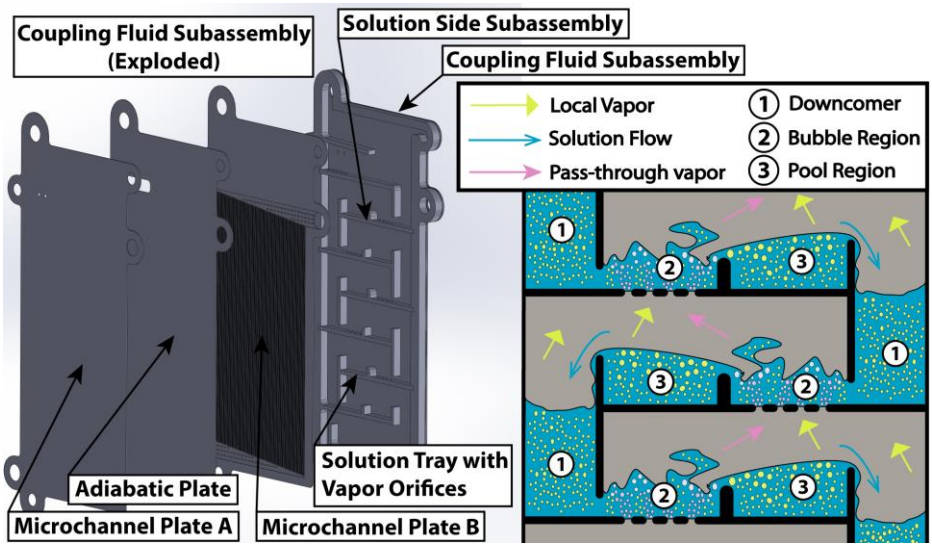

Figure 6.2: Design Concept A, component assembly (left), target flow pattern (right)

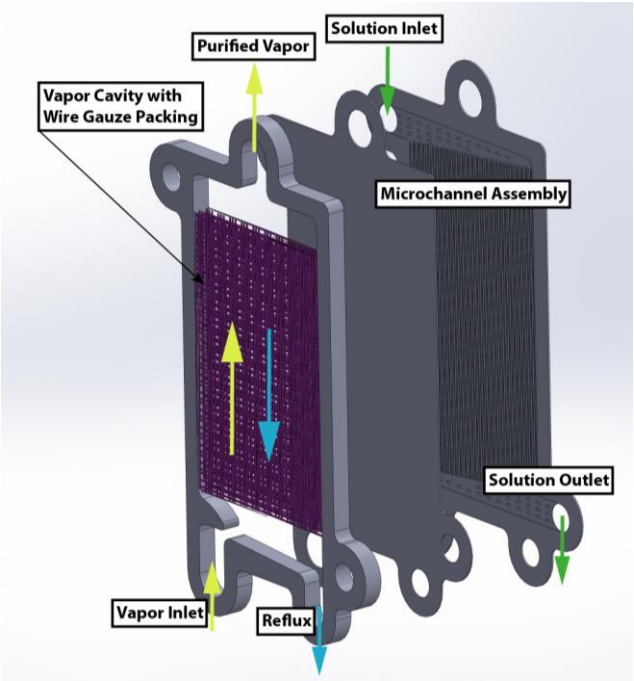

Figure 6.3: Rectifier design concept

separated from the solution and exits the desorber. Orifices in each tray allow for the formation of bubble regions where vigorous liquid-vapor contact facilitates purification of hotter vapor from the lower desorber sections.

The working fluid liquid-vapor countercurrent flow required for the effective operation imposes hydrodynamic limitations not conducive to the use of microscale geometries. Chapter 4 investigated hydrodynamic limitations inherent to liquid-vapor counter flow geometries. Unlike conventional distillation columns, in this application, the vapor flow rate varies dramatically throughout the component from very low mass flow rates at the bottom of the component to a much higher flow rate leaving at the top. Based on the results of the hydrodynamic investigation of the desorber, the internal tray geometry, i.e., the number of orifices per tray, is varied to accommodate these changing vapor-phase flow rates and ensure proper operating conditions at each tray location. The

Table 6.1: Specification for desorber and rectifier operating conditions

Operating Conditions	
Operating pressure, kPa	1878
Concentrated solution flow rate, g s^{-1}	11.5
Concentrated solution ammonia mass fraction	0.47
Target vapor mass flow rate leaving rectifier, g s^{-1}	3
Target dilute solution temperature leaving desorber, °C	137
Heat source coupling fluid mass flow rate, kg s^{-1}	0.14
Rectifier heat sink inlet temperature, °C	42
Rectifier vapor outlet ammonia mass fraction	0.9985

target operating flow conditions are shown in Figure 6.2 (right). The design operating conditions for the system are listed in Table 6.1. A detailed heat and mass transfer model for these designs was presented in Chapter 5. The model was used to determine component size requirements to achieve target vapor production rates at the specified purity. Component geometry specifications are listed in Table 6.2.

Microchannel plates were fabricated from 304 stainless steel with a thickness of 0.635 mm. A photochemical etching process was used to create design channel

Table 6.2: Specification for desorber and rectifier designs

Operating Conditions	Desorber	Rectifier
Material	304 stainless steel	304 stainless steel
Number of working fluid plates	8	8
Number of coupling fluid plates	16	8
Number of regular trays	5	N/A
Number of coupling fluid channels	1344	400
Overall component dimensions (H×W×D), mm	220×124×74	170×76×58
Overall component weight, kg	9.3	3.1

geometries, similar to the techniques described by Nagavarapu (2012). As shown in Figure 6.2, the component subassembly consists of two microchannel plates that are separated with a blank adiabatic sheet. The geometries for both microchannel plates are identical, but mirrored. Figure 6.4 shows a photograph of a fabricated microchannel plate with adiabatic partition.

Given the hydrodynamic limitations of liquid-vapor countercurrent flow, microchannel geometries cannot be applied to the working fluid side of the component. A working fluid depth of 6.3 mm is created with a machined frame that lines the perimeter of microchannel plates. Individual trays with the same depth are distributed throughout each working fluid assembly as shown in Figure 6.5. Tray geometry varies from the bottom of the component to the top, increasing the number of tray orifices with increasing vapor flow rate.

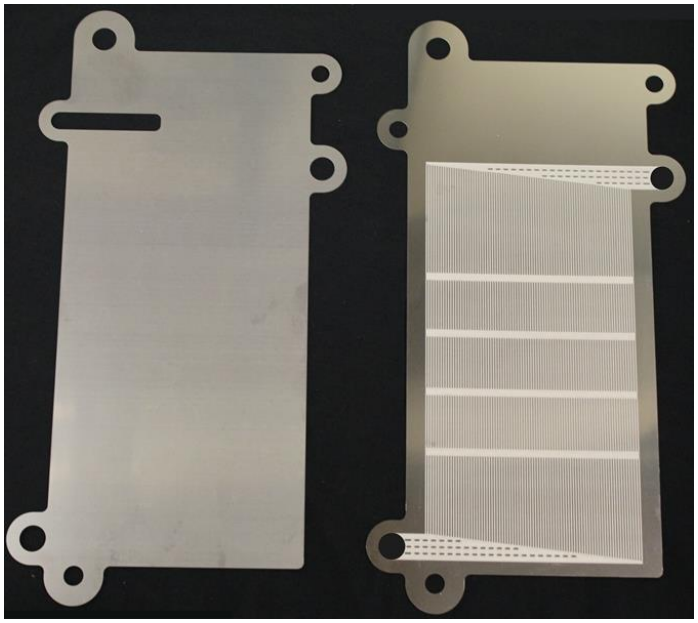

Figure 6.4: Desorber microchannel plate and adiabatic partition sheet

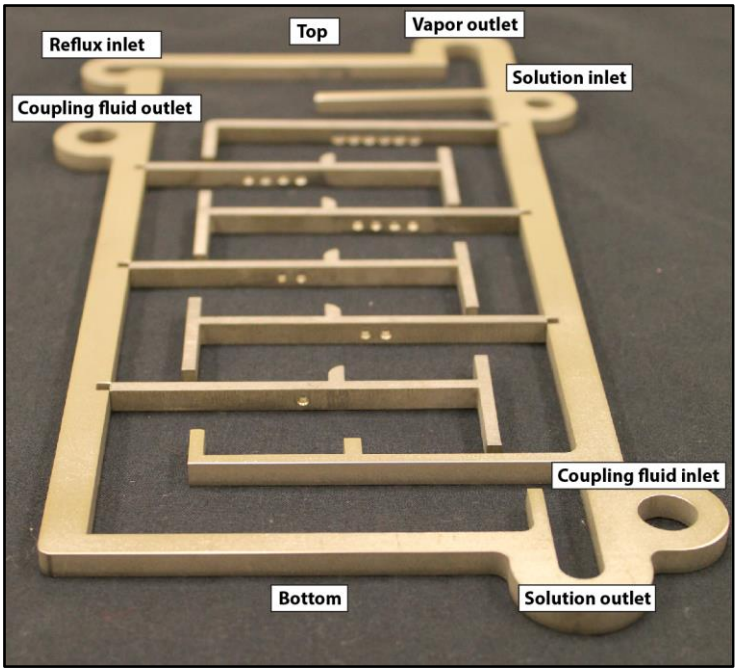

Figure 6.5: Working fluid side subassembly – machined frame with trays

Microchannel plate fabrication for the rectifier is identical to that of the desorber. The component subassembly consists of one microchannel plate, one microchannel cover plate and one working fluid frame. Countercurrent flow limitations must also be considered on the working fluid side geometry of the rectifier. Similar to the desorber, a machined frame lines the perimeter of the microchannel plate assembly. Wire gauze packing is inserted in the working fluid side cavity to enhance liquid-vapor contact while continuous heat transfer is provided from the walls of the microchannel assembly. It also facilitates greater vapor-phase heat transfer coefficients, which increases overall component effectiveness. Figure 6.6 shows microchannel and working fluid components for the rectifier. A close-up image of the wire gauze packing with dimensions is shown in Figure 6.7. Evaluation of the hydrodynamic characteristics of this packing, specifically flooding limitations, was also investigated in Chapter 4. Based on those results, four layers of wire gauze packing are inserted in the working fluid side cavity.

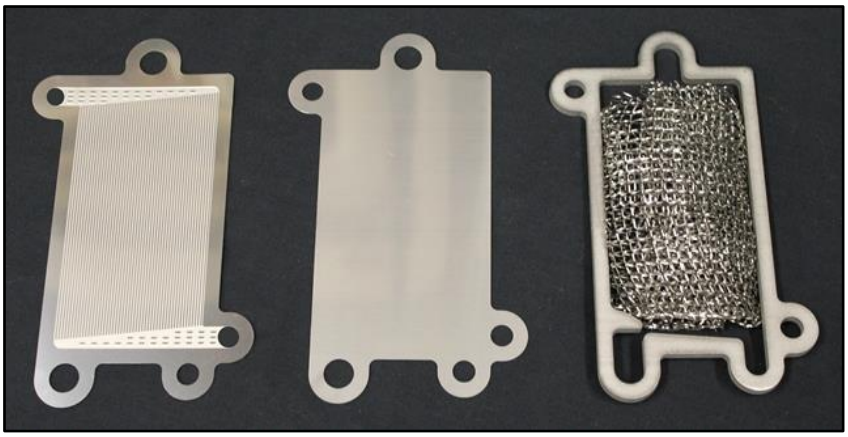

Figure 6.6: Rectifier assembly parts

The desorber and rectifier are sealed using back and front cover plates, where the front plate features integrated connections for fluid routing of the component. Finite element analysis was used to confirm that material thicknesses selected are sufficient for a design pressure of 500 kPa. Strategically placed structural features as shown in the header regions in Figure 6.4 were added to accommodate a safety factor of 1.25. A brazing process was used to bond the heat exchanger assembly. This process and its application to microscale heat exchangers is described in detail by Nagavarapu (2012). Both outside layers of the wire gauze packing in the rectifier are brazed to the walls of

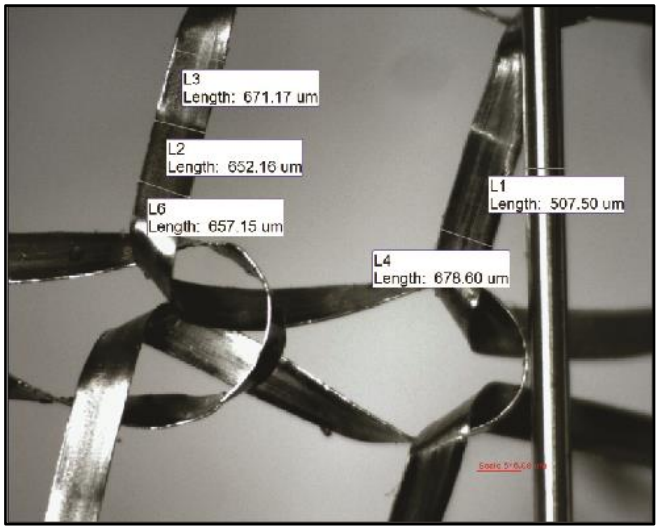

Figure 6.7: Wire gauze packing with dimensions

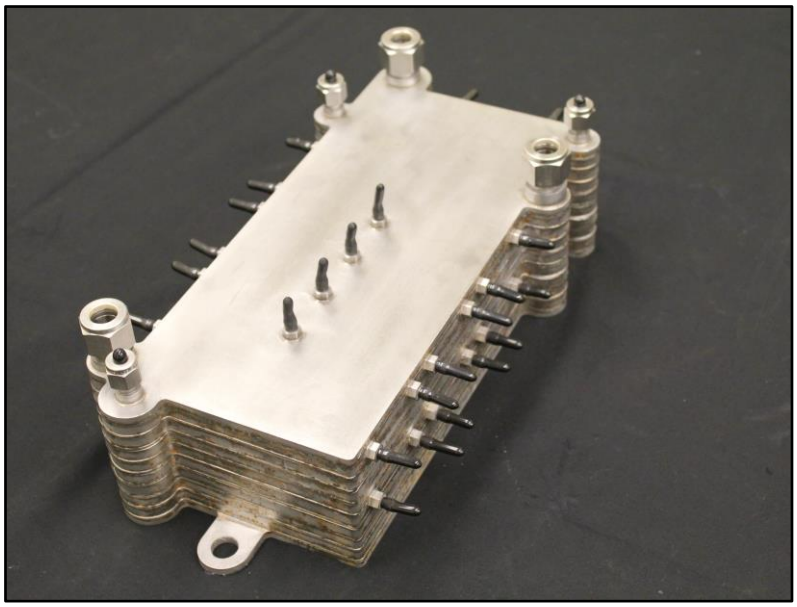

Figure 6.8: Desorber with intra-component instrumentation ports

the microchannel subassembly, which provides an extended surface effect.

While the desorber and rectifier are presented here as discrete components, they can be integrated into a unitary assembly with minimal modification of both components. This provides further size reduction advantages by eliminating fluid routing between both components. The completed assembly of the desorber with additional instrumentation and measurement ports is shown in Figure 6.8.

6.3 Experimental Facility and System Operation

A schematic of the experimental facility is shown in Figure 6.9. The system is designed to operate with two pressures (representative of high and low side pressures) in a regular absorption system. This enables the evaluation of the refrigerant vapor production rates and required energy and exergy demands under realistic operating conditions. Figure 6.10 shows a photograph of the test facility.

In addition to the desorber and rectifier, a shell-and-tube absorber, a microchannel condenser, and a microchannel solution heat exchanger are installed in the system to

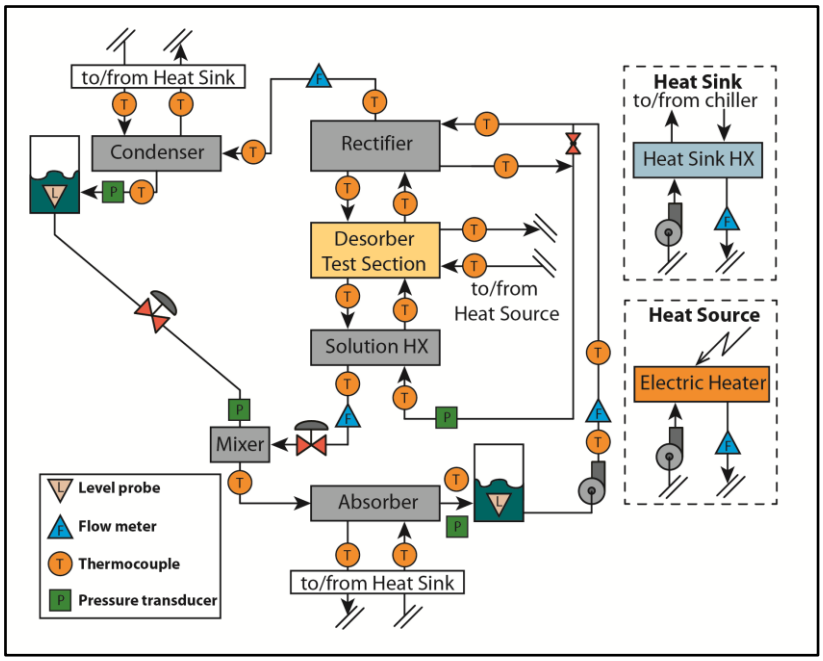

Figure 6.9: Schematic of experimental facility

complete the cycle. Working fluid reservoirs are installed at the outlet of the condenser and absorber to enable accurate adjustment of solution concentration and system pressures. Electronic control valves (Carel® E2V Series with 480 motor steps) are used for the expansion of refrigerant and throttling of dilute solution. A positive displacement diaphragm pump (Hydra-Cell® P100, maximum volumetric flow rate of 0.1 m^3 hr^{-1}) with a variable frequency drive is used for concentrated solution flow rate. Sight glasses are installed to provide visual access to the vapor streams leaving the desorber and the rectifier to verify that no flooding or entrainment of liquid into the vapor stream occurs. Auxiliary components include system heat source and sink. A mineral oil heat source coupling fluid (Paratherm™ NF) is used to couple the desorber to an 8 kW electric immersion heater (Watlow® FON Series). A hydronic loop with distilled water is used as the absorber and condenser heat sink. This loop has a centrifugal pump coupled to a brazed plate heat exchanger, which is in turn coupled to a high capacity, laboratory chilled water loop.

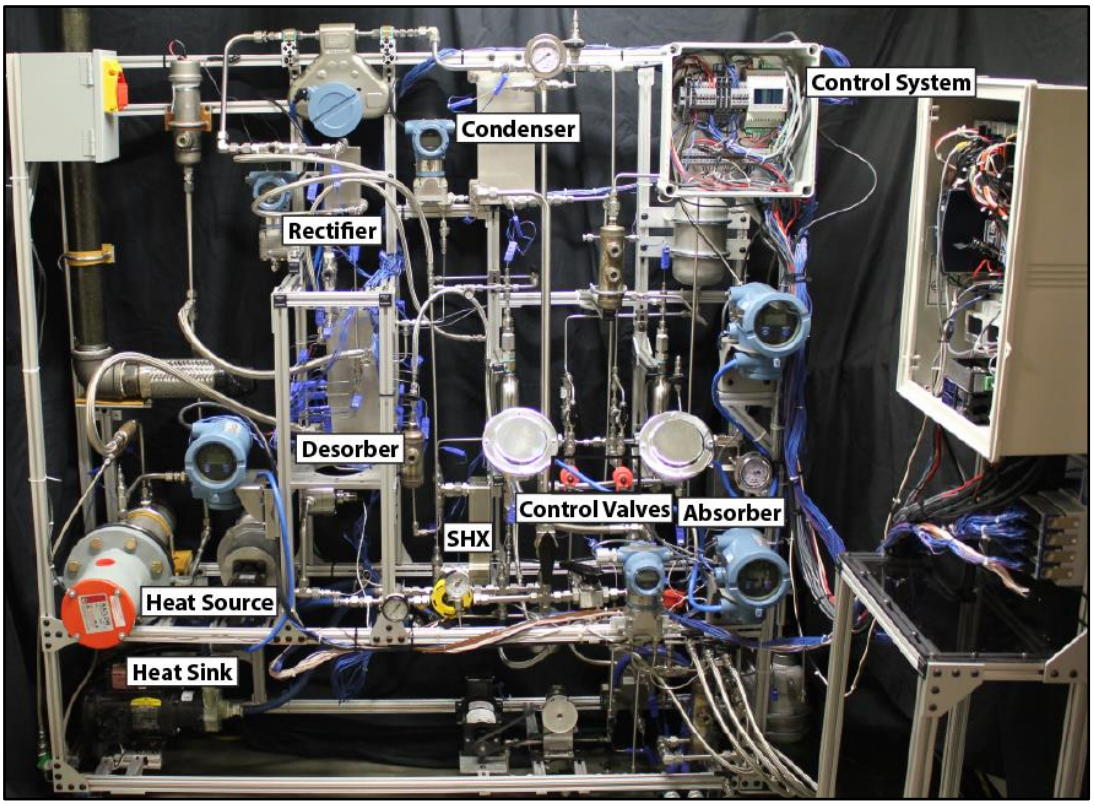

Figure 6.10: Photograph of test facility

Instrumentation for temperature, flow rate and pressure measurements is included as shown in Figure 6.9 to directly measure or infer these variables for all relevant state points. A list of relevant instrumentation is provided in Table 6.3. At the subcomponent level, thermocouples for liquid and vapor are included at each tray for one working fluid side plate as shown in Figure 6.8. Heat source coupling fluid temperature is measured at six locations within one coupling fluid plate. A data acquisition and control system was developed within the National Instruments™ LabVIEW® platform implemented in a National Instruments™ CompactRIO® cRIO 9024 Process Automation Controller (PAC). System control includes continuous speed modulation of the heat source coupling fluid pump with a variable speed drive, which provides accurate heat source mass flow rate control. Similarly, speed control of the concentrated solution pump is implemented for continuous and accurate control of solution flow. The expansion and throttling valves can

both be continuously modulated with the control system. Pulse-width-modulation (PWM) control of the electric mineral oil heater is used to control heat input to the system.

6.3.1 Test Points

Test conditions simulate a range of system level operating conditions, i.e., ambient temperature, evaporator temperature and system capacity. However, the effect of these conditions on internal operating parameters is system specific and requires assumptions such as heat exchanger closest approach temperature (*CAT*) values. Therefore, system internal parameters that are directly affected by operating conditions are identified and varied during experiments. Ambient temperature, i.e., heat rejection temperature for the absorber and condenser, directly affects high-side pressure, P_{high}, through saturation conditions in the condenser. Under the assumption of a nominal *CAT* value between saturated liquid in the condenser and the ambient temperature, i.e., 5°C, a

Table 6.3: List of test facility instrumentation

Instrument	Manufacturer/Part	Range	Accuracy
Thermocouples	Omega® T-type	-250 – 300ºC	±0.25°C
Pressure transmitter (high side pressure)	Rosemount™ 3051T	0 – 3000 kPa	±1.5 kPa
Pressure transmitter (low side pressure)	Rosemount™ 3051T	0 – 1000 kPa	±0.5 kPa
Mass flow rate (concentrated solution)	Micromotion™ CMFS010M	0 – 12 g s^{-1}	±0.1%
Mass flow rate (dilute solution)	Micromotion™ CMFS010M	0 – 10 g s^{-1}	±0.1%
Mass flow rate (concentrated solution)	Micromotion™ CMF010H	0 – 3.3 g s^{-1}	±0.1%
Volumetric flow rate (heat source coupling fluid)	AW-Lake JVS-30	0 – 1.6 m^3 hr^{-1}	±0.5%
Working fluid reservoir level (solution and refrigerant)	Gems® Sensors CT-1000	0 – 200 mm	±1%

representative value for P_{high} can be calculated. For a set of ambient temperatures of 25, 37 and 50°C, P_{high} is 1310, 1878 and 2617 kPa, respectively. Similarly, representative values for concentrated solution mass fraction, x_{cs}, are determined. These values are affected by the concentrated solution liquid saturation temperature in the absorber at a specific pressure. Absorber saturation temperature is determined with a *CAT* value of 5°C for the range of ambient temperatures under consideration. Absorber pressure directly affects refrigerant temperature in the evaporator. Therefore, a representative range of refrigerant evaporator inlet temperatures is used for each ambient temperature to determine the range of x_{cs} values to be tested. Hence, combinations of P_{high} and x_{cs} reflect specific operating conditions for ambient temperature and evaporator refrigerant inlet temperature. However, *CAT* values cannot be assumed constant and depend on system load and specific heat exchanger designs. Thus, direct control of P_{high} and x_{cs} provides a more consistent and widely applicable data set. For each test condition, the dilute solution temperature leaving the desorber, T_{ds} is varied. T_{ds} is used as a representative value for desorption temperature and an effective process variable for system optimization as shown in Chapter 3. The range of T_{ds} is specific for each operating condition but includes

Table 6.4: Test Matrix

Condenser pressure, P_{high}	**1300 kPa**			**1900 kPa**				**2600 kPa**		
NH_3 mass fraction, x_{cs}	**0.42**	**0.47**	**0.52**	**0.37**	**0.42**	**0.47**	**0.52**	**0.37**	**0.42**	**0.47**
$T_{ds} = T_{opt,II} - 10°C$				×	×	×	×			
$T_{ds} = T_{opt,II}$	×	×	×	×	×	×	×	×	×	×
$T_{ds} = T_{opt,I} - 10°C$	×	×	×	×	×	×	×	×	×	×
$T_{ds} = T_{opt,I}$	×	×	×	×	×	×	×	×	×	×
$T_{ds} = T_{opt,II} + 10°C$	×	×	×	×	×	×	×	×	×	×
$T_{ds} = T_{opt,II} + 20°C$	×	×	×	×	×	×	×	×	×	×

two optimal desorption temperature values, $T_{opt,I}$ and $T_{opt,II}$, as discussed above. The resulting test matrix is summarized in Table 6.4.

6.3.2 System Operation and Control

A constant concentrated solution mass flow rate, $\dot{m}_{cs}$, is maintained (9 g s^{-1}) for this set of experiments. Solution flow rate is controlled through solution pump speed modulation. Target P_{high} values are achieved through manipulation of condenser heat sink temperature. Using the common heat sink temperature for the absorber, P_{low} is controlled through an automatic feedback control loop with the refrigerant expansion valve as the control variable. This automatically adjusts x_{cs} to achieve a specified steady state value of P_{low}. The set point for P_{low} depends on target x_{cs} values. Adjustments to the absorber and condenser heat sink flow rates are made individually to achieve exact target values for x_{cs} and P_{high}.

Heat source temperature is adjusted through a feedback control loop to achieve a target value for T_{ds}. The PAC uses a PID controller with PWM for on/off control of the electric heater to modulate heat source inlet temperature to the desorber. Heat source mass flow rate is adjusted to maintain relatively constant temperature profiles for all test points. Specifically, the ratio of temperature differences between solution and coupling fluid of desorber top and bottom location, ΔTR_{CF}, as define in Eq. 6.1 is maintained at a value of approximately $\Delta TR_{CF} = 3$ for all tests. The effect of variation of ΔTR_{CF} was discussed in detail in Chapter 5 and a target value of $\Delta TR_{CF} = 3$ was suggested, which is maintained is this study.

$$\Delta TR_{CF} = \frac{T_{CF,out} - T_{cs}}{T_{CF,in} - T_{ds}} \quad 6.1$$

Finally, the heat sink of the solution cooled rectifier, i.e., concentrated solution flow to the rectifier, is controlled with a manual bypass valve to manipulate refrigerant vapor temperature leaving the rectifier. This maintains a target refrigerant ammonia mass fraction.

6.4 Data Reduction

To completely define the thermodynamic state of the ammonia-water binary mixture, three independent properties must be known or assumed. All relevant temperature values are measured directly. System pressures are directly measured at the absorber and rectifier outlets. It is assumed that pressure drop of the working fluid in the absorber, desorber and rectifier does not have an appreciable effect on working fluid properties and can therefore be neglected. A third variable is required, and quality or ammonia mass fraction is typically used. Ammonia mass fraction is challenging to measure directly with low uncertainty and may be inferred from available data and assumptions. For some state points, a saturated liquid or saturated vapor assumption is justified. Dilute solution leaving the desorber is assumed to be saturated liquid, while the vapor streams leaving the desorber and the rectifier are assumed to be saturated vapor. Mass and species balances can then be applied to determine all state points completely. Concentrated solution and dilute solution mass flow rates are measured and used to determine refrigerant mass flow. Direct measurement of refrigerant vapor mass flow leaving the rectifier was used only to validate steady state conditions.

The *Engineering Equation Solver* (EES) software (Klein, 2015) platform is used for data reduction and analysis. Built-in thermodynamic property routines (Ibrahim and Klein, 1993) are used to determine all state points. Liquid thermal conductivity is determine based on the correlation of Cuenca *et al.* (2013). Liquid-phase viscosity and surface tension are evaluated based on the correlation of Conde (2006). Liquid-phase binary diffusion is based on the data of Frank *et al.* (1996). Vapor-phase transport properties are determined through the *Chapman-Enskog Kinetic Theory* (Mills, 1995). Collected measurements are assumed to be uncorrelated and random variables with manufacturer specified uncertainties. Propagation of uncertainties in calculated variables is based on the method of Taylor and Kuyatt (1994) and is determined with a built-in tool in *Engineering Equation Solver* (Klein, 2015).

6.4.1 Heat Duties and Losses

Overall heat input to the thermal compressor can be determined through heat source coupling fluid temperature and flow rate measurements as shown in Eq. 6.2 where specific heat, $c_{P,CF}$ is temperature dependent and an average value based on inlet and outlet temperatures is used.

$$\dot{Q}_{CF} = \dot{m}_{CF}\bar{c}_{p,CF}\left(T_{CF,in} - T_{CF,out}\right) \tag{6.2}$$

Rectifier heat duty is determined through direct measurements of flow rate and temperatures of concentrated solution. Rectifier duty is controlled with partial diversion of concentrated solution as shown in Figure 6.9. Given direct measurement of $\dot{m}_{cs}$, solution inlet temperature and the temperature of re-combined concentrated solution

downstream of the rectifier are used to determine an enthalpy difference and heat duty as shown in Eq. 6.3.

$$\dot{Q}_{rect} = \dot{m}_{cs}\left(h_{cs,out} - h_{cs,in}\right) \tag{6.3}$$

For both, desorber and rectifier, coupling fluid heat duty is compared with working fluid enthalpy changes for the component, determined through thermodynamic states and measured flow rates. A mismatch is expected due to losses but with consideration of properly calculated losses, good agreement of the energy balance is achieved with an average error of less than 3%.

Three heat loss values are estimated: overall thermal compressor heat loss, $\dot{Q}_{loss,TC}$, desorber heat loss, $\dot{Q}_{loss,des}$, and rectifier heat loss, $\dot{Q}_{loss,rect}$. This allows for the determination of net heat input values for the desorber and rectifier, as well as the overall thermal compressor. For example, the net heat input to the thermal compressor is shown in Eq. 6.4.

$$\dot{Q}_{TC} = \dot{Q}_{CF} - \dot{Q}_{loss,TC} \tag{6.4}$$

The total thermal compressor heat loss is comprised of component and fluid routing losses that are determined individually. Desorber heat loss is shown in Eq. 6.5, where the ambient temperature, T_{amb}, is measured continuously for all tests and the average heat source coupling fluid temperature, $\overline{T}_{CF}$, is assumed to drive heat losses.

$$\dot{Q}_{loss,des} = \frac{\left(\overline{T}_{CF} - T_{amb}\right)}{R_{loss,des}} \tag{6.5}$$

The resistance to heat loss, $R_{loss,des}$ is determined using Eq. 6.6 and includes a thermal resistance from insulation and resistances at the insulation surface in parallel due to convection and radiation. Here, the radiation heat transfer coefficient, α_{rad} is defined as in Eq. 6.7 (Bergman *et al.*, 2011).

$$R_{loss,des} = \left(\frac{th}{kA}\right)_{ins} + \frac{1}{\left(\alpha_{conv} + \alpha_{rad}\right) A_{sur}} \tag{6.6}$$

$$\alpha_{rad} = \varepsilon\sigma\left(T_{sur} + T_{amb}\right)\left(T_{sur}^2 + T_{amb}^2\right) \tag{6.7}$$

6.5 Thermal Compressor Analysis and Results

Two figures of merit for thermal compressor performance were proposed in Chapter 3. The specific heat input is defined as shown in Eq. 6.8.

$$q_{des} = \frac{\dot{Q}_{TC}}{\dot{m}_{ref}} \tag{6.8}$$

It denotes the required heat input per unit mass of refrigerant produced by the thermal compressor and can be readily calculated using the measurements discussed above. The second figure of merit is thermal compressor efficiency as shown in Eq. 6.9, which is based on second law considerations.

$$\eta_{TC} = \frac{\dot{m}_{ref}\left(\psi_{out} - \psi_{in}\right)}{\dot{m}_{CF}\left(\psi_{CF,in} - \psi_{CF,out}\right) - Ex_{loss,TC}} \tag{6.9}$$

Given that the primary energy input to the thermal compressor is heat, an exergy based efficiency value is appropriate. The numerator in Eq. 6.9 is determined from the

definition of flow exergy at thermal compressor inlet and outlet conditions as shown in Eq. 6.10. The denominator, i.e., exergy input is calculated from the change in exergy of the heat source coupling fluid, also applying Eq. 6.10.

$$\psi_i = \left(h_i - h_0\right) - T_0\left(s_i - s_0\right) \qquad 6.10$$

Heat source exergy input is discounted by the exergy lost due to heat loss from the thermal compressor to maintain generality of these results irrespective of specific system insulation. In this study, both figures of merit are evaluated without the consideration of pump work. This provides results with general applicability because the energetic and exergetic cost of high grade energy to drive the pump, e.g., electricity may differ for various applications. Moreover, it should be noted that pump work is marginal and on the order of 1% of heat input, which justifies the omission of pump work from the evaluation of thermodynamic performance (Herold *et al.*, 1996).

6.5.1 Thermal Compressor Heat Input Results

Results for specific thermal compressor heat input, q_{des}, are shown in Figure 6.11 as a function of T_{ds} for three x_{cs} values at an operating pressure, P_{high}, of 1900 kPa with the corresponding modeling results (Chapter 3). A minimum for q_{des} can be observed in the model predictions as well as the experimental results. The minimum measured heat input temperature, $T_{opt,I}$, is within approximately 10°C of the predicted value. The prediction of the absolute value of q_{des} agrees well with the experimental results for xcs values of 0.52 and 0.47, with an average error of less than 10%. Deviations from model predictions are noticeable at lower concentrations and higher desorption temperatures.

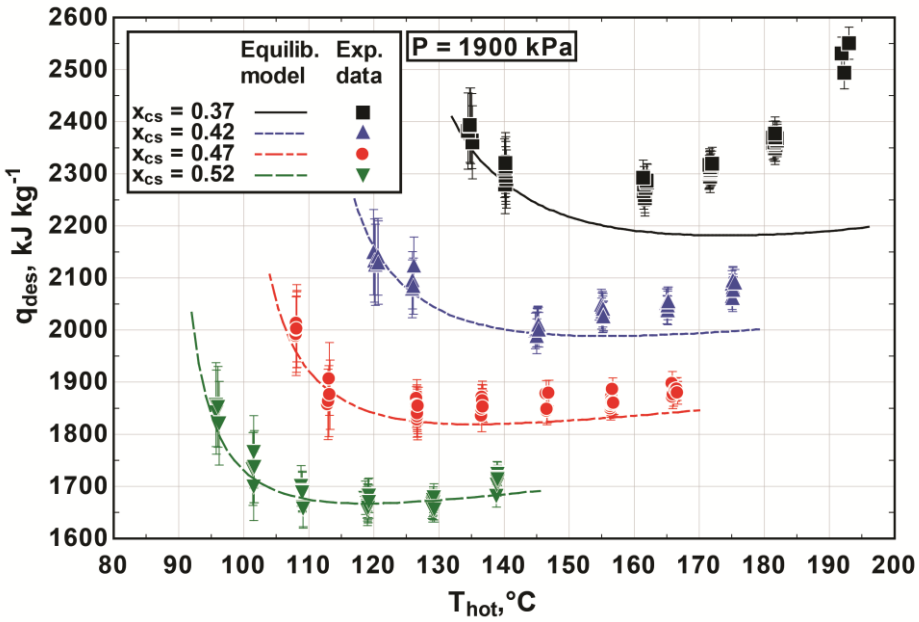

Figure 6.11: Specific thermal compressor heat input at P_{high} = 1900 kPa

Also, the experimental value of $T_{opt,I}$ is more distinct compared to the equilibrium model at higher desorption temperatures and lower concentration values. This behavior is due to the component performance assumptions, e.g., solution heat exchanger effectiveness and internal vapor purification efficiency of the desorber, being maintained constant in the equilibrium model, while they vary in an actual system. Examination of required rectification loads provides insight into this trend. The diabatic distillation desorber targets reduction of vapor temperatures leaving the desorber to values that approach those of concentrated solution entering the desorber. As desorption temperatures and vapor flow rates increase, vapor purification performance of the desorber is reduced. Concentrated solution flow rates are maintained at constant values while T_{ds} is varied, which results in increased vapor flow rates at higher desorption temperatures. Consequently, vapor temperatures leaving the desorber increase as T_{ds} increases. Therefore, a relative increase of heat rejection from the rectifier compared to the equilibrium model predictions (Chapter 3) implies a relative increase in q_{des}. Figure 6.12

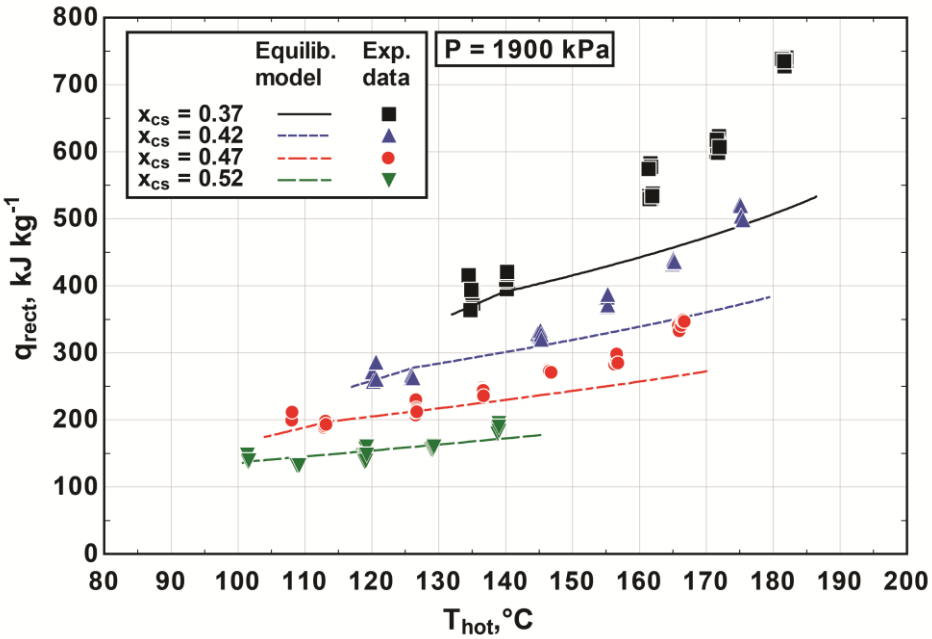

Figure 6.12: Rectifier specific heat input, model predictions and experimental results

compares experimental results for rectifier heat duty with predictions from the equilibrium model. Here, specific heat duties are reported, i.e., $q_{rect} = \dot{Q}_{rect} / \dot{m}_{ref}$. Experimental results for x_{cs} = 0.52 are in good agreement (within 5%) of model predictions. An increase in rectifier heat duty and deviation from the equilibrium model can be seen at higher desorption temperatures and lower x_{cs} values. This can be explained by a reduction of desorber purification performance at lower concentrations and higher desorption temperatures. As a consequence, rectifier vapor inlet temperatures are higher, requiring an increase in rectifier duty to maintain constant x_{ref} values.

The effect of different operating pressures on q_{des} and $T_{opt,I}$ is explored in Figure 6.13 and Figure 6.14. Figure 6.13 compares various x_{cs} values at a fixed pressure of 1300 kPa, while Figure 6.14 compares heat input at three different condenser pressures at a fixed x_{cs} value of 0.47. Again, both model and experiment show a distinct value for $T_{opt,I}$. Agreement of measured $T_{opt,I}$ within 10°C of the predicted value shows that the

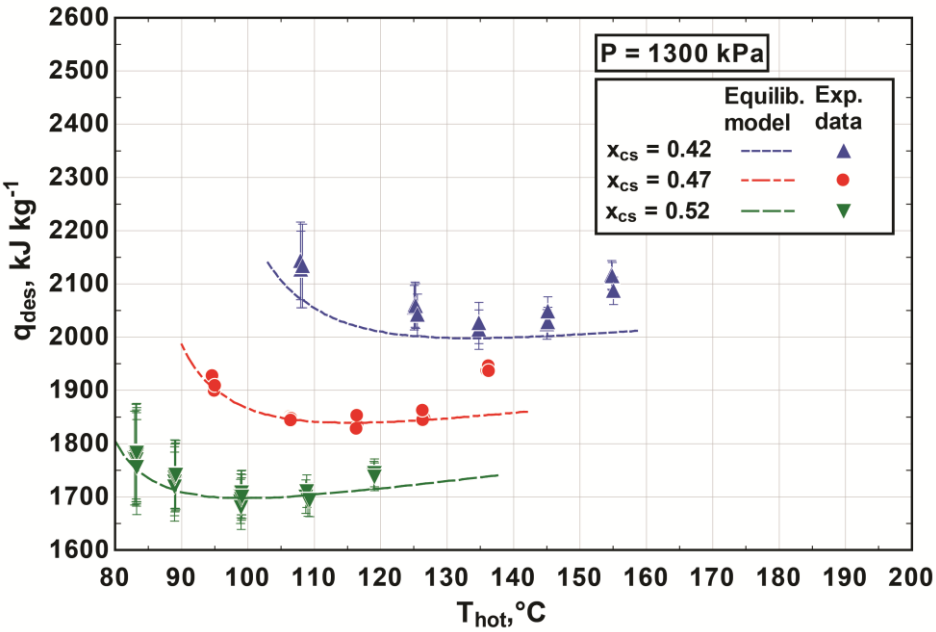

Figure 6.13: Specific desorber heat input at P_{high} = 1300 kPa

previously developed equilibrium model (Chapter 3) can be applied for prediction of $T_{opt,I}$. Deviation of actual values of q_{des} from equilibrium model predictions >10% are also observed at higher desorption temperatures and lower concentrations, and can be explained with the same reasoning as discussed above. For all operating conditions, thermal compressor performance consistently improves with increasing x_{cs} and decreasing P_{high} regardless of T_{ds}, which is expected.

6.5.2 Thermal Compressor Efficiency

The concept of thermal compressor efficiency was introduced above as an appropriate figure of merit given that both energy quantity and grade demands are dependent on operating conditions. Thermal compressor efficiency as defined in Eq. 6.9 was evaluated with the thermodynamic equilibrium model (Chapter 3) and for experimental data in this study. Figure 6.15 compares experimental results with equilibrium model predictions for

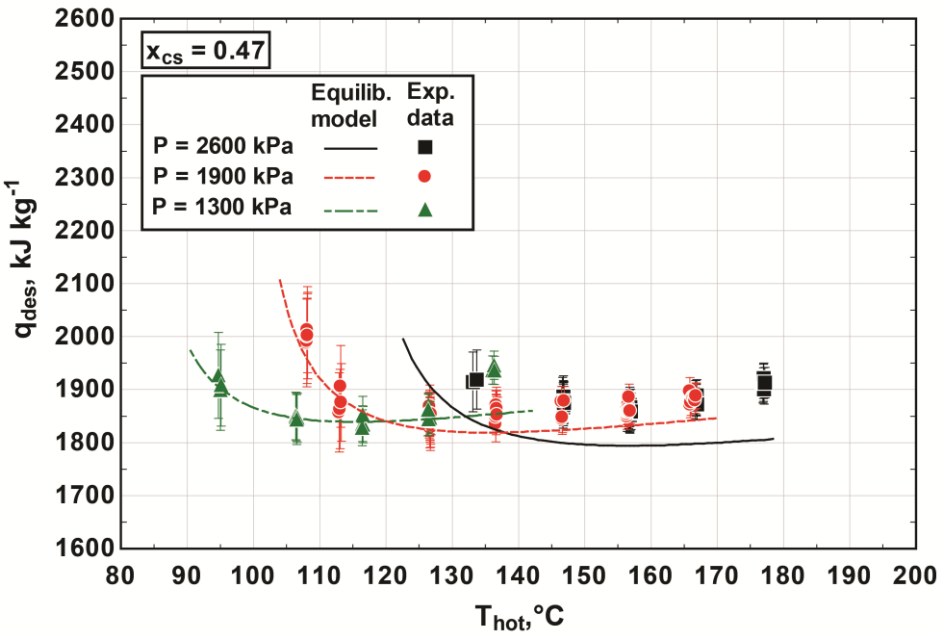

Figure 6.14: Specific desorber heat input for various pressures at x_{cs} = 0.47

a range of T_{ds} at a value for P_{high} of 1900 kPa. The equilibrium model predicts a distinct maximum for all four x_{cs} values investigated. The value of T_{ds} at which η_{TC} is maximized is defined as $T_{opt,II}$, suggestive of its origin based on second law considerations. The predicted efficiency maximum is more pronounced at higher concentration values. Indeed, at high concentration values, experimental results show a distinct maximum for η_{TC}. A weak maximum is somewhat discernable for both of the lower solution concentration values. Model predictions show that the efficiency peak is less distinct at lower x_{cs} values. Given the trend in the data, it is reasonable to expect that further reduction of T_{ds} at lower x_{cs} values will be accompanied by a reduction of thermal compressor efficiency. However, as discussed below, further reduction of T_{ds} also results in much higher circulation ratios. Experimental limitations did not permit further increase in circulation ratio while maintaining consistent experimental conditions in the remainder of the system. These results show that predicted values of $T_{opt,II}$ are within 10°C of the

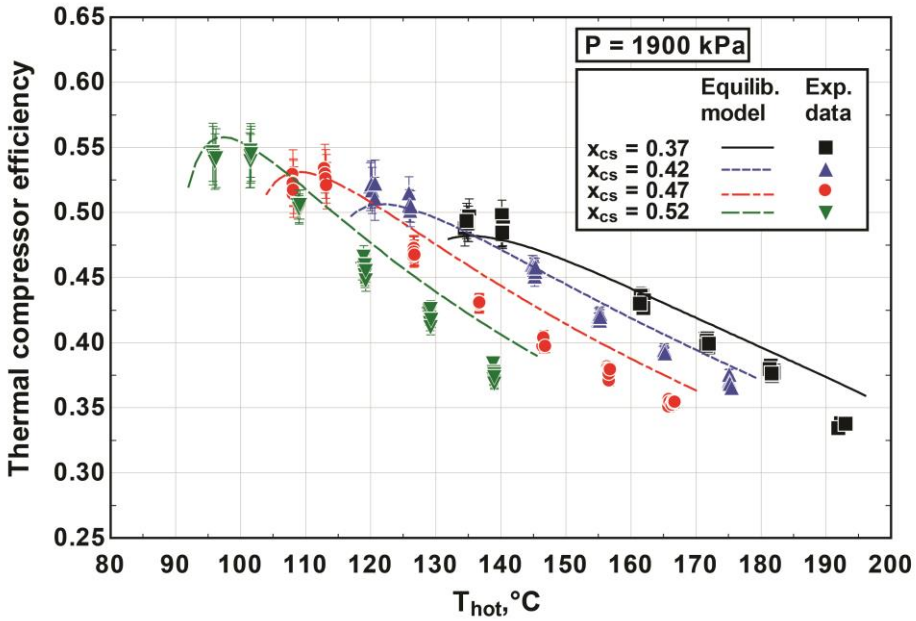

Figure 6.15: Thermal compressor efficiency at P_{high} = 1900 kPa

data. Absolute values of experimental η_{TC} values are within 10% of predicted values. Deviations from model predictions for η_{TC} are significantly greater at higher T_{hot} values. This is due to fixed values of assumptions for solution heat exchanger effectiveness and internal desorber vapor purification efficiency, as previously discussed.

Results for a different operating pressure, P_{high} = 1300 kPa, are presented in Figure 6.16. The range of tested values for T_{ds} at this pressure did not include values below the predicted $T_{opt,II}$. However, given the experimental validation of the existence of a maximum value for η_{TC} in Figure 6.15 and good agreement of η_{TC} with model predictions (less than 10% maximum error) in Figure 6.16, it is reasonable to expect maximum thermal compressor efficiency values near predicted $T_{opt,II}$ values. Similarly, Figure 6.17 compares thermal compressor efficiency at various operating pressures for a fixed x_{cs} value of 0.47.

This set of thermal compressor results shows that, unlike results for q_{des}, an increase in concentration or reduction in pressure does not necessarily result in

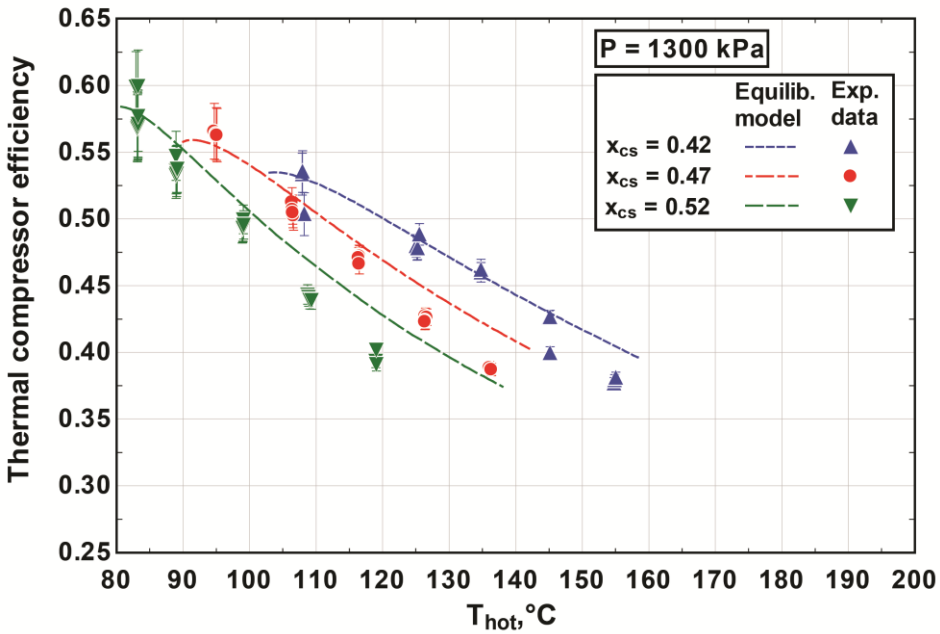

Figure 6.16: Thermal compressor efficiency at P_{high} = 1300 kPa

performance improvement. For example, if T_{hot} is held constant at 140°C, thermal compressor efficiency decreases as concentration is increased or pressure decreased. This is indicative of a greater than required grade of energy input at higher concentrations and lower pressures.

6.5.3 Assessment of the Thermal Compressor Concept

Experimental results show that performance optimization for q_{des} exists at a specific temperature, $T_{opt,I}$, as predicted by thermodynamic models. It was shown that T_{ds} is an effective process variable for the assessment of thermal compressor performance. It can be measured easily is therefore a suitable process variable for feedback control. The prediction of a desorption temperature that optimizes system level performance, i.e., *COP* has been discussed in the literature (Engler *et al.*, 1997). Minimization of q_{des} is analogous to *COP* maximization at the system level. It can be explained with increasing

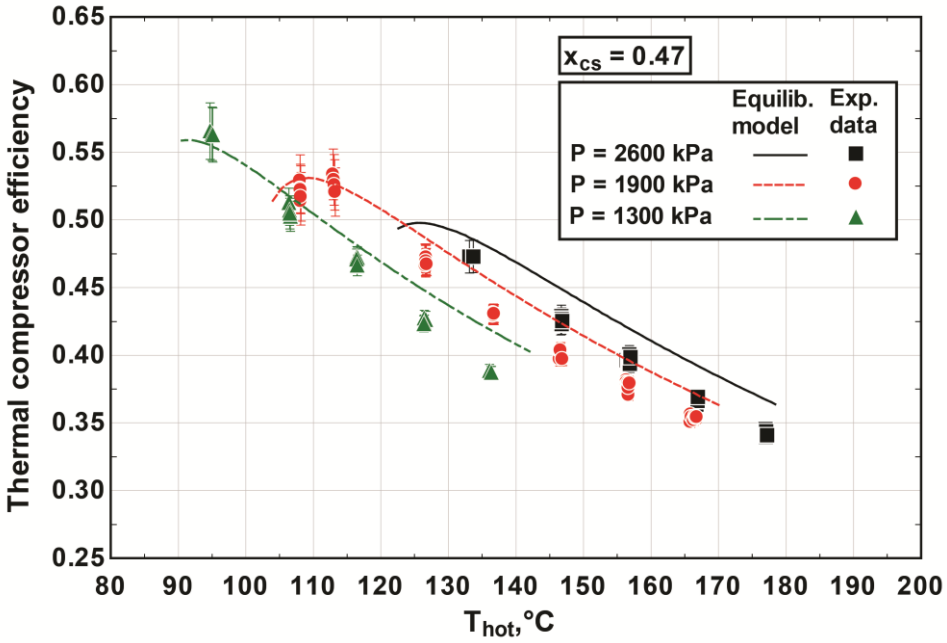

Figure 6.17: Thermal compressor efficiency at x_{cs} = 0.47

circulation ratio, as defined in Eq. 6.11, at decreasing desorption temperatures. This causes increasing sensible heat rejection through increased dilute solution mass flow.

$$CR = \frac{\dot{m}_{cs}}{\dot{m}_{ref}} \tag{6.11}$$

At temperatures greater than $T_{opt,I}$, increases in vapor temperature result in greater rectification requirements that lead to performance reduction as discussed above. Quantitative thermal compressor characterization presented here provides an intermediate level, sub-system level, approach. It is shown that factors that affect $T_{opt,I}$ can be reduced to two internal parameters, P_{high} and x_{cs}. This allows for concise characterization of optimal performance as a function of these two variables.

This study also provides experimental validation for optimal desorption temperature that has not been reported in the literature. The existence of $T_{opt,I}$ was validated and it was shown that its value can be predicted accurately and reliably through

thermodynamic equilibrium models. In addition to specific thermal compressor configuration, some system specific assumptions, refrigerant outlet purity, solution heat exchanger effectiveness, desorber vapor purification and reflux heat recovery in the rectifier, are still required for the thermodynamic model. It was shown that variation of system capacity and operation can affect desorber vapor purification, which results in relatively small discrepancies between absolute values of q_{des} and model prediction. However, generally reasonable agreement suggests that results from a thermodynamic model can be used as good estimates for q_{des}. Therefore, it can be concluded that both, $T_{opt,I}$ as well as q_{des} can be accurately characterized as functions of x_{cs} and P_{high} through modeling alone. The existence of a maximum for thermal compressor efficiency, i.e., exergetic optimization, was validated experimentally and its predictability through thermodynamic models was shown. It was also shown that thermal compressor efficiency is maximized at lower T_{ds} than minimization of q_{des}, i.e., $T_{opt,I} > T_{opt,II}$. This raises the question of what the purpose of these two different performance metrics is.

Results show that further reduction of T_{ds} below $T_{opt,II}$ causes a dramatic decrease of η_{TC}, accompanied by a dramatic increase in q_{des}. This performance degradation is due to excessive circulation ratios at low desorption temperatures. An illustration of this effect is shown in Figure 6.18. As T_{ds} approaches the saturation temperature of concentrated solution entering the desorber, *CR* values escalate. Thermodynamically, there is no justification for system operation at $T_{ds} < T_{opt,II}$. A lack of heat source temperature availability could necessitate that state. However, experimental system operation revealed that meaningful vapor generation rates at $T_{ds} < T_{opt,II}$ are limited by the capacity of the solution pump. This suggests that operation at $T_{ds} < T_{opt,II}$ is practically

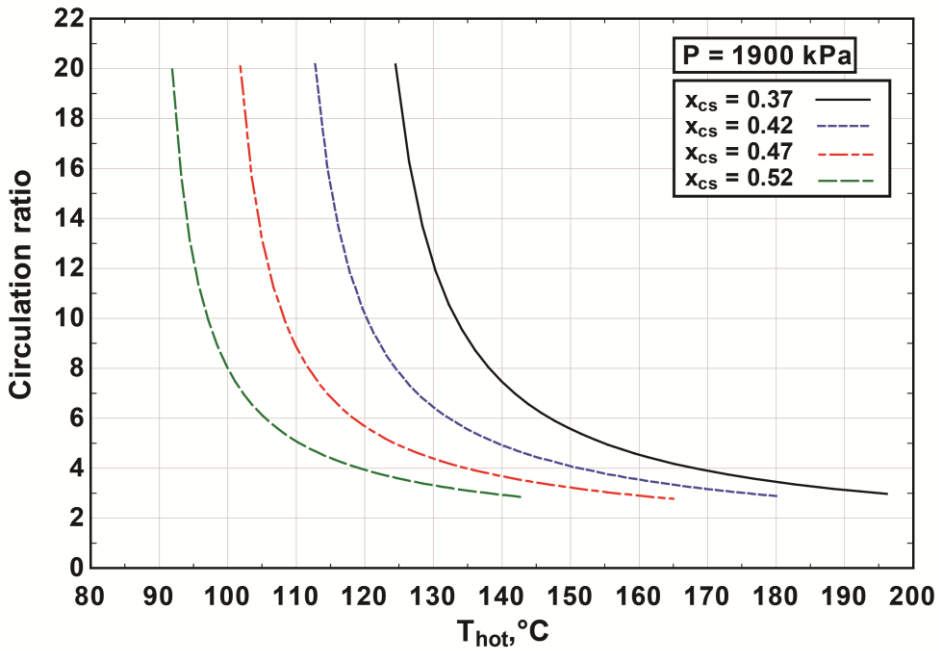

Figure 6.18: Circulation ratio vs T_{ds} for various concentrations

infeasible. Therefore, $T_{opt,II}$ is a suitable parameter for a minimum required desorption temperature. While a minimum operating temperature, or "cut-in" temperature, is mentioned in the literature, a thermodynamically justified definition has been elusive. $T_{opt,II}$ can be readily characterized as a function of x_{cs} and P_{high} with a thermodynamic model. $T_{opt,II}$ can be applied at the design stage to adequately size the solution pump and assess the viability of absorption systems for particular heat sources at specific operating conditions. In a control system, the temperature range $T_{opt,II} < T_{ds} \leq T_{opt,I}$ can be treated as the target operating range for heat source temperature control. Finally, the results for η_{TC} emphasize the true thermodynamic penalty of operating at desorption temperature greater than $T_{opt,I}$. While q_{des} increases are moderate for $T_{ds} > T_{opt,I}$, reduction in η_{TC} is much more drastic, which supports the notion of an ideal operating range, i.e., $T_{opt,II} < T_{ds} \leq T_{opt,I}$. Exergy destruction in the desorber depends strongly on the type of heat source coupling and downstream utilization of the heat source stream. Therefore, the absolute value of η_{TC}

is highly application dependent and the main quantitative merit for thermal compressor efficiency is the characterization of $T_{opt,II}$ which is not significantly affected by heat source variation.

Direct control of T_{ds} for system optimization is different from previous control strategies where desorption temperature is used as an active control variable for capacity regulation (Goyal *et al.*, 2015). Therefore, the results of this study can be considered for the development of control strategies that seek to continuously optimize system operation at all operating conditions.

6.6 Conclusions

The thermal compressor concept and figures of merit were investigated in this study. Desorption and rectification designs that are based on diabatic distillation principles and optimize thermal compressor performance were fabricated to yield highly compact, small-capacity components for ammonia-water absorption systems. Thermal compressor performance and its optimal operation were investigated over a range of conditions. Experimental results agreed well with results from the thermodynamic equilibrium model. Optimal desorption temperatures were validated for a wide range of operating conditions. These experimentally validated models could also be used to develop modules of simple algebraic equations for optimal thermal compressor control.

CHAPTER 7. HEAT AND MASS TRANSFER EXPERIMENTS

7.1 Introduction

Novel design concepts for desorbers and rectifiers in small-capacity ammonia-water absorption systems were presented in Chapter 4. These designs apply diabatic distillation principles, which facilitate thermodynamic optimization and compact component design (Chapter 3). A depiction of the microchannel design concept and the desired liquid-vapor countercurrent flow pattern is shown in Figure 7.1. The rectifier is shown in Figure 7.2, where wire gauze packing is inserted on the working fluid side to facilitate liquid-vapor contact. Both designs utilize microchannel geometries for the coupling heat source/sink. The development of a heat and mass transfer model for these components was presented in Chapter 5. The model uses hydrodynamic parameters required for heat and mass transfer modeling such as liquid-vapor interfacial area and

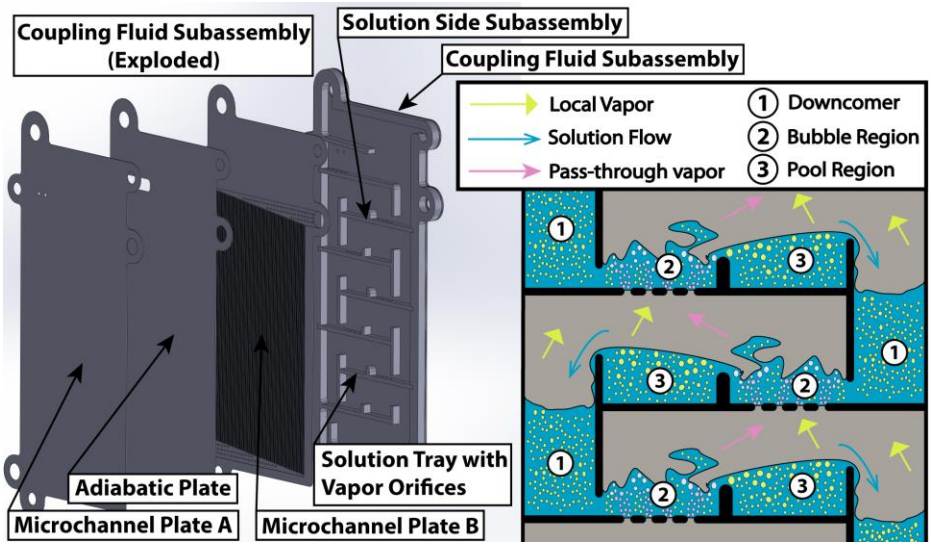

Figure 7.1: Design Concept A, component assembly (left), target flow pattern (right)

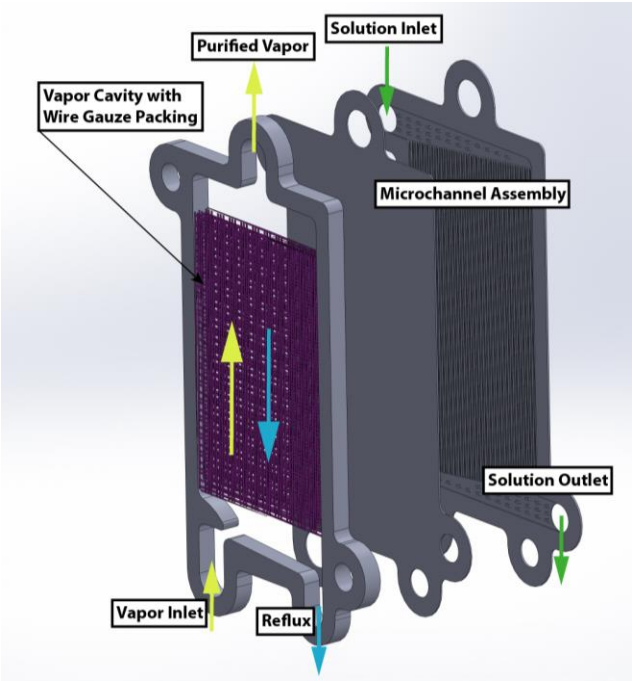

Figure 7.2: Rectifier design concept

heat transfer areas, which were reported in Chapter 4.

Component and system level performance of these designs was demonstrated experimentally in Chapter 6. That study provided a detailed description of the test facility. A schematic of the facility is shown in Figure 7.3 and a photograph is provided in Figure 7.4. In the present study, this test facility is used to heat and mass transfer characteristics of the desorber and rectifier over a range of realistic operating pressures and temperatures in detail. High side pressure, P_{high}, and concentrated solution ammonia mass fraction, x_{cs}, are effective system parameters to simulate variation of operating conditions such as condenser and absorber heat sink temperature and evaporator temperature (Chapter 6). Table 7.1 and Table 7.2 show the test matrix for this study in terms of these parameters, which spans a range of x_{cs} and P_{high} values that represent a wide range of absorption system operating conditions. Each combination of values for x_{cs}

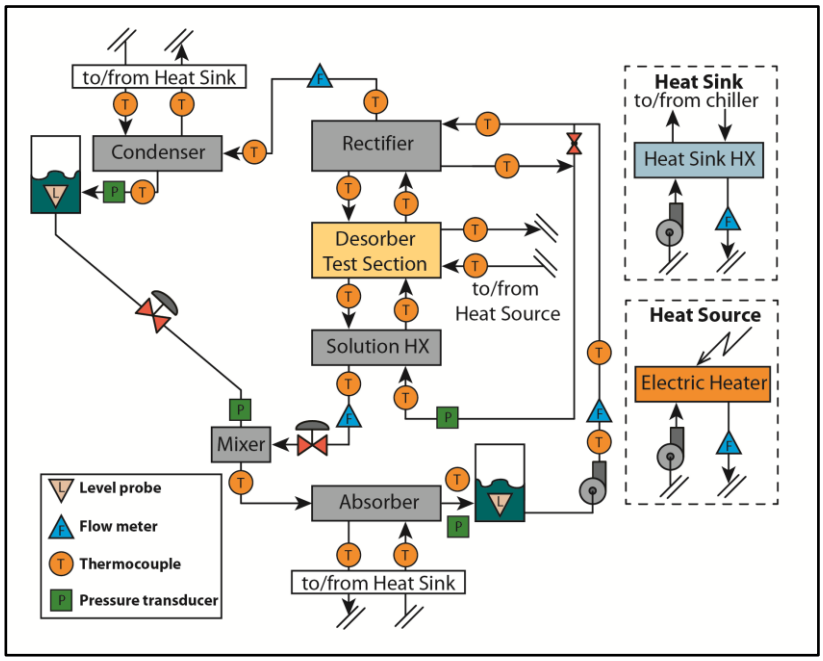

Figure 7.3: Schematic of experimental facility

and P_{high} includes a range of desorption temperatures. Here, the dilute solution temperature leaving the absorber, T_{ds}, represents desorption temperature and was identified as an effective process variable for performance optimization (Chapter 3). They showed that optimal temperature values for T_{ds} exist that optimize energetic and exergetic system performance, i.e., $T_{opt,I}$ and $T_{opt,II}$, respectively. In Test Matrix I, shown in Table 7.1, a constant concentrated solution mass flow rate of $\dot{m}_{cs}$ = 9 g s^{-1} is maintained, while

Table 7.1: Test Matrix I

Condenser pressure, P_{high}	**1300 kPa**			**1900 kPa**				**2600 kPa**		
NH_3 mass fraction, x_{cs}	**0.42**	**0.47**	**0.52**	**0.37**	**0.42**	**0.47**	**0.52**	**0.37**	**0.42**	**0.47**
$T_{ds} = T_{opt,II} - 10°C$				×	×	×	×			
$T_{ds} = T_{opt,II}$	×	×	×	×	×	×	×	×	×	×
$T_{ds} = T_{opt,I} - 10°C$	×	×	×	×	×	×	×	×	×	×
$T_{ds} = T_{opt,I}$	×	×	×	×	×	×	×	×	×	×
$T_{ds} = T_{opt,II} + 10°C$	×	×	×	×	×	×	×	×	×	×
$T_{ds} = T_{opt,II} + 20°C$	×	×	×	×	×	×	×	×	×	×

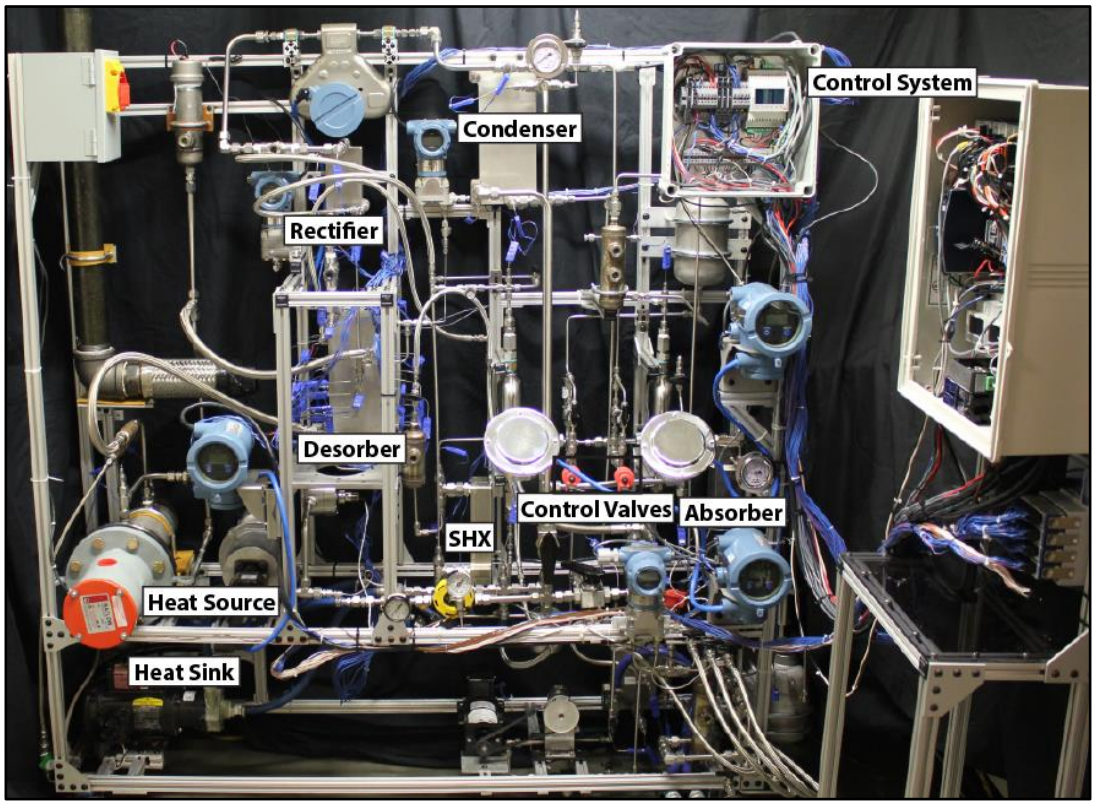

Figure 7.4: Photograph of test facility

in Test Matrix II, shown in Table 7.2, a range of solution flow rates for various values of x_{cs} is investigated. The desorption temperature for Test Matrix II is maintained at $T_{opt,I}$. For both test matrices, the desorber heat source temperature profile is maintained constant. The heat source profile is controlled with desorber heat source coupling mass flow rate. The temperature difference ratio between heat source coupling fluid and solution temperatures at the bottom and top of the desorber is defined as shown in Eq. 7.1

.

$$\Delta TR_{CF} = \frac{T_{CF,out} - T_{cs}}{T_{CF,in} - T_{ds}} \tag{7.1}$$

A constant value of ΔTR_{CF} was targeted throughout the study. This approach minimizes the effects of temperature profile variation on average heat transfer coefficients.

Table 7.2: Test Matrix II

Condenser pressure, P_{high}	1900 kPa		
NH_3 mass fraction, x_{cs}	0.42	0.47	0.52
$\dot{m}_{cs}$ = 11.5 g s^{-1}	×	×	×
$\dot{m}_{cs}$ = 9 g s^{-1}	×	×	×
$\dot{m}_{cs}$ = 6.5 g s^{-1}	×	×	×
$\dot{m}_{cs}$ = 4 g s^{-1}	×	×	×

The results from these experiments are used to obtain heat and mass transfer characteristics of the desorber and rectifier, which are compared with corresponding predictions from the literature. In addition, correlations for liquid mass transfer coefficient and binary mixture correction factor are developed to improve heat and mass transfer predictions for the geometries under consideration. Component level results, e.g., overall heat transfer coefficient and internal component purification efficiency, are discussed and their utility for application at the cycle design stage and to dynamic system modeling are discussed.

7.2 Data Reduction

A detailed description of the experimental facility was provided in Chapter 6. Mass flow rates of concentrated solution entering the desorber, dilute solution leaving the desorber, and vapor leaving the rectifier are measured directly. However, the last measurement is only used during testing to validate steady state conditions by ensuring that the difference in solution mass flow rates equals vapor leaving the rectifier, thereby minimizing uncertainties in the calculated results.

7.2.1 Concentrated Solution Ammonia Mass Fraction

Direct measurement of x_{cs} with low uncertainty is challenging and impractical. The working fluid inventory of a small capacity system is relatively small, and repeated

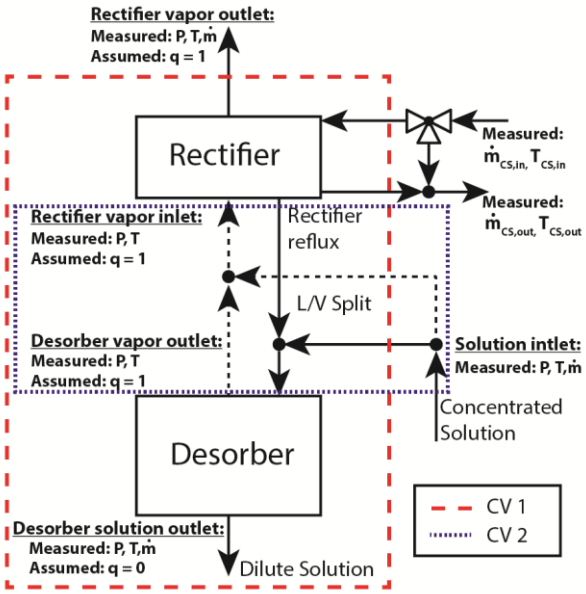

Figure 7.5: Control volumes used for data reduction

sampling of solution leads to inadvertent charge adjustments, and could also induce undue transients. Moreover, a separate process is required to determine x_{cs} from a sample. This prevents fast adjustments of temperatures and flow rates based on x_{cs} feedback to meet target values. A more practical approach is a mass and species balance for a control volume (CV) containing the desorber and rectifier as shown in . Here, x_{cs} can be readily determined if saturated vapor and liquid states are assumed for rectifier vapor outlet and desorber solution outlet, respectively.

CV 2 in Figure 7.5 is used to determine mass flow rates between desorber and rectifier. The x_{cs} value determined above is used to establish the state of solution entering the desorber/rectifier control volume. Typically, a recuperative solution heat exchanger (SHX) is used for heat recovery from the dilute solution leaving the desorber to the concentrated solution. At some operating conditions, this could result in a two-phase state of solution entering the desorber. This vapor quality can be determined by accounting for

the liquid-vapor split at the inlet of the desorber, where vapor produced in the desorber is combined with vapor entering with concentrated solution. While reflux flow rates from the rectifier are small, they cannot be neglected as noticeable errors in mass balance and transfer coefficients would be incurred. Therefore, rectifier reflux is included by combining it with liquid solution entering the desorber. The rectifier vapor outlet state is fully defined and the rectifier inlet state can be determined by applying the saturated vapor assumption in combination with locally measured temperature and pressure. With rectifier vapor inlet and outlet states fully defined, reflux concentration can be estimated using the average concentration of saturated liquid at rectifier inlet and outlet temperatures. This assumption linearly averages reflux generation along the length of rectifier, which provides computational simplicity and a reasonable approximation based on segmented modeling results in Chapter 5.

Eqs. 7.2 through 7.5 list the mass and species balance for CV 2 in Figure 7.5. Additionally, mass and species balance for the rectifier working fluid side are added to the equation set with Eqs. 7.6 and 7.7 to match the number of unknown variables. Simultaneous solution of these conservation equations provides the remaining mass flow rates needed to exactly determine all liquid and vapor flow rates for the desorber and rectifier.

$$\dot{m}_{L,des,in} = \dot{m}_{cs}\left(1-q_{cs}\right)+\dot{m}_{reflux} \tag{7.2}$$

$$\dot{m}_{L,des,in}x_{L,des,in} = \dot{m}_{cs}x_{cs,L}\left(1-q_{cs}\right)+\dot{m}_{reflux}x_{reflux} \tag{7.3}$$

$$\dot{m}_{V,rect,in} = \dot{m}_{cs}q_{cs}+\dot{m}_{V,des,out} \tag{7.4}$$

$$\dot{m}_{V,rect,in}x_{V,rect,in} = \dot{m}_{cs}x_{cs,V}q_{cs}+\dot{m}_{V,des,out}x_{V,des,out} \tag{7.5}$$

$$\dot{m}_{V,rect,out} = \dot{m}_{V,rect,in} - \dot{m}_{reflux} \tag{7.6}$$

$$\dot{m}_{V,rect,out} x_{V,rect,out} = \dot{m}_{V,rect,in} x_{V,rect,in} - \dot{m}_{reflux} x_{reflux} \tag{7.7}$$

7.2.2 Heat Transfer Coefficients

Working fluid heat transfer coefficients are determined through a heat transfer resistance network as shown in Figure 7.6 for the desorber. Of primary interest is the solution heat transfer coefficient during binary mixture boiling, α_L. Total system heat input, $\dot{Q}_{CF}$, is determined from the measured coupling fluid flow rate and its temperature change. Accounting for heat losses as described in Chapter 6, a net desorber heat input is determined as shown in Eq. 7.8.

$$\dot{Q}_{des} = \dot{Q}_{CF} - \dot{Q}_{loss,des} \tag{7.8}$$

This value is used to determine the component heat transfer conductance, UA_{des}, as shown in Eq. 7.9.

$$\dot{Q}_{des} = UA_{des} \cdot LMTD \tag{7.9}$$

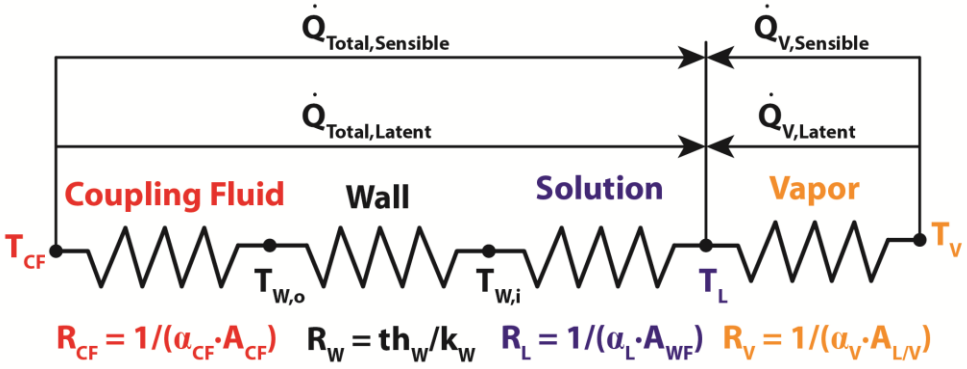

Figure 7.6: Desorber thermal resistance network

This provides a value for the total component thermal resistance, R_{des} as shown in Eq. 7.10, where all temperature are measured.

$$\frac{1}{R_{des}} = UA_{des} \tag{7.10}$$

Given the resistance network shown in Figure 7.6 the contribution of the solution-side heat transfer resistance to the overall resistance is determined using Eq. 7.11.

$$R_L = \frac{LMTD_{des}}{\dot{Q}_{des}} - R_{CF} - R_{wall} \tag{7.11}$$

Finally, α_L can be determined using Eq. 7.12.

$$\alpha_L = \frac{1}{R_L \cdot A_L} \tag{7.12}$$

Given the geometries and hydrodynamic behavior of the tested desorber design, the value of the solution-side heat transfer area, A_L, is variable and depends on liquid and vapor flow rates. A hydrodynamic investigation of these geometries was conducted as shown in Chapter 4. Air-water flow visualization experiments were conducted to obtain estimates for hydrodynamic parameters relevant to heat and mass transfer, including liquid heat transfer area as well as liquid-vapor interfacial area for the range for volumetric liquid and vapor flow rates encountered in this study. Moreover, each desorber tray is bonded to heat source plates. This provides additional active heat transfer area of the tray itself, which is incorporated in the overall area calculation as an extended surface idealized as rectangular fin (Mills, 1995).

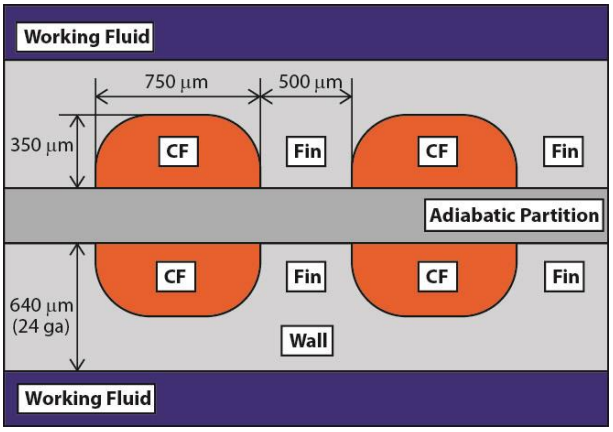

Figure 7.7: Cross-section of desorber microchannel geometry

Wall and heat source coupling fluid resistances, R_{CF} and R_{wall}, are determined using the methodology of Nagavarapu and Garimella (2011), in which microchannel geometries of the coupling fluid, shown in Figure 7.7 are modeled as a fin array. The approach is modified for semicircular shapes with an adiabatic base, with non-negligible thermal entrance lengths (Hong and Bergles, 1976) due to the relatively high Prandtl numbers (Pr = 40-60)of the Paratherm^{TM} NF coupling fluid. Typical coupling fluid convection coefficients in this study are approximately 1200 to 1300 W m^{-2} K^{-1}. Figure 7.7 shows design dimensions of the microchannel side of the desorber.

Component level heat transfer parameters are also obtained to facilitate incorporation of this design in cycle models as well as dynamic system modeling efforts. Overall heat transfer conductance values, UA_{des}, are used to determine an overall heat transfer coefficient, U. A nominal area value, i.e., the sum of the face area of each heated wall, is used to determine U.

7.2.3 Mass Transfer Coefficients

Non-equilibrium effects cause concentration gradients from the liquid-vapor interface to the vapor and liquid bulk. Liquid mass transfer resistance causes a local depression of the concentration of the more volatile component leading to an increase in saturation temperature at the liquid-vapor interface. The resulting reduction in heat transfer coefficient is commonly addressed with a correction factor applied to the ideal pooling coefficient (Táboas *et al.*, 2007). The ideal pool boiling coefficient can be calculated as the molar average of pure substance coefficients and can be compared with the experimentally determined liquid heat transfer coefficient obtained from Eq. 7.12. This ratio, i.e., the binary mixture correction factor can be compared with correlations from the literature. The non-equilibrium framework presented by Price and Bell (1974) based on the work of Colburn and Drew (1937) is used to deduce mass transfer coefficients, β_L, from the data. The total desorption flux can be expressed as shown in Eq. 7.13 where $\tilde{z}$ is the molar concentration of the desorption flux as defined in Eq. 7.14 while $\tilde{x}_{L,int}$ and $\tilde{x}_{L,bulk}$ are liquid molar concentration at liquid-vapor interface and in the bulk liquid, respectively.

$$\dot{n}_T = \beta_L \frac{\rho_L}{M_L}\left(\frac{\tilde{z}-\tilde{x}_{L,int}}{\tilde{z}-\tilde{x}_{L,bulk}}\right) \tag{7.13}$$

$$\tilde{z} = \frac{\dot{n}_{NH_3}}{\dot{n}_T} \tag{7.14}$$

The bulk concentration is the average of inlet and outlet liquid concentrations. Liquid interface concentration is determined by assuming saturation conditions at average liquid

inlet and outlet temperatures. Similarly, vapor conditions at the interface are determined by applying the saturated vapor assumption at the average liquid temperature. The interface conditions are used to determine the desorption flux concentration as follows. Following the procedure by Hewitt *et al.* (1994), Eqs. 7.15 and 7.16 are used to obtain $\tilde{z}$, the ammonia mole fraction of the desorption flux.

$$h_{latent} = h_{V,int} - h_{L,int} \tag{7.15}$$

$$h_{latent} = z \cdot h_{latent,NH_3} + (1-z) \cdot h_{latent,H_2O} \tag{7.16}$$

The total mass flow rate of vapor generated in the desorber was determined using the control volume analysis in Figure 7.5. This value is now applied to determine the total molar flux across the liquid-vapor interface as shown in Eq. 7.17.

$$\dot{n}_T \cdot A_{int} = \frac{\dot{m}_{V,out}}{\left(\tilde{z} \cdot M_{H_2O} + (1-\tilde{z}) M_{NH_3}\right)} \tag{7.17}$$

Thus, the liquid mass transfer coefficient can be determined using Eq. 7.13.

Similarly, the mass transfer coefficient is evaluated using Eq. 7.18 in combination with results from the equation set above.

$$\dot{n}_T = \beta_V C_T \left(\frac{\tilde{z} - \tilde{x}_{V,int}}{\tilde{z} - \tilde{x}_{V,bulk}} \right) \tag{7.18}$$

Here, C_T is the total vapor molar concentration. Vapor conditions at the liquid-vapor interface were determined above and vapor bulk conditions are determined through the saturated vapor state at an average vapor temperature in the desorber. Vapor outlet temperature is measured directly and the highest vapor temperature in the desorber is assumed to be that of dilute solution leaving the desorber. This is a justifiable assumption

as vapor generation from solution occurs continuously throughout the component. Finally, a value for interfacial liquid-vapor area is required in Eq. 7.17. This value is variable and depends on liquid and vapor flow rates. As discussed above, results provided in Chapter 4 are used as estimates for liquid-vapor interfacial area.

Mass transfer coefficients determine the internal vapor purification performance of the desorber, a key objective of this component. Overall vapor purification efficiency with respect to the hottest, least pure vapor generated can be defined as shown in Eq. 7.19 where $x_{V,out,des}$ is the ammonia mass fraction of saturated vapor at the temperature of dilute solution leaving the desorber.

$$\eta_{pur} = \frac{x_{V,out,des} - x_{V,in,des}}{x^{*}_{V,out,des} - x_{V,in,des}} \tag{7.19}$$

$x^{*}_{V,out,des}$ is the ammonia mass fraction of saturated vapor at the temperature of concentrated solution entering the desorber, i.e., the highest possible refrigerant concentration of vapor leaving the desorber. This component level result can be calculated from the data. Purification purity and overall heat transfer coefficient, *U,* provide effective component performance results that can be readily applied for high level design, cycle modeling and dynamic system modeling.

7.2.4 Rectifier Heat and Mass Transfer

Reliable estimates for liquid-vapor interfacial area in the rectifier are not feasible given the relatively very low mass flow rates of liquid reflux generated. Therefore, the non-equilibrium framework used for the desorber cannot be used for the rectifier. The equilibrium method of Silver (1947) as further developed by Bell and Ghaly (1972), commonly referred to as the Silver-Bell-Ghaly (SBG) method is used. This analysis is used to compare working fluid side sensible heat transfer coefficient with suitable correlations in the literature and to investigate the effect of mass transfer on overall rectifier heat transfer coefficients.

As shown in Figure 7.5, the rectifier heat sink is concentrated solution that is split in a bypass control arrangement to achieve target vapor outlet conditions. Rectifier heat duty is established by conducting an energy balance of the working fluid side given the information determined above. Alternatively, the enthalpy difference on the solution side can be established with available measurements and the value of x_{cs} determined above. Accounting for heat losses from the rectifier and bypass lines, both values were determined to be in good agreement (less than 5% error) for all test points. A *UA-LMTD* analysis with a resistance network analogous to Eq. 7.11 is used for rectifier microchannel geometries. The rectifier working fluid side heat transfer coefficient, α_{rect} , is then determined based on an ideal condensation heat transfer coefficient and a sensible vapor heat transfer coefficient as shown in Eq. 7.20.

$$\frac{1}{\alpha_{rect}} = \frac{1}{\alpha_{cond}} + \frac{Z_{SBG}}{\alpha_{sens}} \qquad 7.20$$

According to the SBG methodology, the Z_{SBG} term accounts for the contribution of sensible heat transfer to the overall heat transfer resistance. Given that partial condensation of this zeotropic binary mixture is accompanied by a reduction in temperature, this approach approximates the effect of mass transfer on overall heat transfer resistance by considering the proportion of sensible heat duty to overall heat duty. The weighting factor Z_{SBG} is defined as shown in Eq. 7.21.

$$Z_{SBG} = \frac{\dot{Q}_{sens}}{\dot{Q}_{total}} \tag{7.21}$$

The ideal condensation coefficient is determined using the correlation of (Rose *et al.* (1999)) in Eq. 7.22.

$$\alpha_{ideal} = \bar{T}_{V,rect}^{0.8}\left[5 + 0.63\left(\bar{T}_{V,rect} - \bar{T}_{wall,rect}\right)\right] \tag{7.22}$$

It should be noted that the choice of ideal condensation correlation has little impact on the overall result if the second term on the right hand side of Eq. 7.20 is dominant. Finally, the sensible vapor heat duty calculated as shown in Eq. 7.23 is used to obtain the sensible vapor heat transfer coefficient.

$$\dot{Q}_{sens} = \bar{\dot{m}}_{V,rect}\bar{c}_p\left(T_{V,rect,in} - T_{V,rect,out}\right) \tag{7.23}$$

7.3 Results

These data were analyzed as discussed above on the *Engineering Equation Solver* (EES) software platform by Klein (2015). Data for the design operating point are first compared with model predictions. The development of a heat and mass transfer model for

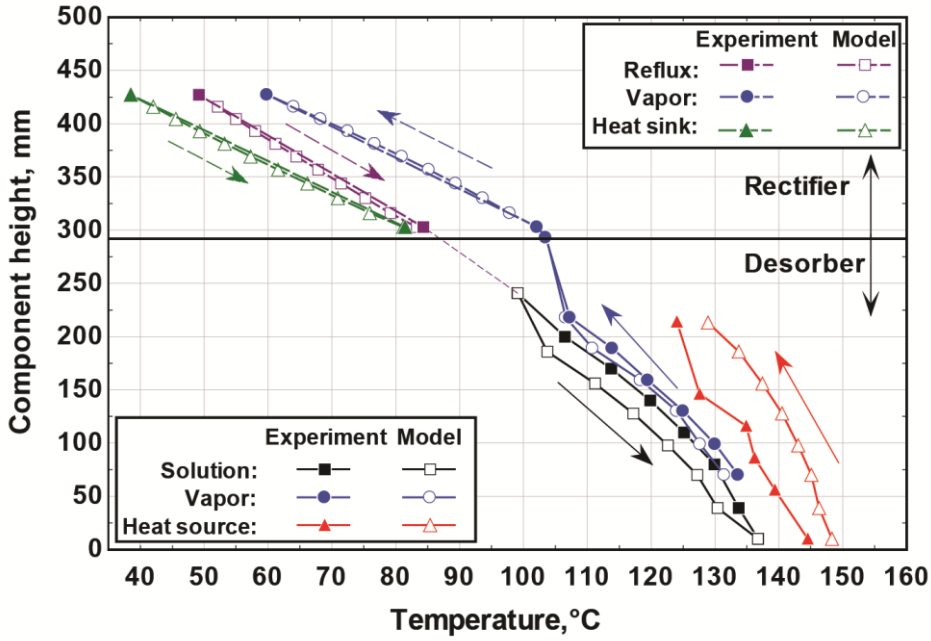

Figure 7.8: Temperature profile comparison of experiment and model

the desorber and rectifier designs investigated in this study was presented in Chapter 5. Concentrated solution inlet conditions as well as rectifier vapor outlet and dilute solution temperatures, and heat source coupling fluid mass flow rate are provided as inputs to the model. For a case with $P_{high} = 1900\,\text{kPa}$, $x_{cs} = 0.47$ and $\dot{m}_{cs} = 11.5\,\text{g s}^{-1}$, Figure 7.8 shows model and experimental temperature profiles for the desorber and rectifier. Measured solution temperatures are higher than the model predictions in the upper region of the desorber. The subsequent temperature increase in the center section of the desorber is similar for model and experiment. However, a greater increase in solution temperature is predicted by the model in the bottom segment of the desorber. The solution inlet region contains an adiabatic inlet tray. The model assumes that no external heat transfer occurs in this tray; however, this tray is likely to experience some longitudinal conduction from the heat source stream which exits the desorber just below the inlet tray. Also,

hydrodynamic behavior in the component could be different from the assumptions in the model. Specifically, large-than-expected liquid-vapor interfacial area causes increased heat recovery from the rising vapor stream to the solution, increasing its temperature. The vapor temperature profile in that region, i.e., a relatively large decrease in vapor temperature, supports this explanation. Favorable hydrodynamics also leads to a larger solution heat transfer wall area.

Vapor temperatures are very close to model predictions but solution-vapor temperature differences are noticeably smaller in the experiments. This could be explained based on the measurement technique and tray geometries. Vigorous, liquid-vapor interaction causes the formation of a bubble region in each tray. Thermocouples were positioned in vapor-only regions based on flow visualization investigations for this desorber design (Chapter 4). However, given the relatively small tray geometries, a slight increase in the bubble region size could cause intermittent contact of the thermocouple with the solution and could thereby reduce the measured temperature. Ultimately, vapor temperature leaving the desorber is of primary interest, irrespective of component internal solution and vapor temperatures. Vapor exit temperatures determine rectifier load and overall system performance. Based on these results, model predictions are very close, i.e., within 1°C, to the measured vapor temperature leaving the desorber.

A noticeable difference can be seen in the heat source temperature profile. Experimental heat source temperature values entering and leaving the desorber are approximately 4°C lower than model predictions. This is indicative of an overall lower heat transfer resistance, requiring lower *LMTD* values for similar heat duties. The lower heat transfer resistance is likely due to a greater solution-side heat transfer coefficient

compared to model predictions, which used an ideal heat transfer coefficient based on Mostinski (1963) with a binary mixture correction factor recommended by Táboas *et al.* (2007). The experimental heat source temperature profile is not as smooth as the model prediction. This is likely due to some measurement inconsistencies. Repeatable thermocouple insertion depth in microscale geometries is challenging. Particularly, with a laminar temperature profile present in the microchannel, these variations result in measurement variations. However, the inlet and outlet temperatures are measured in a larger diameter line for the entire heat source mass flow stream. This ensures accurate inlet and outlet heat source temperature measurements.

Rectifier temperature profiles are in very good agreement, which is indicative of an accurate model. A more detailed investigation of heat and mass transfer coefficients on the working fluid side provides better insight into the entire data set to generalize and explain the results obtained in this study.

7.3.1 Desorber Heat Transfer Results

Overall heat transfer conductance results are shown for the entire data set in Figure 7.9. Uncertainties are consistently very low, with values of less than ± 20 W m^{-2} K^{-1} or ±2%. The source of uncertainty is primarily solution and heat source coupling fluid outlet temperatures. A clear difference in the trends for the two test matrices is seen. Test Matrix I results show no clear sensitivity of overall heat transfer conductance to heat flux, whereas a clear positive correlation is observed for Test Matrix II. A very similar trend is observed, indicating that variations in overall heat transfer coefficient are primarily caused by variations in solution-side heat transfer coefficient.

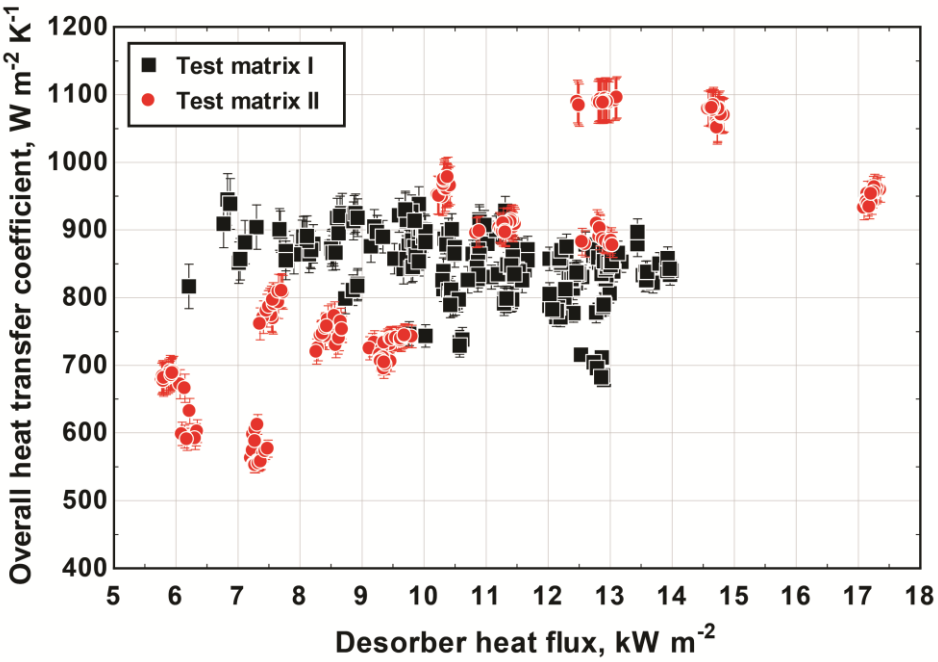

Figure 7.9: Overall desorber heat transfer coefficient vs heat flux

It is expected that increasing heat flux causes an increase in pool boiling heat transfer coefficient (Ghiaasiaan, 2007). Therefore, the invariance of overall conductance with heat flux for Test Matrix I is explored in more detail by analyzing other factors that influence solution-side heat transfer coefficient. Ammonia mass fraction also strongly affects pool boiling heat transfer coefficients (Táboas *et al.*, 2007). Values of x_{cs} and x_{ds} are varied in this study. For Test Matrix I, the average solution ammonia mass fraction in the desorber, $x_{sol} = \frac{1}{2}\left(x_{cs} + x_{ds}\right)$, decreases as T_{ds} is increased. As T_{ds} is increased, heat flux increases, given that $\dot{m}_{cs}$ is maintained at a constant value. An increase in solution heat transfer coefficient is expected with an increase in heat flux. However, relatively constant heat transfer coefficients are observed. This suggests that average solution ammonia mass fraction and heat flux are competing factors that result in relatively constant solution heat transfer coefficients. Specifically, for the range of x_{sol} values investigated in this study

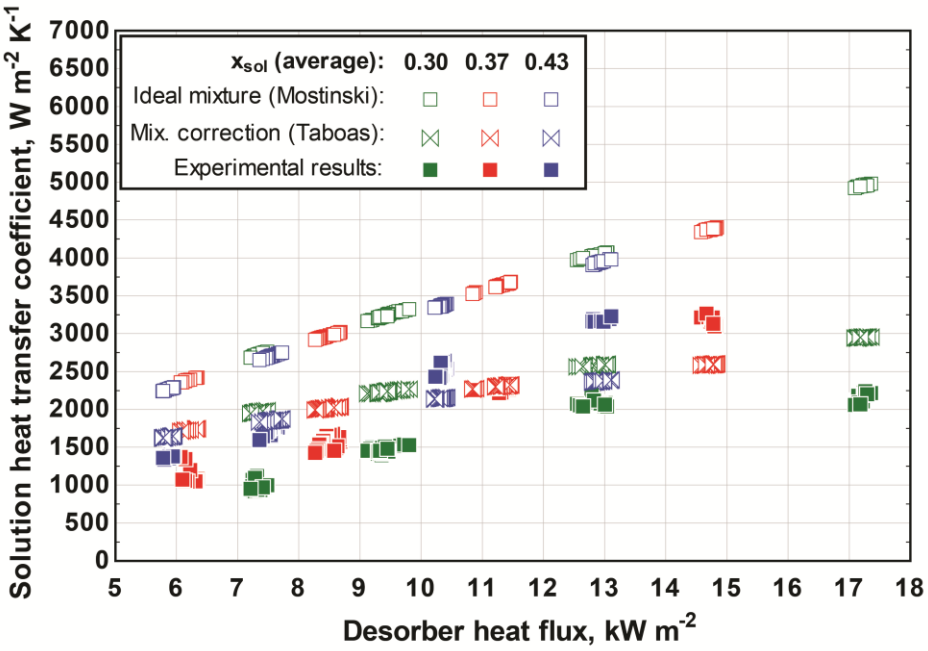

Figure 7.10: Solution heat transfer coefficient comparison vs heat flux for test matrix II

($0.22 < x_{sol} < 0.45$), a decrease in ammonia mass fraction results in a negative effect on heat transfer coefficients.

In Test Matrix II, on the other hand, T_{ds} is maintained constant while $\dot{m}_{cs}$ is varied for a particular value of x_{cs}. Therefore, heat flux is controlled directly and vapor generation rates vary proportionally to heat flux. Hence, the positive trend of α_L with heat flux is consistent with what is expected from typical pool boiling correlations. Figure 7.10 shows the variation of α_L with heat flux for three different values of x_{cs} investigated in Test Matrix II. A two-fold trend can be discerned: increase in α_L with increasing heat flux, as well as increasing values of x_{cs}.

Comparison of experimental solution heat transfer coefficients with the literature provides guidance for the selection of appropriate correlations for the design of the components investigated in this study. Results shown in Figure 7.10 include ideal heat

transfer coefficients for experimental heat flux values. Here, the ideal heat transfer coefficient is the molar average of pure component pool boiling coefficients at the same temperature and pressure as shown in Eq. 7.24.

$$\alpha_{ideal} = \left[\frac{\tilde{x}_{sol}}{\alpha_{NH_3}} + \frac{1-\tilde{x}_{sol}}{\alpha_{H_2O}} \right]^{-1} \tag{7.24}$$

The pool boiling correlation by Mostinski (1963) is applied based on the recommendation by Táboas *et al.* (2007). As expected, experimental results are lower than ideal pool boiling values. A binary mixture correction coefficient can then be applied to the ideal heat transfer coefficient to account for the effect of mass transfer during boiling as shown in Eq. 7.25.

$$\alpha_L = \frac{\alpha_{ideal}}{(1+K)^A} \tag{7.25}$$

Táboas *et al.* (2007) also provide a correction factor correlation based on results from the literature. Figure 7.10 shows reasonable agreement between their correlation and experimental results from this study. While good agreement between experimental results and the predictions of Táboas *et al.* (2007) is also shown for Test Matrix I in Figure 7.11, this comparison also reveals a different effect of x_{sol}. Instead of the positive effect of increasing x_{sol} values on heat transfer coefficient, Táboas *et al.* (2007) predict the opposite trend.

The comparison with the literature is extended in Table 7.3 where various combinations of pool boiling and binary mixture correction factors are applied to the entire experimental dataset. Significant variation in the agreement between experimental

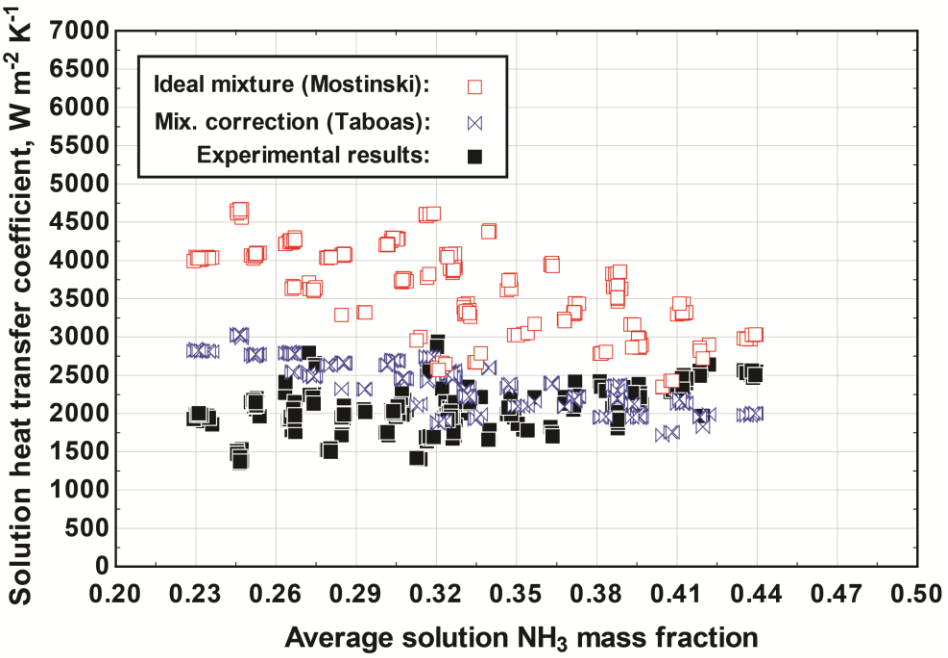

Figure 7.11: Solution heat transfer coefficient comparison vs average ammonia mass fraction for test matrix I

results and correlations from the literature is seen, suggesting that there is a strong need for further understanding of binary mixture boiling in general and for the ammonia-water pair specifically. This comparison also supports the results of Táboas *et al.* (2007), who proposed a binary mixture correction correlation in combination with the pool boiling correlation by Mostinski (1963). The binary mixture correction coefficient by Thome and Shakir (1987) in combination with the pool boiling correlation of either Mostinski (1963) or Gorenflo (1993) also perform relatively well in predicting the experimental results from the present study.

7.3.2 Mass Transfer Results

Experimentally determined liquid mass transfer coefficients are presented and compared with values determined through the heat and mass transfer analogy as well as with two correlations from the literature. The first approach, the heat and mass transfer

Table 7.3: Average deviation (*AD*) and absolute average deviation (*AAD*) between experimental results and literature

Pool boiling correlations (columns) vs. binary mixture correction (rows)	Mostinski (1963)	Gorenflo (1993)	Stephan and Abdelsalam (1980)
Táboas *et al.* (2007)	**AD = -10.6% AAD = 22.7%**	**AD = -23.6% AAD = 26.1%**	**AD = 14.7% AAD = 32.5%**
Stephan and Körner (1969)	**AD = 115.3% AAD = 115.3%**	**AD = 26.5% AAD = 41.8%**	**AD = 212% AAD = 212%**
Schlünder (1982)	**AD = 50.1% AAD = 51.8%**	**AD = 36.5% AAD = 39.2%**	**AD = 77.0% AAD = 77.9%**
Thome and Shakir (1987)	**AD = 5.9% AAD = 24.3%**	**AD = -7.6% AAD = 22.8%**	**AD = 32.8% AAD = 40.6%**

analogy shown in Eq. 7.26, is used with experimental solution heat transfer results to determine the mass transfer counterpart.

$$\frac{Sh_i}{Nu_i} = \left(\frac{Sc_i}{Pr_i} \right) \tag{7.26}$$

The two correlations selected for comparison are Calderbank and Moo-Young (1961) and Akita and Yoshida (1974). The former was developed for several designs of liquid-vapor agitators and contactors in chemical process engineering. The latter was specifically determined for bubble column mass transfer. Given the design of this desorber component, the target application for both correlations makes them suitable for comparison with the results from this study.

Figure 7.12 shows sensitivity of these results to liquid Reynolds number. Both correlations from the literature are in strong agreement with each other and with large portions of experimental data. A consistent positive trend with Reynolds number is shown. But correlations predict a small liquid mass transfer decrease with increased average solution concentration. Consequently, both correlations somewhat under predict liquid mass transfer at higher average ammonia mass fraction. Nevertheless, both

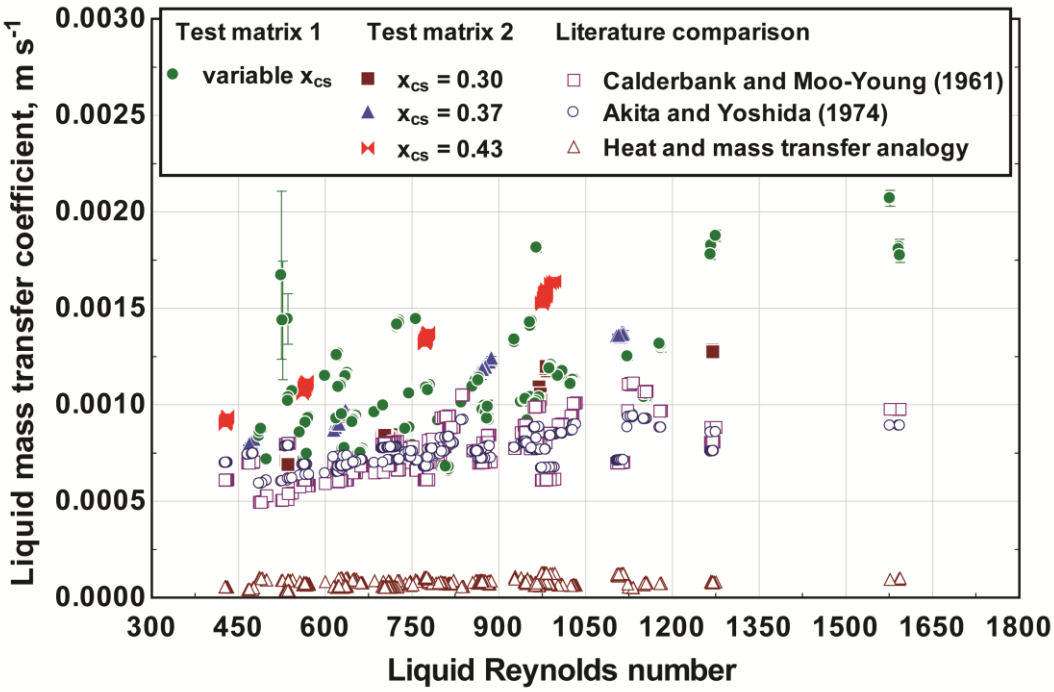

Figure 7.12: Liquid mass transfer coefficient versus liquid Reynolds number

correlations can be recommended to provide somewhat conservative design guidance for this desorber design. Results for the heat and mass transfer analogy under predict experimental liquid mass transfer significantly and cannot be recommended for component design. The discrepancy can be explained by vigorous liquid-vapor interaction in the bubble region of the tray that facilitates liquid mass transfer. The analogy to a less agitated liquid pool cannot be made. Moreover, typical values for liquid Prandtl number, *Pr*, range between 0.7-0.9 while typical Schmidt numbers, *Sc*, range between 9-10. The large difference between *Pr* and *Sc* may lead to deviations from the heat and mass transfer analogy. This contributes to the large difference between experimentally determined liquid mass transfer coefficients and predictions using the heat and mass transfer analogy.

Vapor mass transfer results are compared with the literature in Figure 7.13. Here, the correlation by Onda *et al.* (1968) was developed for packed bed liquid-vapor contractors, which is similar to the present bubble tray geometry. Colombet *et al.* (2013) provide results of a numerical investigation of bubble internal heat and mass transfer and recommend a Sherwood number value of 18 for the conditions encountered in this study. Vapor mass transfer predictions by Colombet *et al.* (2013) are generally lower than those by Onda *et al.* (1968). Experimental results for x_{cs} = 0.30 in test matrix II show excellent agreement with Onda *et al.* (1968). Deviation from experimental results occurs increasingly as x_{cs} is increased, with greater mass transfer performance observed experimentally in this study. Better than predicted vapor mass transfer performance is likely due to specific hydrodynamics of liquid-vapor interaction for the geometries investigated.

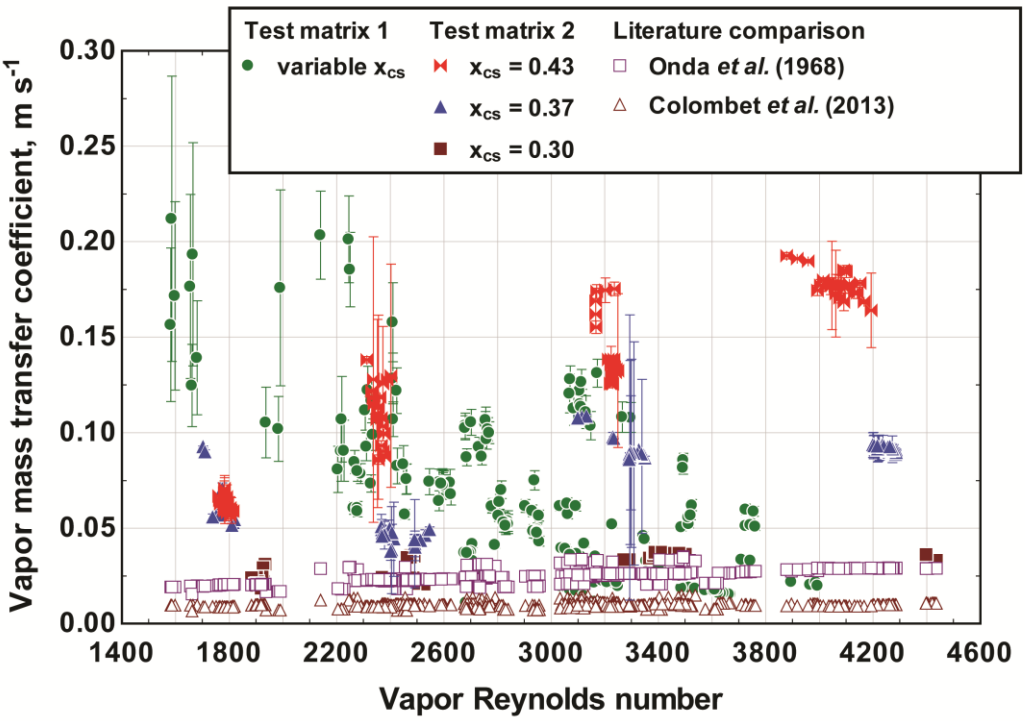

Figure 7.13: Vapor mass transfer coefficient versus vapor Reynolds number

Finally, results for overall desorber vapor purification efficiency as defined in Eq. 7.19 were evaluated. Experimental values for this efficiency are relatively constant and fall largely between 0.90 to 0.94. These values are recommended as component level estimates for η_{pur}.

7.4 Proposed Correlation

Comparison of experimental results with the literature showed relatively good agreement for solution heat transfer coefficient and reasonable agreement for mass transfer coefficients. Further improvement of predictive accuracy of heat and mass transfer performance can be achieved with a new correlation for the binary mixture correction factor. The ideal pool boiling correlation by Mostinski (1963) is used to develop a binary mixture heat transfer correction, *K*, as shown in Eq. 7.25. Several correlations are in the format shown in Eq. 7.27 (Thome and Shakir, 1987; Fujita and Tsutsui, 1997; Inoue *et al.*, 1998).

$$K = \frac{\alpha_{ideal}}{q''}\left(1 - exp\left(\Lambda \cdot q''\right)\right)\Delta T_{glide} \qquad 7.27$$

Here, the temperature glide is the difference in bubble- and dew-point temperatures. The value of Λ is either an empirical constant (Inoue *et al.*, 1998), a combination of thermodynamic and transport properties (Thome and Shakir, 1987) or a combination of both (Fujita and Tsutsui, 1997). An inverse dependence of Λ on the liquid mass transfer coefficient is included in most correlations available in the literature. However, a fixed value is assumed for most, e.g., Thome and Shakir (1987). Based on the somewhat stronger variation of β_L observed in this study, the liquid mass transfer

coefficient can be correlated to Re_L and x_{sol} as shown in the results of a regression analysis in Eq. 7.28.

$$\beta_L = 0.471 \cdot Re_L \cdot x_{sol} \qquad 7.28$$

Figure 7.14 shows good agreement between values predicted with this expression and the data: *AD* and *AAD* values are 3.5% and 11.1%, respectively, with 94.6% of predicted values falling within ±25% of experimental results. The proportional dependence of β_L on Re_L and x_{sol} found in Eq. 7.28 is used in combination with the inverse dependence of Λ on β_L commonly applied in the literature to develop and empirical correlation for Λ. The resulting expression is shown in Eq. 7.29 and its application with Eq. 7.27 allows for the determination of a binary mixture correction factor that implicitly accounts for the variation of liquid mass transfer.

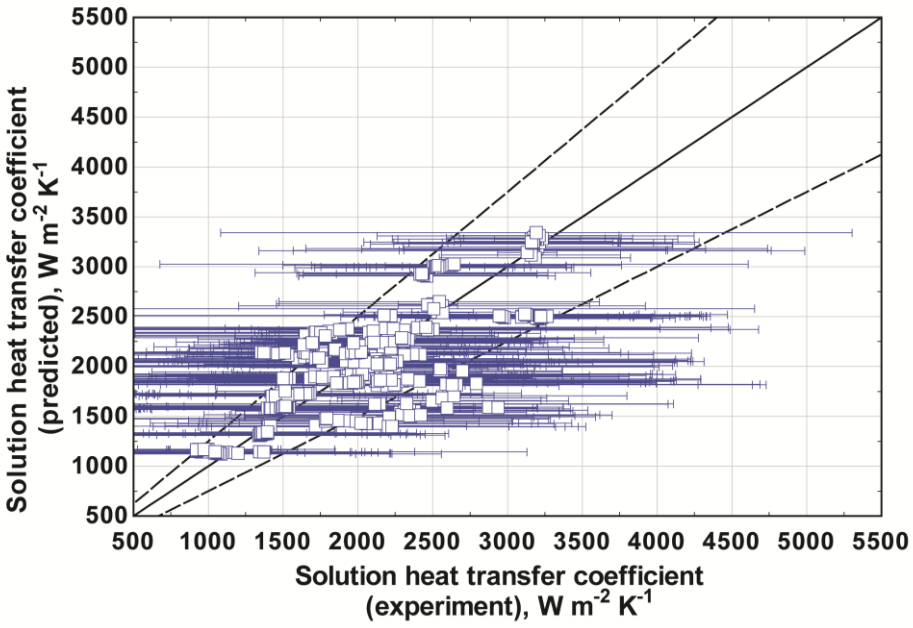

Figure 7.14: Binary fluid mixture boiling heat transfer coefficients

$$\Lambda = -7.28\times10^{-7} + \frac{1.62\times10^{-2}}{Re_L} - \frac{2.03\times10^{-6}}{x_{sol}} + \frac{1.05\times10^{-3}}{Re_L\, x_{sol}^2} - \frac{1.32}{x_{sol}\, Re_L^2} \qquad 7.29$$

Using this result to determine binary mixture pool boiling coefficients with Mostinski (1963) for the ideal boiling coefficients, Figure 7.14 shows reasonable agreement with experimental results. Values for *AD* and *AAD* are 2.7% and 13.6%, respectively, with 86% of predicted values falling within ±25% of experimental results. This is a significant improvement from the capabilities of the correlations from the literature shown in Table 7.3. Uncertainty values for α_L are also shown in Figure 7.14. They are relatively high and are governed primarily by the ±25% uncertainty assigned to the convective heat transfer coefficient on the coupling fluid side (Hong and Bergles, 1976)

7.5 Rectifier Performance

The partial condensation process in the rectifier is limited by sensible vapor heat transfer. Design of the component included wire gauze packing to facilitate both, liquid-vapor interaction, as well as an increase in sensible vapor heat transfer. The Nusselt number correlation for packed beds by Mills (1995), shown in Eq. 7.30, was used for modeling this component(Chapter 5). A strong vapor Reynolds number dependence is expected.

$$Nu_{D_h} = \left(0.5\cdot\sqrt{\mathrm{Re}_{D_h}} + 0.2\cdot\mathrm{Re}_{D_h}^{2/3}\right)\mathrm{Pr}^{1/3} \qquad 7.30$$

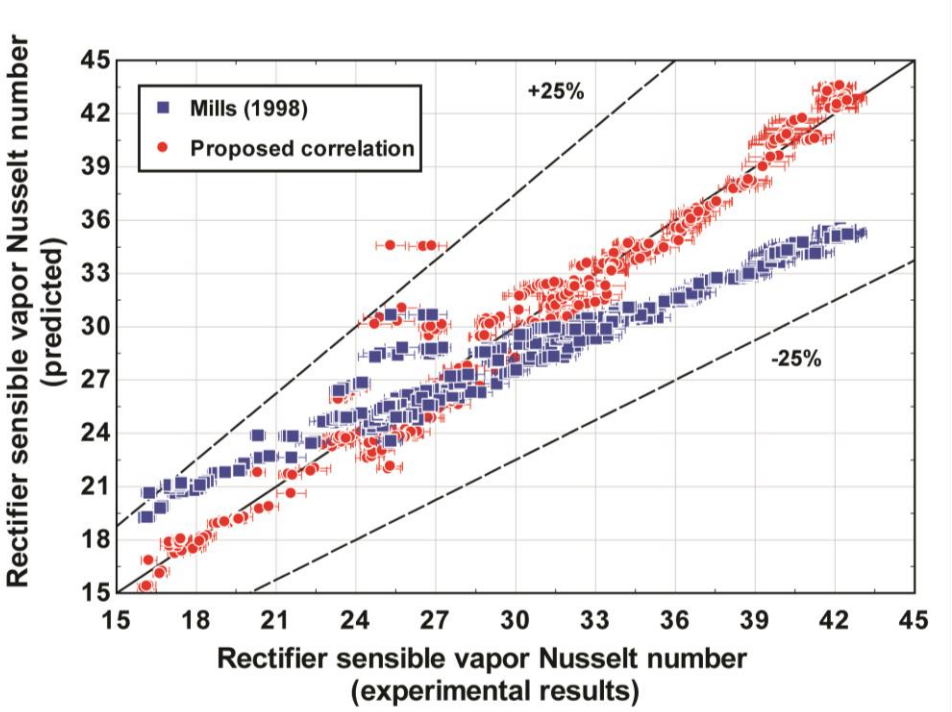

Figure 7.15: Rectifier Nusselt number comparison to experimental results

Implementation of the SBG method as outlined in Eqs. 7.20 through 7.23 provides the sensible heat transfer coefficient. Using the unpacked hydraulic diameter of each vapor passage in the rectifier, the Nusselt number is determined and compared with the correlation by (Mills (1995)). Figure 7.15 shows good agreement between the correlations from the literature and experimental results from the present study. Uncertainty values are relatively small and are primarily due to temperature measurements. Accuracy of the Nusselt number prediction for this design is further improved with a proposed correlation obtained from a regression analysis of the data as shown in Eq. 7.31.

$$Nu_{D_h} = \left(\frac{4.477}{100} \cdot \mathrm{Re}_{D_h} \right) \mathrm{Pr}^{1/3} \qquad 7.31$$

Figure 7.15 shows that this correlation provides accurate Nusselt number predictions for the proposed rectifier design. These results demonstrate the suitability of the SBG method in combination with an appropriate sensible vapor heat transfer correlation.

7.6 Conclusion

An experimental investigation of the heat and mass transfer performance of a diabatic distillation desorber and rectifier for small capacity ammonia-water absorption systems was presented. Results show good agreement with predictions of heat and mass transfer models. Measured heat and mass transfer coefficients show reasonable agreement with some correlations from the literature. Increased predictive accuracy is achieved with the proposed new correlations for liquid mass transfer and binary mixture correction coefficients in the desorber and vapor sensible heat transfer coefficient in the rectifier. These results validate and refine the models developed for these components. Component level results presented in this study facilitate cycle modeling and dynamic system modeling efforts. The experimental validation of heat and mass transfer performance of these highly compact components increases the feasibility of ammonia-water absorption systems for small capacity applications.

The results of this study add to the limited number of experimental investigations on the boiling of ammonia-water binary mixtures in the literature. The comparative assessment of various correlations from the literature provides insight into the suitability of these correlations to ammonia-water desorption. The correlations developed in this study are particularly suitable for applications in similar geometries. Moreover, trends observed in the data contribute to the understanding of binary mixture boiling. In

particular, the functional dependence of the binary mixture correction coefficient on Re_L and x_{sol} provides guidance for future binary mixture boiling investigations.

Results for rectification validate the suitability of an equilibrium modeling approach for binary mixture condensation of ammonia-water at typical operating conditions. The Silver-Bell-Ghaly approach simplifies modeling of rectification components while maintaining predictability of component performance. Furthermore, it is found that the vapor-phase heat transfer correlation for packed beds is applicable for diabatic ammonia-water rectification components utilizing this type of packing.

CHAPTER 8. DIRECT-COUPLED DESORBERS

8.1 Introduction

Heat sources for absorption chillers and heat pumps are often available in the form of hot gas, e.g., waste heat streams. For some systems, it is beneficial to directly couple the hot gas stream with the desorber, i.e., the component in the absorption system that utilizes heat to generate refrigerant vapor. This facilitates system size and weight reduction as well as minimization of exergy destruction. Small-capacity systems, in particular, require the development of novel and compact heat exchangers to ensure their technological and economic feasibility. Waste heat is inherently dispersed and its sources are often small-capacity systems. Engine waste heat recovery for refrigerated trucking or diesel generator exhaust utilization for space conditioning in military forward operating bases are representative examples. While waste heat recovery is a strong motivation for the development of compact and effective direct-coupled desorption components, direct-fired systems also benefit. Absorption systems that are directly driven by the combustion of a fuel such as natural gas or biofuels rely on both, radiative and convective heat transfer. The former takes place in the combustion chamber but the latter requires a relatively large heat transfer area and dictates the size and weight of the combustion-desorption assembly. Effective gas-coupled desorption concepts can be adapted to include a close-coupled combustion chamber and reduce overall system size and weight.

Studies in the literature are typically limited to steady-state simulations and focus on the thermodynamic feasibility of waste heat utilization. Cao *et al.* (2015) provide a summary of recent and representative investigations related to waste heat recovery from

shipping vessels. Talbi and Agnew (2002) offer a comparative simulation study of various configurations of cooling use from an absorption system driven by diesel engine waste heat. It was found that a combination of engine cooling and space conditioning optimizes waste heat recovery and emphasizes the potential of small-capacity absorption systems.

Very few experimental studies of waste heat driven absorption systems are available in the literature. Horuz (1999) coupled a commercially available 10 kW cooling capacity, natural gas fired ammonia-water absorption system to a 6 L diesel engine. Only minor modifications to the desorber were required for waste heat utilization. While the feasibility of waste heat utilization was demonstrated, the investigation showed that engine performance was reduced due to increased backpressure and additional control capability is required to respond to variation in waste heat availability. Kren (2006) provides a comprehensive study of flue gas-fired absorption chillers, which includes an experimental investigation of a large-capacity water/lithium bromide system with a gas burner capacity of 315 kW. The balance between gas-side pressure drop and gas-side heat transfer coefficient is discussed and an optimization criterion is proposed as shown Eq. 8.1. It is suggested that geometric variation of a heat exchanger design concept will result in a local maximum of this criterion, which can guide optimal heat exchanger design.

$$\Phi = \frac{\alpha_{gas}}{\sqrt{\Delta P_{gas}}} \qquad 8.1$$

In the present study, a gas-coupled desorber concept for ammonia-water absorption systems is presented. The design uses diabatic distillation for small-capacity applications, i.e., cooling capacities less than 10 kW. Design considerations and

parameters on the gas side and solution side are discussed. A heat and mass transfer model is developed for performance prediction. A prototype desorber is fabricated and performance is evaluated in an ammonia-water absorption test facility. Results show better-than-predicted component performance and validate the suitability of this design for small-capacity ammonia-water absorption applications. The application of this design for a packaged waste heat recovery chiller for military application is discussed as an example case.

8.2 Design Concept, Considerations and Conditions

The proposed design uses diabatic distillation, which is thermodynamically favorable compared to conventional ammonia-water desorption designs, including separate heat input and adiabatic distillation stages (Kotas, 2013). In this approach, heat input is distributed throughout the component and integrated with vapor purification stages. This also allows for the design of more compact components compared to the conventional design of a reboiler in combination with an adiabatic column. Figure 8.1 shows the conceptual component layout and flow pattern. The design relies on liquid/vapor countercurrent flow. Concentrated solution enters the column at the top and dilute solution leaves the column at the bottom. Vapor is generated throughout the component. Hot gas tubes span the height of the component for heat source distribution. The component consists of a multitude of trays with pool boiling and bubble regions. Liquid enters the pool region through the downcomer. Trays in the pool region are joined to the hot gas tubes to create a liquid pool and provide heat transfer area. Solution flows over the weir into the bubble region, where vapor from lower trays passes through annuli formed between the tray and gas tubes. Bubbling of vapor through built-up liquid

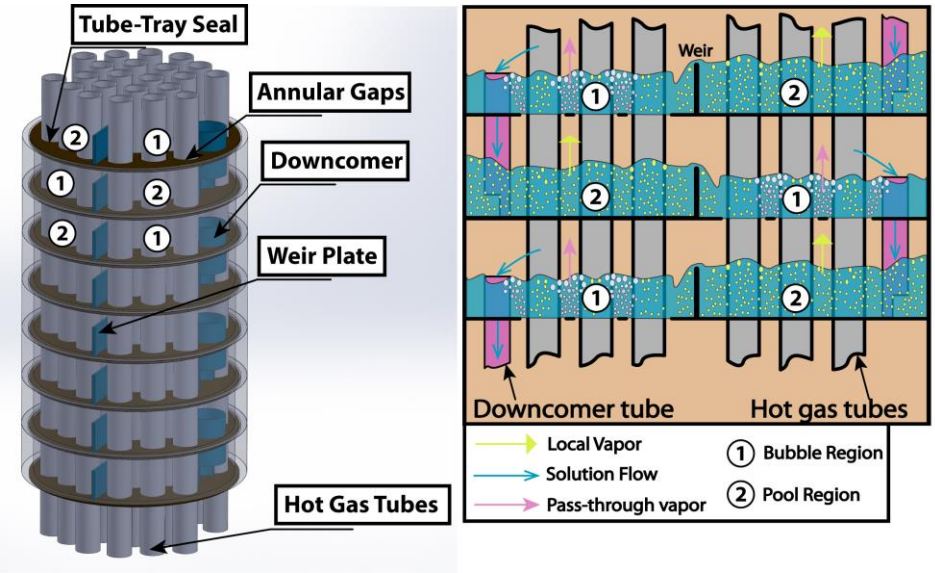

Figure 8.1: Direct-coupled component assembly (left), target flow pattern (right)

achieves vapor generation and purification. A more detailed review of desorber designs and a description of the proposed design was shown in Chapter 4.

Several design considerations govern the optimal configuration. Gas-side optimization is particularly important and is the focus of this paper. The primary objective is to minimize pressure drop while maximizing heat transfer coefficients. The key independent parameters are gas-side tube diameter and number of tubes. The design problem is further constrained with the secondary objectives to minimize the number of tubes to reduce tube-wall joints, improve economic viability and facilitate fabrication. However, the bubble region of the tray relies on liquid-vapor interaction in the annuli formed between the tubes and trays. This necessitates a larger number of tubes to minimize the possibility of flooding and flow reversal. Also, the lowest feasible component shell size is sought. This reduces shell wall thickness requirements given the linear relationship between shell diameter and hoop stress. Finally, it is advantageous to minimize overall component height to limit overall system size.

Table 8.1: Design conditions for a single desorption column

Design Conditions	
Operating pressure, kPa	1760
Concentrated solution flow rate, g s^{-1}	6
Concentrated solution ammonia mass fraction	0.47
Concentrated solution inlet temperature,°C	96
Target dilute solution temperature leaving desorber,°C	137
Target vapor mass flow rate leaving rectifier, g s^{-1}	1.6
Maximum available heat source inlet temperature,°C	440
Target heat source outlet temperature,°C	215
Maximum heat source pressure drop target, Pa	1000
Rectifier vapor outlet ammonia mass fraction	0.9985
Target heat transfer rate, kW	3.2

Solution-side design is based on the component geometry determined by the gas-side constraints. Solution-side considerations include number of trays, weir height, and cross-sectional area of tube-tray annuli in the bubble region of the tray. The solution-side design methodology and associated hydrodynamic limitations were discussed in Chapter 4.

Desorber operating conditions are listed in Table 8.1. Typical pressure and concentrated solution conditions are chosen. Dilute solution temperature is based on thermodynamically optimal performance (Chapter 3).

8.3 Gas-Side Design

A gas-side heat transfer and pressure drop model is developed to conduct a parametric study, varying tube count and tube diameter to determine the geometric parameters. Gas-side flow pattern is shown in Figure 8.2. A solution-side model is not required at this stage because it is assumed that the heat transfer resistance on the solution side is significantly smaller than that on the air side, i.e. $\alpha_{gas} A_{gas} \ll \alpha_L A_L$. This assumption is justified as expected gas-side heat transfer coefficients are ~100 W m^{-2} K^{-1},

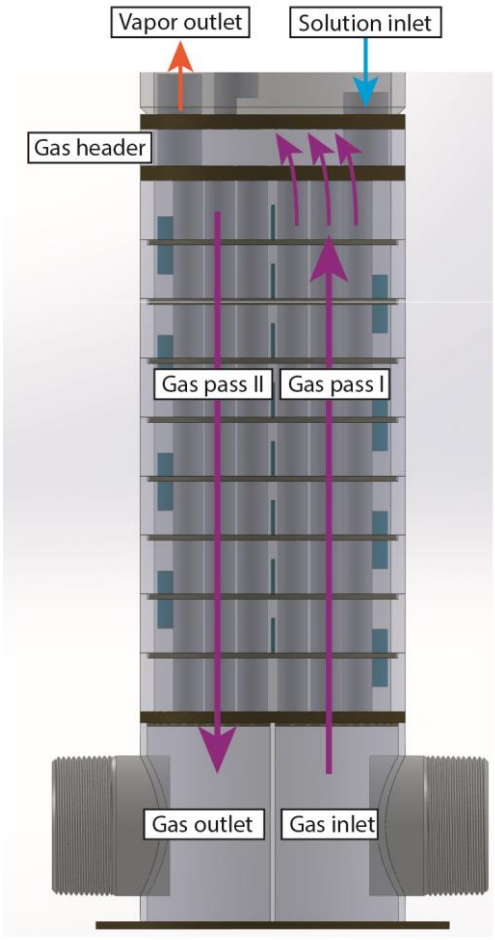

Figure 8.2: Heat source gas flow pattern

while solution side heat transfer coefficients are expected to be > 1000 W m^{-2} K^{-1} (Chapter 5). Heat transfer areas are comparable for both sides.

Both gas passes shown in Figure 8.2 are treated separately using the *UA-LMTD* method, but the length for both passes is constrained to have the same value. The Churchill (1977a) correlation is used to determine the convective gas-side heat transfer coefficient. The flue gas header is considered as additional heat transfer area. Here, an impinging jet correlation for an array of circular nozzles (Martin, 1977) is applied to model the heat transfer coefficient for the upper wall of the header. The area of the header is determined from the diameter of the shell, which, in turn, is determined from

the number of gas tubes. Here, a constant longitudinal and transverse tube spacing in a staggered arrangement is used and the smallest possible shell size available in the North American NPS standard is used. For example, 11 gas tubes per pass (22 gas tubes in the shell) are used with a 4 inch NPS pipe (114 mm outside diameter).

The heat transfer rate is then calculated in combination with energy conservation for each pass and the header as shown in Eqs. 8.2 and 8.3.

$$\dot{Q}_i = \alpha_{gas,i} A_{gas,i} \cdot LMTD_i \tag{8.2}$$

$$\dot{Q}_i = \dot{m}_{gas} c_{p,i} \Delta T_i \tag{8.3}$$

Closure is provided with the overall heat duty requirement as shown in Eq. 8.4 and the required tube length is determined for every combination of tube count and tube diameter. Heat source inlet and outlet temperatures are maintained at constant values as shown in Table 8.1 during the parametric study.

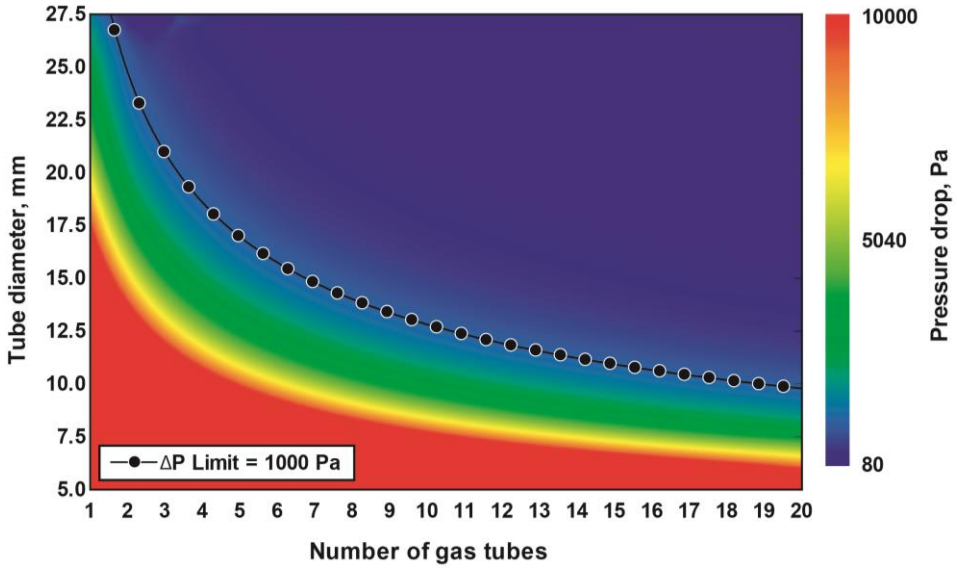

Figure 8.3: Gas pressure drop as a function of tube count and tube diameter

$$\dot{Q}_{total} = \sum_{i=1}^{3} \dot{Q}_i \qquad 8.4$$

With the tube length, tube count and diameter established, the frictional pressure drop in the tubes and the header is calculated using the Churchill (1977b) correlation. Additionally, minor losses due to sudden contraction and expansion at the inlet and outlet of each pass, respectively, are considered. Properties for atmospheric air at average gas temperatures are used to determine thermophysical gas properties. The analysis is conducted on the Engineering Equation Solver software (Klein, 2015) platform.

Figure 8.3 shows a contour plot of pressure drop as the number of tubes and the tube diameter are varied. As expected, an increase in tube number and diameter results in a decrease in pressure drop. The 1000 Pa pressure drop limit curve indicates that only tube count/diameter combinations to the right of this line are permissible. Figure 8.4 shows a contour plot of tube length for the same independent variables. For a given tube

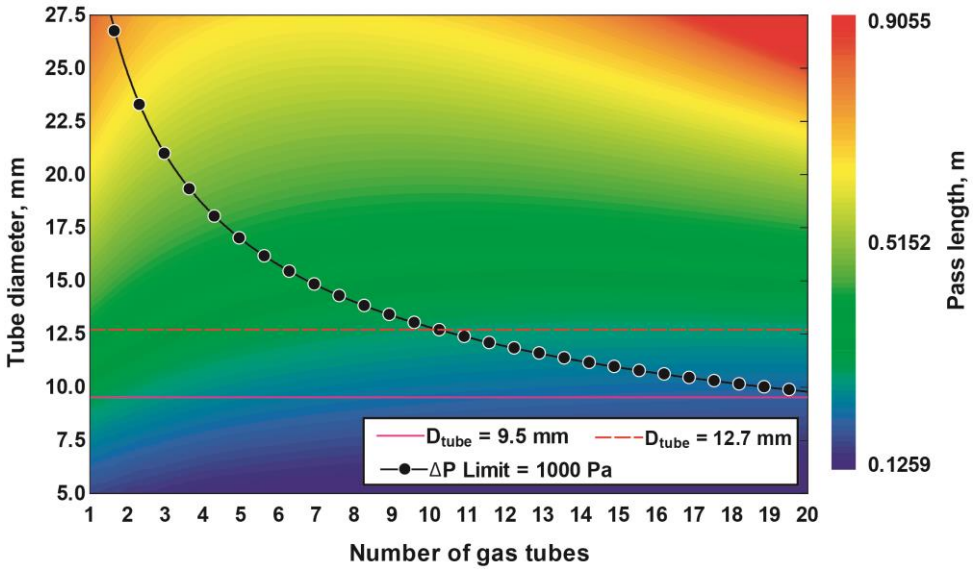

Figure 8.4: Required gas tube pass length as a function of tube count and tube diameter

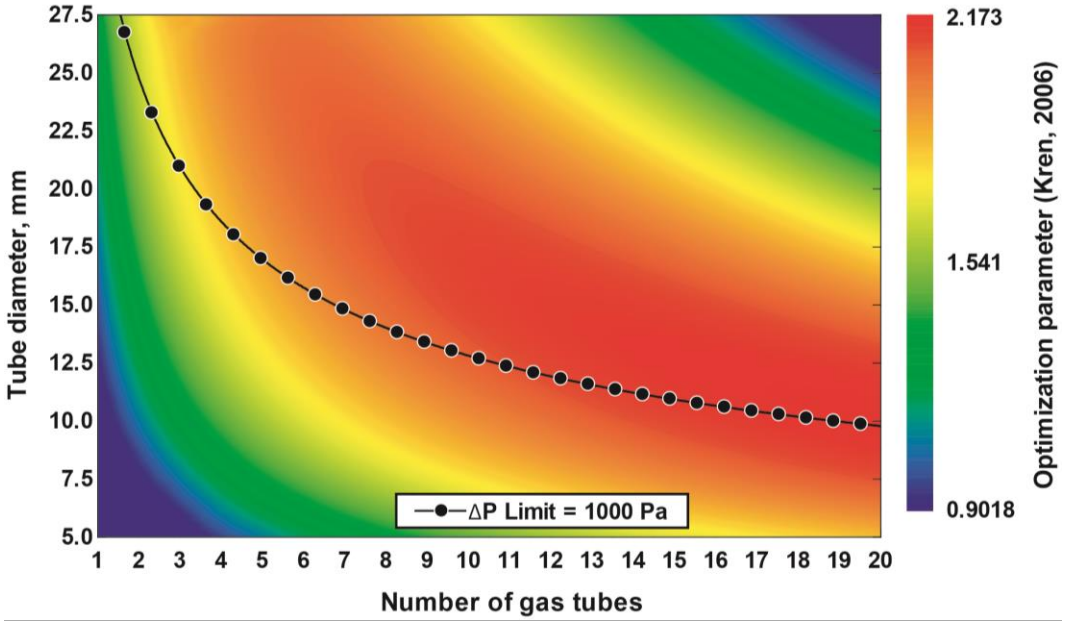

Figure 8.5: Optimization criterion by Kren (2006) as a function of tube count and tube diameter

diameter, a minimum tube length is observed as tube count is varied. Limiting the choice of tubes to standard diameters and wall thicknesses, with the objective of minimizing the number of tubes (reduction of shell size and tube-wall joints), yields the combination of 11 tubes at an outside diameter of 12.7 mm with a wall thickness of 0.9 mm. Finally, the contour plot in Figure 8.5 shows the results of the criterion by Kren (2006) as a function of tube count and diameter. While good agreement with the geometry selected here is shown; however, it can be seen that the criterion might need modification to determine the optimal geometric design for a given application.

8.4 Solution-side and Component Model

A hydrodynamic investigation of this component geometry was conducted in Chapter 4, in which hydrodynamic limitations such as flooding and weeping were addressed through variation of the vapor annulus size, tray spacing and weir height.

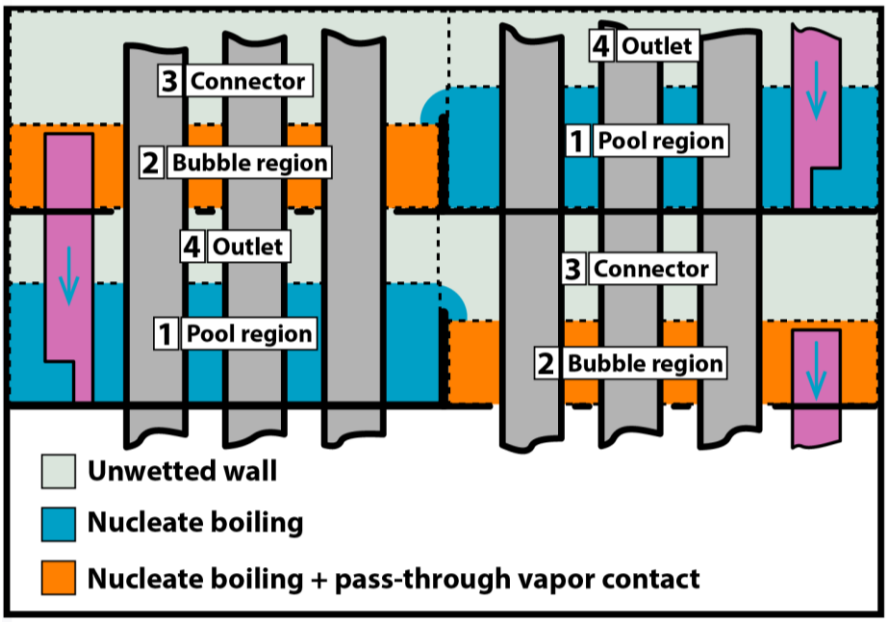

Figure 8.6: Solution heat and mass transfer model regions

Estimates for bubble size, bubble velocity and bubble density were obtained. These results are used here to develop a heat and mass transfer model. Three regions are identified in Figure 8.6. Liquid in the pool region experiences pool boiling of the binary mixture, while pool boiling and liquid-vapor interaction occurs in the bubble region. Modules for each region based on the approach by Colburn and Drew (1937) and Price and Bell (1974) developed (Chapter 5) for the modeling of a microchannel desorber with similar processes are adapted for the present geometry. The pure substance pool boiling correlation of Mostinski (1963) in combination with the binary mixture correction coefficient proposed by Táboas *et al.* (2007) was shown to have good agreement with experimental results (Chapter 7) and is used here. The vapor region module is modified and a single-phase heat transfer correlation for flow over staggered tubes by Žukauskas and Ulinskas (1985) is used for the vapor phase.

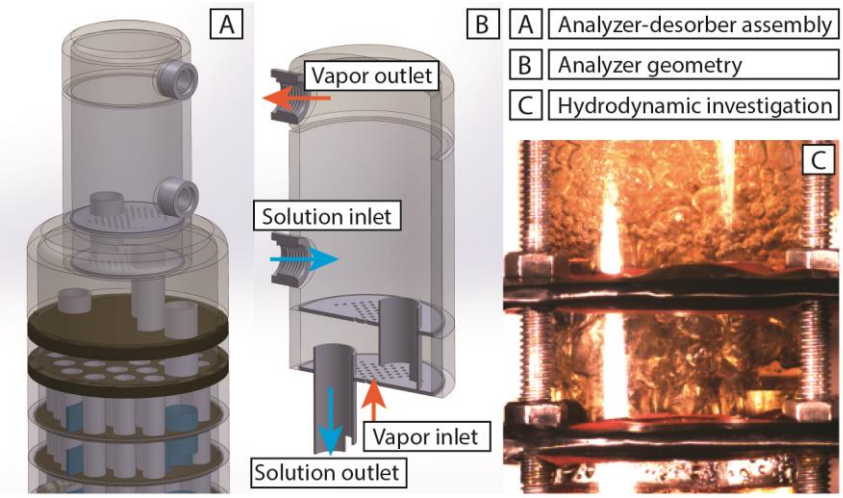

Figure 8.7: Adiabatic analyzer section with integration into diabatic column

An adiabatic analyzer section shown in Figure 8.7 is integrated with the column to maximize vapor purity leaving the column. A hydrodynamic investigation was conducted to ensure tray activation and ensure the absence of flooding (Chapter 4). The modeling approach by Colburn and Drew (1937) as applied by Price and Bell (1974) mentioned above is also used to model liquid-vapor contact in the analyzer. The gas hold-up correlation applicable for bubble columns by Hikita *et al.* (1980) is used in combination with bubble size estimates by Pohorecki *et al.* (2005).

8.5 Fabrication and Testing

The component dimensions obtained based on the modeling described above are shown in Figure 8.8A. Additional details on tray design can be found in Chapter 4 and the desorber fabricated using a combination of welding and brazing is shown in Figure 8.8B.

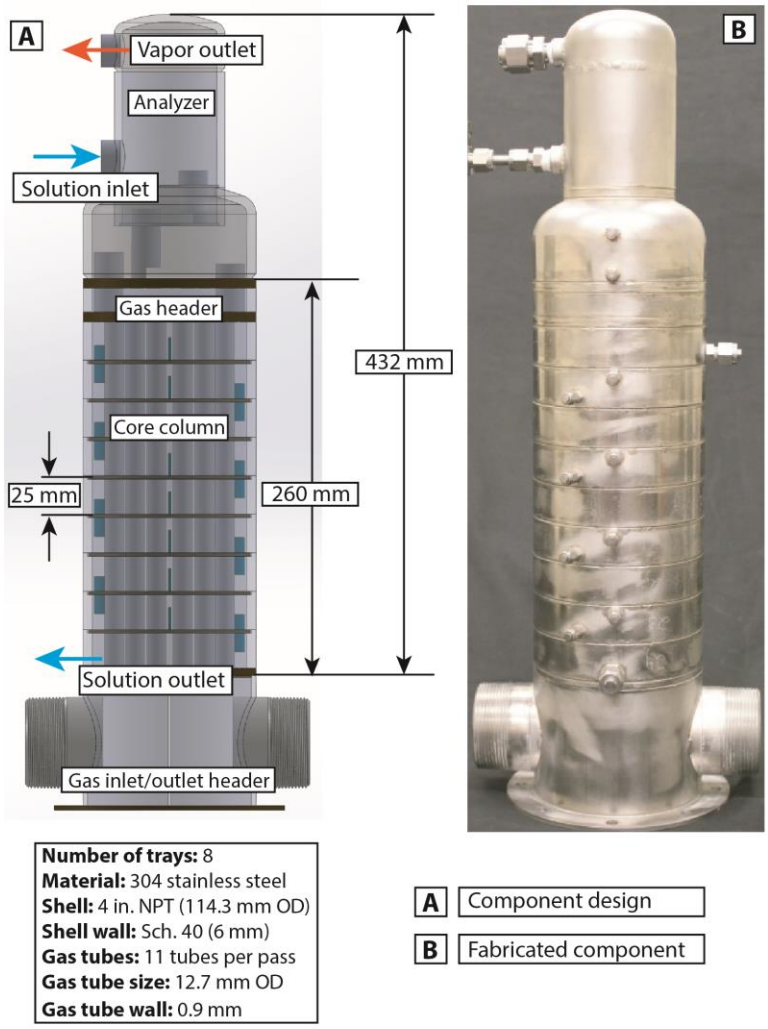

Figure 8.8: Component design specifications and fabricated test unit

A test stand was designed to operate as a two-pressure absorption system without the use of an evaporator. This allows for simulation of representative operating conditions in an absorption system. A rectifier was installed and operated during testing to achieve a nominal vapor ammonia-mass fraction of 99.85%, which allows for vapor conditions that correspond to realistic absorption system operation. Additional details on the test facility and the rectifier were presented in Chapter 6. The test stand was modified to incorporate a hot gas heat source simulator as shown in Figure 8.9. The simulator is an

assembly of air blower, electric heater and air flow measurement. Feedback control of the electric heater is used to provide target gas temperatures and a variable frequency drive is used to modulate blower speed for gas mass flow control. An orifice plate with differential pressure measurement, located upstream of the electric heater and air blower is used to determine heat source mass flow. A summary of test facility instrumentation and heat source simulator details is provided in Table 8.2.

The system was operated at a constant pressure of 1760 kPa. Given an ammonia vapor mass fraction of 99.85%, this corresponds to a condenser saturation temperature of 44.5ºC, which is representative of ambient temperatures of ~37ºC. Three concentrated solution ammonia mass fraction conditions were investigated. Ammonia mass fraction of the concentrated solution is determined from a combination of evaporator and ambient temperatures. Evaporator temperature determines low side pressure, P_{low}, and the ambient temperature sets the saturated liquid temperature in the absorber. The combination of

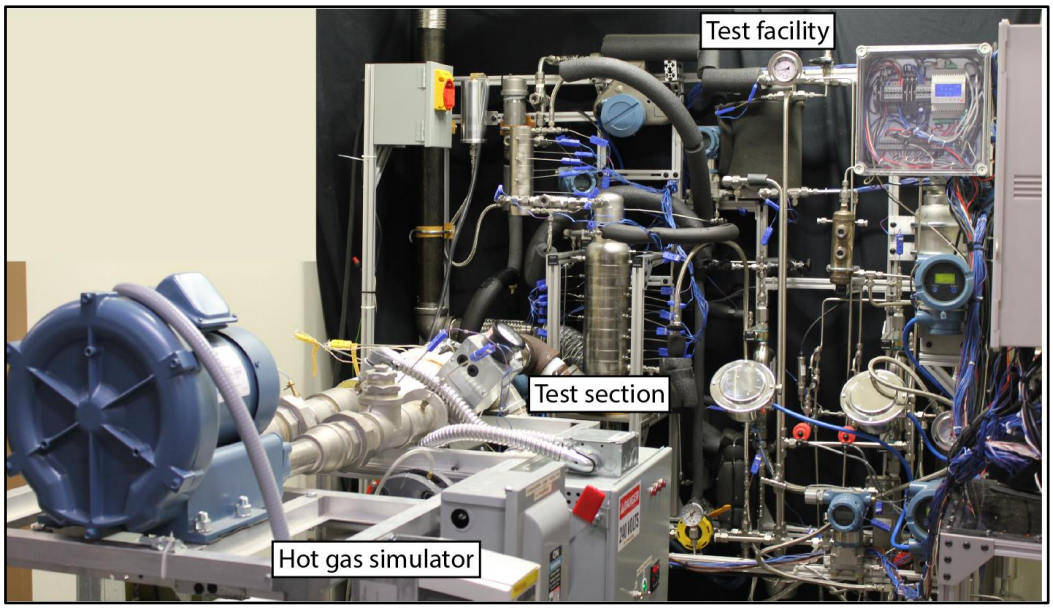

Figure 8.9: Photograph of test facility

pressure and saturated liquid temperature in the absorber then determines ammonia mass fraction of the concentrated solution. A range of solution flow rates was tested to investigate the effect of working fluid flow rates and demonstrate capacity variation, i.e., component turn-down. At target operating conditions, the highest solution flow rate corresponds to an evaporator cooling capacity of approximately 1.75 kW. Circulation ratio as defined in Eq. 8.5 is maintained at approximately constant values. This is because active control of dilute solution temperature to maintain optimal operating conditions, as discussed below, results in relatively constant *CR* values. Thus, variation of solution flow rate corresponds to a commensurate variation in vapor generation and cooling capacity.

$$CR = \frac{\dot{m}_{ref}}{\dot{m}_{cs}} \tag{8.5}$$

For all test points, a target dilution solution temperature, T_{ds}, is imposed. This temperature was identified as a suitable control variable for heat input control (Chapter 3). It was shown that an optimal T_{ds} value exists that minimizes energy input per unit mass of refrigerant generated. This value is defined as $T_{opt,I}$ and depends on P_{high} and x_{cs}. For this test matrix, $T_{opt,I}$ values for x_{cs} values of 0.42, 0.47 and 0.52 are 155ºC, 137ºC and 119ºC, respectively. This results in an approximately constant circulation ratio value of CR = 3.9. Gas mass flow rate was modulated to achieve a target gas outlet temperature at all operating conditions. The inlet gas temperature was varied to some extent during testing of various capacity conditions, i.e., solution flow rates to achieve the target T_{ds} value.

8.6 Data Reduction and Results

Desorber heat input is determined with gas mass flow data in combination with gas inlet and outlet temperatures. The average gas temperature is used to determine thermophysical properties of the heat source. Gas side pressure drop is measured directly with a differential pressure transmitter as shown in Table 8.2. Flow rates of the concentrated solution, dilute solution, and vapor leaving the rectifier are measured. A mass balance error of less than 1% was maintained. Working fluid temperatures were

Table 8.2: List of test facility instrumentation and heat source simulator

Instrument	Manufacturer/Part	Range	Accuracy
Thermocouples	Omega® T-type	-250 – 300ºC	±0.25°C
Pressure transmitter (high side pressure)	Rosemount™ 3051T	0 – 3000 kPa	±1.5 kPa
Pressure transmitter (low side pressure)	Rosemount™ 3051T	0 – 1000 kPa	±0.5 kPa
Mass flow rate (concentrated solution)	Micromotion™ CMFS010M	0 – 12 g s^{-1}	±0.1%
Mass flow rate (dilute solution)	Micromotion™ CMFS010M	0 – 10 g s^{-1}	±0.1%
Mass flow rate (concentrated solution)	Micromotion™ CMF010H	0 – 3.3 g s^{-1}	±0.1%
Volumetric flow rate (heat source coupling fluid)	AW-Lake JVS-30	0 – 1.6 m^3 hr^{-1}	±0.5%
Working fluid reservoir level (solution and refrigerant)	Gems® Sensors CT-1000	0 – 200 mm	±1%
Air blower (regenerative)	Rotron®	105 SCFM (max), 1HP	-
Electric heater	Sylvania	18 kW	-
Air flow orifice plate	Dwyer® OP-F-1	50 SCFM	±0.6% (full scale)
Differential pressure transmitter (Orifice)	Rosemount™ 3051T	0 – 20000 Pa	±1%
Differential pressure transmitter (Test section)	Rosemount™ 3051T	0 – 1500 Pa	±1%

collected throughout the column and several assumptions are made about working fluid states. Dilute solution leaving the column is assumed to be saturated liquid while all vapor states in the test section are assumed to be saturated vapor. Working fluid pressure was measured at the top of the column. It is assumed that working fluid pressure drop is sufficiently small to ignore its effect on properties. This assumption was validated in the hydrodynamic investigation presented in Chapter 4. With all relevant thermodynamic states determined, control volume analyses are conducted on the desorber and rectifier to determine flowrates between both components as well as concentrated solution ammonia mass fraction values, x_{cs}. A more detailed description of this methodology was given in Chapter 7.

Vapor purification efficiency for the diabatic column as well as the overall column (including analyzer section) is determined. Here, a modification of the classic Murphree efficiency (Murphree, 1925) is proposed for diabatic columns as shown in Eq. 8.6. It is defined with respect to the least pure vapor in the column, i.e., vapor at the temperature of dilute solution leaving the column. This vapor ammonia mass fraction, $x_{V,in,des}$ can be determined from pressure and temperature data. The highest possible ammonia mass fraction is determined as saturated vapor at the temperature of solution entering the column, $x^*_{V,out,des}$, which can also be determined from the measured pressure and temperature.

$$\eta_{pur} = \frac{x_{V,out,des} - x_{V,in,des}}{x^*_{V,out,des} - x_{V,in,des}} \tag{8.6}$$

The average gas side heat transfer coefficient is determined using a heat transfer resistance network in combination with a *UA-LMTD* analysis. Two analyses are

conducted simultaneously; one counter-current and one parallel flow, for the first and second gas pass, respectively, as shown in Eqs. 8.7 and 8.8.

$$\dot{Q}_1 = U_{average} A_{gas} \cdot LMTD_1 \tag{8.7}$$

$$\dot{Q}_2 = U_{average} A_{gas} \cdot LMTD_2 \tag{8.8}$$

In combination with energy conservation for each pass, analogous to Eq. 8.3, the average overall heat transfer coefficient is determined. It should be noted that the header heat transfer resistance is lumped into the overall average heat transfer resistance. The overall heat transfer resistance is given by Eq. 8.9, and the average gas-side heat transfer resistance is determined using Eq. 8.10.

$$R_{total} = \frac{1}{U_{average} A_{gas}} \tag{8.9}$$

$$R_{total} = R_{wall} + R_L + R_{gas} \tag{8.10}$$

If wall and solution side resistances are known, the gas-side heat transfer coefficient, α_{gas}, can be calculated using Eq. 8.11.

$$R_{gas} = \frac{1}{\alpha_{gas} A_{gas}} \tag{8.11}$$

Values for α_L cannot be reliably determined from the data in this study. To evaluate R_L in Eq. 8.10, a value for R_{gas} has to be estimated. However, correlations predicting α_{gas} have high uncertainties (±25%) and the values for α_{gas} are at least an order of magnitude smaller than those for α_L. Therefore, a small variation in α_{gas} values leads to excessive variation in α_L values and the uncertainty in α_{gas} leads to

unacceptably large uncertainties in the results for α_L. Therefore, only values for α_{gas} are determined from the data, and R_L is estimated using correlations for binary mixture pool boiling and estimates for solution area. The latter is determined with estimates for liquid height in each tray (Chapter 4). The extended surface effect in the pool region of each tray due to the tube-tray joints is also accounted for. The tray is modeled as hexagonal fins around each tube (Perrotin and Clodic, 2003), with typical fin efficiency values of approximately 30%. These low values are due to the relatively high solution-side heat transfer coefficients, α_L. The pure substance pool boiling correlation of Mostinski (1963) in combination with the binary mixture correction correlation proposed by Táboas *et al.* (2007) was shown to provide reasonable prediction of heat transfer coefficients (Chapter 7), and is used here to estimate values for α_L with an assigned uncertainty of ±25%. Wall resistance is determined from the tube thickness and material thermal conductivity.

Mass transfer coefficients are determined for the liquid and vapor phase with the methodology described in Chapter 7. Vapor generation rates are determined from mass flow measurements. Liquid and vapor mass transfer coefficients are determined using the methodology of Colburn and Drew (1937) and Price and Bell (1974). These analyses were conducted using Engineering Equation Solver software (Klein, 2015).

A comparison of the predicted and measured temperature profiles at the test conditions corresponding to the design operating conditions is shown in Figure 8.10. Measured vapor temperatures show a closer approach to solution temperature throughout the column, but particularly in the analyzer. Liquid temperatures are slightly higher throughout the component compared to model predictions, while vapor temperatures are significantly lower. This result can be explained by better-than-expected internal liquid-

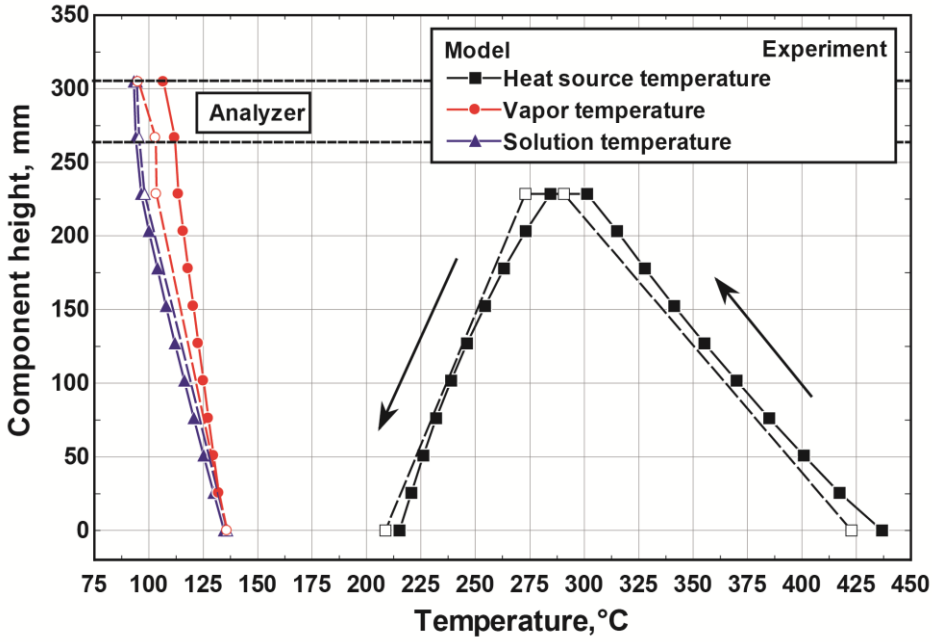

Figure 8.10: Measured and predicted temperature profiles

vapor heat recovery, and indicates high column and overall vapor purification efficiencies. The heat source temperature profiles shows that the actual required heat source temperatures are lower than those predicted by the model. This is because actual α_{gas} values are slightly higher than predicted values, with an absolute average deviation of 2.2%. Therefore, total heat input requirement is commensurately lower than model prediction as discussed below. Also, the better vapor purification observed in the experiments leads to a slight reduction in vapor mass flow rate and enthalpy leaving the component, which results in a lower heat input requirement. The reduced heat input due to the better internal vapor purification also decreases the rectification load, with these combined influences leading to an increase in system COP. It should be emphasized that the vapor mass flow rate leaving the rectifier, i.e., the mass flow rate that determines cooling capacity, is constant in both cases. The reduced vapor flow rate leaving the

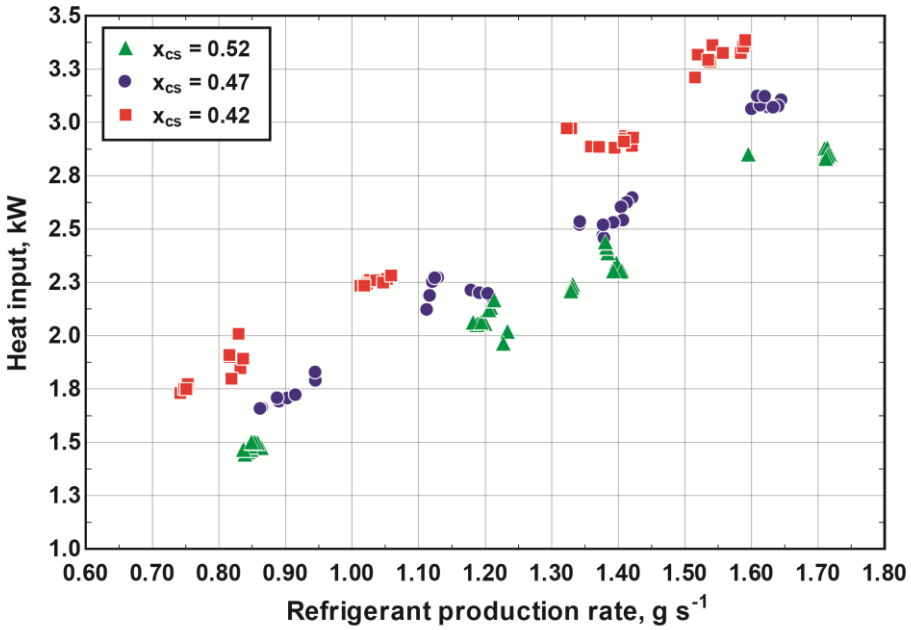

Figure 8.11: Heat input versus refrigerant production rate

desorber is accompanied with a commensurate reduction in reflux flow rate from the rectifier and vice versa.

Capacity response is explored in Figure 8.11 , where heat input is plotted versus refrigerant production rate. Given a relatively constant circulation ration, *CR*, vapor production rate increases linearly as solution flow rate is varied. Due to constant pressure and fixed values for x_{cs}, heat input also varies linearly with vapor production rate. A dependence of heat input rate on x_{cs} can be seen: heat input increases as solution concentration is reduced, due to the increased fraction of water with its high heat of vaporization. The highest vapor production rates achieved at tested flow rates and x_{cs} values are > 1.7 g s^{-1}. This shows that further capacity increases can be achieved if gas-side pressure drop restrictions are relaxed so that heat source flow rates and temperatures can be increased.

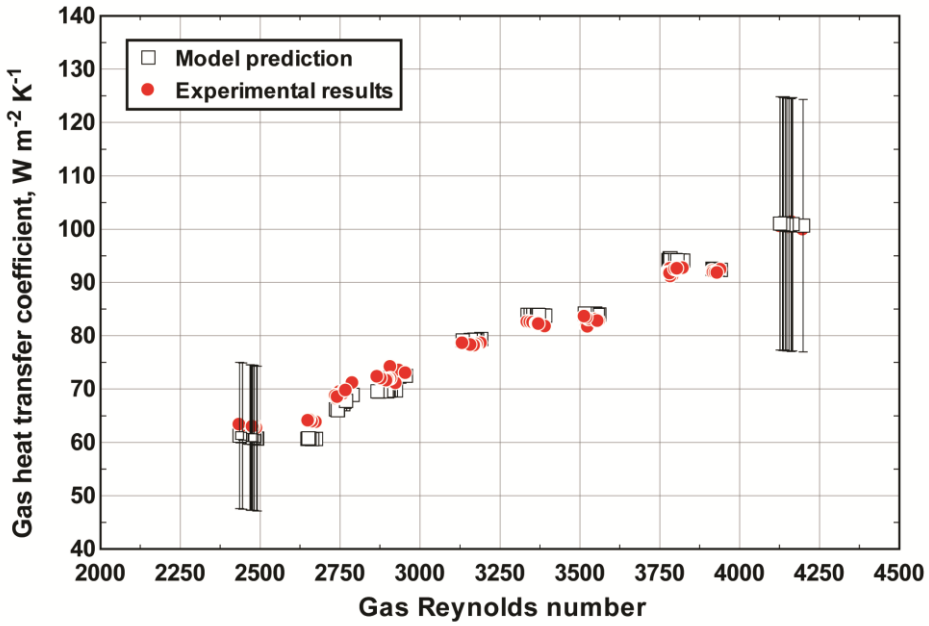

Figure 8.12: Average gas-side heat transfer coefficient versus gas Reynolds number

Gas side heat transfer coefficient values, α_{gas}, agree well with the predictions of the model, as shown in Figure 8.12, implying that the use of the Churchill (1977a) and Martin (1977) correlations is appropriate. An average deviation (*AD*) of 0.9% and absolute average deviation (*AAD*) of 2.2% was found. Figure 8.13 shows reasonable agreement between the measured and predicted pressure drops, with *AD* and *AAD* values of 0.5% and 5.0%, respectively. A slightly greater than predicted Reynolds number dependence is seen in measured values, leading to more conservative predictions at high flow rates.

Liquid mass transfer results are compared with the predictions of two correlations (Calderbank and Moo-Young, 1961; Akita and Yoshida, 1974) from the literature as well as the heat and mass transfer analogy as shown in Eq. 8.12 in Figure 8.14.

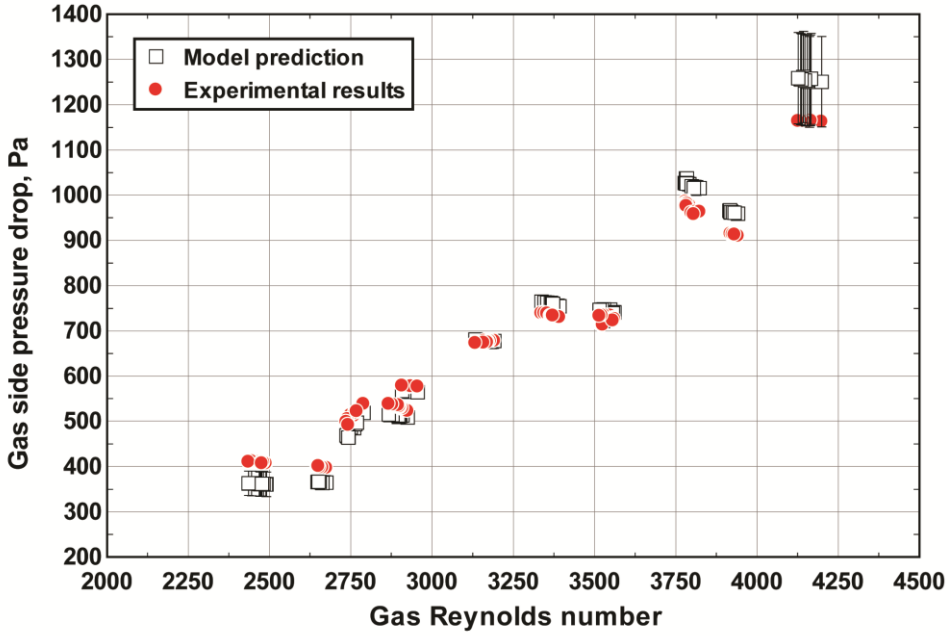

Figure 8.13: Measured and predicted pressure drop versus Gas Reynolds number

$$\frac{Sh_i}{Nu_i} = \left(\frac{Sc_i}{Pr_i} \right) \qquad 8.12$$

The last approach uses estimates for solution-side heat transfer coefficient. These results show that the heat and mass transfer analogy is inadequate for predicting liquid mass transfer coefficients. None of the correlations from the literature show the dependence on liquid Reynolds number. This may be because of the assumption of constant liquid-vapor interfacial area used to obtain experimental values, whereas the actual interfacial area would vary with flow rate, most probably decreasing as liquid and vapor flow rates decrease. This would compensate for the trend in the data and yield better agreement with the literature. The correlation of Akita and Yoshida (1974) is in better agreement with the data than the correlation of Calderbank and Moo-Young

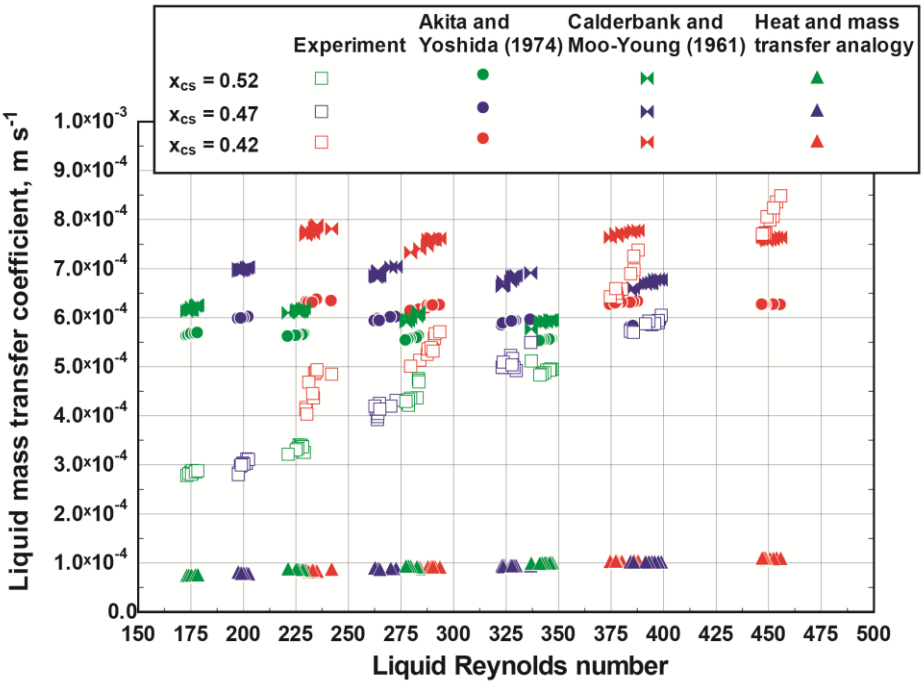

Figure 8.14: Experimental and predicted liquid mass transfer versus liquid Reynolds number

(1961). The latter also shows a much stronger dependence on x_{cs} which is not observed in the experiments.

Figure 8.15 shows a comparison between the measured vapor mass transfer coefficients and predictions of the correlation by Onda *et al.* (1968), as well as a constant Sherwood number value, $Sh = 18$, suggested by Colombet *et al.* (2013). While reasonable agreement between experimental results and predictions of both these approaches is shown for $x_{cs} = 0.47$, a stronger dependence on x_{cs} is observed in the experimental results. Further investigations of the mass transfer effectiveness of diabatic liquid-vapor contactors with these particular geometries are required to provide a better understanding of mass transfer coefficient dependencies.

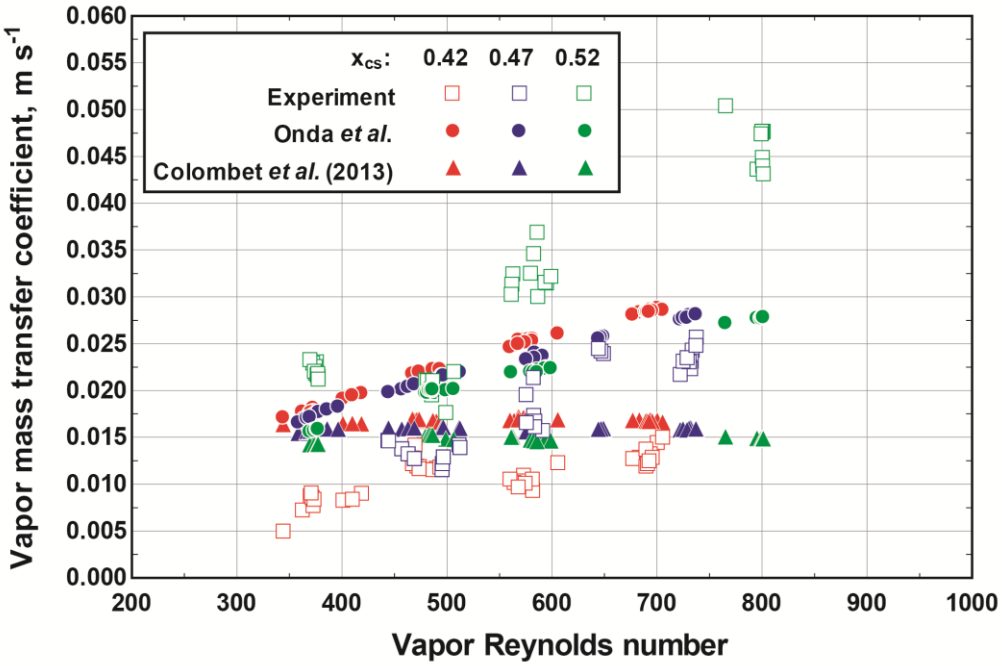

Figure 8.15: Experimental and predicted vapor mass transfer coefficients versus vapor Reynolds number

The purification efficiency defined in Eq. 8.6 for both the core column only and the overall component including the analyzer is shown for the entire data set in Figure 8.16. While these values are relatively constant, the greatest dependence was observed on the variation of dilute solution leaving the column, T_{ds}. This is expected as vapor at higher temperatures is less concentrated in ammonia and requires greater purification to achieve comparable ammonia vapor mass fractions at the outlet. These results show that the core column achieves high vapor purification efficiency, which is further supplemented by the addition of the analyzer.

8.7 Comparative Assessment

The results of this study demonstrate the effectiveness of the proposed desorber design for direct-coupled gas driven ammonia-water absorption. The design of a

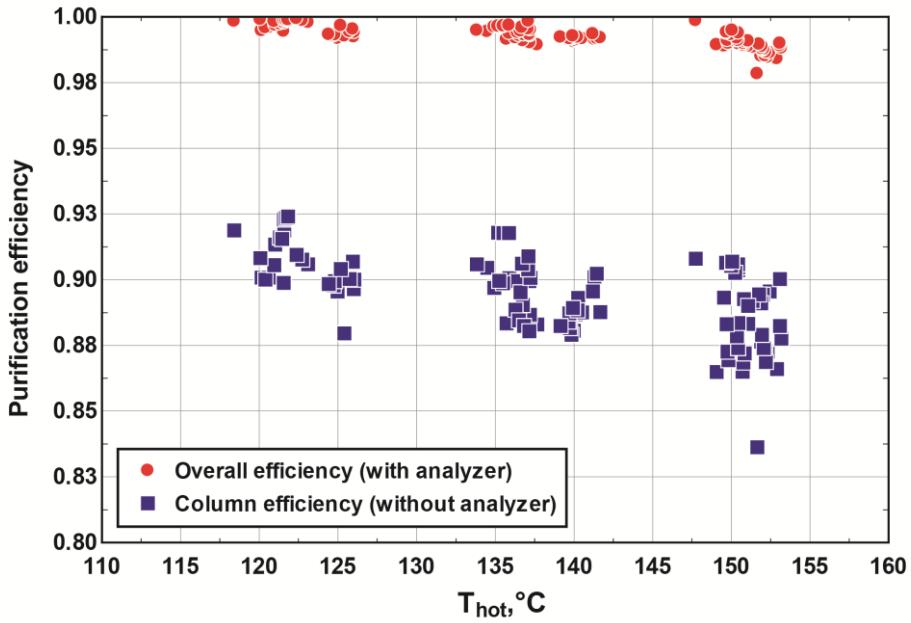

Figure 8.16: Purification efficiency values versus dilute solution temperature

microchannel desorber for use with a heat source coupling fluid was presented in Chapter 5 and experimentally validated in Chapter 6. The microchannel desorber design requires a coupling fluid loop in combination with a primary heat exchanger that is coupled to the heat source, e.g., combustion chamber or hot gas stream. Table 8.3 shows a selection of relevant criteria for a comparative assessment. Direct-coupled systems allow for overall system size and weight minimization if a hot gas stream or combustion process is used as the primary energy input. A heat source coupling fluid circuit, including the circulation pump, is eliminated in the direct-coupled design. Therefore, small capacity, mobile applications favor a direct-coupled desorber such as the design proposed in this study. Indirect coupled desorbers are, however, more compact due to liquid coupling. This minimizes system charge and favors larger capacity system designs where the heat source is physically removed from the core absorption system. Exergy destruction is minimized with direct-coupled systems due to the elimination of the additional heat exchange and

potential losses in the coupling fluid loop, including electricity consumption by the coupling fluid pump. Increased accuracy in desorption temperature control and control of desorption temperature profiles can be achieved with the use of a coupling fluid. Mechanical design constraints discussed above, e.g., desorber shell size, are more challenging for the direct-coupled desorber. Fabrication, however, is considered to be simpler for the proposed direct-coupled design. Gas-side fouling is of particular importance in engine waste heat applications. A detailed analysis of the effect of fouling on this particular desorber design was conducted by Aiello (2016). If significant fouling is expected, its management is facilitated if desorber and exhaust gas heat exchanger are decoupled. Heat source versatility is greater with an indirect desorber since an application-specific heat exchanger can be designed for the heat source in the coupling fluid loop. Finally, cascaded and distributed systems also favor indirect coupled desorbers. As the actual operating temperatures in the desorber are much lower than those specified for the heat source in gas-coupled desorbers, a lower temperature liquid can be used if it is available from a primary process. This allows for the integration of upstream processes that require higher temperatures or for lower gas temperatures in combination with a larger heat source heat exchanger. Sometimes, a centralized heat source is present that supplies a large amount of waste heat. In this case, the integration of a multitude of smaller capacity absorption systems for distributed use favors an indirect coupled desorber. A centralized waste heat recovery heat exchanger can act as the heat source with distribution of a relatively low temperature heating liquid to individual absorption systems that operate based on individual demand. Evaluation of these criteria shows that the recommended desorber design, i.e., direct-coupled gas driven vs indirect-coupled

Table 8.3: Comparative desorber design criteria comparison

Design Criterion	Direct	Indirect	Comment
Overall system size/weight	+	-	Direct-coupling eliminates heat source fluid circuit, e.g., pump, fluid routing and primary heat exchanger
Desorber size	-	+	Heat source microchannel design reduces component size drastically, minimizing working fluid volume
Solution-side heat and mass transfer	O	O	Solution-side heat transfer is not typically affected by design choice
Exergy destruction minimization	+	-	The additional heat transfer process is accompanied by additional exergy destruction
System control	-	+	Better control of working fluid temperature for thermodynamic optimization
System scalability	-	+	Low gas side heat transfer coefficient lead to large desorbers as capacity is increased
Fabrication	+	-	Conventional shell-and-tube fabrication techniques are suitable for direct-coupled design
Fouling management	-	+	A separate primary heat exchanger facilitates fouling management (isolation from working fluid)
Heat source versatility	-	+	A generic heat source can be used with an indirect design, not limited to hot gas
Cascaded and distributed systems	-	+	• Indirect design allows for centralized heat source with spatial separation from core absorption system • Use of lower temperature liquid stream in cascaded thermal system

microchannel desorber, depends on the specific application under consideration. For example, the proposed design was implemented in the development of a 2.65 kW absorption chiller at extreme ambient conditions for military applications (Ponkala *et al.*, 2018). Waste heat from diesel generators is used as the heat source to maximize energy utilization of fuel supply. Figure 8.17 shows the compact packaged system with two

Figure 8.17: 2.63 kW cooling capacity chiller for diesel engine waste heat applications at severe ambient conditions (Ponkala *et al.*, 2018)

parallel desorption columns such as those developed in the present study, which can meet system capacity needs.

8.8 Conclusions

An investigation of direct, gas-coupled desorption for ammonia-water absorption was conducted. An approach that focused on gas-side limitations and adapted a previously developed solution-side model was used to develop the diabatic distillation column that served as a desorber. The component was fabricated and tested for a range of operating conditions typically encountered in ammonia-water absorption systems. Internal vapor purification achieved was better than expected and predictions for gas-side heat transfer coefficient and pressure drop were shown to be in good agreement with the data. Finally, direct gas-coupled and indirect desorber designs were compared. It was shown that the choice of desorber configuration strongly depends on the specific

application, with direct and indirect coupled desorbers being suitable for different applications. This investigation provides a viable design solution for small-capacity applications where direct gas-coupling is favorable.

CHAPTER 9. THERMAL COMPRESSOR CONTROL

9.1 Introduction

Vapor absorption systems provide an alternative to conventional vapor compression cycles, which require high-grade mechanical or electrical energy input. Absorption systems can utilize a variety of low-grade heat sources, including waste heat and solar thermal energy. Their application can contribute to more efficient overall energy utilization. Recent developments of small-capacity ammonia-water absorption systems by Garimella *et al.* (2016) as well as the investigation presented in Chapter 2 show the potential for a wide range of applications of absorption systems. However, further development of system control methodology is needed to increase the feasibility of widespread adoption of this technology. A comprehensive review of vapor absorption system control is provided by Goyal *et al.* (2018). The review reveals that research on this topic is limited. Many control strategies rely on on/off type control that causes performance degradation through significant transient behavior. Some strategies rely on simplified models that are only applicable for a limited operating range. Internal system parameters such as expansion valve and solution flow rates are generally neglected, not utilizing the potential for system optimization. A methodology for the integration of accurate thermodynamic models for controls purposes is needed to continuously minimize heat input requirements. More details on thermodynamic models relevant to absorption system control are provided by Goyal *et al.* (2018) as well as in Chapter 3.

The main objective of a controller is performance regulation and system optimization. Chiller performance is adequate if it meets cooling capacity requirements at

a specified cooling temperature. Absorption system control must accommodate external disturbances such as variations in ambient temperature, heat source temperature or demand variation in the form of cooling temperature and/or cooling capacity. An integral part of the controller is the mathematical description of the system that is regulated. The thermodynamic model plays a critical role in identifying and quantifying the most suitable control variables. The significance of the thermodynamic model is further increased if the definition of system performance is extended to include off-design *COP* and flexibility, i.e., part-load capacity control.

A brief discussion of the control of a packaged absorption system was presented in Chapter 2. A 7 kW cooling capacity, standalone chiller driven by natural gas was designed, fabricated and tested. Several control loops were identified for the achievement of autonomous steady state operation. Dilute solution temperature leaving the desorber, T_{hot}, was identified as an effective process variable for heat input control. Heat source coupling fluid flow rate and inlet temperature were used to achieve a fixed set point value for T_{hot}. Proportional regulation of gas input to a combustion unit through a feedback controller provided the required heat source coupling fluid inlet temperature at any given flow rate. Coupling fluid mass flow rate was set with a feedforward controller that scaled with total heat input. Solution pump speed was controlled with a feedforward control scheme that scaled with vapor generation rates. While the target operation was at a fixed, nominal capacity, solution pump speed was identified as an effective control variable for capacity control. Finally, a temperature glide control, ΔT_{glide}, of refrigerant across the evaporator was used as the process variable in a feedback control loop for the refrigerant expansion valve, which was also demonstrated by (Garimella *et al.*, 2016).

In this investigation, the initial system control work shown in Chapter 2 is extended to provide a general control strategy for vapor absorption systems with two main objectives:

- Flexible and fast response to changes in operation conditions and system load
- Optimal operation that minimizes energy input requirements and exergy destruction

The control strategy, based on the thermal compressor concept, the variable speed thermal compressor, is first described conceptually. The controller requires two core elements: first, a thermodynamic model that can be implemented in a controller and, second, a quantitative characterization of the actual system. The thermal compressor model developed in Chapter 3 is applied, eliminating the explicit specification of Thot, removing this variable as a required input variable. A data-driven system characterization model is developed for a specific absorption system. The latter is developed with a data set for a wide range of operating conditions. The methodology uses statistical techniques, e.g., regression and Artificial Neural Networks (ANN) to maximize predictive capability of the model, and the suitability of both methods for implementation in a controller is compared. The control strategy is also validated using an experimental investigation.

9.2 Control Strategy

The proposed control strategy is presented in several steps. First, the thermal compressor concept is reviewed and the benefit of its delineation from the remainder of the absorption cycle is shown. The overall controls objective and inputs for the thermal

compressor are defined. The core operating principle based on solution pump speed modulation is described, and its effectiveness as a control variable for response to variation in operating conditions is demonstrated. Then, detailed block diagrams for pump speed control and heat source regulation are presented and discussed. The significance of data driven models for thermodynamics and system characterization in this control scheme is illustrated.

9.2.1 Thermal Compressor Delineation

The thermal compressor has been used extensively in the literature as a qualitative descriptor to provide a conceptual analogy to the vapor compression cycle. Figure 9.1 shows the grouping of several components in the absorption cycle into a single entity that receives low pressure refrigerant vapor at the inlet and delivers high pressure refrigerant at the outlet. Quantitative characterization of this thermal compressor module, as shown by Chapter 3, has several advantages. It provides a simple way to analyze absorption cycles at a preliminary level similar to what is possible for vapor compression cycles.

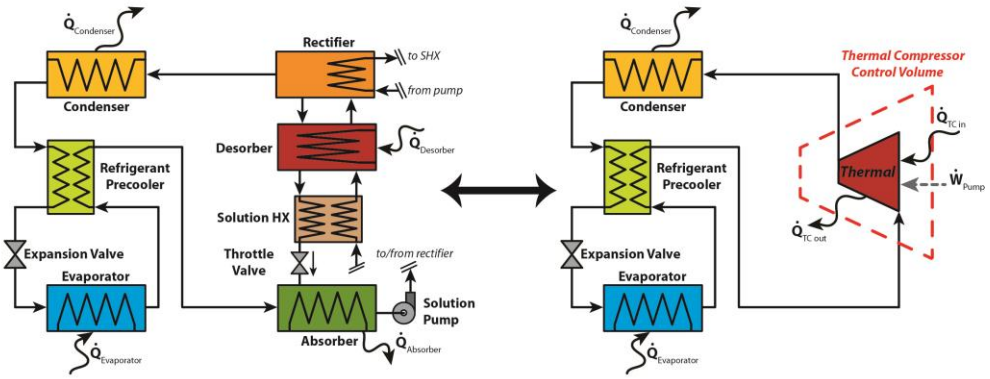

Figure 9.1: Absorption cycle (left), conceptual representation of thermal compression cycle (right)

Thus, it can be used to conduct preliminary screening of various thermal compressor configurations and identify optimal designs. In addition, it can be used to develop flexible and efficient control algorithms for absorption systems. The analogy to the mechanical compressor of a vapor compression cycle can also be used to benefit from the larger body of literature on vapor compression system control. Representative vapor compression control schemes are reviewed by Afram and Janabi-Sharifi (2014a, b) and Naidu and Rieger (2011a, b).

The evaporator refrigerant inlet temperature, T_{low}, and a non-dimensional capacity demand value, Θ, are the demand input values provided to the thermal compressor. Refrigerant production rates required by the thermal compressor vary with cooling load in the evaporator and are linked through Θ. T_{low} depends on evaporator pressure, P_{low}, which is affected by absorber saturated liquid solution conditions. Set points for both values, Θ and T_{low}, are determined through a separate feedback controller called the *refrigerant controller*. This controller adjusts both set points based on external cooling load and temperature input parameters, as well as evaporator characteristics, e.g., approach temperature between refrigerant inlet and chilled water outlet. This controller also governs refrigerant expansion valve operation. Typically, the refrigerant temperature difference between inlet and outlet, ΔT_{glide}, in the evaporator is used as the process variable for this controller. A block diagram for the delineation between refrigerant controller and thermal compressor control is shown in Figure 9.2. Thermal compressor heat sink temperature, i.e., ambient temperature, T_{amb}, can be considered a disturbance input to thermal compressor control. The subdivision into two controllers manages the complexity of absorption system control while maintaining the ability for flexible and

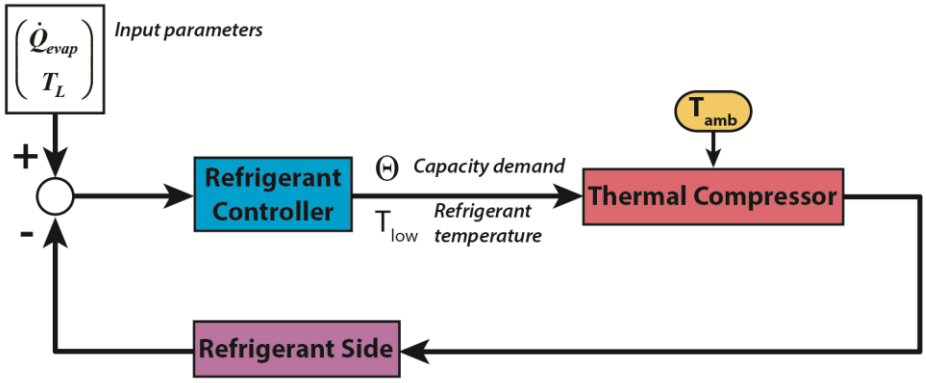

Figure 9.2: Block diagram showing delineation between refrigerant controller and thermal compressor control

optimal control. This facilitates additional overall system level optimization. For example, the refrigerant controller can dynamically adjust set points for Θ, T_{low} and ΔT_{glide} to optimize performance of the entire thermal system. With the focus on the thermal compressor here, additional detail about the refrigerant controller is beyond the scope of this study. However, since coupling between the refrigerant controller and thermal compressor control is accomplished through Θ and T_{low}, this delineation provides significant flexibility for the refrigerant controller. The set point for T_{low} is determined by the refrigerant controller to achieve a set point for the chilled medium, T_L, shown in Figure 9.2. Thus, this set point is determined based on specific evaporator characteristics, e.g., closest approach temperature (*CAT*), which are addressed by the refrigerant controller.

9.2.2 Variable Speed Thermal Compressor

The core element of the control algorithm is solution pump speed modulation. It is assumed that a positive displacement pump is employed in the solution circuit with a proportional relationship between pump speed and concentrated solution volumetric flow

rate. This provides the ability to effectively control ammonia mass fraction in the thermal compressor as well as solution flow rate. The former will be shown to effectively respond to variations in the set points for T_{low} and $T_{amb,}$ while the latter will be shown to effectively control thermal compressor capacity.

The value of P_{low}, and therefore T_{low}, is determined through the saturation conditions of concentrated solution in the absorber. At a given absorber temperature, i.e., ambient temperature, ammonia-mass fraction in the absorber can be actively adjusted to affect a change of P_{low}. This is illustrated in Figure 9.3. During baseline operation, a mass flow balance between thermal compressor inlet and outlet is maintained (Figure 9.3A). Vapor generation rates can be biased from the nominal target value dictated by the capacity demand input Θ. Two scenarios can be foreseen: "Overdrive mode" (Figure 9.3B) and "underdrive mode" (Figure 9.3C). In the former scenario, a positive bias causes the thermal compressor to produce more refrigerant vapor than is received. This causes a net migration of ammonia from the solution reservoir in the thermal compressor to the refrigerant reservoir at the condenser outlet. If absorber temperature is maintained constant, the reduction in ammonia-mass fraction at solution saturation causes a reduction

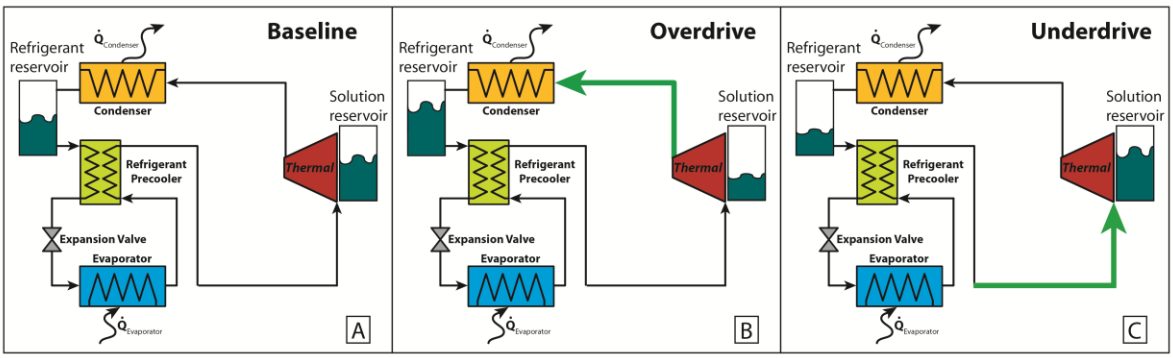

Figure 9.3: Various thermal compressor operating modes

in P_{low} and T_{low}. If the set point for T_{low} is unchanged, a higher absorber temperature, i.e., higher ambient temperature, can be tolerated while maintaining a constant P_{low} value.

In "underdrive mode" (Figure 9.3C), the inverse occurs. A negative bias for pump speed reduces vapor generation rates, causing a net flow of ammonia into the thermal compressor which is stored as increased ammonia mass fraction in concentrated solution. Absorber solution saturation conditions now require a lower temperature or a higher pressure. Thus, an increase in the set point for T_{low} can be achieved or a reduction in ambient temperature can be accommodated.

The block diagram for the variable speed thermal compressor is shown in Figure 9.4. The baseline capacity demand signal, Θ, is multiplied by the factor K_1 to provide a nominal pump speed signal. Simultaneously, a feedback controller compares the set point value for T_{low} with the corresponding process variable. This error is used to calculate a bias signal, K_2, that is multiplied with the nominal pump speed signal to provide the actual pump speed signal. The values of K_1 and K_2 are determined as discussed below.

9.2.3 Pump Speed Control

The use of data-driven control is demonstrated first with the detailed block

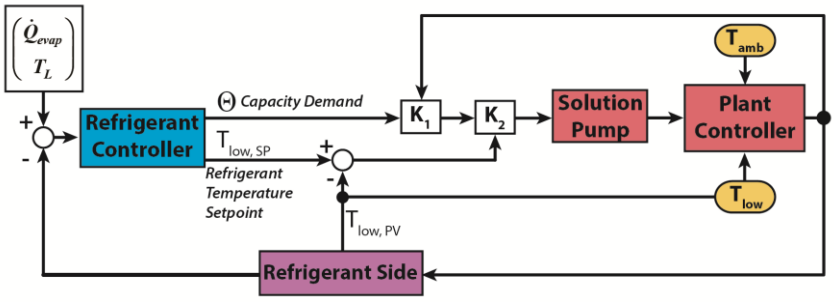

Figure 9.4: Block diagram of *variable speed* thermal compressor control

diagram for solution pump speed control. This is shown in Figure 9.5. This block diagram also provides details about the calculation of values for K_1 and K_2 in Figure 9.4. Measurement inputs are used in a system characterization model to provide estimates for concentrated solution density, ρ_{cs}, and circulation ratio, $CR = \dot{m}_{cs} / \dot{m}_{ref}$. The latter scales refrigerant flow demanded by the refrigerant controller to concentrated solution mass flow rate, $\dot{m}_{cs}$, while the former converts solution mass flow rate to volumetric pump flow rate demand. These results are multiplied with a baseline capacity demand from the refrigerant controller and a scaling constant, providing a nominal volumetric flow rate demand to the solution pump. A separate feedback controller is used to meet the set point for T_{low}. The controller provides an additional bias factor for volumetric pump flow rate demand. The nominal bias factor value is unity but a ±0.2 variation can be imposed to effect a concentration shift into or out of the thermal compressor as discussed with respect to Figure 9.3. Finally, a pump characterization model is used to correlate volumetric pump flow to pump speed to provide a proportional signal, e.g., frequency for an alternating current pump motor.

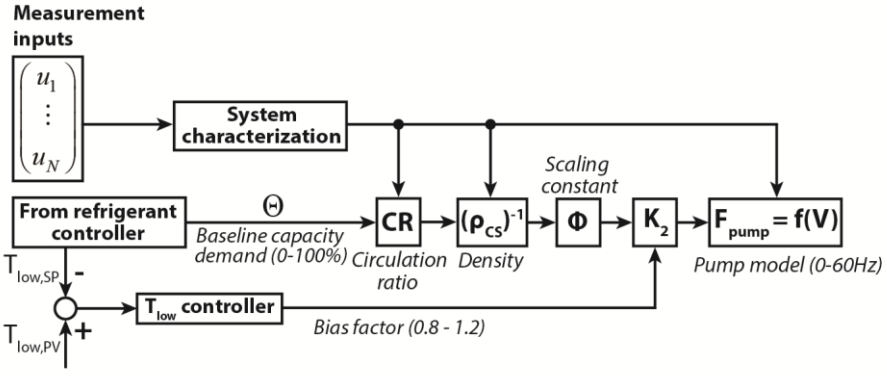

Figure 9.5: Pump speed control

9.2.4 Heat Source Control

The plant controller discussed above is mainly responsible for providing optimal regulation of desorption temperature and heat source flow rate. As shown in Chapter 3 and discussed below, desorber dilute solution outlet temperature, T_{hot}, is an effective process variable to control optimal thermal compressor performance. But optimal desorption temperature depends on operating conditions and must be determined with a thermodynamic model. Therefore, the thermodynamic model is the second model layer of this control scheme, which is also a data-driven model developed with statistical analyses. The heat source control scheme is shown in Figure 9.6 for two implementation

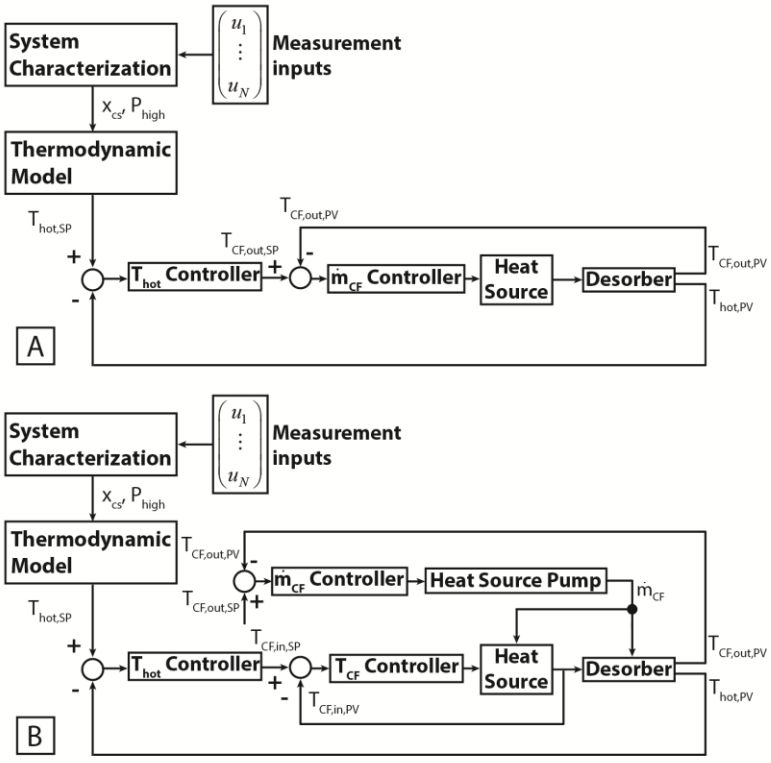

Figure 9.6: Heat source control for desorption. A: without heat source temperature control. B: with heat source temperature control

types: with and without the ability for active heat source temperature control. Measurement inputs are used with the system characterization, i.e., the first model layer. Results of the first layer are used as inputs to the thermodynamic model which, in turn, provides a set point for desorption temperature. A feedback controller is used to achieve a set point for T_{hot}.

Figure 9.6A shows a control scheme where active heat source temperature control is not available. For example, direct coupling of the desorber to an exhaust gas stream for waste heat recovery applications may not provide the ability to actively control heat source temperature. However, it is assumed that mass flow can be actively controlled with, for example, an exhaust gas bypass damper. Figure 9.6A shows how the T_{hot} controller output determines the set point for heat source outlet temperature from the desorber, $T_{CF,out}$. The limits of this set point can be adjusted continuously by the controller to reflect current operating conditions. Heat source mass flow variation affected by the T_{CF} controller results in a temperature profile variation in the desorber. This, in turn, affects overall desorber heat transfer rate and a change in T_{hot}.

Figure 9.6B shows heat source integration that allows for active heat source temperature control. Here, the T_{hot} controller determines a set point for the heat source entering the desorber. The T_{CF} controller then seeks to meet that set point through actively regulating heat source energy input, e.g., through fuel input control to a combustion module. Heat source mass flow is regulated with an additional controller similar to Figure 9.6A where the heat source outlet temperature is used to determine mass flow. In the example of a liquid-coupled heat source, a constant displacement pump with variable speed control can provide the final control element. In the experimental portion

of this investigation, the control scheme shown in Figure 9.6B is implemented. Heat source energy input modulation is simulated with a proportionally controlled electric heater. A thermal oil coupling fluid loop and constant displacement pump are used to provide heat source mass flow control. The value of $T_{cf,out,SP}$ is determined by maintaining a relatively constant temperature profile, defined by the ratio of temperature differences between solution and coupling fluid at the desorber top and bottom locations, ΔTR_{CF}, as shown in Eq. 9.1. It is maintained at a value of approximately $\Delta TR_{CF} = 3$ for all tests. A more detailed discussion about the effect of heat source temperature profile was given in Chapter 5.

$$\Delta TR_{CF} = \frac{T_{CF,out} - T_{cs,des,in}}{T_{CF,in} - T_{hot}} \tag{9.1}$$

Both temperature control schemes for T_{hot} shown in Figure 9.6 use a cascaded controller. Heat source mass flow (Figure 9.6A) or heat source temperature Figure 9.6B) receive set point inputs from a primary T_{hot} feedback controller. While the output from the primary controller could be used directly with the final control element, e.g., fuel supply or damper position, it was found that the secondary, cascaded controller provides additional tuning ability to improve response time and stability.

9.3 Thermodynamic Model

A thermodynamic model enables the identification and quantification of the most suitable process and control variables, and can be used to achieve continuous system optimization and flexibility. Specifically, an accurate thermodynamic model will allow precise and fast response to changes in ambient and evaporator temperature while

maintaining highest possible *COP*. Capacity control and part-load operation can be optimized through accurate thermodynamic models. Goyal *et al.* (2018) provide a detailed review of the significance of thermodynamic models to absorption system control. Various types of models were reviewed in Chapter 3. It was noted that thermodynamic models range from highly detailed thermodynamic cycle studies to black-box type models. The former requires a high number of inputs with few assumptions and provide a high number of model outputs while the latter is purely based on available data without the requirement of physical insight and assumptions. While control systems benefit from the accuracy of detailed thermodynamic models, complexity prohibits their implementation in a model based controller.

This limitation was addressed in Chapter 3 by bridging both modeling approaches. Statistical methods, e.g., regression analyses and Artificial Neural Networks (ANN) were used for a large data set generated with a detailed thermodynamic model for the thermal compressor over a wide range of operating conditions. The results of this characterization provide simple and accurate algebraic equations for key variables needed in the model based controller developed in this study. Specifically, the temperature of dilute solution leaving the desorber, T_{hot}, was identified as an important process variable. Two optimal temperatures, $T_{opt,I}$ and $T_{opt,II}$, were identified to optimize first- and second-law performance of the thermal compressor, respectively. Effective independent variables were identified as concentrated solution concentration, x_{cs} and high side pressure, P_{high}. Results of the regression analysis are shown in Eqs. 9.2 and 9.3 for the range $0.30 \leq x_{cs} \leq 0.64$ and $0.30 \leq P_{high} \leq 0.64$.

$$T_{opt,I} = -9.96\times10^{1} + 2.8\times10^{-2}P_{high} + 8.5\times10^{-6}P_{high}^{2} - 2.54\times10^{-9}P_{high}^{3} + 1.9\times10^{3}x_{cs} - 5\times10^{3}x_{cs}^{2} + 3.67\times10^{3}x_{cs}^{3}\left(\mathbf{R^2=99.88\%}\right) \quad 9.2$$

$$T_{opt,II} = 2.19\times10^{2} + 4.41\times10^{-2}P_{high} - 3.68\times10^{-6}P_{high}^{2} - 5.04\times10^{2}x_{cs} + 2.77\times10^{2}x_{cs}^{2}\left(\mathbf{R^2=99.90\%}\right) \quad 9.3$$

It was shown that x_{cs} depends directly on heat sink temperature, T_{amb} and evaporator refrigerant inlet temperature, T_{low}. It was further demonstrated that T_{low} is an adequate proxy variable for P_{low} despite binary mixture effects. Hence, Equations 9.4 and 9.5 were developed to quantify the independent variables for a range of 20°C ≤ T_{abs} ≤ 55°C and -20°C ≤ T_{low} ≤ 20°C.

$$x_{cs} = 7.72\times10^{-1} + 9.80\times10^{-3}T_{low} + 2.67\times10^{-5}T_{low}^{2} - 9.03\times10^{-3}T_{abs,sat} + 3.44\times10^{-5}T_{abs,sat}^{2} - 6.26\times10^{-5}T_{low}T_{abs,sat} \quad 9.4$$

$$P_{high} = 5.64\times10^{2} + 5.64T_{con,sat} + 4.68\times10^{-1}T_{con,sat}^{2} \quad 9.5$$

$T_{abs,sat}$ and $T_{con,sat}$ can be determined through a system specific characterization as shown in Eqs. 9.6 and 9.7 where ΔT_{abs} and ΔT_{con} are determined from system specific data. Various cycle configurations and component types can be accommodated by this methodology. A different data set can be generated from a modified detailed thermodynamic model to update the equation set presented in this study.

$$T_{abs,sat} = T_{amb} + \Delta T_{abs} \quad 9.6$$

$$T_{con,sat} = T_{amb} + \Delta T_{con} \quad 9.7$$

9.4 System Characterization through Data

Implementation of the thermodynamic model requires knowledge of x_{cs} and P_{high}. Additional variables needed for the thermodynamic model based controller are low side pressure, P_{low}, concentrated solution density, ρ_{cs} as well as dilute solution concentration, x_{ds}. In addition, the relationship between constant displacement pump speed and solution mass flow rate is established.

9.4.1 Data Set

An extensive data set with over 500 data points was collected in an experimental investigation of the thermal compressor presented in Chapters 6 and 7. In these studies, a test facility for the thermal compressor that included a microchannel based desorber and rectifier was constructed. More detail of these core components was presented Chapter 5. Additionally, an absorber, solution heat exchanger and condenser were included to enable simulation of realistic absorption heat pump conditions. A proportionally controlled electric heater with a thermal oil coupling was used for desorber heat input. A constant displacement gear pump was used with a variable pump speed controller to regulate desorber heat source coupling fluid flow rate. Similarly, a constant displacement diaphragm pump was used as a solution pump with a variable speed controller. Electronic proportional valves were used for dilute solution throttling and refrigerant expansion. The system was operated at split pressures, i.e., P_{high} and P_{low} values that correspond to realistic absorption system conditions. Temperature, mass flow rate and pressure measurements were taken to allow for complete thermodynamic definition at all points in the cycle and accurately determine heat and mass transfer rates. P_{high} and x_{cs} were varied

independently throughout a test matrix to obtain data for a wide range of operating conditions. A detailed description of test facility, instrumentation and test matrix was given in Chapter 6. In the present study, the data are used with statistical methods, e.g., regression analyses and ANN, to develop a system characterization. Generally, it is desirable to obtain simple, algebraic equations with high accuracy for ease of model implementation in a controller, and avoidance of overfitting. While a regression analysis may achieve this, an ANN analysis may be required if no acceptable regression results are available. Both methods and their applicability to the present investigation will be compared.

9.4.2 Low-side Pressure

The use of T_{low} as an adequate proxy variable for P_{low} was discussed in Chapter 3. This eliminates P_{low} as a required input variable to the model based controller and reduces instrumentation requirements in an actual system. With the assumption of a nominal refrigerant ammonia mass fraction, x_{ref}, of 0.99 and evaporator inlet quality of 0.1, Eq. 9.8 provides an accurate prediction of P_{low} (kPa) as a function of T_{low} (°C) (R^2 = 99.99%). The equation is not system specific and may be treated as a thermodynamic state equation for ammonia-water absorption systems under the assumptions stated above for a range of -20°C ≤ T_{low} ≤ 20°C. Figure 9.7 shows excellent agreement between the data and the predictions of this equation, validating the use of T_{low} as a proxy variable for P_{low}, despite binary mixture effects during evaporation. Therefore, T_{low} can replace P_{low} as an input variable in a model-based controller. It also reduces sensor requirements by eliminating the need to measure P_{low} directly, and instead using, inexpensive temperature

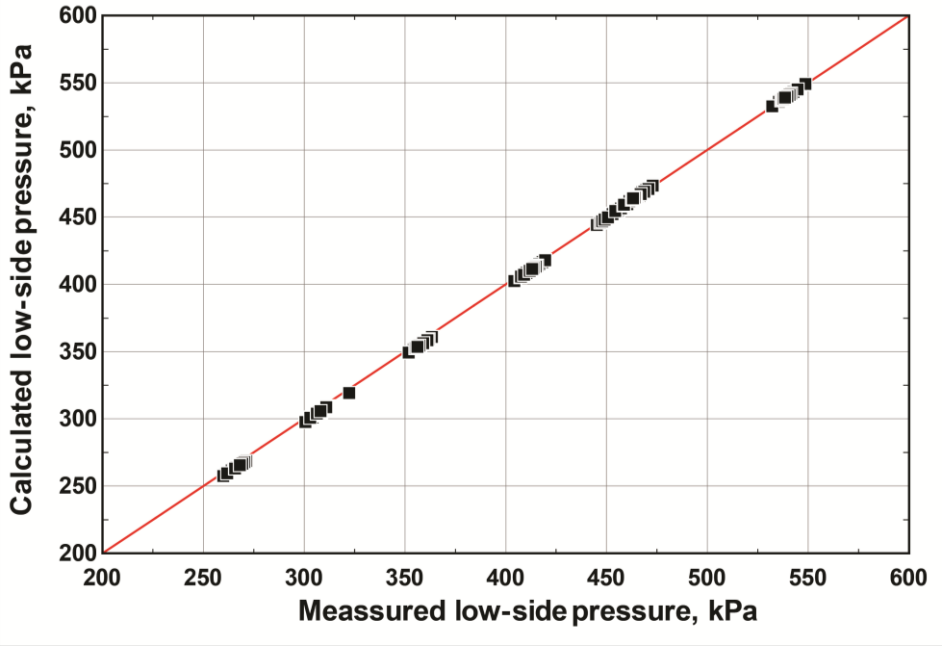

Figure 9.7: Low-side pressure prediction through evaporator inlet temperature

measurements. A regression analysis yielded this relatively simple but accurate result, obviating the need for ANN analysis for P_{low} prediction.

$$P_{low} = 425 + 16.3T_{low} + 0.233T_{low}^2 \qquad 9.8$$

9.4.3 Concentrated Solution Ammonia Mass Fraction

Real-time, in-situ measurement of ammonia mass fraction is not economically feasible due to instrumentation requirements. A regression analysis and ANN were used to provide a system specific prediction of x_{cs} based on Eqs. 9.4 and 9.6. Input variables to this model are absorber heat sink inlet and outlet temperature, solution outlet temperature, and T_{low}. Results shown in Figure 9.8 demonstrate that x_{cs} can be predicted through temperature inputs alone. This provides the controller with a real time estimate of x_{cs} for use in Eq. 9.4 as well as for other calculations. Both statistical methods provide

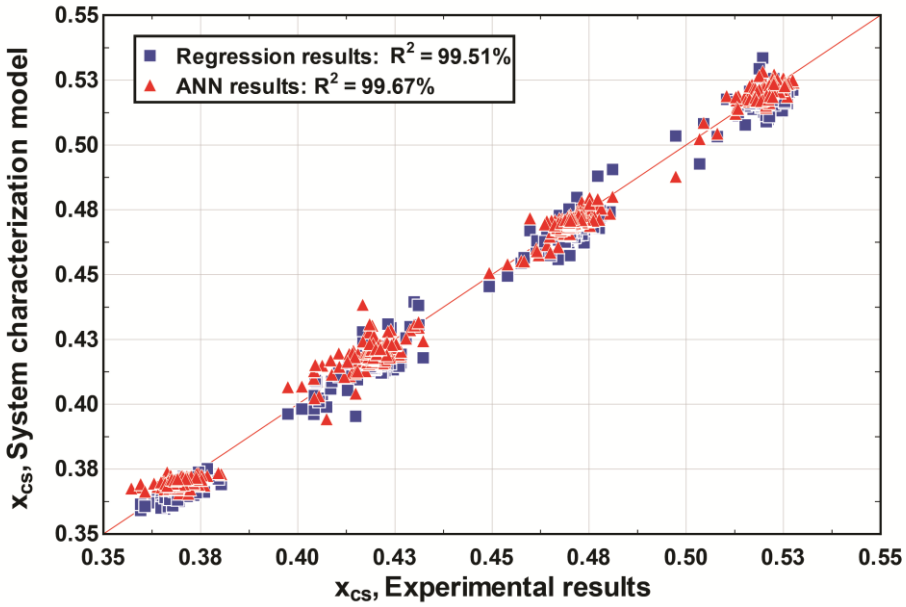

Figure 9.8: Concentrated solution ammonia mass fraction prediction

comparable results with high R^2 values. The use of ANN for this analysis is preferred because additional data can be used "retrain" the network, further increasing accuracy and avoiding overfitting. The regression result produced a relatively complex expression and does not provide a significant benefit at the implementation stage over ANN.

9.4.4 Solution Mass Flow Rate

The use of a constant displacement solution pump provides the ability to accurately control and estimate flow rates. Pump speed is proportional to volumetric flow rate, $\dot{V}_{cs}$, and a simple, directly proportional relationship was determined with a regression analysis of the data set as shown in Figure 9.9. This validates the use of pump speed to directly control and obtain a real time estimate for solution flow rate. Volumetric solution flow rate is multiplied with a density estimate to determine solution mass flow. An explicit expression for concentrated solution flow rate, i.e., ρ_{cs} = *f(Tlow,xcs)* was

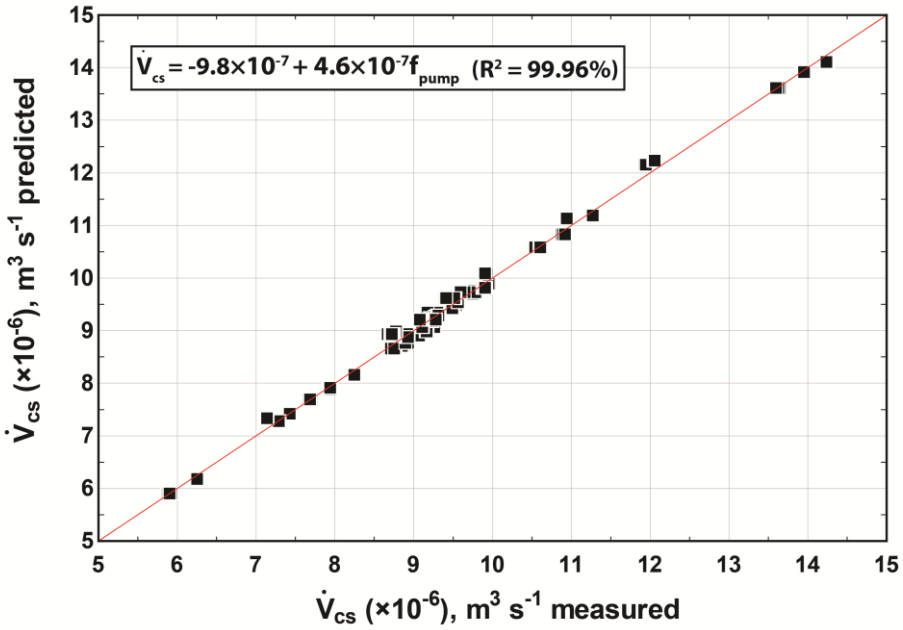

Figure 9.9: Solution volumetric flow rate prediction with solution pump speed

determined (R2 = 99.97%) from the same data set used to develop Eqs. 9.4 and 9.5. Using real time estimates for xcs and measurement of Tlow, $\dot{m}_{cs}$ can be determined and pump speed can be modified to achieve a target value as shown in Figure 9.5 and discussed above.

9.4.5 Dilute Solution Ammonia Mass Fraction and Circulation Ratio

Refrigerant and dilute solution flow rates can be determined from concentrated solution flow rate if the circulation ratio is known. Circulation ratio (*CR*) can be defined as shown in Eq. 9.9.

$$CR = \frac{x_{ref} - x_{ds}}{x_{cs} - x_{ds}} \qquad 9.9$$

Given that values for x_{ref} are very close to 1, it has very little effect on *CR* and a nominal fixed value, e.g., x_{ref} = 0.99, can be assumed. Knowing P_{high} and T_{hot} from direct measurements, x_{ds} can be directly determined through a saturated liquid assumption at the dilute solution desorber exit. A data set for the range of 1100 kPa $\leq P_{high} \leq$ 2600 kPa and the full possible range of T_{hot} at each pressure was generated, forming the basis of a regression analysis that provided an expression for x_{ds} with a coefficient of determination of R^2 = 99.92% shown in Eq. 9.10.

$$x_{ds} = 0.656 + 2.6\times10^{-4} P_{high} - 2.3\times10^{-8} P_{high}^2 - 6.3\times10^{-3} T_{hot} + 9.8\times10^{-6} T_{high}^2 - 4\times10^{-7} P_{high} T_{high} \quad 9.10$$

This expression is based on thermodynamic properties and is, therefore, similar to an equation of state for saturated liquid at specified pressure and temperature. The value for *CR* is then used with the model based controller. Dilute solution mass flow rate $\dot{m}_{ds}$ can now also be determined for active control. In this study, a separate feedback control loop was used to modulate a proportional dilute solution throttling valve to achieve the calculated $\dot{m}_{ds}$ value. This required a mass flow meter for $\dot{m}_{ds}$ process variable feedback. In an actual system, a feedforward valve controller can be used with a characteristic mass flow curve to provide $\dot{m}_{ds}$ control. Discrete level switches in the desorber for high and low liquid accumulation can be used to provide corrections to the feedforward $\dot{m}_{ds}$ controller. A regression analysis allowed for the determination of an accurate and relatively simple expression for x_{ds}. An ANN analysis was, therefore, not conducted for this variable.

9.4.6 Robustness and Model Corrections

The robustness of the model controller depends on uncertainties associated with the thermodynamic model, system-specific characterization, and data used for model inputs. An uncertainty propagation of the complete model is used to assess its robustness. Using standard deviations of the absolute error between model predictions in Equations 9.2 and 9.3 and their underlying data sets, uncertainties for $T_{opt,I}$ and $T_{opt,II}$ are ±0.4°C and ±0.7°C, respectively. Using the same procedure for x_{cs}, the uncertainty due to errors between predictions and the data (Figure 9.8) is ±1%. The x_{ds} correlation uncertainty for Eq. 9.10 was determined to be ±3%. Solution density and volumetric flow rate prediction through pump speed have correlation uncertainties of ±0.5% and ±1.1%, respectively.

In addition to the correlation uncertainty, model inputs obtained from instrumentation, i.e., temperature and pressure measurements, introduce uncertainty. A calibrated thermocouple uncertainty of ±0.25°C and a pressure transmitter uncertainty of ±1% are assumed. A nominal refrigerant ammonia mass fraction at the thermal compressor outlet with uncertainty of x_{ref} = 0.99±0.01 is assumed. The thermodynamic and system characterization models are combined with the steady-state data set to conduct an uncertainty propagation using Engineering Equation Solver software (Klein, 2015). Expected uncertainties for optimal temperature set points are $\Delta T_{opt,I}$ = ±2°C and $\Delta T_{opt,II}$ = ±2°C. Uncertainties in pressure measurement as well as x_{cs} are the primary causes for this uncertainty. This is well within acceptable limits given that performance curves for the thermal compressor are relatively flat around optimal temperatures (Chapter 3). Uncertainties in volumetric flow rate prediction based on pump speed and circulation ratio prediction based on x_{cs} and x_{ds} cause an expected error of the control

scheme shown in Figure 9.5 of ±4%. This is also acceptable because the proposed control scheme is inherently self-correcting. This error manifests itself in either the depletion or accumulation of ammonia in the thermal compressor. This, in turn, causes set point deviation of T_{low} and response of the bias controller shown in Figure 9.4. In addition, the controller can incorporate a correction scheme, whereby the scaling constant, Φ, as shown in Figure 9.5, is modified. Specifically, Φ can be multiplied with the bias factor if the bias controller output remains at the upper or lower limit beyond a specific maximum duration.

The methodology for system characterization can be readily applied for a generic system with an operational data set. System specific characterization for x_{cs} and pump flow are unique to a particular system. The solution pump can be characterized using manufacturer data. Thus, the only system-specific characterization that requires operational data is the prediction of x_{cs}. The thermodynamic state equations developed in this study are generally valid for the specified range and assumptions. An ANN analysis is recommended for the prediction of x_{cs}, while relatively simple regression results can be applied for all other results.

9.5 Experimental Facility and Algorithm Implementation

The experimental facility described above (Chapter 6) was used to conduct a series of transient tests to investigate system response to changes in operating condition. The control scheme and both data-driven model layers, thermodynamic and system characterization, were implemented in a Process Automation Controller (PAC) by National Instruments™ (NI). The CompactRIO® embedded controller was used with all input and output modules required for data acquisition. The control scheme was

integrated with NI LabVIEW® software. Proportional-integral-derivative (PID) controllers were implemented for all feedback loops. Controller tuning exercises achieved fixed values for proportional gain, integral time and derivative time. During the initial testing phase, it was also found that the cascaded heat source control scheme as shown in Figure 9.6 and discussed above enables faster response than direct heat source control through desorption temperature control. This step adds minimal complexity to the control scheme but significantly improves system response. Validation of the control strategy included the following six response tests:

1) **Ambient temperature variation:**
    a) Increase in ambient temperature
    b) Decrease in ambient temperature
2) **Evaporator refrigerant inlet temperature target:**
    a) Increase in evaporator temperature target
    b) Decrease in evaporator temperature target
3) **Response to demand variation of thermal compressor refrigerant supply**
    a) Thermal compressor refrigerant supply demand increase
    b) Thermal compressor refrigerant supply demand decrease

9.5.1 Ambient Temperature Variation

An increase in ambient temperature was simulated by increasing the heat sink temperature of the absorber and condenser. In this study, a coupling fluid loop connected to a chilled water system was used as the heat sink for the system. The experimental facility includes active heat sink temperature control for the simulation of ambient temperature variation. Figure 9.10 shows thermal compressor response as a result of the

control strategy developed in this study. A continuous increase in heat sink temperature from 30°C to 40°C begins at 200 seconds over a five minute period. The set point for T_{low} is maintained constant at 3.5°C. An immediate increase in refrigerant temperature and low side pressure occurs as expected. The bias controller automatically reacts to the deviation of T_{low} from its set point and pump speed is increased, resulting in an increase

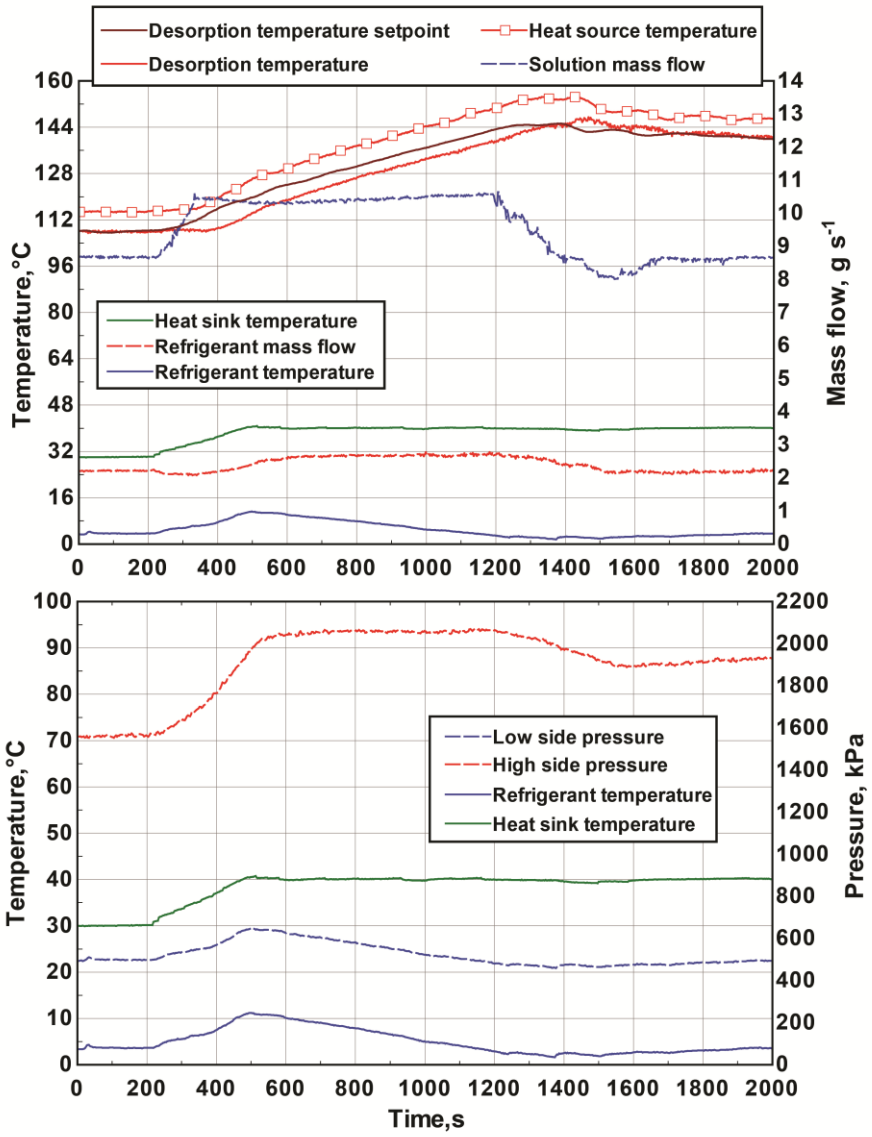

Figure 9.10: System response to increase in ambient temperature

in solution mass flow rate as shown in the top graph. The "overdrive mode" results in net ammonia reduction in the thermal compressor, lowering x_{cs}. This has the effect of reducing P_{low} as well as T_{low} as shown in the bottom graph. As T_{low} is reduced to its set point value, the bias controller reduces pump speed to return to baseline solution mass flow rates. It can be seen that refrigerant mass flow rate, $\dot{m}_{ref}$, is increased during "overdrive mode" but returns to its initial value once the response to the increase in T_{amb} is completed. During this process, x_{cs} decreased from 0.52 to 0.46 to accommodate the increase in absorber temperature while maintaining constant T_{low}. Condenser pressure also increases, as expected. During the transient process, condenser pressure is actually greater than the final condenser pressure due to the increased refrigerant flow and condenser load during "overdrive mode" as shown in the bottom graph of Figure 9.10. In response, the heat source controller requires a higher desorption temperature, T_{hot}, as shown in the top graph. The model based controller varies $T_{hot,SP}$ from an initial value of 108°C to 139°C which corresponds to the change in $T_{opt,I}$. A heat sink temperature reduction was also tested in this study and produced the opposite behavior. Both tests show that this control scheme can autonomously respond to heat sink variations in a stable and effective manner.

9.5.2 Evaporator Refrigerant Inlet Target Temperature Variation

The refrigerant controller may require a change in the set point of T_{low}. This could be due to user requirements or a system-level optimization scheme. The proposed control strategy can accommodate T_{low} set point variations as shown in Figure 9.11. The system initially operates at steady state with a set point for T_{low} of -5°. At 300 seconds, a step

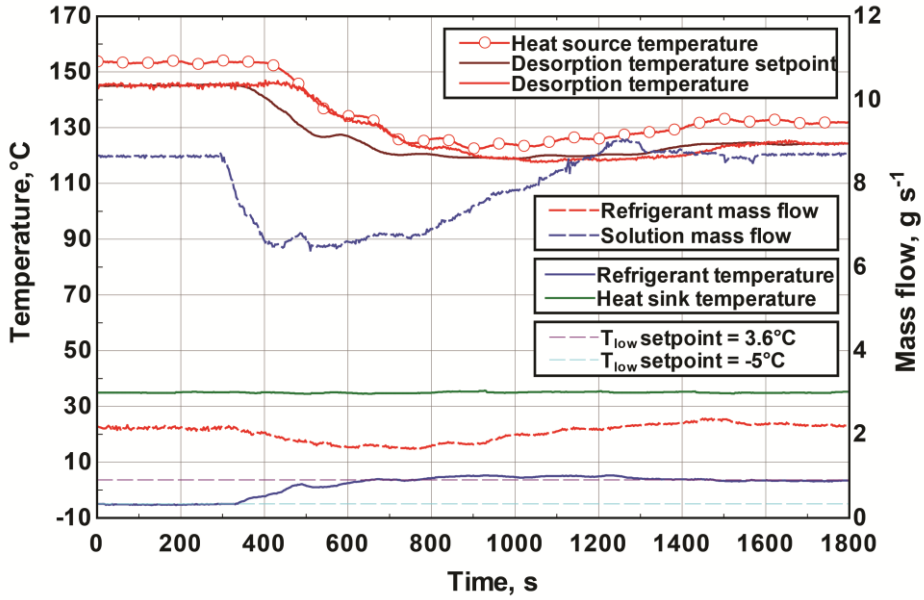

Figure 9.11: System response to change in setpoint of T_{low}

change in the set point for T_{low} to 3.6°C occurs. The bias controller responds by reducing the bias factor for "underdrive mode". This results in a net positive ammonia flow into the thermal compressor and x_{cs} increases. As the heat sink temperature is maintained constant, the saturation conditions in the absorber result in a higher value of P_{low} and an increase in T_{low}. The new set point for T_{low} was achieved after 350 seconds, demonstrating fast response. A small overshot occurs while the bias controller moves from "underdrive mode" to baseline operation. Refrigerant mass flow after the transient response is identical to that prior to the set point change of T_{low} as baseline demand was unchanged. The net increase of ammonia in the thermal compressor results in a change of x_{cs} from 0.43 to 0.49, and the heat source temperature requirement, i.e., $T_{opt,I}$, decreases commensurately. A small reduction in P_{high} can be observed during the transient due to a temporary decrease in $\dot{m}_{ref}$, but the final value is virtually identical to the initial pressure, given that condenser load and heat sink temperatures are maintained constant. This test

shows that the *variable speed thermal compressor* control strategy can provide effective control of set point changes for T_{low}.

9.5.3 Response to Thermal Compressor Capacity Demand Variation

An important aspect of the proposed control strategy is the ability of continuous turndown, i.e., capacity reduction to meet refrigerant flow rate demands. This ability eliminates the need for on/off control, enabling effective response to dynamic load patterns. The functionality was tested by simulating a rapid variation of the baseline demand signal issued by the refrigerant controller. The results are shown in Figure 9.12. Heat sink temperature is maintained at a constant value and low-side pressure is also nominally constant. At 350 seconds, a series of step changes to the baseline demand signal increases thermal compressor load from 44% to full capacity. During this process, very fast response of refrigerant mass flow rate follows. This shows that the time constant associated with this particular thermal compressor configuration is relatively short, allowing for flexible control strategies. The shape of the input, i.e., a series of step changes was chosen arbitrarily. Further optimization of thermal compressor response can be investigated with various input transient shapes. This includes detail about specific refrigerant controller configurations and is beyond the scope of this study. While condenser heat sink temperature is maintained constant, the capacity change results in an increase in P_{high} as condenser load is also increased. The condensation saturation temperature increases in response. This causes in an increase in $T_{opt,I}$ and, therefore, a model prescribed increase in the set point for T_{hot} from 117°C to 130°C as shown in the top graph of Figure 9.12. This shows that optimal operation is affected not only by operating temperature, i.e., T_{low} and T_{amb}, but also through system load. This is due to

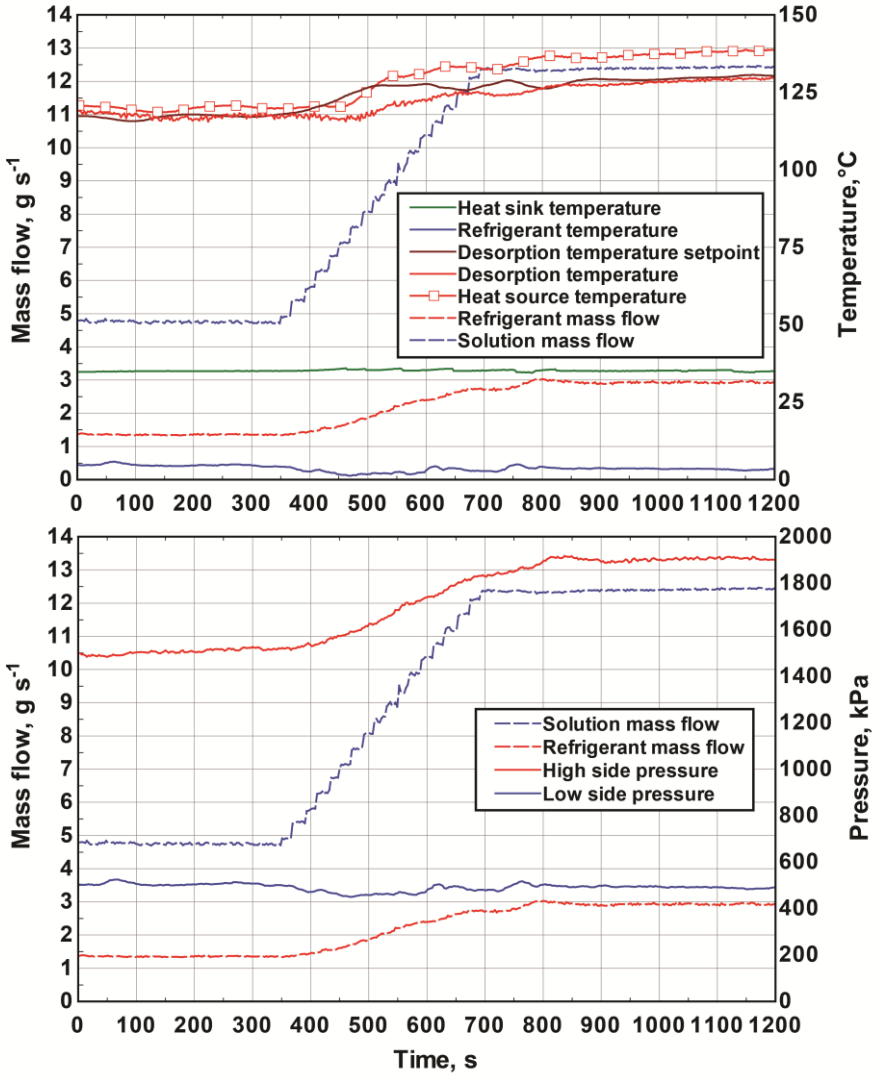

Figure 9.12: System response to increase in capacity demand

fixed heat exchanger sizes that result in different approach temperatures as flow rates are varied. While this results in different temperature lift values and affects system *COP*, active control of $T_{opt,I}$ minimizes these effects on system performance. A capacity reduction test was also conducted with exactly the opposite results, e.g., immediate reduction of refrigerant flow, lower P_{high} and $T_{opt,I}$. Both tests validate continuous capacity modulation as the core functionality of the *variable speed thermal compressor*.

9.6 Conclusions

A control strategy for ammonia-water absorption systems was developed. The concept of the thermal compressor and its significance to effective control of absorption systems was reviewed. The *variable speed thermal compressor* controller, based on a data-driven, model-based control strategy, was presented. A detailed thermodynamic model for the thermal compressor is reduced to simple algebraic equations for implementation in a controller using statistical methods. The system was also characterized using data-driven, statistical methods to determine state points. This approach reduces the number of model input variables as well as sensor requirements. Desorption temperature was eliminated as a required input variable by using optimal values dictated by a thermodynamic model. Evaporator temperature was shown to be an effective proxy variable for pressure despite binary mixture effects during evaporation. A comparison between regression analysis and ANN was made, showing that regression analyses are largely sufficient but ANN is beneficial for prediction of concentrated solution mass fraction. Solution pump speed was shown to be an effective control variable. An experimental validation demonstrated the functionality of this control strategy by achieving accurate and fast responses to changes in heat sink temperature, evaporator temperature set point, and thermal compressor vapor production rate demand. Much of the complexity associated with absorption system control is addressed with this control scheme and contained within the thermal compressor control module. The flexibility of the control scheme facilitates integration with a refrigerant controller. The analogy to vapor compression cycles allows for the cross-application of research results for vapor compression control to effectively design a refrigerant controller. The results of

this study address an important aspect for further development and adoption of absorption technology to achieve increased thermal energy utilization.

CHAPTER 10. CONCLUSIONS AND RECOMMENDATIONS

10.1 Conclusions

A comprehensive optimization study of the thermal compressor for small-capacity ammonia-water absorption systems was conducted. The results of a system-level investigation identified optimization of the thermal compressor as the primary research focus for further development of small-capacity absorption technology. For this system-level investigation, a 7-kW cooling capacity chiller, driven with natural gas was developed. The purpose of this development was to demonstrate the feasibility of small-capacity absorption systems through the use of microchannel heat exchangers. This included thermodynamic cycle modeling, heat exchanger design, and fabrication of a standalone, compact system. Scale-up of microchannel heat exchangers from prototype to component level scales was demonstrated. Integration of the heat and mass exchangers into two monolithic assemblies reduced overall system size. Target cooling capacity of 7 kW at a chilled water deliver temperature of 7.2°C and ambient temperature of 35°C was achieved. An overall system *COP* value of 0.44 was demonstrated. This is in contrast to a *COP* value of 0.53 predicted with the thermodynamic system model. Performance discrepancy was determined to be caused by lower-than-expected vapor generation and purification efficiency.

This system level investigation demonstrated the feasibility of small-capacity ammonia-water absorption using microchannel heat exchangers. While thermal compressor optimization was identified as the main research objective for further development of this technology, it was shown that particular focus needs to be directed

toward the development of effective desorption and rectification components. Both components are key elements of the thermal compressor determining performance, size and weight. Advances in system control were demonstrated, but further development of absorption control strategies was recommended to increase operational autonomy and continuous optimization. A list of research objectives for thermal compressor optimization was presented. These objectives include the production of high purity refrigerant vapor while minimizing energy and exergy demands, minimization of component size and weight, use of various heat sources, and flexible and optimal thermal compressor control. These research objectives motivated the remainder of this study.

A series of research tasks was identified in order to systematically address the listed objectives for thermal compressor optimization. These tasks consist of thermodynamic considerations, hydrodynamic considerations, heat and mass transfer model development and the development of optimal thermal compressor control strategies. The results of these tasks resulted in the development of novel desorption and rectification designs as well as a novel control strategy for optimized absorption system operation. Finally, an experimental investigation validated the solutions developed in this study.

The development of a thermodynamic framework for the thermal compressor was presented. A thermal compressor efficiency based on exergetic performance was defined. The heat input per unit mass of refrigerant produced was defined as an alternative figure of merit based on energetic considerations. It was shown that dilute solution temperature leaving the desorber, T_{ds}, is a suitable independent variable for the optimization of both figures of merit. Optimal T_{ds} values exist that maximize exergetic and energetic thermal

compressor performance. It was further shown that exergetic optimization occurs at a lower T_{ds} value than energetic optimization, i.e., $T_{opt,II} < T_{opt,I}$. An analytic justification that generalized this finding was provided.

The thermodynamic model was applied in a comparative study to identify the optimal configuration for desorption and rectification components in a single-effect cycle. It was shown that the application of diabatic distillation principles to the design of the desorber and rectifier results in increased thermal compressor performance and is conducive to the development of highly compact components. Finally, a statistical approach was used to develop a generalized thermal compressor model for the optimal configuration. Regression and Artificial Neural Networks were used to develop a model for the prediction of important thermal compressor parameters such as $T_{opt,II}$ and $T_{opt,I}$. Results of this part of the study provide guidance for the development of desorption and rectification components. These results also provide a quantitative thermal compressor module that facilitates absorption cycle design and can be incorporated into the development of optimal thermal compressor control strategies.

Two desorption and one rectification design concepts were developed based on diabatic distillation principles. Two different desorption designs enable a wide range of applications for the thermal compressor. A microchannel based desorber design provides a compact solution if the heat source is available in a liquid stream, e.g., a thermal oil. Alternatively, a direct-coupled desorber design is presented for application where the heat source is in the form of a gas stream, e.g., direct-coupled exhaust gas heat recovery.

A hydrodynamic investigation was conducted to validate the feasibility of the proposed desorption and rectification design concepts. These designs rely on liquid-vapor

countercurrent flow that is subject to two limitations, activation and flooding. A design methodology based on the approach by (Wallis (1969)) was applied to specify relevant geometric features while maintaining target flow patterns for a wide range of operating conditions. An air-water experiment was used to simulate hydrodynamic conditions in ammonia-water systems at typical operating conditions. The hydrodynamic feasibility of all design concepts was established.

The hydrodynamic investigation also included high-speed flow visualization. Hydrodynamic parameters relevant for heat and mass transfer were identified and quantified in the flow visualization study. These parameters include liquid-vapor interfacial area, bubble sizes and velocities, and heat transfer areas. Correlations for these parameters as a function of superficial gas velocity were developed and can be directly used in a heat and mass transfer model.

Heat and mass transfer models were developed. Various correlations for pool boiling and binary mixture correction were compared. It was shown that the choice of pool boiling correlations has little effect on overall component performance predictions. The choice of correlation for the binary mixture correction factor results in significantly greater variation in model predictions. This is indicative of a lack of understanding of mixture effects during boiling.

All design concepts were successfully fabricated. The thermal compressor concept was investigated and it was shown that optimal operating temperatures for energetic and exergetic optimization, $T_{opt,II}$ and $T_{opt,I}$, can be accurately predicted with the thermal compressor model developed in this study. The investigation of heat and mass transfer coefficients determined that solution side heat transfer coefficients range between

950 - 3250 W m^{-2} K^{-1}. A comparison between model predictions and experimental results showed that *AD* and *ADD* values of 10.6% and 22.7%, respectively. The development of a correlation for binary mixture pool boiling correction factors improved agreement between model predictions and experimental results with *AD* and *AAD* values of 3.5% and 11.1%, respectively, and 94.6% of predicted values falling within ±25% of experimental results.

The system level investigation identified solution pump speed as an effective central control variable for capacity control of an absorption system. This finding was combined with the results from thermodynamic considerations and a parametric study of the heat and mass transfer model to develop a novel control strategy for absorption systems. The *variable speed thermal compressor* controller utilizes pump speed in combination with system specific operating data to maintain set points for evaporator temperature and refrigerant production rate. Responses to variations in operating conditions, e.g., ambient temperatures, and set points changes can be accommodated with this control scheme. Desorption temperature is variable and based on the thermal compressor model as well as operating data. It was shown that this approach eliminates the need for an explicit desorption temperature input. It was also shown that continued performance optimization of the thermal compressor can be achieved with this control scheme. Experimental validation of this control strategy was demonstrated. Fast response to changes in operating conditions, capacity demand and evaporator temperature was shown. The thermal compressor control scheme provides the ability to delineate control aspects unique to absorption systems from the remainder of the cycle. Not only does this simplify absorption system control in general, but it also provides the opportunity to

apply research results from a large body of literature associated with vapor compression system control.

The results from this study can also be applied beyond ammonia-water absorption systems. For example, the development of desorption and rectification components, their hydrodynamic investigation and heat and mass transfer modeling efforts are relevant to other thermal process engineering applications. These applications include various separation and absorption processes such as desalination and distillation at small capacities. Also, the investigation of heat and mass transfer contributes to the limited amount of literature on binary mixture boiling of ammonia-water.

10.2 Recommendations

Several areas of future research are identified. The following research topics build directly on the results of this study and will contribute to further development of thermally activated heat pumps.

System Level Studies:

The primary recommendation is that the findings of this study be applied to the development of small-capacity ammonia-water absorption systems. This includes the validation of performance at the system level, i.e., *COP* improvement. It also includes integration of the control scheme with the refrigerant side of the cycle. The interaction between the refrigerant controller and thermal compressor control is of particular interest. The response to global operating conditions and demand variation while maintaining stability during the interaction of both controllers should be demonstrated. Validation of the control scheme at the system level will enable optimization of cascaded thermal systems with vapor absorption subsystems.

Thermodynamic Models:

The modeling approach for the quantitative performance characterization of the thermal compressor can be extended to other cycle configurations. It is recommended that the statistics based approach be adapted to characterize a thermal compressor for advanced cycle configurations and different working pairs. It is also recommended that the steady-state thermodynamic model be integrated with system characterization to provide a single-layer model instead of the two-layer approach presented in this study. This includes variable heat exchanger effectiveness as a function of operating conditions and system load as well as variable refrigerant vapor ammonia mass fraction.

Hydrodynamic Studies:

Computational Work: Computational simulation of liquid-vapor countercurrent flow in the novel geometries should be investigated. Successful validation of simulation results with experimental studies will facilitate the design and optimization of novel component designs. These simulations have the potential to replace experimental characterization of CCFL. Also, the behavior of hydrodynamic parameters such as interfacial area can be better understood and more accurately characterized. This can eventually contribute to better understanding of heat and mass transfer processes during binary mixture boiling.

Experimental Work: Flow visualization in this study was conducted at adiabatic and ambient conditions with air, water and an ethanol/water mixture. This provided the ability to conservatively characterize CCFL and provide estimates for hydrodynamic parameters relevant to heat and mass transfer. However, it is recommended that flow visualization studies be conducted for typical operating conditions during ammonia-water

desorption. This incorporates the effect of local vapor generation and provides a more suitable baseline for the validation of simulation studies.

Heat and Mass Transfer in Binary Mixture Boiling:

A better understanding of binary mixture boiling is required to improve heat and mass transfer models for binary mixture desorption. A combination of mechanistic modeling and experimental validation is recommended. Understanding of the effect of vapor flow rates in heat and mass transfer during boiling, i.e., the contribution of flow boiling effects, can lead to improved component designs through the application of diabatic bubble trays as presented in this study.

Fabrication and Component Scale-up:

The component design concepts developed in this study are generally applicable for small capacity systems. It is recommended that scale-up of the presented desorption and rectification design concepts be demonstrated for absorption systems with a cooling capacity of up to 10-12 kW. Fabrication of microchannel heat exchanger parts using high-volume manufacturing techniques should also be pursued.

Techno-economic Considerations and Component Fabrication:

Economic viability of potential applications is an essential requirement for the adoption of this technology. It is recommended that detailed techno-economic analyses be conducted for specific potential applications. The tools developed in this study, e.g., quantitative characterization of the thermal compressor module, facilitate these analyses. Also, economic viability depends on the reduction of capital costs. It is recommended that viable and cost effective high-volume manufacturing techniques be investigated and demonstrated.

APPENDIX A. Heat and Mass Transfer Model Sample Calculations

Sample Calculation Heat and Mass Transfer Model		
Inputs	**Equation**	**Result**
Pr_V = 18	$Nu_V = Sh_V \left(\frac{Pr_V}{Sc_V} \right)^{\frac{1}{3}}$	Nu_V = 22.56
Nu_V = 22.56 k_V = 0.039 W m-^{1} K^{-1} D_{bubble} = 0.49×10^{-3} m $D_{aw,V}$ =2.51×10^{-6} m^2 s^{-1}	$\alpha_V = \frac{Nu_V k_V}{D_{bubble}}$ $\beta_V = \frac{Sh_V D_{aw,V}}{D_{bubble}}$	α_V = 180 W m-^{2} K^{-1} β_V = 0.0095 m s^{-1}
$T_{V,avg}$ = 121.6°C P_V = 1878 kPa R_{gas} = 8.314 kJ kmol^{-1} K^{-1}	$C_T = \frac{P_V}{R_{gas} T_V}$	C_T = 0.5722 kmol m^{-3}

Sample Calculation Heat and Mass Transfer Model (continued)		
Inputs	**Equation**	**Result**
M_{NH_3} = 17.03 kg kmol^{-1} M_{H_2O} = 18.02 kg kmol^{-1} $x_{V,int}$ = 0.9415 x_V = 0.9302	$\tilde{x}_{V,int} = \frac{\frac{x_{V,int}}{M_{NH_3}}}{\frac{x_{V,int}}{M_{NH_3}} + \frac{(1-x_{V,int})}{M_{H_2O}}}$ $\tilde{x}_V = \frac{\frac{x_V}{M_{NH_3}}}{\frac{x_V}{M_{NH_3}} + \frac{(1-x_V)}{M_{H_2O}}}$	$\tilde{x}_{V,int}$ = 0.9444 $\tilde{x}_V$ = 0.9337
β_V = 0.0095 m s^{-1} C_T = 0.5722 kmol m^{-3} $\tilde{x}_{V,int}$ = 0.9444 $\tilde{x}_V$ = 0.9337 $\tilde{z}$ = 1.025	$\dot{n}_T = \beta_V C_T \, ln\left(\frac{\tilde{z}-\tilde{x}_{V,int}}{\tilde{z}-\tilde{x}_V}\right)$ $\dot{n}''_{NH_3} = \dot{n}_T \cdot \tilde{z}$ $\dot{n}''_{H_2O} = \dot{n}_T \cdot (1-\tilde{z})$	$\dot{n}_T$ = 6.79×10^{-4} kmol m^{-2} s^{-1} $\dot{n}''_{NH_3}$ = 6.96×10^{-4} kmol m^{-2} s^{-1} $\dot{n}''_{H_2O}$ = -1.70×10^{-5} kmol m^{-2} s^{-1}
M_{NH_3} = 17.03 kg kmol^{-1} M_{H_2O} = 18.02 kg kmol^{-1} $\dot{n}_{NH_3}$ = 6.96×10^{-4} kmol m^{-2} s^{-1} $\dot{n}_{H_2O}$ = -1.70×10^{-5} kmol m^{-2} s^{-1}	$\dot{m}''_{des,NH_3} = M_{NH_3} \cdot \dot{n}_{NH_3}$ $\dot{m}''_{des,H_2O} = M_{H_2O} \cdot \dot{n}_{H_2O}$ $\dot{m}''_{des} = \dot{m}''_{des,H_2O} + \dot{m}''_{des,NH_3}$	$\dot{m}''_{des,NH_3}$ = 1.19×10^{-2} kg m^{-2} s^{-1} $\dot{m}''_{des,H_2O}$ = -3.03×10^{-4} kg m^{-2} s^{-1} $\dot{m}''_{des}$ = 1.16×10^{-3} kg m^{-2} s^{-1}

Sample Calculation Heat and Mass Transfer Model (continued)		
Inputs	**Equation**	**Result**
T_L = 114.9°C $T_{V,in}$ = 124.8°C $T_{V,out}$ = 118.3°C	$LMTD_V = \frac{\left(T_{V,in} - T_L\right) - \left(T_{V,out} - T_L\right)}{\frac{\left(T_{V,in} - T_L\right)}{\left(T_{V,out} - T_L\right)}}$	$LMTD_V$ = 6.127 K
α_V = 180 W m^{-2} K^{-1} A_{int} = 2.27×10^{-3} m^2 $\dot{n}''_{NH_3}$ = 6.96×10^{-4} kmol m^{-2} s^{-1} $\dot{n}''_{H_2O}$ = -1.70×10^{-5} kmol m^{-2} s^{-1} $c_{p,V}$ = 2.8 kJ kg^{-1}	$\phi_V = \frac{\dot{m}''_{des} c_{p,V}}{\alpha_V}$ $\dot{Q}_V = \alpha_V \left(\frac{\phi_V}{1 - e^{-\phi_V}} \right) A_{int} \cdot LMTD_V$	ϕ_V = -0.1798 $\dot{Q}_V$ = 2.7 W
$\dot{m}_{V,in}$ = 1.364×10^{-4} kg s^{-1} $\dot{m}_{V,out}$ = 1.627×10^{-4} kg s^{-1} $T_{V,in}$ = 124.8°C $\dot{Q}_V$ = 2.7 W	$\dot{m}_V = \frac{\dot{m}_{V,in} + \dot{m}_{V,in}}{2}$ $\dot{Q}_V = \dot{m}_V c_{p,V} \left(T_{V,in} - T_{V,out}\right)$	$\dot{m}_V$ = 1.149 kg s^{-1} $T_{V,out}$ = 118.9°C
$\dot{m}_{V,in}$ = 1.364×10^{-4} kg s^{-1} $\dot{m}_{V,in}$ = 1.364×10^{-4} kg s^{-1} $\dot{m}_{V,out}$ = 1.627×10^{-4} kg s^{-1}	$\dot{m}_{V,out} = \dot{m}_{V,in} + \dot{m}''_{des} A_{int}$ $x_{V,out} = \frac{\left(\dot{m}_{V,in} x_{V,in} + \dot{m}''_{des,NH_3} A_{int}\right)}{\dot{m}_{V,out}}$	$\dot{m}_{V,out}$ = 1.627×10^{-4} kg s^{-1} $x_{V,out}$ = 0.9386
$\dot{m}_{V,in}$ = 1.364×10^{-4} kg s^{-1} $\dot{m}_{V,out}$ = 1.627×10^{-4} kg s^{-1} $\dot{m}_{L,in}$ = 1.26×10^{-3} kg s^{-1}	$\dot{m}_{L,out} = \dot{m}_{L,in} + \dot{m}_{V,in} - \dot{m}_{V,out}$	$\dot{m}_{L,out}$ = 1.23×10^{-3} kg s^{-1}

Sample Calculation Heat and Mass Transfer Model (continued)		
Inputs	**Equation**	**Result**
$\dot{m}_{V,in}$ = 1.364×10^{-4} kg s^{-1} $h_{V,in}$ = 1605 kJ kg^{-1} $\dot{m}_{V,out}$ = 1.627×10^{-4} kg s^{-1} $h_{V,out}$ = 1570 kJ kg^{-1} $\dot{m}_{L,in}$ = 1.26×10^{-3} kg s^{-1} $h_{L,in}$ = 286.2 kJ kg^{-1} $\dot{m}_{L,out}$ = 1.23×10^{-3} kg s^{-1} $h_{L,out}$ = 302.7 kJ kg^{-1}	$\dot{Q}_{ext} = \dot{m}_{L,in}h_{L,in} + \dot{m}_{V,in}h_{V,in} - \dot{m}_{V,out}h_{V,out} - \dot{m}_{L,out}h_{L,out}$	$\dot{Q}_{ext}$ = 49.3 W
$\dot{Q}_{ext}$ = 49.3 W A_{sol} = 1.76×10^{-3} m^2	$q'' = \frac{\dot{Q}_{ext}}{A_{sol}}$	q'' = 28072 W m^{-2}
q'' = 28072 W m^{-2} T_L = 114.9°C P_L = 1878 kPa	$\alpha_{NH_3} = f(q'', P_L, T_L)$ $\alpha_{H_2O} = f(q'', P_L, T_L)$	α_{NH_3} = 7492 W m^{-2} K^{-1} α_{H_2O} = 6079 W m^{-2} K^{-1}
α_{NH_3} = 7492 W m^{-2} K^{-1} α_{H_2O} = 6079 W m^{-2} K^{-1} $\tilde{x}_L$ = 0.3908 E = 1 K = 0.9685	$\alpha_{NB,ideal} = \left[\frac{\tilde{x}}{\alpha_{NH_3}} + \frac{1-\tilde{x}}{\alpha_{H_2O}}\right]^{-1}$ $\frac{\alpha_{NB}}{\alpha_{NB,ideal}} = \frac{1}{(1+K)^E}$	α_{H_2O} = 6563 W m^{-2} K^{-1} α_{NB} = 3334 W m^{-2} K^{-1}
α_{NB} = 3334 W m^{-2} K^{-1} A_{sol} = 1.76×10^{-3} m^2	$T_{wall} = \frac{\dot{Q}_{ext}}{\alpha_{NB}A_{sol}} + T_L$	T_{wall} = 123.3°C

APPENDIX B. Data and Uncertainty Analysis

Sample Calculation Thermal Compressor Data Analysis		
Inputs	**Equation**	**Result**
Refrigerant mass flow rate		
$\dot{m}_{cs}$ = 0.007717 ± 0.000007717 kg s^{-1} $\dot{m}_{ds}$ = 0.005707 ± 0.000005707 kg s^{-1}	$\dot{m}_{ref} = \dot{m}_{cs} - \dot{m}_{ds}$	$\dot{m}_{ref}$ = 0.002011 ± 0.000005707 (±0.28%)
Refrigerant vapor ammonia mass fraction		
T_{ref} = 60.73 ± 0.25°C P_{high} = 1889 ± 1.24 kPa q_{ref} = 1	$x_{ref} = f\left(T_{ref}, P_{high}, q_{ref}\right)$	x_{ref} = 0.9983 ± 0.00004686
Dilute solution ammonia mass fraction		
T_{ds} = 136.50 ± 0.25°C P_{high} = 1889 ± 1.24 kPa q_{ds} = 0	$x_{ds} = f\left(T_{ds}, P_{high}, q_{ds}\right)$	x_{ds} = 0.2856 ± 0.001027
Concentrated solution ammonia mass fraction		
$\dot{m}_{cs}$ = 0.007717 ± 0.000007717 kg s^{-1} $\dot{m}_{ds}$ = 0.005707 ± 0.000005707 kg s^{-1} $\dot{m}_{ref}$ = 0.002011 ± 0.000005707 (±0.28%)	$x_{cs} = \frac{\dot{m}_{ref} x_{ref} + \dot{m}_{ds} x_{ds}}{\dot{m}_{cs}}$	x_{cs} = 0.4713 ± 0.001064

Sample Calculation Thermal Compressor Data Analysis (continued)		
Inputs	**Equation**	**Result**
Desorber heat and exergy input		
$\dot{m}_{CF}$ = 0.06574 ± 0.000329 kg s^{-1} $T_{CF,in}$ = 143.00 ± 0.25°C $T_{CF,out}$ = 119.40 ± 0.25°C $\bar{c}_{P,CF}$ = 2.385 ± 0.000759 kJ kg^{-1} K^{-1} T_o = 316.2K	$\dot{Q}_{CF} = \dot{m}_{CF}\bar{c}_{P,CF}\left(T_{CF,in} - T_{CF,out}\right)$ $\Delta Ex_{CF} = \dot{m}_{CF}\bar{c}_{P,CF}\left(\left(T_{CF,in} - T_{CF,out}\right) - T_o \ln\left(\frac{T_{CF,in,K}}{T_{CF,out,K}}\right)\right)$	$\dot{Q}_{CF}$ = 3.69 ± 0.05893 kW ΔEx_{CF} = 0.804 ± 0.01289 kW
Refrigerant flow exergy		
$\dot{m}_{ref}$ = 0.002011 ± 0.000005707 (±0.28%) T_{ref} = 60.73 ± 0.25°C P_{high} = 1889 ± 1.24 kPa q_{ref} = 1 $T_{ref,TC,in}$ = 42.14 ± 0.25°C P_{low} = 540.6 ± 0.413 kPa T_o = 316.2K	$h_{ref} = f\left(T_{ref}, P_{high}, q_{ref}\right)$ $s_{ref} = f\left(T_{ref}, P_{high}, q_{ref}\right)$ $Ex_{ref} = \dot{m}_{ref} h_{ref} - T_o s_{ref}$ $x_{ref,TC,in} = x_{ref}$ $\dot{m}_{ref,TC,in} = \dot{m}_{ref}$ $h_{ref,TC,in} = f\left(T_{ref,TC,in}, P_{low}, x_{ref,TC,in}\right)$ $s_{ref,TC,in} = f\left(T_{ref,TC,in}, P_{low}, x_{ref,TC,in}\right)$ $Ex_{ref,TC,in} = \dot{m}_{ref,TC,in} h_{ref,TC,in} - T_o s_{ref,TC,in}$ $\Delta Ex_{ref} = Ex_{ref} - Ex_{ref,TC,in}$; $\eta_{TC} = \frac{\Delta Ex_{ref}}{\Delta Ex_{CF}}$	h_{ref} = 1341 ± 0.8667 kJ kg^{-1} s_{ref} = 4.24 ± 0.0026 kJ kg^{-1} K^{-1} $x_{ref,TC,in}$ = 0.9983 ± 0.00004686 $\dot{m}_{ref,TC,in}$ = 0.002011 ± 0.000005707 kg s^{-1} $h_{ref,TC,in}$ = 1367 ± 0.0552 kJ kg^{-1} $s_{ref,TC,in}$ = 4.864 ± 0.0004675 kJ kg^{-1} K^{-1} ΔEx_{ref} = 0.3408 ± 0.000903 kW η_{TC} = 42.38 ± 0. 6889 %

Sample calculation Desorber heat loss		
Inputs	**Equation**	**Result**
A_{ins} = 0.2985 m^2 $T_{CF,in}$ = 143.00 ± 0.25°C $T_{CF,out}$ = 119.40 ± 0.25°C th_{ins} = 0.0127 m k_{ins} = 0.04 W m^{-1} K^{-1} $\dot{Q}_{loss,des} = \frac{\left(\bar{T}_{CF} - T_{ins}\right)}{R_{ins}}$ T_{amb} = 25°C T_{ins} = 33.67°C $\dot{Q}_{CF}$ = 3.69 ε_{ins} = 0.8	$\bar{T}_{CF} = \frac{\left(T_{CF,in} + T_{CF,out}\right)}{2}$ $R_{ins} = \frac{th_{ins}}{k_{ins} A_{ins}}$ $\dot{Q}_{loss,des} = \dot{Q}_{loss,des,conv} + \dot{Q}_{loss,des,rad}$ $\dot{Q}_{loss,des,conv} = \frac{\left(T_{ins} - T_{amb}\right)}{R_{conv}}$ $\dot{Q}_{loss,des,rad} = \frac{\left(T_{ins} - T_{amb}\right)}{R_{rad}}$ $R_{conv} = \frac{\alpha_{conv}}{A_{ins}}$ $R_{rad} = \frac{1}{A_{ins}\sigma_{rad}\varepsilon_{ins}\left(T_{ins} + T_{amb}\right)\left(T_{ins}^2 + T_{amb}^2\right)}$ $\dot{Q}_{des} = \dot{Q}_{CF} - \dot{Q}_{des,loss}$	$\bar{T}_{CF}$ = 131.2°C R_{ins} = 0.3175 K W^{-1} R_{rad} = 0.6179 K W^{-1} R_{conv} = 0.1117 K W^{-1} $\dot{Q}_{loss,des}$ = 91.7 W $\dot{Q}_{des}$ = 3.60 kW

Sample Calculation Desorber Component Performance		
Inputs	**Equation**	**Result**
Overall heat transfer coefficient		
A_{ins} = 0.2985 m^2 $T_{CF,in}$ = 143.00 ± 0.25°C $T_{CF,out}$ = 119.40 ± 0.25°C T_{ds} = 136.5 ± 0.25°C T_{cs} = 99.16 ± 0.25°C	$LMTD_{des} = \frac{\left(T_{CF,in} - T_{ds}\right) - \left(T_{CF,out} - T_{cs}\right)}{\ln\left(\frac{T_{CF,in} - T_{ds}}{T_{CF,out} - T_{cs}}\right)}$ $U_{des} = \frac{\dot{Q}_{des}}{A_{des} \cdot LMTD_{des}}$	$LMTD_{des}$ = 12.04 ± 0.297°C U_{des} = 766.6 ± 27.21 W m^{-2} K^{-1}
Overall vapor purification efficiency		
T_{ds} = 136.5 ± 0.25°C T_{cs} = 99.16 ± 0.25°C $T_{V,out,des}$ = 105.2 ± 0.25°C P_{high} = 1889 ± 1.24 kPa $q_{V,in,des}$ = 1 $q_{V,out,des}$ = 1	$x_{V,in,des} = f\left(T_{ds}, P_{high}, q_{V,in,des}\right)$ $x_{V,out,des} = f\left(T_{V,out,des}, P_{high}, q_{V,out,des}\right)$ $x^{*}_{V,out,des} = f\left(T_{cs}, P_{high}, q_{V,out,des}\right)$ $\eta_{pur} = \frac{x_{V,out,des} - x_{V,in,des}}{x^{*}_{V,out,des} - x_{V,in,des}}$	$x_{V,in,des}$ = 0.8631 ± 0.001224 $x_{V,out,des}$ = 0.9629 ± 0.0004547 $x^{*}_{V,out,des}$ = 0.9727 ± 0.0003593 η_{pur} = 91.06 ± 0.5194%

Sample Calculation Desorber Solution Heat Transfer		
Inputs	**Equation**	**Result**
Solution heat transfer coefficient		
$\bar{T}_{CF}$ = 131.2°C th_{wall} = 0.64×10^{-3} m k_{wall} = 16 W m^{-1} K^{-1} $\eta_{fin-array}$ = 0.9622 $D_{h,CF}$ = 3.76×10^{-4} m V_{CF} = 0.286 m^2 s^{-1} k_{CF} = 0.09928 W m^{-1} K^{-1} $\dot{Q}_{des}$ = 3.60 ± 0.059 kW $LMTD_{des}$ = 12.04 ± 0.297°C A_{sol} = 0.3656 ± 0.007827 m^2	$R_{des} = \frac{LMTD_{des}}{\dot{Q}_{des}}$ $R_{wall} = \frac{th_{wall}}{k_{wall} A_{wall}}$ $Nu_{CF} = f(L/D_h, Re_{CF}, Pr_{CF}) \pm 25\%$ (Hong and Bergles, 1976) $Pr_{CF} = \frac{c_{p,CF}\mu_{CF}}{k_{CF}}$ $Re_{CF} = \frac{\rho_{CF} V_{CF} D_{h,CF}}{\mu_{CF}}$ $\alpha_{CF} = \frac{Nu_{CF} k_{CF}}{D_{h,CF}}$ $R_{CF} = \frac{1}{\alpha_{CF} A_{CF} \eta_{fin-array}}$ $R_{CF,wall} = R_{CF} + R_{wall}$ $R_{sol} = R_{des} - R_{CF,wall}$, $\alpha_L = \frac{1}{A_{sol} R_{sol}}$	R_{des} = 0.00346 ± 0.0000876 K W^{-1} Pr_{CF} = 50.37 Re_{CF} = 42.12 Nu_{CF} = 4.533 α_{CF} =1195 W m^{-2} K^{-1} $R_{CF,wall}$ = 0.00212 ± 0.000506 K W^{-1} $R_{CF,wall}$ = 0.00212 ± 0.000506 K W^{-1} α_L = 2231 ± 1084 W m^2 K^{-1}

Sample Calculation Desorber Solution Heat Transfer (continued)		
Inputs	**Equation**	**Result**
Ideal pool boiling heat transfer coefficient		
$\dot{Q}_{des}$ = 3.60 ± 0.059 kW A_{sol} = 0.3656 ± 0.007827 m^2 T_{ds} = 136.5 ± 0.25°C T_{cs} = 99.16 ± 0.25°C P_{high} = 1889 ± 1.24 kPa x_{ds} = 0.2856 ± 0.001027 x_{cs} = 0.4713 ± 0.001064	$q''_{des} = \frac{\dot{Q}_{des}}{A_{sol}}$ $\bar{T}_L = \frac{(T_{cs} + T_{ds})}{2}$ $\alpha_{H_2O,NH_3} = f\left(P_{high}, \bar{T}_L, q''_{des}\right)$ (Mostinski , 1963) $x_{L,bulk} = \frac{(x_{cs} + x_{ds})}{2}$ $\tilde{x}_{L,bulk} = \frac{\bar{x}_L}{M_{NH_3}}\left(\frac{\bar{x}_L}{M_{NH_3}} + \frac{1-\bar{x}_L}{M_{H_2O}}\right)^{-1}$ $\alpha_{L,ideal} = \left[\frac{\tilde{x}_{L,bulk}}{\alpha_{NH_3}} + \frac{1-\tilde{x}_{L,bulk}}{\alpha_{H_2O}}\right]^{-1}$	q''_{des} = 9841 ± 274 W m^{-2} $\bar{T}_L$ = 117.9 ± 0.177°C α_{H_2O} = 3604 ± 70.28 W m^2 K^{-1} α_{NH_3} = 2926 ± 57.06 W m^2 K^{-1} $x_{L,bulk}$ = 0.3716 ± 0.0008201 $\tilde{x}_{L,bulk}$ = 0.3848 ± 0.0008314 $\alpha_{L,ideal}$ = 3309 ± 64.58 W m^2 K^{-1}

Sample Calculation Desorber Solution Heat Transfer (continued)		
Inputs	**Equation**	**Result**
Binary mixture correction factor		
$E = 1$ $\alpha_L = 2231 \pm 1084$ W m^2 K^{-1} $\alpha_{L,ideal} = 3309 \pm 64.58$ W m^2 K^{-1}	$K = \left(\frac{\alpha_{L,ideal}}{\alpha_L} \right)^{\frac{1}{E}} - 1$	$K = 0.4829 \pm 0.6296$

Sample Calculation Desorber Mass Transfer		
Inputs	**Equation**	**Result**
Liquid mass transfer coefficient		
$\bar{T}_L$ = 117.9 ± 0.177°C $\bar{x}_L$ = 0.3716 ± 0.0008201 $\tilde{x}_{L,bulk}$ = 0.3848 ± 0.0008314 P_{high} = 1889 ± 1.24 kPa $q_{L,int}$ = 0 $\dot{m}_{V,out,des}$ = 0.001949 kg s^{-1} $A_{L\text{-}V,int}$ = 0.1035 ± 0.000745 m^2 $\tilde{z}$ = 0.7756±000621	*Interface condition:* $x_{L,int} = f\left(\bar{T}_L, P_{high}, q_{L,int}\right)$ $\tilde{x}_{L,int} = \frac{\tilde{x}_{L,int}}{M_{NH_3}}\left(\frac{\tilde{x}_{L,int}}{M_{NH_3}} + \frac{1-\tilde{x}_{L,int}}{M_{H_2O}}\right)^{-1}$ $\bar{\rho}_L = f\left(\bar{T}_L, P_{high}, q_{L,int}\right)$ $\bar{M}_L = M_{H_2O}\left(1-\tilde{x}_{L,bulk}\right) + M_{NH_3}\tilde{x}_{L,bulk}$ $\dot{n}_T = \frac{\dot{m}_{V,des,out}}{A_{L-V,int}}\left(\tilde{z}\cdot M_{NH_3} + \left(1-\tilde{z}\right)\cdot M_{H_2O}\right)$ $\dot{n}_T = \beta_L \frac{\bar{\rho}_L}{\bar{M}_L}\ln\left(\frac{\tilde{z}-\tilde{x}_{L,int}}{\tilde{z}-\tilde{x}_{L,bulk}}\right)$ $h_{L,int} = f\left(\bar{T}_L, P_{high}, q_{L,int}\right)$	$x_{L,int}$ = 0.3653 ± 0.000807 $\tilde{x}_{L,int}$ = 0.3784 ± 0.000819 $\bar{M}_L$ = 17.65±0.000808 $\dot{n}_T$ = 0.001091±0.000008 kmol m^{-2} s^{-1} β_L = 0.001519±0.00001202 m s^{-1} $h_{L,int}$ = 310.8±0.9936 kJ kg^{-1}

Sample Calculation Desorber Mass Transfer (continued)		
Inputs	**Equation**	**Result**
Vapor mass transfer coefficient		
T_{ds} = 136.5 ± 0.25°C $T_{V,des,out}$ = 105.2 ± 0.25°C $\bar{T}_L$ = 117.9 ± 0.177°C $q_{V,int}$ = 1 $\dot{n}_T$ = 0.001084±0.000008 kmol m^{-2} s^{-1} h_{fg,NH_3} = 1066 kJ kg^{-1} h_{fg,H_2O} = 1905 kJ kg^{-1} P_{high} = 1889 ± 1.24 kPa $\bar{R}$ = 8.314 kJ kmol^{-1} K^{-1}	$\bar{T}_V = \frac{\left(T_{V,des,out} + T_{ds}\right)}{2}$ $x_{V,int} = f\left(\bar{T}_L, P_{high}, q_{V,int}\right)$ $x_{V,bulk} = f\left(\bar{T}_V, P_{high}, q_{V,int}\right)$ $h_{V,int} = f\left(\bar{T}_L, P_{high}, q_{V,int}\right)$ $\tilde{x}_{V,int} = \frac{x_{V,int}}{M_{NH_3}}\left(\frac{x_{V,int}}{M_{NH_3}} + \frac{1-x_{V,int}}{M_{H_2O}}\right)^{-1}$ $\tilde{x}_{V,bulk} = \frac{x_{V,bulk}}{M_{NH_3}}\left(\frac{x_{V,bulk}}{M_{NH_3}} + \frac{1-x_{V,bulk}}{M_{H_2O}}\right)^{-1}$ $h_{latent} = h_{V,int} - h_{L,int}$ $h_{latent} = z \cdot h_{fg,NH_3} + (1-z) \cdot h_{fg,H_2O}$ $\tilde{z} = \frac{z}{M_{NH_3}}\left(\frac{z}{M_{NH_3}} + \frac{1-z}{M_{H_2O}}\right)^{-1}$	$\bar{T}_V$ = 121.2±0.1758 $x_{V,int}$ = 0.9339±0.000501 $x_{V,bulk}$ = 0.9239±0.000556 $h_{V,int}$ = 1573±1.003 kJ kg^{-1} $\tilde{x}_{V,int}$ = 0.9373±0.0004779 $\tilde{x}_{V,bulk}$ = 0.9277±0.0005302 h_{latent} = 1262±0.07664 kJ kg^{-1} z = 0.7657±0.00006402 $\tilde{z}$ = 0.7756±0.0000621 C_T = 0.5761±0.00045 β_V = 0.03111±0.001535 m s^{-1}

Sample Calculation Desorber Mass Transfer (continued)		
Inputs	**Equation**	**Result**
	$C_T = \frac{P_{high}}{\bar{R}\bar{T}_{V,K}}$ $\dot{n}_T = \beta_V C_T \ln\left(\frac{\tilde{z} - \tilde{x}_{V,int}}{\tilde{z} - \tilde{x}_{V,bulk}}\right)$	

REFERENCES

Afram, A. and F. Janabi-Sharifi (2014a). *Review of Modeling Methods for Hvac Systems*.

Afram, A. and F. Janabi-Sharifi (2014b), "Theory and Applications of Hvac Control Systems – a Review of Model Predictive Control (Mpc)," *Building and Environment* Vol. 72 pp. 343–355 DOI: 10.1016/j.buildenv.2013.11.016.

Aiello, V. C. (2016). *Investigation of Fouling Mechanisms to Guide the Design of Diesel Engine Exhaust Driven Absorption Heat Pumps*. Mechanical Engineering. Atlanta, GA, Georgia Institute of Technology, Vol. M.Sc.

Akita, K. and F. Yoshida (1973), "Gas Holdup and Volumetric Mass Transfer Coefficient in Bubble Columns. Effects of Liquid Properties," *Industrial & Engineering Chemistry Process Design and Development* Vol. 12(1) pp. 76-80 DOI: 10.1021/i260045a015.

Akita, K. and F. Yoshida (1974), "Bubble Size, Interfacial Area, and Liquid-Phase Mass Transfer Coefficient in Bubble Columns," *Industrial & Engineering Chemistry Process Design and Development* Vol. 13(1) pp. 84-91 DOI: 10.1021/i260049a016.

Anand, G. and D. C. Erickson (1999), "Compact Sieve-Tray Distillation Column for Ammonia-Water Absorption Heat Pump: Part I--Design Methodology," *ASHRAE Transactions* Vol. 105 p. 796

Aprhornratana, S. and I. W. Eames (1995), "Thermodynamic Analysis of Absorption Refrigeration Cycles Using the Second Law of Thermodynamics Method," *International Journal of Refrigeration* Vol. 18(4) pp. 244-252 DOI: http://dx.doi.org/10.1016/0140-7007(95)00007-X.

Ataer, E. Ö. and Y. Göğüs (1991), "Comparative Study of Irreversibilities in an Aqua-Ammonia Absorption Refrigeration System," *International Journal of Refrigeration* Vol. 14(2) pp. 86-92 DOI: http://dx.doi.org/10.1016/0140-7007(91)90080-Z.

Bell, K. J. and M. A. Ghaly (1972), "Approximate Generalized Design Method for Multicomponent/Partial Condensers," *American Institute of Chemical Engineers, Papers*

Bell, K. J. and M. A. Ghaly (1973). *An Approximate Generalized Design Method for Multicomponent/Partial Condensers*. American Institute of Chemical Engineers Symposium, Vol. 69 pp. 72-79.

Bergman, T. L., F. P. Incropera, D. P. DeWitt and A. S. Lavine (2011). *Fundamentals of Heat and Mass Transfer*, Wiley.

Beutler, A., L. Hoffmann, F. Ziegler, G. Alefeld, K. Gommed, G. Grossman and A. Shavit (1996), "Experimental Investigation of Heat and Mass Transfer on Horizontal and Vertical Tubes," *Proceedings of the International Sorption Heat Pump Conference, 17-20 September 1996, Montreal, Canada*, pp. 409-419.

Blass, E. (1990), "Formation and Coalescence of Bubbles and Droplets," *International chemical engineering* Vol. 30(2) pp. 206-221

Bogart, M. J. P. (1982), "Pitfalls in Ammonia Absorption Refrigeration," *International Journal of Refrigeration* Vol. 5(4) pp. 203-208 DOI: http://dx.doi.org/10.1016/0140-7007(82)90020-2.

Boman, D. B., D. C. Hoysall, M. A. Staedter, A. Goyal, M. J. Ponkala and S. Garimella (2017), "A Method for Comparison of Absorption Heat Pump Working Pairs," *International Journal of Refrigeration* Vol. 77 pp. 149-175

Calderbank, P. H. and M. B. Moo-Young (1961), "The Continuous Phase Heat and Mass-Transfer Properties of Dispersions," *Chemical Engineering Science* Vol. 16(1) pp. 39-54 DOI: http://dx.doi.org/10.1016/0009-2509(61)87005-X.

Cao, T., H. Lee, Y. Hwang, R. Radermacher and H.-H. Chun (2015), "Performance Investigation of Engine Waste Heat Powered Absorption Cycle Cooling System for Shipboard Applications," *Applied Thermal Engineering* Vol. 90(Supplement C) pp. 820-830 DOI: https://doi.org/10.1016/j.applthermaleng.2015.07.070.

Chaumat, H., A. M. Billet-Duquenne, F. Augier, C. Mathieu and H. Delmas (2005), "Mass Transfer in Bubble Column for Industrial Conditions—Effects of Organic Medium, Gas and Liquid Flow Rates and Column Design," *Chemical Engineering Science* Vol. 60(22) pp. 5930-5936 DOI: http://dx.doi.org/10.1016/j.ces.2005.04.026.

Chen, L., T. Zheng, F. Sun and C. Wu (2006), "Irreversible Four-Temperature-Level Absorption Refrigerator," *Solar Energy* Vol. 80(3) pp. 347-360 DOI: http://dx.doi.org/10.1016/j.solener.2005.01.013.

Chisholm, D. (1967), "A Theoretical Basis for the Lockhart-Martinelli Correlation for Two-Phase Flow," *International Journal of Heat and Mass Transfer* Vol. 10(12) pp. 1767-1778 DOI: https://doi.org/10.1016/0017-9310(67)90047-6.

Churchill, S. W. (1977a), "Comprehensive Correlating Equations for Heat, Mass and Momentum Transfer in Fully Developed Flow in Smooth Tubes," *Industrial & Engineering Chemistry Fundamentals* Vol. 16(1) pp. 109-116 DOI: 10.1021/i160061a021.

Churchill, S. W. (1977b), "Friction Factor Equation Spanning All Fluid Flow Regimes," *Chemical Engineering (New York)* Vol. 84(24) pp. 91-92

Clift, R., J. R. Grace and M. E. Weber (1978). *Bubbles, Drops, and Particles*, Academic Press.

Colburn, A. P. and T. B. Drew (1937), "The Condensation of Mixed Vapours," *AIChE Transactions* Vol. 33 pp. 197-212

Colombet, D., D. Legendre, A. Cockx and P. Guiraud (2013), "Mass or Heat Transfer inside a Spherical Gas Bubble at Low to Moderate Reynolds Number," *International Journal of Heat and Mass Transfer* Vol. 67 pp. 1096-1105 DOI: http://dx.doi.org/10.1016/j.ijheatmasstransfer.2013.08.069.

Conde, M. (2006). Thermophysical Properties of Ammonia-Water Mixtures for the Industrial Design of Absorption Refrigeration Equipmentp.

Cuenca, Y., D. Salavera, A. Vernet and M. Vallès (2013), "Thermal Conductivity of Ammonia + water Mixtures over a Wide Range of Concentrations," *International Journal of Refrigeration* Vol. 36(3) pp. 998-1003 DOI: http://dx.doi.org/10.1016/j.ijrefrig.2012.10.039.

Davidson, J. F. and B. O. G. Schüler (1960), "Bubble Formation at an Orifice in a Viscous Liquid," *Trans. Inst. Chem. Engrs* Vol. 38 pp. 335-342

de Koeijer, G. and R. Rivero (2003), "Entropy Production and Exergy Loss in Experimental Distillation Columns," *Chemical Engineering Science* Vol. 58(8) pp. 1587-1597 DOI: http://dx.doi.org/10.1016/S0009-2509(02)00627-9.

de Koeijer, G., A. Røsjorde and S. Kjelstrup (2004), "Distribution of Heat Exchange in Optimum Diabatic Distillation Columns," *Energy* Vol. 29(12–15) pp. 2425-2440 DOI: http://dx.doi.org/10.1016/j.energy.2004.03.034.

de Koeijer, G. M., S. Kjelstrup, P. Salamon, G. Siragusa, M. Schaller and K. H. Hoffmann (2002), "Comparison of Entropy Production Rate Minimization Methods for Binary Diabatic Distillation," *Industrial & Engineering Chemistry Research* Vol. 41(23) pp. 5826-5834 DOI: 10.1021/ie010872p.

Deendarlianto, T. Höhne, D. Lucas and K. Vierow (2012), "Gas–Liquid Countercurrent Two-Phase Flow in a Pwr Hot Leg: A Comprehensive Research Review," *Nuclear Engineering and Design* Vol. 243 pp. 214-233 DOI: http://dx.doi.org/10.1016/j.nucengdes.2011.11.015.

Delahanty, J. C., S. Garimella and M. A. Garrabrant (2015), "Design of Compact Microscale Geometries for Ammonia–Water Desorption," *Science and Technology for the Built Environment* Vol. 21(3) pp. 365-374 DOI: 10.1080/23744731.2015.1015906.

Determan, M. D. and S. Garimella (2011), "Ammonia–Water Desorption Heat and Mass Transfer in Microchannel Devices," *International Journal of Refrigeration* Vol. 34(5) pp. 1197-1208 DOI: http://dx.doi.org/10.1016/j.ijrefrig.2011.02.004.

Determan, M. D. and S. Garimella (2012), "Design, Fabrication, and Experimental Demonstration of a Microscale Monolithic Modular Absorption Heat Pump," *Applied Thermal Engineering* Vol. 47 pp. 119-125 DOI: http://dx.doi.org/10.1016/j.applthermaleng.2011.10.043.

Dincer, I. and S. Dost (1996), "A Simple Model for Heat and Mass Transfer in Absorption Cooling Systems (Acss)," *International Journal of Energy Research* Vol. 20(3) pp. 237-243

Engler, M., G. Grossman and H. M. Hellmann (1997), "Comparative Simulation and Investigation of Ammonia-Water: Absorption Cycles for Heat Pump Applications," *International Journal of Refrigeration* Vol. 20(7) pp. 504-516 DOI: http://dx.doi.org/10.1016/S0140-7007(97)00038-8.

Fernandez-Seara, J. and J. Sieres (2006), "The Importance of the Ammonia Purification Process in Ammonia-Water Absorption Systems," *Energy Conversion and Management* Vol. 47(13-14) pp. 1975-1987 DOI: DOI 10.1016/j.enconman.2005.09.002.

Fernandez-Seara, J., J. Sieres and M. Vazquez (2003), "Distillation Column Configurations in Ammonia-Water Absorption Refrigeration Systems," *International Journal of Refrigeration*(1) p. 28 DOI: 10.1016/S0140-7007(02)00037-3.

Fernández-Seara, J., J. Sieres and M. Vázquez (2002), "Simultaneous Heat and Mass Transfer of a Packed Distillation Column for Ammonia–Water Absorption Refrigeration Systems," *International Journal of Thermal Sciences* Vol. 41(10) pp. 927-935 DOI: http://dx.doi.org/10.1016/S1290-0729(02)01385-6.

Frank, M. J. W., J. A. M. Kuipers and W. P. M. van Swaaij (1996), "Diffusion Coefficients and Viscosities of Co2 + H2o, Co2 + Ch3oh, Nh3 + H2o, and Nh3 +

Ch3oh Liquid Mixtures," *Journal of Chemical & Engineering Data* Vol. 41(2) pp. 297-302 DOI: 10.1021/je950157k.

Fujita, Y. and M. Tsutsui (1997), "Heat Transfer in Nucleate Boiling of Binary Mixtures: Development of a Heat Transfer Correlation," *JSME International Journal Series B Fluids and Thermal Engineering* Vol. 40(1) pp. 134-141

Gandhi, A. B., P. P. Gupta, J. B. Joshi, V. K. Jayaraman and B. D. Kulkarni (2009), "Development of Unified Correlations for Volumetric Mass-Transfer Coefficient and Effective Interfacial Area in Bubble Column Reactors for Various Gas−Liquid Systems Using Support Vector Regression," *Industrial & Engineering Chemistry Research* Vol. 48(9) pp. 4216-4236 DOI: 10.1021/ie8003489.

Garimella, S. (1999). *Miniaturized Heat and Mass Transfer Technology for Absorption Heat Pumps*. Proceedings of the International Sorption Heat Pump Conference. Munich, Germany, March 24-26 1999 pp. 661-670.

Garimella, S. (2003), "Innovations in Energy Efficient and Environmentally Friendly Space-Conditioning Systems," *Energy* Vol. 28(15) pp. 1593-1614 DOI: http://dx.doi.org/10.1016/S0360-5442(03)00120-8.

Garimella, S., R. N. Christensen and D. Lacy (1996), "Performance Evaluation of a Generator-Absorber Heat-Exchange Heat Pump," *Applied Thermal Engineering* Vol. 16(7) pp. 591-604 DOI: http://dx.doi.org/10.1016/1359-4311(95)00041-0.

Garimella, S., C. M. Keinath, J. C. Delahanty, D. C. Hoysall, M. A. Staedter, A. Goyal and M. A. Garrabrant (2016), "Development and Demonstration of a Compact Ammonia–Water Absorption Heat Pump Prototype with Microscale Features for Space-Conditioning Applications," *Applied Thermal Engineering* Vol. 102(Supplement C) pp. 557-564. DOI: https://doi.org/10.1016/j.applthermaleng.2016.03.169.

Ghiaasiaan, S. M. (2007). *Two-Phase Flow, Boiling, and Condensation: In Conventional and Miniature Systems*, Cambridge University Press.

Gómez-Díaz, D., J. M. Navaza and B. Sanjurjo (2008), "Interfacial Area Evaluation in a Bubble Column in the Presence of a Surface-Active Substance: Comparison of Methods," *Chemical Engineering Journal* Vol. 144(3) pp. 379-385 DOI: http://dx.doi.org/10.1016/j.cej.2008.02.002.

Gordon, J. M. and K. C. Ng (1995), "A General Thermodynamic Model for Absorption Chillers: Theory and Experiment," *Heat Recovery Systems and CHP* Vol. 15(1) pp. 73-83 DOI: http://dx.doi.org/10.1016/0890-4332(95)90038-1.

Gorenflo, D. (1993). *Pool Boiling*. VDI Waermeatlas, Dusseldorf, Germany.

Goyal, A., A. S. Rattner and S. Garimella (2015), "Model-Based Feedback Control of an Ammonia-Water Absorption Chiller," *Science and Technology for the Built Environment* Vol. 21(3) pp. 357-364 DOI: 10.1080/10789669.2014.982412.

Goyal, A., M. A. Staedter and S. Garimella (2018), "Control of Absorption Systems: A Review," *Renewable & Sustainable Energy Reviews* Vol. In review.

Grossman, G. (1994). *Modular and Flexible Simulation of Advanced Absorption Systems*. International Absorption Heat Pump Conference, Jan 19-21, 1994. New Orleans, United States, Vol. 31 pp. 345-352.

Hellmann, H.-M. and F. F. Ziegler (1999), "Simple Absorption Heat Pump Modules for System Simulation Programs," *ASHRAE Transactions* Vol. 105 pp. 780-787

Herold, K. E., R. Radermacher and S. A. Klein (1996). *Absorption Chillers and Heat Pumps*, Taylor & Francis.

Hewitt, G. F., G. L. Shires and T. R. Bott (1994). *Process Heat Transfer*, CRC Press.

Hikita, H., S. Asai, K. Tanigawa, K. Segawa and M. Kitao (1980), "Gas Hold-up in Bubble Columns," *The Chemical Engineering Journal* Vol. 20(1) pp. 59-67 DOI: http://dx.doi.org/10.1016/0300-9467(80)85006-4.

Hong, S. W. and A. E. Bergles (1976), "Augmentation of Laminar Flow Heat Transfer in Tubes by Means of Twisted-Tape Inserts," *Journal of Heat Transfer* Vol. 98(2) pp. 251-256 DOI: 10.1115/1.3450527.

Horuz, I. (1999), "Vapor Absorption Refrigeration in Road Transport Vehicles," *Journal of Energy Engineering* Vol. 125(2) pp. 48-58 DOI: 10.1061/(ASCE)0733-9402(1999)125:2(48).

Hoysall, D. C., K. Keniar and S. Garimella (2017), "Visualization of Two-Phase Flow in Serpentine Heat Exchanger Passages with Microscale Pin Fins," *Journal of Heat Transfer* Vol. 140(1) pp. 011802-011802-011809 DOI: 10.1115/1.4037342.

Hu, X. and A. M. Jacobi (1996), "The Intertube Falling Film: Part 2—Mode Effects on Sensible Heat Transfer to a Falling Liquid Film," *Journal of Heat Transfer* Vol. 118(3) pp. 626-633 DOI: 10.1115/1.2822678.

Ibrahim, O. M. and S. A. Klein (1993), "Thermodynamic Properties of Ammonia-Water Mixtures," *ASHRAE Transactions* Vol. Symposia, CH-93-21-2 (1993) pp. 1495–1502

Idogawa, K., H. Ikeda, T. Fukuda and S. Morooka (1987), "Formation and Flow of Gas Bubbles in a Pressurized Bubble Column with a Single Orifice or Nozzle Gas Distributor," *Chemical Engineering Communications* Vol. 59(1-6) pp. 201-212 DOI: 10.1080/00986448708911995.

Imroz Sohel, M. and B. Dawoud (2006), "Dynamic Modelling and Simulation of a Gravity-Assisted Solution Pump of a Novel Ammonia–Water Absorption Refrigeration Unit," *Applied Thermal Engineering* Vol. 26(7) pp. 688-699 DOI: http://dx.doi.org/10.1016/j.applthermaleng.2005.09.006.

Incropera, F. P. and D. P. DeWitt (1996). *Fundamentals of Heat and Mass Transfer, (1996)*, John Wiley & Sons Inc., New York.

Inoue, T., N. Kawae and M. Monde (1998), "Characteristics of Heat Transfer Coefficient During Nucleate Pool Boiling of Binary Mixtures," *Heat and Mass Transfer* Vol. 33(4) pp. 337-344 DOI: 10.1007/s002310050199.

Inoue, T., M. Monde, Y. Teruya and H. Ikeda (2002), "Pool Boiling Heat Transfer in Binary Mixtures of Ammonia/Water: Effect of Heat of Dilution and Dissolution on Heat Transfer Coefficient," *Heat Transfer—Asian Research* Vol. 31(4) pp. 272-283 DOI: 10.1002/htj.10034.

Kang, Y. T., Y. Kunugi and T. Kashiwagi (2000), "Review of Advanced Absorption Cycles: Performance Improvement and Temperature Lift Enhancement," *International Journal of Refrigeration* Vol. 23(5) pp. 388-401 DOI: http://dx.doi.org/10.1016/S0140-7007(99)00064-X.

Kantarci, N., F. Borak and K. O. Ulgen (2005), "Bubble Column Reactors," *Process Biochemistry* Vol. 40(7) pp. 2263-2283 DOI: http://dx.doi.org/10.1016/j.procbio.2004.10.004.

Keinath, C., D. Hoysall, J. Delahanty, M. Determan and S. Garimella (2014). *Experimental Assessment of a Compact Branched Tray Generator for Ammonia-Water Desoprtion*. Proceedings of the International Sorption Heat Pump Conference. College Park, Maryland, USA, March 31 – April 2, 2014.

Keinath, C. M., S. Garimella and M. A. Garrabrant (2017), "Modeling of an Ammonia–Water Absorption Heat Pump Water Heater for Residential Applications," *International Journal of Refrigeration* Vol. 83(Supplement C) pp. 39-50 DOI: https://doi.org/10.1016/j.ijrefrig.2017.06.007.

Keinath, C. M., D. Hoysall, J. C. Delahanty, M. D. Determan and S. Garimella (2015), "Experimental Assessment of a Compact Branched Tray Generator for Ammonia–Water Desorption," *Science and Technology for the Built Environment* Vol. 21(3) pp. 348-356 DOI: 10.1080/23744731.2014.1000797.

Klein, S. A. (2015), "Engineering Equation Solver," *V9.911 F-Chart Software.*

Kolev, N., S. Nakov, L. Ljutzkanov and D. Kolev (2006), "Comparison of the Effective Surface Area of Some Highly Effective Random Packings Third and Fourth Generation," *I.ChemE Symposium Series* Vol. 152 pp. 754 - 763.

Kotas, T. J. (2013). *The Exergy Method of Thermal Plant Analysis*, Elsevier.

Kren, C. (2006), "Flue Gas Fired Absorption Chillers,"

Kühn, A. and F. Ziegler (2005). *Operational Results of a 10kw Absorption Chiller and Adaptation to the Characteristic Equation*. International Conference of Solar Air Conditioning Bad Staffelstein, Germany, 6-7, October 2005.

Kulkarni, A. A. and J. B. Joshi (2005), "Bubble Formation and Bubble Rise Velocity in Gas−Liquid Systems: A Review," *Industrial & Engineering Chemistry Research* Vol. 44(16) pp. 5873-5931 DOI: 10.1021/ie049131p.

Lau, R., R. Mo and W. S. Beverly Sim (2010), "Bubble Characteristics in Shallow Bubble Column Reactors," *Chemical Engineering Research and Design* Vol. 88(2) pp. 197-203 DOI: http://dx.doi.org/10.1016/j.cherd.2009.07.008.

Lee, S., L. K. Bohra and S. Garimella (2008). *In-Situ Measurement of Absorption Rates in Horizontal-Tube Falling-Film Ammonia-Water Absorbers: Part I– Measurement Technique*. International Refrigeration and Air Conditioning Conference at Purdue, July 12-17, 2008. West Lafayette, IN Purdue University.

Lockhart, R. W., and Martinelli, R. C. (1949), "Proposed Correlation of Data for Isothermal Two-Phase, Two-Component Flow in Pipes," *Chemical Engineering Progress* Vol. 45(1) pp. 39-45

Martin, H. (1977), "Heat and Mass Transfer between Impinging Gas Jets and Solid Surfaces," *Advances in heat transfer* Vol. 13 pp. 1-60

MathWorks, I. (2017). *Matlab : The Language of Technical Computing : Computation, Visualization, Programming - Neural Network Toolbox™*, Natwick : Math Works Inc., 2017.

Meacham, J. and S. Garimella (2002). *Experimental Demonstration of a Prototype Microchannel Absorber for Space-Conditioning Systems*. International Sorption Heat Pump Conference. Shanghai, China, 24-27 September 2002 pp. 270–276.

Mendelson, H. D. (1967), "The Prediction of Bubble Terminal Velocities from Wave Theory," *AIChE Journal* Vol. 13(2) pp. 250-253 DOI: 10.1002/aic.690130213.

Mills, A. (1995). *Heat and Mass Transfer*, Taylor & Francis.

Morosuk, T. and G. Tsatsaronis (2008), "A New Approach to the Exergy Analysis of Absorption Refrigeration Machines," *Energy* Vol. 33(6) pp. 890-907

Morosuk, T. and G. Tsatsaronis (2013), "Strengths and Limitations of Advanced Exergetic Analyses," *Proceedings of the ASME 2013 International Mechanical Engineering Congress and Exposition IMECE2013 November 15-21, 2013, San Diego, California, USA*

Moser, H. and R. Rieberer (2006). *Biomassebetriebene Absorptions-Wärmepump-Anlage Zum Heizen Und Kühlen (Bioawp)*. Deutsche Kälte-Klima-Tagung 2006 Dresden, Germany p. II.1.20

Mostinski, I. L. (1963), "Application of the Rule of Corresponding States for Calculation of Heat Transfer and Critical Heat Flux," *Teploenergetika*(4) p. 66

Murphree, E. V. (1925), "Rectifying Column Calculations," *Industrial & Engineering Chemistry* Vol. 17(7) pp. 747-750 DOI: 10.1021/ie50187a044.

Nagavarapu, A. K. (2012). *Binary Fluid Heat and Mass Exchange at the Microscales in Internal and External Ammoniawater Absorption*. Mechanical Engineering Atlanta, GA USA, Georgia Institute of Technology, Vol. PhD p. 448.

Nagavarapu, A. K. and S. Garimella (2011), "Design of Microscale Heat and Mass Exchangers for Absorption Space Conditioning Applications," *Journal of Thermal Science and Engineering Applications* Vol. 3(2) pp. 021005-021005 DOI: 10.1115/1.4003720.

Naidu, D. S. and C. G. Rieger (2011a), "Advanced Control Strategies for Heating, Ventilation, Air-Conditioning, and Refrigeration Systems—an Overview: Part I: Hard Control," *HVAC&R Research* Vol. 17(1) pp. 2-21 DOI: 10.1080/10789669.2011.540942.

Naidu, D. S. and C. G. Rieger (2011b), "Advanced Control Strategies for Hvac&R Systems—an Overview: Part Ii: Soft and Fusion Control," *HVAC&R Research* Vol. 17(2) pp. 144-158 DOI: 10.1080/10789669.2011.555650.

Onda, K., H. Takeuchi and Y. Okumoto (1968), "Mass Transfer Coefficients between Gas and Liquid Phases in Packed Column," *Journal of Chemical Engineering of Japan* Vol. 1(1) pp. 56-62 DOI: 10.1252/jcej.1.56.

Osakabe, M. and Y. Kawasaki (1989), "Top Flooding in Thin Rectangular and Annular Passages," *International Journal of Multiphase Flow* Vol. 15(5) pp. 747-754 DOI: http://dx.doi.org/10.1016/0301-9322(89)90038-4.

Ousaka, A., A. Kariyasaki and T. Fukano (2006), "Prediction of Flooding Gas Velocity in Gas–Liquid Counter-Current Two-Phase Flow in Inclined Pipes," *Nuclear engineering and design* Vol. 236(12) pp. 1282-1292

Oyevaar, M. H. and K. R. Westerterp (1989), "Mass Transfer Phenomena and Hydrodynamics in Agitated Gas—Liquid Reactors and Bubble Columns at Elevated Pressures: State of the Art," *Chemical Engineering and Processing: Process Intensification* Vol. 25(2) pp. 85-98 DOI: http://dx.doi.org/10.1016/0255-2701(89)80034-0.

Perrotin, T. and D. Clodic (2003), "Fin Efficiency Calculation in Enhanced Fin-and-Tube Heat Exchangers in Dry Conditions," *International Congress of Refrigeration*, Citeseer, pp. 17-22.

Pohorecki, R., W. Moniuk, P. Bielski and P. Sobieszuk (2005), "Diameter of Bubbles in Bubble Column Reactors Operating with Organic Liquids," *Chemical*

Engineering Research and Design Vol. 83(7 A) pp. 827-832 DOI: 10.1205/cherd.04340.

Polli, M., M. D. Stanislao, R. Bagatin, E. A. Bakr and M. Masi (2002), "Bubble Size Distribution in the Sparger Region of Bubble Columns," *Chemical Engineering Science* Vol. 57(1) pp. 197-205 DOI: http://dx.doi.org/10.1016/S0009-2509(01)00301-3.

Ponkala, M., A. Goyal, M. A. Staedter and S. Garimella (2018), "A Packaged Waste-Heat Driven Chiller for Severe Ambient Conditions," *Manuscript in preparation*

Price, B. C. and K. J. Bell (1974), ""Design of Binary Vapor Condensers Using the Colburn-Drew Equations," *AIChE Symposium Series - Heat Transfer - Research and Design* Vol. 70(138) pp. 163-171

Priedeman, D. K., M. A. Garrabrant, J. A. Mathias, R. E. Stout and R. N. Christensen (2001), "Performance of a Residential Sized Gax Absorption Chiller," *Journal of Energy Resources Technology* Vol. 123(9) pp. 236-241

Puig-Arnavat, M., J. López-Villada, J. C. Bruno and A. Coronas (2010), "Analysis and Parameter Identification for Characteristic Equations of Single- and Double-Effect Absorption Chillers By means of Multivariable Regression," *International Journal of Refrigeration* Vol. 33(1) pp. 70-78 DOI: http://dx.doi.org/10.1016/j.ijrefrig.2009.08.005.

Qin, X., L. Chen, F. Sun and L. He (2007), "Model of Real Absorption Heat Pump Cycle with a Generalized Heat Transfer Law and Its Performance," *Proceedings of the Institution of Mechanical Engineers, Part A: Journal of Power and Energy* Vol. 221(7) pp. 907-916 DOI: 10.1243/09576509JPE424.

Rose, J., Y. Utaka and I. Tanasawa (1999). Dropwise Condensation. *Handbook of Phase Change: Boiling and Condensation*. M. S. S. G. Kandlikar and V. K. Dhir. Philadelphia, PA, Taylor and Francis pp. 581-594.

Rossa, J. and E. Bazzo (2009), "Thermodynamic Modeling of an Ammonia-Water Absorption System with a Microturbine," *International Journal to Thermodynamics* Vol. 12(1) pp. 38-43

Schäfer, R., C. Merten and G. Eigenberger (2002), "Bubble Size Distributions in a Bubble Column Reactor under Industrial Conditions," *Experimental Thermal and Fluid Science* Vol. 26(6–7) pp. 595-604 DOI: http://dx.doi.org/10.1016/S0894-1777(02)00189-9.

Schlünder, E. U. (1982), "Heat Transfer in Nucleate Boiling of Mixtures," *International Chemical Engineering* Vol. 23 p. 589e599.

Schubert, K., J. Brandner, M. Fichtner, G. Linder, U. Schygulla and A. Wenka (2001), "Microstructure Devices for Applications in Thermal and Chemical Process Engineering," *Microscale Thermophysical Engineering* Vol. 5(1) pp. 17-39 DOI: 10.1080/108939501300005358.

Schumpe, A. and W. D. Deckwer (1982), "Gas Holdups, Specific Interfacial Areas, and Mass Transfer Coefficients of Aerated Carboxymethyl Cellulose Solutions in a Bubble Column," *Industrial & Engineering Chemistry Process Design and Development* Vol. 21(4) pp. 706-711 DOI: 10.1021/i200019a028.

Shah, Y. T., B. G. Kelkar, S. P. Godbole and W. D. Deckwer (1982), "Design Parameters Estimations for Bubble Column Reactors," *AIChE Journal* Vol. 28(3) pp. 353-379 DOI: 10.1002/aic.690280302.

Sieres, J. and J. Fernández-Seara (2007), "Mass Transfer Characteristics of a Structured Packing for Ammonia Rectification in Ammonia–Water Absorption Refrigeration Systems," *International Journal of Refrigeration* Vol. 30(1) pp. 58-67 DOI: http://dx.doi.org/10.1016/j.ijrefrig.2006.04.009.

Silver, L. (1947), "Gas Cooling with Aqueous Condensation," *Industrial Chemist and Chemical Manifacturer* Vol. 23(269) pp. 380-386

Sparrow, E. M. and A. Haji-Sheikh (1965), "Laminar Heat Transfer and Pressure Drop in Isosceles Triangular, Right Triangular, and Circular Sector Ducts," *ASME J. Heat Transfer* Vol. 87 pp. 426–427

Stephan, K. and M. Abdelsalam (1980), "Heat Transfer Correlation for Natural Convection Boiling," *International Journal of Heat and Mass Transfer* Vol. 23 pp. 73-87

Stephan, K. and M. Körner (1969), "Berechnung Des Wärmeübergangs Verdampfender Binärer Flüssigkeitsgemische," *Chemie Ingenieur Technik* Vol. 41(7) pp. 409-417 DOI: 10.1002/cite.330410702.

Táboas, F., M. Vallès, M. Bourouis and A. Coronas (2007), "Pool Boiling of Ammonia/Water and Its Pure Components: Comparison of Experimental Data in the Literature with the Predictions of Standard Correlations," *International Journal of Refrigeration* Vol. 30(5) pp. 778-788 DOI: http://dx.doi.org/10.1016/j.ijrefrig.2006.12.009.

Táboas, F., M. Vallès, M. Bourouis and A. Coronas (2010), "Flow Boiling Heat Transfer of Ammonia/Water Mixture in a Plate Heat Exchanger," *International Journal of Refrigeration* Vol. 33(4) pp. 695-705 DOI: http://dx.doi.org/10.1016/j.ijrefrig.2009.12.005.

Talbi, M. and B. Agnew (2002), "Energy Recovery from Diesel Engine Exhaust Gases for Performance Enhancement and Air Conditioning," *Applied Thermal Engineering* Vol. 22(6) pp. 693-702 DOI: https://doi.org/10.1016/S1359-4311(01)00120-X.

Taylor, B. N. and C. E. Kuyatt (1994). *Guidelines for Evaluating and Expressing the Uncertainty of Nist Measurement Results*.

Thome, J. R. and S. Shakir (1987). A New Correlation for Nucleate Pool Boiling of Aqueous Mixtures. *Heat Transfer: Pittsburgh 1987*.

Thorat, B. N., A. V. Kulkarni and J. B. Joshi (2001), "Design of Sieve Plate Spargers for Bubble Columns: Role of Weeping," *Chemical engineering & technology* Vol. 24(8) pp. 815-828

Tsatsaronis, G. (1999). Strengths and Limitations of Exergy Analysis. *Thermodynamic Optimization of Complex Energy Systems*. A. Bejan and E. Mamut. Dordrecht, Springer Netherlands pp. 93-100.

Vazquez, G., E. Alvarez and J. M. Navaza (1995), "Surface Tension of Alcohol Water and Water from 20 to 50 Deg C," *Journal of Chemical & Engineering Data* Vol. 40(3) pp. 611-614 DOI: 10.1021/je00019a016.

Wallis, G. B. (1969). *One-Dimensional Two-Phase Flow*, McGraw-Hill.

Webb, D. R., M. Fahrner and R. Schwaab (1996), "The Relationship between the Colburn and Silver Methods of Condenser Design," *International Journal of Heat and Mass Transfer* Vol. 39(15) pp. 3147-3156 DOI: http://dx.doi.org/10.1016/0017-9310(96)00001-4.

Whitaker, S. (1972), "Forced Convection Heat Transfer Correlations for Flow in Pipes, Past Flat Plates, Single Cylinders, Single Spheres, and for Flow in Packed Beds and Tube Bundles," *AIChE Journal* Vol. 18(2) pp. 361-371 DOI: 10.1002/aic.690180219.

Wijn, E. F. (1999), "Weir Flow and Liquid Height on Sieve and Valve Trays," *Chemical Engineering Journal* Vol. 73(3) pp. 191-204

Winterson, R. H. S. (1994), "A Simple Method of Predicting Bubble Size in Bubble Columns," *Chemical Engineering and Processing: Process Intensification* Vol. 33(1) pp. 1-5 DOI: http://dx.doi.org/10.1016/0255-2701(94)87001-2.

Zapke, A. and D. G. Kröger (2000), "Countercurrent Gas–Liquid Flow in Inclined and Vertical Ducts — Ii: The Validity of the Froude–Ohnesorge Number Correlation for Flooding," *International Journal of Multiphase Flow* Vol. 26(9) pp. 1457-1468 DOI: http://dx.doi.org/10.1016/S0301-9322(99)00098-1.

Zavaleta-Aguilar, E. W. and J. R. Simões-Moreira (2012), "Thermal Design of a Tray-Type Distillation Column of an Ammonia/Water Absorption Refrigeration Cycle," *Applied Thermal Engineering* Vol. 41 pp. 52-60 DOI: http://dx.doi.org/10.1016/j.applthermaleng.2011.12.009.

Zetsche, M., T. Koller, T. Brendel and K. Spindler (2010). *Entwicklung Einer Ammoniak/Wasser Kaelteanlage Zur Solaren Kuehlung - Abschliessende Bewertung*. Deutsche Kälte-Klima-Tagung 2006 Magdeburg, Germany p. AA.II.1.17.

Ziegler, F. (2002), "State of the Art in Sorption Heat Pumping and Cooling Technologies," *International Journal of Refrigeration* Vol. 25(4) pp. 450-459 DOI: http://dx.doi.org/10.1016/S0140-7007(01)00036-6.

Zotter, G. and R. Rieberer (2015), "Experimental Analysis of a Novel Concept of a "Thermally Driven" Solution Pump Operating a Small-Capacity Ammonia/Water Absorption Heat Pumping System," *International Journal of Refrigeration* Vol. 60 pp. 190-205 DOI: http://dx.doi.org/10.1016/j.ijrefrig.2015.06.024.

Žukauskas, A. and R. Ulinskas (1985), "Efficiency Parameters for Heat Transfer in Tube Banks," *Heat Transfer Engineering* Vol. 6(1) pp. 19-25 DOI: 10.1080/01457638508939614.